UNIVERSITY OF SOUTHERN QUEENSLAND
AUSTRALIA

DEVELOPMENT OF RIGOROUS METHODS IN FLUID MECHANICS AND THEORY OF WATER WAVES

A Thesis submitted by
Andrei Ermakov,
BAppMaths, MThAppMech

For the award of
Doctor of Philosophy

2019

ABSTRACT

The thesis consists of five chapters where the following problems are considered – the transformation of long linear waves in an ocean with a variable depth; long wave scattering in a canal with a rapidly varying cross-section; long linear surface waves on stationary currents in a canal of constant depth and variable width; and a resonant interaction of a solitary wave with external pulse-type perturbations within the framework of forced Korteweg-de Vries equation.

Chapter 1 reviews the history of these problems, and notes previous literature and research in this area.

In Chapter 2, the transformation of long linear waves in an ocean of a variable depth is studied. The transformation coefficients are considered as functions of frequency and the total depth drop for three typical models of bottom profile variation: piecewise linear, piecewise quadratic and hyperbolic tangent profiles. The results obtained for all these profiles are analysed and compared from the physical point of view.

In Chapter 3, long wave scattering in a canal with a rapidly varying cross-section is studied. The scattering coefficients are calculated for all possible incident wave orientations (background current downstream and upstream with respect to the background flow); and current types subcritical, transcritical, and supercritical. It is shown that when the over-reflection or over-transmission occurs, negative energy waves can appear in the flow. A spontaneous wave generation can happen in a transcritical accelerating flow, resembling a spontaneous wave generation on the horizon of an evaporating black hole due to the Hawking effect in astrophysics.

In Chapter 4, long wave transformation is studied in the canal with abrupt variation of width and depth. Again, all possible wave orientation with respect to the background current is considered, and all types of a current is studied (subcritical, transcritical, and supercritical). The transformation coefficients are calculated and analysed as functions of wave frequency, Froud number, and depth drop.

In Chapter 5, we revise the solutions of the forced Korteweg–de Vries equation for the resonant interaction of a solitary wave with the various external pulse-

type perturbations. In contrast to the previous studies, we consider an arbitrary relationship between the width of a solitary wave and external forcing.

In many cases, exact solutions of the forced Korteweg–de Vries equation can be obtained for the specific forcings of arbitrary amplitude. The theoretical outcomes obtained by asymptotic method are in good agreement with the results of direct numerical modelling within the framework of forced Korteweg–de Vries equation.

In Conclusion, we summarise the results obtained within the various models and equations; discuss the future applications and innovation of the results; and suggest further perspectives for the future research.

CERTIFICATION OF THESIS

This Thesis is entirely the work of Andrei Ermakov except where otherwise acknowledged. The work is original and has not previously been submitted for any other award, except where acknowledged.

Principal Supervisor: Professor Yury Stepanyants

Associate Supervisor: Associate Professor Dmitry Strunin

Student and supervisors signatures of endorsement are held at the University.

Statement of Contribution

The following detail is the agreed share of contribution for candidate and co-authors in the presented publications in this thesis:

A. Journal publications:

1. Ermakov A. M. and Stepanyants Y. A. (2019). Transformation of Long Surface and Tsunami-Like Waves in the Ocean with a Variable Bathymetry. Pure Appl. Geophys. Springer International Publishing. (SJR Quartiles Q2; Impact Factor: 1.466 and SNIP: 0.870). DOI: `https://doi.org/10.1007/s00024-019-02259-4`

   The overall contribution of Andrei Ermakov was 60% to the concept development, analysis, drafting and revising the final submission; Yury Stepanyants contributed the other 40% to the problem formulation, concept development, analysis, editing and providing important conceptunal inputs.

2. Ermakov A. M. and Stepanyants Y. A. (2019) Soliton interaction with external forcing within the Korteweg–de Vries equation. Chaos, 29 (1), AIP Publishing, 013117. (SJR Quartiles Q1; Impact Factor: 2.643 and SNIP: 0.827). DOI: `https://doi.org/10.1063/1.5063561`

   The overall contribution of Andrei Ermakov was 60% to the concept development, analysis, drafting and revising the final submission; Yury Stepanyants contributed the other 40% to the problem formulation, concept development, analysis, editing and providing important conceptunal inputs.

3. Churilov S. M., Ermakov A. M., Rousseaux G. and Stepanyants Y. A. (2017) Scattering of long water waves in a canal with rapidly varying cross-section in the presence of a current. Physical Review Fluids, 2 (9). 094805. (SJR Quartiles Q1; Impact Factor: 2.021) DOI: `https://doi.org/10.1103/PhysRevFluids.2.094805`

   The overall contribution of Andrei Ermakov was 40% to the concept development, analysis, drafting and revising the final submission; Semyon

Churilov was 20% to the concept development, analysis, drafting and revising the final submission; Germain Rousseaux was 10% to the concept development, analysis, drafting and revising the final submission; and Yury Stepanyants contributed the other 30% to the problem formulation, concept development, analysis, editing and providing important conceptunal inputs.

4. Churilov S. M., Ermakov A. M. and Stepanyants Y. A. (2017) Wave scattering in spatially inhomogeneous currents. Physical Review D, 96 (6), 064016. ISSN 2470-0010 (SJR Quartiles Q1; Impact Factor: 4.394) DOI: `https://doi.org/10.1103/PhysRevD.96.064016`

   The overall contribution of Andrei Ermakov was 25% to the concept development, analysis, drafting and revising the final submission; Semyon Churilov was 45% to the concept development, analysis, drafting and revising the final submission; and Yury Stepanyants contributed the other 30% to the problem formulation, concept development, analysis, editing and providing important conceptunal inputs. DOI:

B. Conference papers:

1. Ermakov A. M. and Stepanyants Y. A. (2019) Transformation of long surface waves in the coastal zone with a variable bathymetry. Proc. 9th International Congress on Industrial and Applied Mathematics (ICIAM 2019), 15-19 July 2019, Valencia, Spain.
2. Ermakov A. M. and Stepanyants Y. A. (2018) Interaction of Korteweg–de Vries Solitons with External Sources. Proc. 21th Australasian Fluid Mechanics Conference (AFMC 2018), 10-13 Dec 2018, Adelaide, Australia.
3. Ermakov A. M. and Stepanyants Y. A. (2018) Interaction Mathematical problems of long wave transformation in a coastal zone with a variable bathymetry. Proc. 62-nd Annual Meeting of the Australian Mathematical Society (AustMS 2018), 4-7 Dec 2018, Adelaide, Australia.
4. Ermakov A. M. and Stepanyants Y. A. (2018) Interaction of Korteweg–de Vries solitons with external Sources. Abstract of Workshop on Nonlinear waves in Oceanography and Beyond. 26-30 Nov 2018, Toowoomba, Australia.
5. Ermakov A. M. and Stepanyants Y. A. (2018) Application of the concept of a quasi-potential to the fluid flows in curvilinear coordinates. Abstract

of The Eighth Polyakhov's Reading: the International Scientific Conference on Mechanics, 30 Jan - 2 Feb 2018, Saint-Petersburg, Russian Federation.

6. Ermakov A. M. and Stepanyants Y. A. (2016) Description of vortical flows of incompressible fluid in terms of quasi-potential function. Proc. 20-th Australasian Fluid Mechanics Conference (AFMC 2016), 5-8 Dec 2016, Perth, Australia.

   The overall contribution of Andrei Ermakov was 50% to the concept development, analysis, drafting and revising the final submission; Yury Stepanyants contributed the other 50% to the problem formulation, concept development, analysis, editing and providing important conceptunal inputs.

ACKNOWLEDGMENTS

This thesis is dedicated to the memory of my mother Usacheva Tatiana Vladimirovna, Associate Professor in Mathematics of Saint-Petersburg State Marine Technical University, whose ideas and knowledge inspired my own love of mathematics, and a purposeful drive to use mathematics and science to help further shape our world. This thesis not only enabled me to become a specialist in the area of fluid mechanics and theory of water waves, but empowered me to fulfil my long-held dream of migrating to Australia and working within this country's education and science sector. None of this would have been possible without the bright and dedicated minds with whom I have had the honour to meet and work with during this three-year journey.

Firstly, I express my immense gratitude to my principal supervisor Professor Yury Stepanyants for his invaluable assistance, support, patience and guidance during my research period. From the moment I first approached him to be my supervisor, he took me on as his PhD student, not only assisting me with my research but providing me with opportunities to conduct tutorials, mark the course Advanced Engineering Mathematics and conduct lectures for Mathematical Modelling and Dynamical Systems. In collaboration with Yury, I have been published at my highest level so far, of which I am very proud.

My special and gracious gratitude also goes to Associate Supervisor Dmitry Strunin who was my Associate Supervisor, Associate Professor Ron Addie, Senior Lecturer Ravinesh Deo and Lecturer Nawin Raj. Dmitry offered me continuous encouragement, support and valuable suggestions and advice when tutoring and marking Algebra and Calculus II, the first course that I taught in English. Ron demonstrated great faith in me when he asked me to lecture Mathematical Modelling in Financial Economics in his semester-long absence. Finally, Nawin and my Academic Mentor Ravinesh offered me contract marking in Introductory Engineering Mathematics. I also extend my great thanks to Heads of School of ACES Professor Grant Daggard and Associate Professor Linda Galligan for permanent support and opportunities for casual work.

I am especially grateful to Associate Professor Geoff Woolcott at the Southern Cross University for additional work opportunities in the areas of Multivariate

Calculus and Differential Equations and Complex Analysis. My gratitude also goes to Lecturer Lewes Peddell for his involved interactions with my online Linear Algebra tutorials.

This research and subsequent publications would not have been possible without the generous support of the University of Southern Queensland's Research Training Program, in partnership with the Australian Government. This also enabled me a six-month extension to complete my fourth publication. I also wish to thank: the AMSI for the financial support to participate in the month-long AMSI Summer School 2018 at Monash University; the AFMS who assisted me to attend and present my research results at conferences at the University of Western Australia and the University of Adelaide; and once more gracious thanks to the USQ for hosting Wave Transformation workshops which enabled me further organisational and participation experience.

Before this thesis was completed, I was offered and accepted an Australian Postgraduate Research (APR) Intern. This is Australia's only all-sector all-discipline PhD internship program, which uses short-term university research collaborations to enhance Australian businesses through new PhD skills and talent. Again, I am grateful to the USQ, APR-Intern Regional Business Development Connector Adam Lenihan and Industry mentor Jeffrey Popova-Clark (CITEC Confirm) for enabling me to participate in this challenging new opportunity.

Finally, I wish to thank my wife Anastasia, who has always been there for me. Her love and support have always been a source of inspiration. She demonstrated great patience and resolve that we would finally be together. She never gave up, despite two long years of waiting. Thanks to her, and everyone who has supported me since coming to Australia, I have a great opportunity to continue this important research and create results that will help industry and science.

Contents

List of Figures

List of Tables

List of Parameters

t is the time

g is the acceleration due to gravity

τ is the dimensionless time

x is the distance from the origin

ξ is the dimensionless distance from the origin

h is the water depth

b is the width of the duct

h_1, h_2 are the depths of the regions before and after the transient zone

$\hat{h}$ is the dimensionless depth

$h_R(\xi), h_L(\xi)$ are the depth functions

b_1, b_2 are the widths of the duct before and after the transient zone

$X = h_2/h_1$ is the ratio of the depths

$Y = b_2/b_1$ is the ratio between the widths of the duct

x_1, x_2 are the coordinates of the beginning and end of the transient zone

$l_0 = (x_2 - x_1)$ is the width of the transient zone

γ is the parameter for the determination of the conjugation positions on the transient zone

α is the ledge slope angle

λ is the wavelength

ω is the wave frequency

$\hat{\omega}$ is the dimensionless frequency

$D_{i,t}$ is the characteristic lengths of the wave packets

A is the amplitude of the free surface displacement

A_i, A_t, A_r are the amplitudes of the incident, transmitted and reflected waves

$T = A_t/A_i$ is the transmission coefficient

$R = A_r/A_i$ is the reflection coefficient

$c = \sqrt{gh}$ is the propagation speeds of long waves in the linear approximation

c_1, c_2 are the speeds of long waves before and after the transient zone

k is the wavenumber

E is the wave energy

E_i, E_t, E_r are the energies of the incident, transmitted and reflected waves

k_i, k_t, k_r are the wavenumbers of the incident, transmitted and reflected waves

κ, q are the dimensionless wavenumber of the incident and transmitted waves

η^* is the perturbation of a free surface

η is the dimensionless perturbation of a free surface

η_0 is the amplitude of the soliton incident on the ledge

η_i, η_t, η_r are the amplitude of the incident, transmitted and reflected soliton

$\phi(x, y, t)$ is the hydrodynamic potential of velocity

Fr is the Froude number

U is the fluid velocity

V is the dimensionless velocity

$\Psi(\xi), \Phi(\xi)$ are the arbitrary functions

$a, b, c, d, \alpha, \beta, \vartheta$ are the arbitrary constants

$A_{1,2}, B_{1,2}, C_{1,2}, D_{1,2}, E_{1,2}, F_{1,2}, G_{1,2}$ are arbitrary constants for differential equation solutions

ν, μ are arbitrary constants for the special functions orders

$\Gamma(\xi)$ is the Gamma function

$J_i(\xi), Y_i(\xi)$ are the Bessel functions of the first and second kinds

$P_i^j(\xi), Q_i^j(\xi)$ are the Legendre functions of the first and second kinds

${}_2F_1(a, b, c, \xi)$ is the hypergeometric function

J is the energy flux

W is the Wronskian

Γ is the dimensionless amplitude of a solitary wave

Φ is the total phase of the soliton

Ψ is the phase soliton

γ_0 is the inverse half-width of a soliton

Δ_f is the forcing width

K is the ratio of half-widths of external force and initial soliton

ε is the small parameter

$\mathrm{T} = \varepsilon t$ is the “slow time”

Chapter 1

INTRODUCTION AND LITERATURE REVIEW

The century-old problem of the transformation of surface waves over the bottom ledge [32, 88, 156] has always garnered interest from both the theoretical and practical points of view. It is already known that when waves propagate from the open ocean to the coast, they usually have to overcome the shelf zone, in which there is a relatively sharp change in ocean depth. A similar kind of sharp rise along the bottom is often observed in the less deep coastal zones of the seas and oceans, as well as in lakes, rivers and reservoirs. When a wave passes over the bottom its transformation proceeds with the formation of transmitted and reflected waves. In this case, the amplitude of the transmitted wave may be greater than the amplitude of the incident wave. Similar phenomena relating to transforming internal waves have also attracted the attention of researchers in recent years [65]. A great contribution to the study of the transformation of both surface and internal solitary waves has been made by many scientists during the

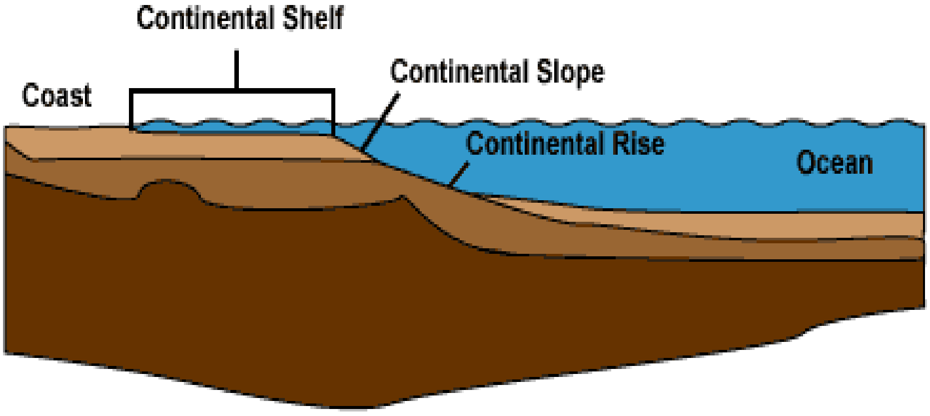

Figure 1.1: A sketch of the typical oceanic profile.

past two centuries.

In order to assess the possible impact of a transmitted wave on offshore engineering structures, platforms, oil and gas pipelines, as well as on beaches, ports, bank protection structures and ships, we need to know the parameters of the transmitted waves as accurately as possible. This problem, as noted above, is also of certain academic interest, because, despite the relative simplicity of the problem statement, its solution has not been fully represented until recently, although quite a lot of theoretical, experimental and numerical works have already been dedicated to the calculation of the coefficients of transformation of the surface and internal waves in the framework of various approximations. [Fig. 1.2] shows schematically the process of wave transformation on an underwater ledge. Let a quasi-monochromatic wave packet with a given frequency ω_i, a wavenumber k_i and an amplitude A_i propagate from region 1 with depth h_1 to region 2 with depth h_2. As a result of its transformation on the underwater ledge at $x = 0$, the transmitted wave packet with the wavenumber k_t and amplitude A_t and the reflected packet with wavenumber k_i are the same as in the incident packet and the amplitude A_r. In this case, the frequency of the wave remains unchanged. The characteristic lengths of the wave packets $D_{i,t}$ are assumed to be significantly *larger* than the carrier wavelengths $\lambda_{i,t} = 2\pi/k_{i,t}$, so that the spatial spectra of wave packets are fairly narrow.

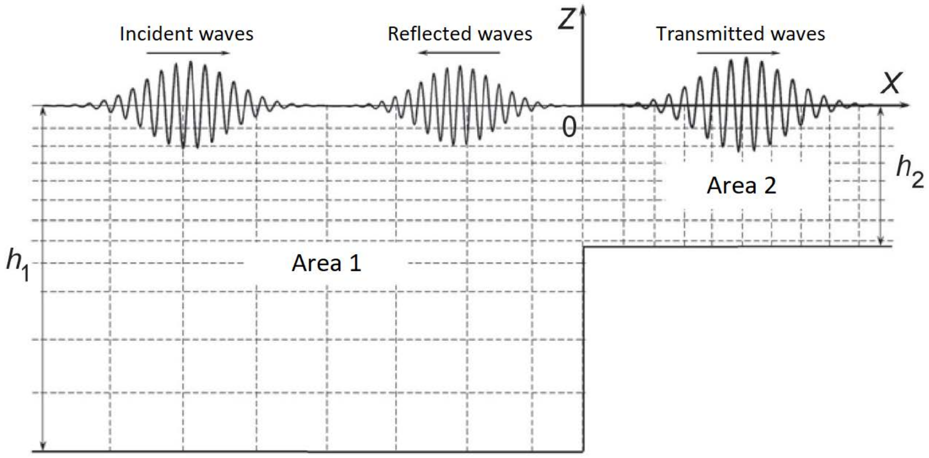

Figure 1.2: Sketch of the wave scattering on a bottom step

Below we describe the problem of determining the parameters of transformed waves depending on the amplitude and wavelength of the incident packet, as well as on the magnitude of the depth difference in the framework of linear theory. Next, we describe the approaches used in determining the parameters of transformed waves based on the amplitude, wavenumber and length of the incident wave packet, as well as on the magnitude of the depth difference. The results obtained within the framework of both linear and nonlinear theories are presented.

1.1 Transformation of surface waves on the bottom ledge

1.1.1 Linear theories

The first theoretical results on the transformation of surface waves over the bottom ledge, apparently, were published by Lamb in his famous monograph [88]. From simple physical considerations, he derived in the long-wave approximation the transformation coefficients for waves of infinitesimal amplitude in a channel of a rectangular cross section with a sharp change in the depth and width. Using the conditions of continuity of pressure, as well as equality of fluid flows to the left and right of the ledge, he obtained expressions for the transformation coefficients, which are now known as Lamb's formulas, as follows:

$$T \equiv \frac{A_t}{A_i} = \frac{2c_1}{c_1 + c_2}, \qquad R \equiv \frac{A_r}{A_i} = \frac{c_1 - c_2}{c_1 + c_2}, \tag{1.1}$$

where A_i is the amplitude of the free surface displacement in the incident wave, and A_t and A_r are the amplitudes of the transmitted and reflected waves, respectively, c_1 and c_2 are the speeds of long waves before and behind the ledge (here Lamb's formulae are given for a channel of constant width). Substituting in (1.1) the well-known expressions for the propagation speeds of long waves in the linear approximation [15, 88, 142] $c = \sqrt{gh}$, one can obtain the transformation coefficients depending only on the ratio of depths before and after the step:

$$T = \frac{2}{1 + \sqrt{h_2/h_1}}, \qquad R = \frac{1 - \sqrt{h_2/h_1}}{1 + \sqrt{h_2/h_1}}. \tag{1.2}$$

The derivation of formulas (1.2), given by Lamb, was subsequently criticized in view of the fact that when they were derived, the vertical velocity component in the wave was neglected, which is not fair in the area of the bottom step. The rigorous formulation of the problem of the transformation of surface waves of arbitrary length on a ledge in the linear approximation was first proposed in the paper by Bartholomeus [9], in which the author took into account the boundary conditions with zero normal velocity components on all solid surfaces. With such a formulation of the problem in the region of the ledge, the wave field consists of both propagating waves (incident, transmitted and reflected), and of an infinite number of non-propagating modes localised near the ledge, exponentially decaying in both directions with increasing distance from it. Matching solutions on both sides of the ledge, Bartholomeus reduced the problem of calculating the transformation coefficients to the Fredholm integral equation of the second kind. However, he was only able to apply to the limit the solution of the derived equation to infinitely long waves, which led to the same Lamb formulas (1.2), confirming their validity in this limit. In the general case, for waves of arbitrary length, no transformation ratios were obtained in his work. Germaine obtained similar results in 1984 [50].

An attempt to calculate the transformation coefficients for waves of finite length was undertaken earlier in the work of Krylov 1949 [85] (see also [142]) for the case where the incident wave length is much less than the depth of region 1 ($k_i h_1 \gg 1$), so this area can be considered infinitely deep. Using the theory of analytic functions of complex variable and the conformal transformation method, Krylov derived the following asymptotic formulas for the transformation coefficients:

- for short incident waves compared to the depth above the ledge ($k_i h_2 \gg 1$):

$$T \approx 1 - \frac{1}{2}\exp(-4k_i h_2), \qquad R \approx \exp(-2k_i h_2); \tag{1.3}$$

- for long incident waves compared to the depth above the ledge ($k_i h_2 \ll 1$):

$$T \approx \frac{1}{\sqrt{1 + \left[\frac{\ln(2/k_i h_2)}{\pi}\right]^2}}, \qquad R \approx \frac{1}{\sqrt{1 + \left[\frac{\pi}{\ln(2/k_i h_2)}\right]^2}}; \tag{1.4}$$

The dependence of the transformation coefficients on the dimensionless wavenumber $k_i h_2$ of the incident wave, plotted on the basis of from these formulas, are shown in [Fig. 1.3]

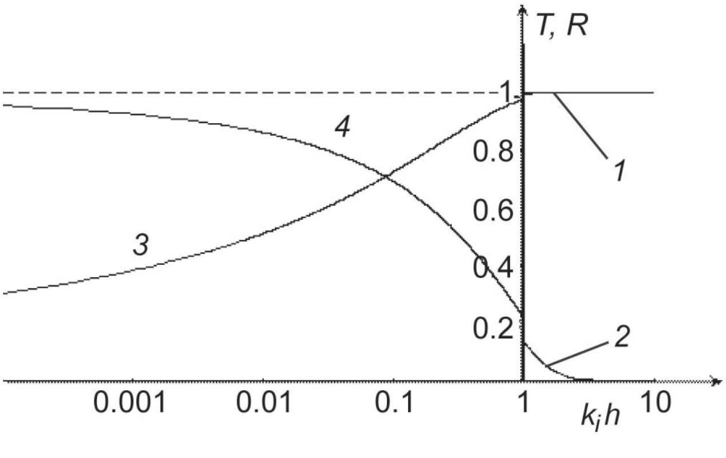

Figure 1.3: The transformation coefficients according to formulas (1.3) and (1.4). 1 - transmission coefficient T with $k_i h_2 \gg 1$; 2 - reflection coefficient R at $k_i h_2 \gg 1$; 3 - transmission coefficient T with $k_i h_2 \ll 1$; 4 - reflection coefficient R with $k_i h_2 \ll 1$.

The curves 1-4, plotted using the asymptotic formulas (1.3) and (1.4), do not hold in the vicinity of $k_ih_2 = 1$. In this case, in the region $k_ih_2 > 1$, curves 1 and 2 very quickly approach their limiting values 1 and 0 respectively. Essentially, these formulas mean that with the transformation of short waves over an underwater ledge, there is only a slight reflection of them, basically the wave almost completely passes into the area behind the ledge. In the case of long waves, the opposite is observed, that is, there is an almost complete reflection of waves from the ledge, and only a small part of them passes into the area behind the ledge. In quantitative terms, however, the transmission coefficient for long waves decreases with a decreasing wavenumber rather slowly (see curve 3 in [Fig. 1.3]). So, even for values $k_ih \sim 10^{-4}$, the transmission coefficient $T \approx 0.3$.

Substantial progress in the calculation of the transformation coefficients of surface waves was made by Takano [148, 149], who presented the wave field in the scarp region as a superposition of traveling and evanescent modes and, using the orthogonality of these modes, reduced the problem of finding transformations to the solution of a system of an infinite number of algebraic equations with respect to the transmission and reflection coefficients of propagating waves, as well as the excitation coefficients of the evanescent modes. Due to the fact that the absolute value of the excitation coefficients of the evanescent modes decreases as the number increases, the infinite system of equations can be limited to a finite number of modes and an approximate solution can be obtained, the accuracy of which depends on the number of evanescent modes taken into account. A similar approach was later used by various authors [104, 105, 113, 114]. In these works, the number of modes taken into account reached 80, but the accuracy of calculating the transformation coefficients was not controlled, the convergence of solutions was not considered, and the excitation coefficients of the pressed modes were not calculated. These gaps were partially filled in [87], in which the number of modes in the calculations reached 500. In addition, it was shown that the number of modes needed to achieve a certain accuracy depended on the depth difference h_2/h_1. In the same was, the excitation coefficients of the evanescent modes were calculated and their effect on the matching of the wave fields in the region of the depth difference was shown.

The problem of the transformation of surface waves over the bottom ledge was also considered by Newman in the 1960s. In [113], he obtained the general symmetry conditions for the wave transformation coefficients:

$$|R_r| = |R_l| \equiv R, \qquad |T_rT_l| = 1 - R^2 \tag{1.5}$$

where R_l, T_l are the transformation coefficients when the wave runs from the left to the ledge, as shown in [Fig. 1.2] (so that $h_2/h_1 < 1$), and R_r, T_r are the transformation coefficients when a wave propagates in the opposite direction (so that $h_2/h_1 > 1$). Note that the first of relations (1.5) for reflection coefficients was derived by Kreissel in 1949 [84]. The transformation coefficients, generally speaking, are complex quantities, which reflect the fact that during the transformation of a wave, not only the amplitudes of the transmitted and reflected waves, but also their phases change. For wave phases, Newman also derived the symmetry relations:

$$\arg T_r = \arg T_l \equiv \delta T, \qquad \arg R_r = \arg R_l \equiv \pi + 2\delta T \tag{1.6}$$

Then, in [113], Newman, using the approach developed in the works of Bartholomeus [9] and Takano [148, 149], essentially calculated for the first time the wave transformation coefficients for the special case where the region of finite depth h_2 is adjacent to the region of infinite depth $h_1 = \infty$. He obtained the dependencies of the transformation coefficients on the frequency using a numerical solution of a system of 80 equations, including both travelling and evanesced modes. In this case, two cases were considered: when a wave runs from an infinitely deep region to a ledge, and when a wave propagates from a region of finite depth to an infinitely deep region. The obtained results were in complete agreement with the symmetry relations (1.5) and (1.6) [Fig. 1.4]. A feature of the problem considered by Newman is that in the case of an infinitely deep fluid, the spectrum

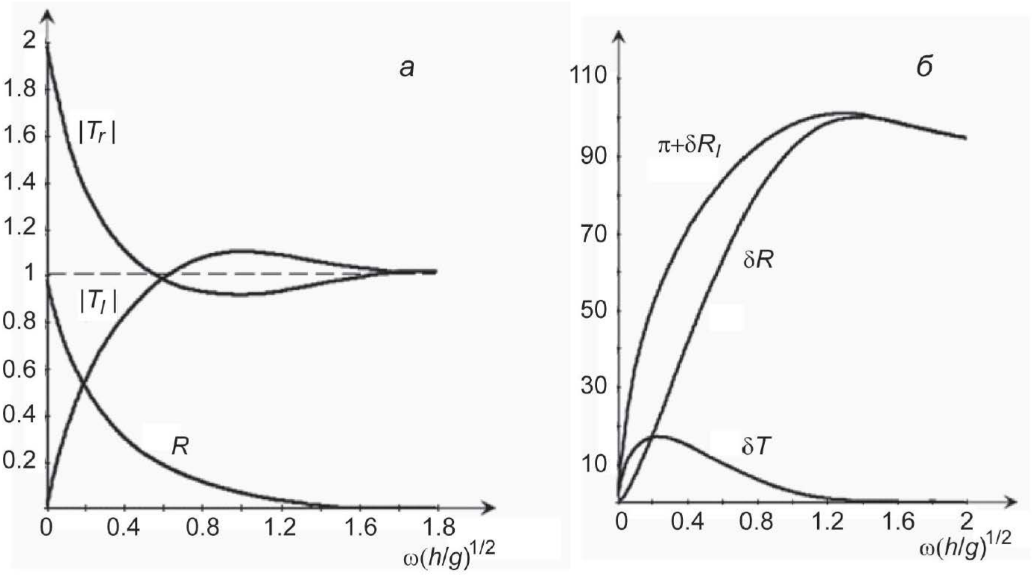

Figure 1.4: The transformation coefficients of surface waves according to [149]. a - transmission $|T_{r,l}|$ and the reflection of R coefficients as functions of the normalized frequency of the incident wave; b - the phases of the transformed waves on the normalized frequency of the incident wave.

of the evanescent modes becomes continuous. As a result, the infinite sum over all pressed modes is replaced by an integral in the region above a deep fluid. A similar problem was considered later by Miles [110], who noted that to calculate the wave transmission coefficient with an error not exceeding 5%, it suffices to confine to only the running modes, completely ignoring the contribution of non-propagating modes (the error in determining the reflection coefficient can reach 90%). This conclusion has been confirmed. Then in [87], in which explicit formulas were derived for the transformation coefficients in accordance with the idea of Miles, but for a fluid of finite depth on both sides of the ledge.

In the long-wave approximation ($k_i, k_t \to 0$) the formulas derived in [87] are transformed into the well-known Lamb formulas (1.2). In the work of Nudner [114], the problem of the wave transformation over a ledge was considered using the method of Takano (apparently developed independently). The transformation coefficients were not calculated, but the elevations of the free surface and the pressure at any point of the liquid were determined. The approach of Takano [148, 149] was also used by Massel [104, 105], who considered the transformation of waves on an underwater obstacle of finite length and, as a particular case, on an infinitely long obstacle, that is, on an underwater ledge. If the length of the obstacle is finite, then resonant effects arise from the multi-reflection of waves from its edges. As a result of this interference, the reflection coefficient as a function of the wavelength is repeatedly turned to zero, which leads to a non-reflective transmission of waves above the underwater barrier. A typical graph of the reflection coefficient of the wavenumber is the traveling wave, as shown in [Fig. 1.5].

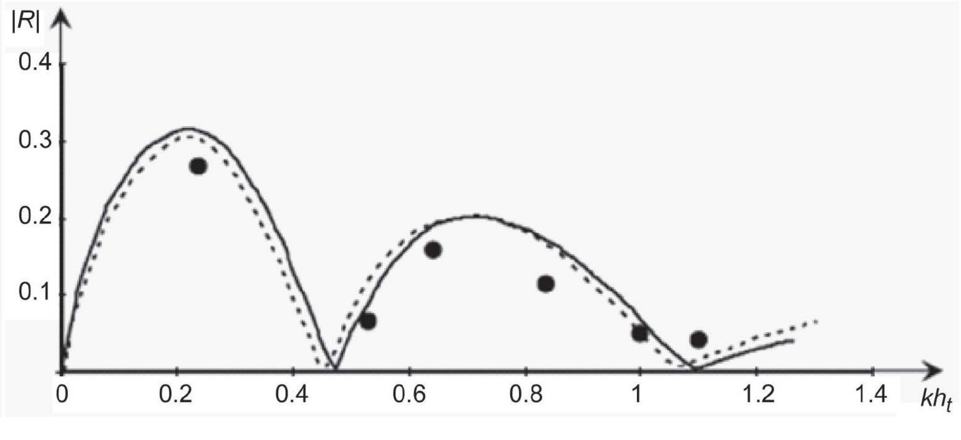

Figure 1.5: A typical graph of the reflection coefficient of the surface wave from an underwater step of finite length according to [104]. Here $h = 0.3$ m is the depth of the reservoir, $h_t = 0.15$ m is the depth of the liquid over an obstacle of length $\lambda = 0.6$ m. The solid line reflects the theoretical results of Massel, the dashed curve is the results of May and Black [108] obtained using the variational approach, and the dots experimental data of [104] are shown.

Considering the problem of the transformation of waves on an underwater ledge, Massel, using a numerical solution of a truncated system of equations for the excitation coefficients of the evanescent modes, obtained the dependencies of the transformation coefficients on the frequency for several fixed values of the depth difference in front of the ledge and beyond. The movement of the incident wave in both directions from left to right and from right to left was considered. The dependencies of the transformation coefficients on the frequency of the wave for the case $h_2/h_1 = 3/16$ ($h_1 = 0.8$ m, $h_2 = 0.15$ m) are shown in [Fig. 1.6]. It is easy to see that the transformation coefficients satisfy the symmetry condition (1.5).

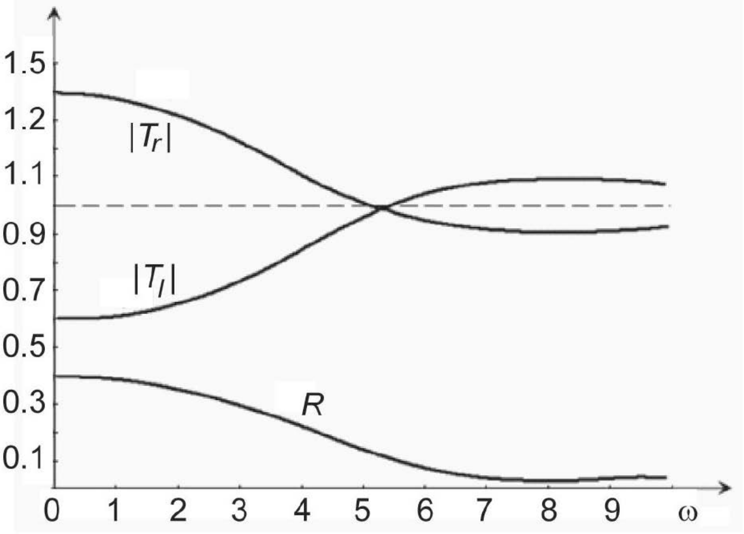

Figure 1.6: Dependencies transformation coefficients of surface waves on the frequency for a given depth ratio $h_2/h_1 = 3/16$ according to [104, 105].

Applying a rigorous approach to solving the problem of transformation of linear surface waves on the bottom ledge has shown that expressions for transformation coefficients can be obtained theoretically with any accuracy by numerical solution of a system of a large number of linear algebraic equations. Practical application of this approach leads to rather cumbersome calculations; sometimes situations arise when the matrix of coefficients of an algebraic system is ill-posted. In this regard, it seems useful to search for fairly simple, albeit approximate, methods for the calculation of transformation coefficients, which make it possible to obtain and analyze the required result relatively quickly with controlled accuracy. Of particular interest are cases where transformation ratios can be represented by analytical formulas.

A different approach to the approximate calculation of the transformation of surface waves over the bottom ledge was proposed in the work by Marshall and Naghdi in 1990 [101]. It is based on an approximate theory of Green – Naghdi, which consists in representing the velocity field as a finite sum of the products of the vertical and horizontal current profiles [53, 54, 56, 55]. It was shown in these papers that the process of calculation of dynamics of surface waves can be greatly simplified by using the specified representation of the velocity field. Using the previously developed approximate theory [53, 54, 56, 55], Marshal and Naghdi [101] considered the propagation of a monochromatic wave of arbitrary length in a pool with a finite number of bottom obstacles in the form of steps and derived the following formulas for the transformation coefficients on one step:

$$T = \frac{2k_t}{k_t + k_i}, \qquad |R| = \frac{k_t - k_i}{k_t + k_i}, \tag{1.7}$$

where k_i and k_t are the wavenumbers of the incident and transmitted waves. In this case, k_t is determined from the following transcendental equation expressing the equality of the frequencies of the waves:

$$k_t \tanh(k_t h_2) = k_i \tanh(k_i h_1) \tag{1.8}$$

It is easy to see that in the long-wave approximation from (1.8) it follows that $(k_i/k_t)^2 = h_2/h_1$; then the dependencies (1.7) reduces to the Lamb formulas (1.2). However, Marshal and Naghdi in their work did not compare the theoretical results they obtained with the data of any laboratory experiments or numerical calculations. The accuracy of calculations by the formulas (1.7) is not high; the results are only partially consistent with the conclusions of a rigorous theory and data of direct numerical calculations.

In [51], approximate formulas were proposed for calculation of the transformation coefficients based on the formal use of Lamb's formulas in the form (1.1), in which instead of the "long-wave" speeds $c_{1,2} = \sqrt{gh_{1,2}}$ speeds, phase or group wave velocities were used, determined from the dispersion relation. It is obvious that in the limit of long waves, when there is no dispersion, the Lamb formulas follow from this approach. The subsequent comparison with the conclusions of the exact theory and the data of direct numerical simulation showed that the best agreement for the transmission coefficient T is provided by substitution of group velocities into formula (1.1); the error does not exceed 5.5% for any wavelengths and depth differences h_2/h_1. For the reflection coefficient, the best agreement is provided by substituting the phase velocities in formula (1.1); however, the calculation error is much higher - it can reach 45%. The corresponding formulas for the transformation coefficients are:

$$T_g \equiv \frac{2c_{g1}}{c_{g1}+c_{g2}} = \frac{q}{\kappa}\frac{\tanh(qh_2/h_1)}{\tanh\kappa}\frac{2}{1+Q\kappa/q}, \quad |R_p| \equiv \frac{|c_{p1}-c_{p2}|}{c_{p1}+c_{p2}} = \frac{|q-\kappa|}{q+\kappa},$$
$$where \quad Q = \left[1+\frac{qh_2}{h_1}\frac{\mathrm{sech}^2(hh_2/h_1)}{\tanh(qh_2/h1)}\right]\left(1+\kappa\frac{\mathrm{sech}^2\kappa}{\tanh\kappa}\right); \tag{1.9}$$

$\kappa = k_i h_1$ - the dimensionless wavenumber of the incident waves; $q = k_t h_1$ the dimensionless wavenumber of the transmitted wave. These numbers are connected by the transcendental equation (1.8), which in the dimensionless form takes the form: $q\tanh(qh_2/h_1) = \kappa\tanh(\kappa)$.

Note that the Marshall and Naghdi formulas (1.7) essentially reduce to the fact that in the Lamb formulas (1.1), for both the transmission coefficient and the reflection coefficient, the wavelength phase velocities are replaced by the wavelengths. As a result, the reflection coefficient, as noted above, is estimated with a maximum error of 45% at $|R| > 0.01$, and the error in determining the coefficient of transmission can exceed 100%, which is much worse than the error of the formulas proposed in [51].

1.1.2 Nonlinear theories

A natural continuation of the study of the transformation of surface waves on the bottom ledge is to take into account the effects of nonlinearity associated with the finite amplitudes of the waves. Nonlinear effects are especially important in the last wave, if the depth of the reservoir over the ledge decreases, for example, when a wave rushes from the open ocean to the shelf area.

In particular, as shown in the monograph by Pelinovsky [124], when tsunami waves propagate in the open ocean, the effects of nonlinearity are weak or substantial when reaching the shore. This leads to an increase in the amplitude of the transmitted wave, to the twisting of its front and, in some cases, to the collapse of the wave behind the ledge. In this regard, of great interest is the problem of the nonlinear transformation of surface waves on the bottom ledge with the study of the subsequent evolution of the transmitted and reflected waves. Mirchina and Pelinovsky [111] considered the transformation of nonlinear waves on the bottom ledge in the long-wave approximation, when the effects of dispersion are not significant.

Using the approximate Lamb approach, consisting of using boundary conditions for maintaining fluid flow and pressure continuity over an underwater ledge, the authors derived a system of nonlinear equations to determine the dependencies of the amplitudes of transmitted and reflected waves depending on the depth difference and amplitude of the incident wave. The resulting system of equations for the amplitudes of the transformed waves in general is too complicated for analysis, but in some particular cases it is possible to get visible results from it. In the limit of infinitely small wave amplitudes, the Lamb formulas (1.2) follow from the resulting system. In the following order in the amplitude of the incident wave, the transformation coefficients take the form:

$$\begin{aligned} T =& T_0 \left\{ 1 + \frac{A_i}{h_1} {T_0}^2 \frac{1+\sqrt{X}}{8\sqrt{X}} \left[3(1-X) + \frac{(3-X)\sqrt{X}{R_0}^2 - 2}{1-\sqrt{X}} \frac{R_0}{T_0} \right] \right\}, \\ R =& R_0 \left[1 + \frac{A_i}{h_1} \frac{T_0}{2(\sqrt{X}-1)} \left(\frac{3-X}{2} {R_0}^2 - \frac{1}{\sqrt{X}} \right) \right]; \end{aligned} \tag{1.10}$$

where A_i is the amplitude of the incident wave, and $X = h_1/h_2$.

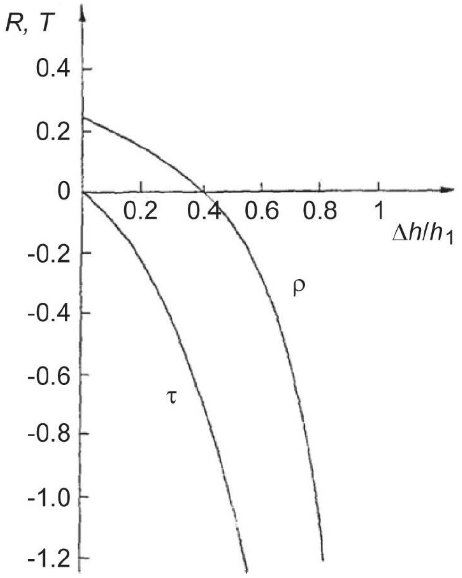

Figure 1.7: Dependencies of normalized corrections to Lamb's formulas $\tau \equiv (\Delta T/T_0)/(A_i/h_1)$ and $\rho \equiv (\Delta R/R_0)/(A_i/h_1)$ on the relative height of the $\Delta h/h_1$ step according to [111, 124].

[Fig. 1.7] shows the relative corrections to the Lamb formulas $\Delta T/T_0 \equiv (T - T_0)/T_0$ and $\Delta R/R_0 \equiv (R - R_0)/T_0$, normalized to A_i/h_1, as functions of the relative height of the ledge $\Delta h/h_1 \equiv (h_1 - h_2)/h_1 = 1 - 1/X$. As can be seen from these graphs, non-linearity leads to an increase in the wave reflection coefficient at $\Delta h/h_1 < 0.4$; for large h/h_1 values, the correction to the reflection coefficient becomes negative. The correction to the transmission coefficient is negative for any values of $\Delta h/h_1$. When $\Delta h/h_1 \to 0$, i.e., when there is no step, the amendment to the reflection coefficient ΔR disappears; Naturally, the reflection coefficient R0 itself disappears, but their ratio formally remains finite

$\Delta R/R_0 \approx 0.22$. In the other limiting case, when $h/h_1 \to 1$, i.e., when $h_2 \to 0$, both corrections, being negative, increase unboundedly in absolute value. Other details of the transformation of nonlinear waves in the long-wave approximation can be found in the original work of the authors [111], and also in the monograph [124]. We note one significant point related to the transformation of nonlinear waves: the obtained transformation coefficients only make sense in the immediate vicinity of the edge of the ledge. Since nonlinear waves are not stationary, as they move away from the edge of the ledge, the transmitted and reflected waves evolve, become twisted, and either turn over or turn into solitons.

In the work of Pelinovsky [122], as well as in the subsequent work [39], the transformation of a soliton on the bottom ledge was studied in the framework of the Korteweg – de Vries (KdV) equation. At the same time, it was shown that with moderate amplitudes of the incident and transmitted waves, the transformation at the ledge edge can be calculated approximately using Lamb's formulas (1.2). Moreover, all three pulses, falling, past and reflected, near the edge of the ledge at x = 0 have the same shape and duration, only the amplitude of the pulses changes:

$$\begin{aligned}
\eta_i(x,t) =& \eta_0 \operatorname{sech}^2\left(\frac{t\sqrt{3g\eta_0}}{2h_1}\right), \\
\eta_t(x,t) =& \frac{2}{1+\sqrt{h_2/h_1}}\eta_0 \operatorname{sech}^2\left(\frac{t\sqrt{3g\eta_0}}{2h_1}\right), \\
\eta_r(x,t) =& \frac{1-\sqrt{h_2//h_1}}{1+\sqrt{h_2//h_1}}\eta_0 \operatorname{sech}^2\left(\frac{t\sqrt{3g\eta_0}}{2h_1}\right). \qquad (1.11)
\end{aligned}$$

Here, η_0 is the soliton incident on the ledge. Taking into account the formulas derived in [111], the transformation coefficients can be refined, taking into account the finiteness of the amplitude of the incident soliton. The preservation of the pulse shape and their durations during the transformation of solitons at a sharp depth jump at the ledge edge was confirmed in subsequent numerical calculations [123] and laboratory experiments [94, 139]. After transformation in the past and reflected pulses, the balance between amplitude and duration, characteristic of a stationary soliton, is disturbed. As a result, transformed pulses in the process of propagation evolve, generating secondary solitons, the number and parameters of which can be calculated using the inverse scattering method (see, for example, [1]). In this case, only one soliton appears in the reflected wave if $h_2/h_1 < 1$; if $h_2/h_1 > 1$, then the reflected pulse has a negative polarity, evolving only into a non-stationary wave packet without solitons.

1.2 Numerical studies of the transformation of waves on the bottom ledge

The transformation of solitary waves was studied in detail in the work of Pelinovsky and co-authors [123]. As in earlier papers [39, 122], the authors used the linear theory to calculate the amplitudes of the waves transformed over the ledge, using the Lamb formulas (1.2). To confirm the conclusions of the theory, calculations of the dynamics of a single wave (soliton) were performed within the framework of various numerical schemes on the basis of the KdV equation, the generalized Boussinesq equation, and also in the framework of the full-non-linear Navier – Stokes model. The calculations performed in the framework of all these schemes showed close to theoretical results, both in the number of secondary solitons and in terms of their amplitudes (the phase coincidences were much worse due to the inaccuracy in determining the soliton velocities within approximate models).

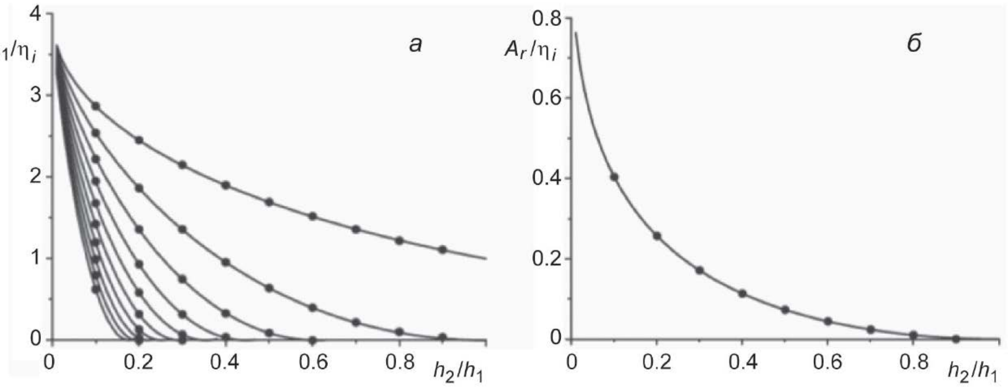

Figure 1.8: The dependencies of the amplitudes of secondary solitons A_{n+1} in the transmitted wave (a) and in the reflected wave (b), normalized to the amplitude of the incident soliton η_i, on the depth difference h_2/h_1 according to [123]. Solid lines are theoretical dependencies, points are numerical data obtained within the framework of the KdV equation.

The figures [Fig. 1.8] from [123] show a comparison of the theoretical dependencies with the numerical data for the amplitudes of secondary solitons arising in the past wave on the depth difference. Note that the maximum amplitude of the highest of the secondary solitons cannot exceed the amplitude of the incident soliton by more than four times. In this case, as follows from Lamb's formulas (1.2), the maximum amplification of the transmitted wave in terms of the incident wave cannot exceed two near the edge of the ledge. Then, as the transformed pulse evolves, secondary solitons form from it, and according to the theory of the KdV equation [39, 122], the maximum amplitude of the secondary soliton can exceed the amplitude of the pulse transformed on the ledge no more than twice.

These figures [Fig. 1.8] demonstrates good agreement of theoretical calculations with numerical data in the framework of the KdV model. This confirms the validity of using Lamb's formulas (1.2), derived within the framework of the linear theory of long waves to calculate the transformation of impulse perturbations of small but finite amplitude, such as, for example, KdV solitons. Direct numerical modelling of the transformation of linear waves of arbitrary length on the bottom ledge was performed only recently in [51, 87]. At the same time, far from the ledge, a quasi-monochromatic wave packet with a central wavenumber k_i was specified. In order to avoid dispersion effects when such a packet propagates, its characteristic width D was chosen rather large compared to the carrier wavelength $\lambda_i = 2\pi/k_i << D$. Numerical calculations were performed using the MITgcm software package, adapted to simulate the transformation of surface waves above the bottom ledge ideal fluid [4, 102, 103]. The view of the two-dimensional computational domain is presented in [Fig. 1.2]; on all vertical sides and at the bottom, the no-flow condition (zeroing of the normal velocity component) was used, and on the free surface standard boundary conditions, kinematic and dynamic, were used [15, 88, 142]. The initial perturbation was defined as a wave packet with a Gaussian envelope in a region with depth h_1:

$$\begin{aligned} \eta_i(x,t) =& \eta_0 \operatorname{sech}^2\left(\frac{t\sqrt{3g\eta_0}}{2h_1}\right), \\ \phi(x,y,0) =& \frac{g}{\omega(k_i)} A_i \exp\left[-\left(\frac{x-x_0}{D}\right)^2\right] \frac{\cosh[k_i(h_1-y)]}{\cosh(k_i h_1)} \sin(k_i x) \end{aligned} \tag{1.12}$$

Here $\eta(x,t)$ - is the disturbance of the free surface, $\phi(x,y,t)$ - is the hydrodynamic potential of velocity, A_i - is the amplitude of the wave packet, g - is the acceleration of gravity, $\omega(k_i)$ is the frequency of the carrier wave associated with the wavenumber dispersion ratio: $\omega(k) = \sqrt{gk\tanh(kh)}$

The amplitude of the initial disturbance was chosen so small that nonlinear effects did not manifest themselves in the computational domain $A_i = \min\{h_2, h_1\}$ /500. Numerical calculations were performed for a depth difference of $0.01 \leq h_2/h_1 \leq 100$, which corresponds to the incidence of waves from a deep region to a greater shallow area, and in the opposite direction. In this case, the depth h_1 in all calculations was set to the same $h_1 = 50$ m, and the depth behind the h_2 ledge was varied. Below are the results of calculations for only three values of dimensionless wavenumbers $k = k_i h_1 = 0.1$, 1, and 10, which successively differ in order. The amplitudes of the transmitted and reflected waves were determined at a sufficient distance from the ledge so that there was no interference with the incident wave. After that, the transmission coefficients are $|T| = |A_t/A_i|$ and the reflections are $|R| = |A_r/A_i|$. The results of numerical simulation of the transformation process for the three specified wavenumbers are presented in [Fig. 1.9] As can

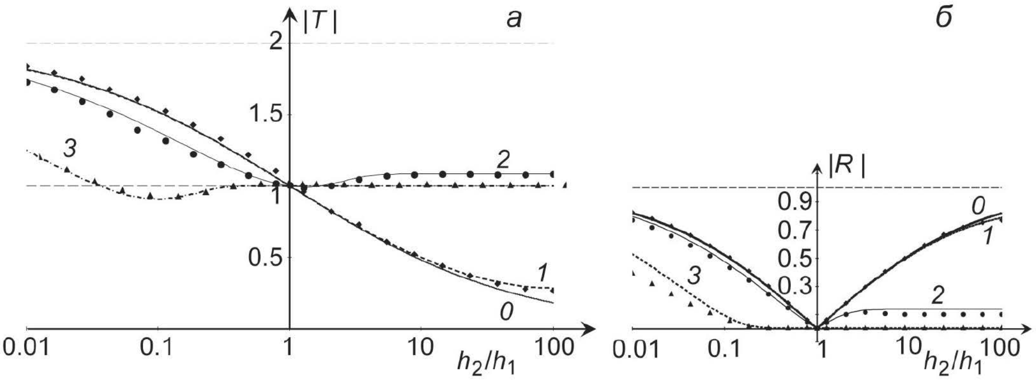

Figure 1.9: The coefficients of transmission (a) and reflection (b) as a function of the depth difference. The results of numerical calculations are represented by various symbols: diamonds - $\kappa = 0.1$; points - $\kappa = 1$; triangles - $\kappa = 10$; solid lines are calculations using Lamb's formulas (1.2). The remaining curves are constructed using approximation formulas (1.9).

be seen from this figure, the approximation formulas (1.9) are in good agreement with the data of direct numerical calculations, not only qualitatively but also quantitatively, reproducing the local minimum of the transmission coefficient at $\kappa = 10$ in the region $h_2/h_1 < 1$, as well as T values in the region $h_2/h_1 > 1$. As was to be expected, the agreement between the transformation coefficients of the waves and the Lamb formulas (2) is observed only for fairly small values of the wavenumbers κ (see, for example, the diamonds in [Fig. 1.9] and curves 1 for the transmission and reflection coefficients for $\kappa = 0.1$). An interesting feature of the transformation coefficients is their non-monotonic dependence on the depth difference. Due to the non-monotonic nature of the transmission coefficient for sufficiently large values of κ, it can turn into a unit not only for $h_2/h_1 = 1$ when there is no step at all, but also for a certain value of $h_2/h_1 < 1$ (see [Fig. 1.9]), which depends on κ. In this case, the reflection coefficient does not vanish again for the second time, and the length of the transmitted wave does not coincide with the length of the initial wave, $q \neq k$. The relationship between the wavenumber of the initial wave κ^* and the depth difference h_2/h_1, at which the transmission coefficient becomes one, can be obtained from the condition $T = 1$ together with equation (1.8). Due to the complexity of the resulting transcendental equation, it is not given here; its numerical solution is presented in [Fig. 1.10]. For small values of $h_2/h_1 << 1$, the dependence of κ^* on h_2/h_1 can be approximated by the simple formula $\kappa^* = 0.36 h_1/h_2$, represented by the dotted line in the double logarithmic scale in [Fig. 1.10]. A somewhat worse agreement between the approximation formulas and the numerical data is observed for the reflection

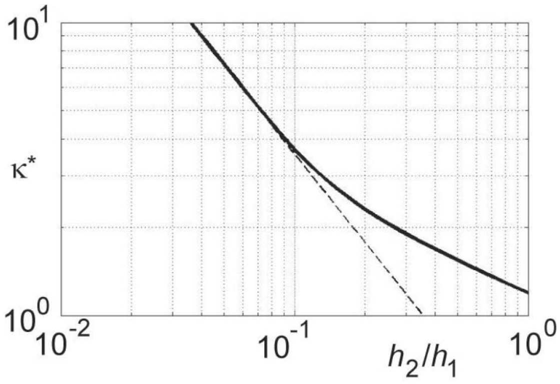

Figure 1.10: The dependence of the dimensionless wavenumber of the incident wave on the depth difference, when the transmission coefficient again vanishes.

coefficient, especially for large κ values in the $h_2/h_1 < 1$. But in general, the agreement with the numerical data can be considered quite satisfactory in this case too.

Generation of solitary waves by transcritical flow over a step was also studied in the work [70]. The authors consider the analogous transcritical flow over a step, primarily in the context of water waves. They used both numerical and asymptotic analytical solutions of the forced Korteweg–de Vries equation, together with numerical solutions of the full Euler equations, to demonstrate that a positive step generates only an upstream-propagating undular bore, and a negative step generates only a downstream-propagating undular bore [Fig. 1.11]. The

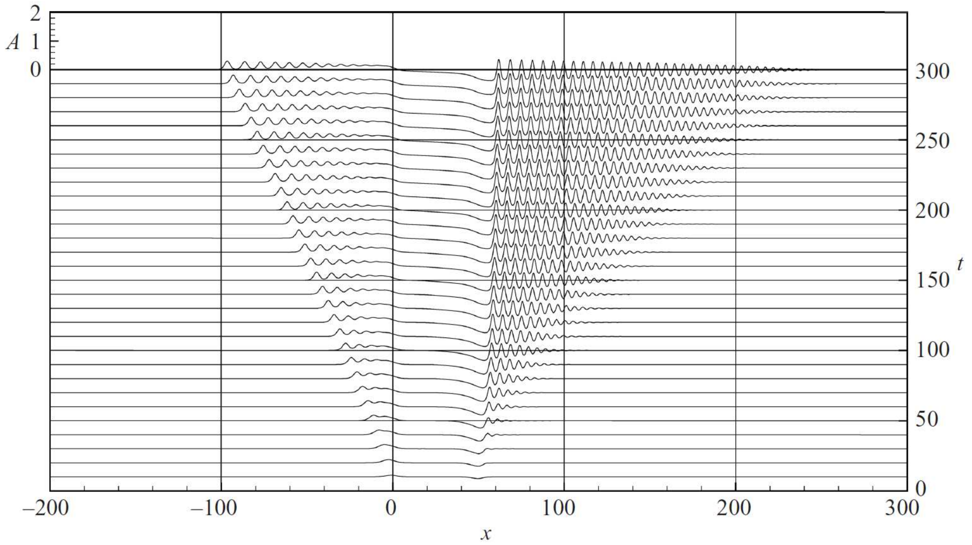

Figure 1.11: Generation of solitary waves by transcritical flow over a step. (The step is not shown.)

numerical study of transformation of a finite-amplitude interfacial solitary wave of depression at a bottom step in a two-layer fluid was also conducted in [97].

The parameter range studied in this paper goes outside the range of the weakly nonlinear theory, viz, the extended Korteweg–de Vries or Gardner equation. The authors described various scenarios of transformation in terms of the incident wave amplitude and the step height. The dynamics and energy balance of the transformation are also described. Several numerical simulations were carried out using the nonhydrostatic model based on the fully nonlinear Navier–Stokes equations in the Boussinesq approximation. Three distinct runs were discussed in detail. The first simulation was done when the ratio of the step height to the lower layer thickness after the step was about 0.4 and the incident wave amplitude was less than the limiting value estimated for a Gardner solitary wave. This shows the applicability of the weakly nonlinear model to describe the transformation of a strongly nonlinear wave in this case. In the second simulation, the ratio of the step height to the lower layer thickness was the same as that in the first run but the incident wave amplitude was increased and then its shape was described by the Miyata–Choi–Camassa solitary wave solution. In this case, the process of wave transformation was accompanied by shear instability and the billows that result in a thickening of the interface layer. In the third simulation, the ratio of the step height to the thickness of the lower layer after the step was 1.33, and then the same Miyata–Choi–Camassa solitary wave passes over the step, it undergoesunderwent stronger reflection and mixing between the layers although the Kelvin–Helmholtz instability was absent. The energy budget of the wave transformation was calculated. It was shown that the energy loss in the vicinity of the step grows with an increase of the ratio of the incident wave amplitude to the thickness of the lower layer over the step.

The numerical study was extended in the paper [150]. The authors continued their work on the interaction of an interfacial solitary wave with a bottom step, considering (i) the energy loss of solitary waves of both positive and negative polarities interacting with a bottom step and (ii) important features of the transformation of a large amplitude internal solitary waves at the step [Figs. 1.12 - 1.14]. It was shown that the dependence of energy loss on the step is not monotonic, but has different maximum positions for different incident wave polarities. The energy loss does not exceed 50% of the energy of an incident wave. The results of numerical modeling were compared with some recent results from the laboratory tank modeling. In all case when a solitary wave amplitude was large enough, generation of a turbulence was observed though the mechanism of Kelvin-Helmholtz instability. This is clearly seen in [Figs. 1.12-1.14].

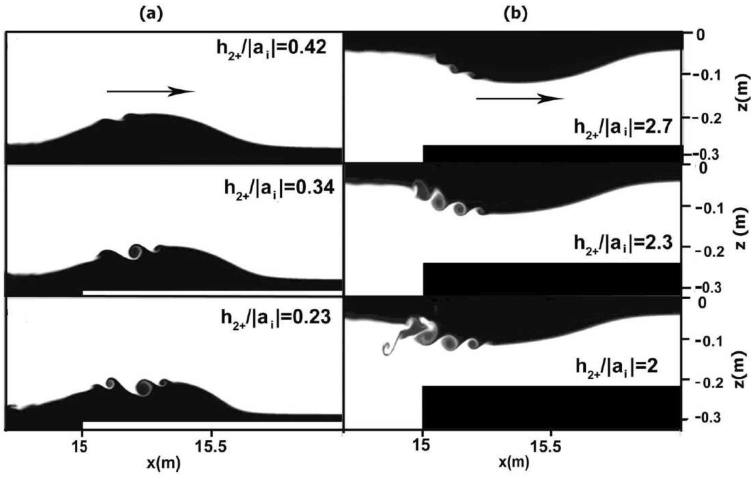

Figure 1.12: The salinity field in the vicinity of the step shows Kelvin-Helmholtz instability for an incident elevation (a) and depression (b) internal solitary waves.

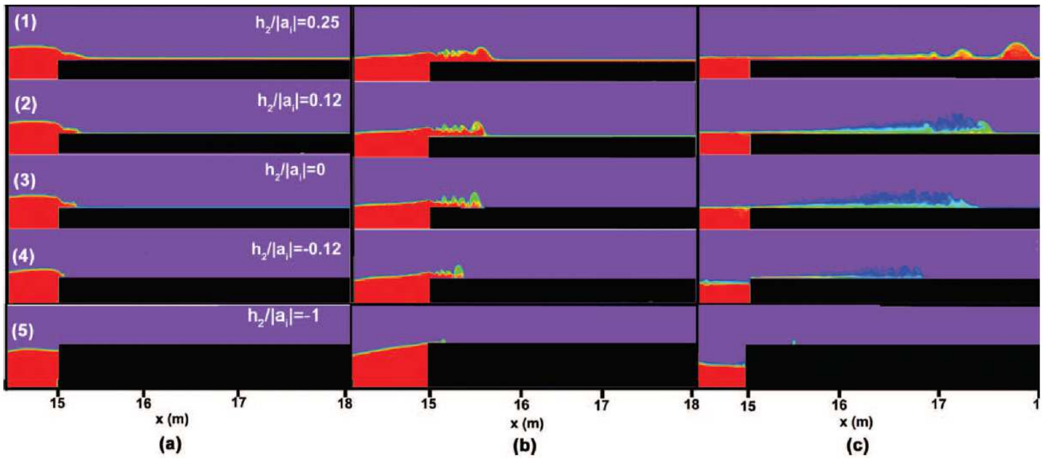

Figure 1.13: The transformation of an incident positive polarity solitary wave of a big amplitude at a bottom step.

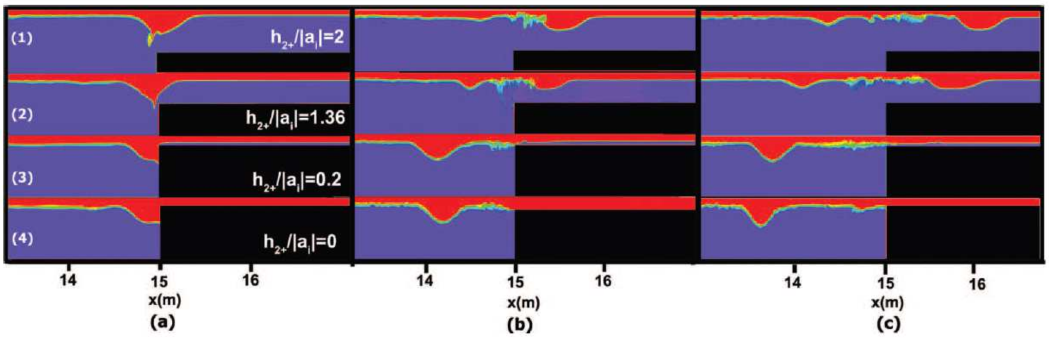

Figure 1.14: The transformation of an incident negative polarity solitary wave of a big amplitude at a bottom step.

1.3 Laboratory experiments on the transformation of waves on the bottom ledge

Apparently, the first work containing a comparison of experimental data on the transformation of surface waves above the underwater scarp with the theoretical results is the work of Newman [113], in which the transition of a quasimonochromatic wave from an infinitely deep region to a region of finite depth was studied. As can be seen from [Fig. 1.15], taken from this work, the laboratory experiment data results are in good agreement with the theoretical results. In subsequent laboratory experiments, only the transformation of long (compared to the depth of the pool) solitary waves was studied. Thus, in [139], the authors present the results of a large series of experiments in which the height of the underwater ledge and the amplitude of the incident solitary wave changed. In this case, the amplitudes of the waves in some cases were not small, so that nonlinear effects were observed, leading even to the collapse of the waves passing behind the ledge.

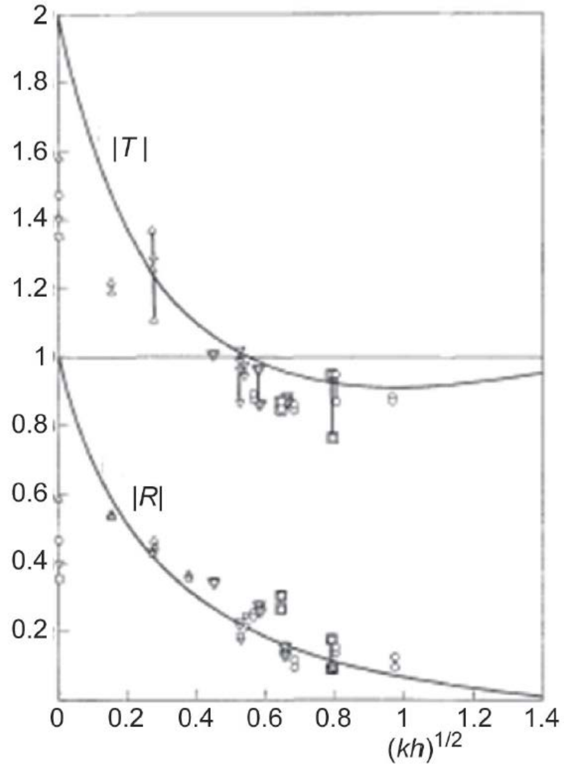

Figure 1.15: The dependence of the coefficient transmission and reflection of waves from the dimensionless parameters $(kh)^{1/2}$ [113], where k is the incident wavenumber, and h - the depth of the reservoir behind the ledge. Different symbols correspond to different depths h, symbols, on the vertical axis indicate the limiting values of the transformation ratios for infinitely long waves according to the Lamb formulas (1.2).

The studies performed with small wave amplitudes demonstrated good agreement with the theoretical formulas obtained in [122]. In particular, in experiments with a certain depth ratio, two or more single pulses were observed in the transmitted wave, whereas only a soliton was formed in the reflected wave. In addition, it was noted that the number and amplitude of the transmitted waves increase with increasing height of the ledge. In another work on the same topic [94], the transformation of solitary waves of both small and large amplitudes was also considered. In this case, both the transformation of solitary waves in the immediate vicinity of the ledge, and the further evolution of the waves passing behind the ledge were studied in detail. According to the observations of the authors of [94], when the wave approaches the underwater ledge, the amplitude of solitary waves increases slightly, and in the region behind the ledge a decrease in the free surface level was observed. Far from the ledge, the results of laboratory experiments were compared with the soliton solution of the KdV equation for the transmitted pulses. For solitons of small amplitude incident on a ledge, satisfactory agreement with theoretical predictions was observed, whereas at large amplitudes, experimental data differed from theoretical results, as well as non-stationary dynamics of transmitted pulses up to their collapse. Based on the accumulated experimental data, a diagram was constructed that defines various modes of transformation of solitary waves depending on the amplitude of the initial wave and on the depth ratio before and after the step in the range $1.0 < h_2/h_1 < 4.3$. It was noted at what parameters the decay of the transmitted pulse into several solitons occurs, the splitting and collapse of the transmitted wave, almost complete transmission, and, conversely, total reflection. In conclusion of this section, we note that the process of transformation of surface waves on the bottom ledge has also been studied experimentally using modelling in nonlinear power lines [145]. As was shown in this paper, in the long-wave approximation, the basic equations describing the propagation of signals in such lines are reduced to the KdV equation. In this case, a good agreement was found between experimental data on soliton transformation at a jump in parameters between two sections of a long line with theoretical conclusions similar to those obtained for waves in a shallow pond [39, 122].

1.4 Wave transformation and analogue gravity

The problems of water wave transformation in a variable-depth fluid have unexpected analogy with the fundamental astrophysical problem of electro-magnetic wave scattering on black holes and Hawking radiation. The deep physical analogy between water waves in inhomogeneous classical continuum media and astrophysical phenomena in the vicinity of black hole horizon was established in 1981 by Unruh [152] who demonstrated the analogy between the long-wave equations in non-uniform media and a curved space-time metric in general relativity. It was shown also that there is an analogy between the Hawking radiation [72] in astrophysics and emission of negative energy waves [46] in non-uniformly moving fluids.

Increased attention occurred in this field when it was discovered that analogue Hawking radiation is mainly disengaged to the Lorentz-violating short-wavelength dispersion [16, 73, 74, 153] ubiquitous in realistic media. There have since been many theoretical and experimental study in various physical systems. This includes optics [11, 127], BEC [143, 144], waves in solids [5, 17, 21] and spin waves [40, 76], acoustic waves [6, 7], and surface waves in water [134, 135, 136, 138]. The well-observed dispersive corrections to the Hawking flux (see e.g. [96, 133]), have garnered greater understanding and cognisance into the possible effects of a quantised spacetime using more accessible systems where microscopic behaviour has been well documented. As all-pervasive as dispersion, dissipation is another vital cog in this relativistic machine [2, 18, 91, 132] and a direct player in all of the analogue gravity systems already mentioned. For example, in BEC, the effect of Landau damping [128] happens when phonon energy is lost due to interactions with the non-condensed thermal cloud. While optical media are all absorptive to some extent, the main dissipative channel of polaritons is the radiation of photons to the environment [17, 21], while losses from spin waves are caused by ohmic dissipation [40, 76]. Although viscosity is the main cause of dissipation in fluids, this also creates several other dissipative effects including friction at the boundaries and absorption in the bulk. Wave breaking is often described as a ‘super-dissipative’ process, where wave energy is lost to turbulence. It is suggested that quantum fluctuations of space-time geometry may act as a dissipative force on black holes [8, 119]. Therefore, it is vital that dissipation is included and gauged in the design and execution of all experiments to optimise and maximise our observations and results. Instead of determining the relevance and scope of dissipation of surface waves on fluids in analogue gravity experiments [136], or quantitatively characterising the lowest-order corrections induced [132], our focus here shall be on minimizing the overall dissipative effects and giving greater emphasis to surface waves on water, in keeping with previous experiments. Where possible, the results will be expressed in the dimensionless form that can apply to many different fluids with one goal being to garner greater attention from experimentalists in fluid mechanics unfamiliar with the analogue gravity program.

1.5 The objectives of this research

The Project is devoted to the development of new exact solutions to classical problems in fluid mechanics. In the long history of development of hydrodynamics, several formulations of the primitive equations have been proposed as the basis for investigation of various aspects of flow dynamics. Unfortunately, in general, equations of fluid motion are very complicated and only in special cases can the exact analytical solutions be found. Such solutions are very important, and therefore researchers continue to look for such formulations as will enable them to construct exact solutions and use them for practical purposes. There are several different approaches which allow one to reduce the original equations to simplified forms containing fewer variables. In this Project, exact solutions for several simplified hydrodynamic problems will be studied using rigorous mathematical approaches.

1.6 Content of this research

In Chapter 1, the history of the problems considered in the Thesis is presented and the existing solutions and methods are reviewed. The transformation of surface waves over underwater obstacles of various shapes is a long-term problem that has grown more pressing due to increasing technological and societal demands. Development of advanced models to describe the influences of depth variation of the ocean or of cross-section of canals, and the current speed effect on wave transformation has many applications, from protecting coastlines or natural treasures such as the Great Barrier Reef to the introduction of higher-level safety mechanisms in marine vessels and offshore structures.

The results obtained in the Thesis are also of interest from the viewpoint of modelling of astrophysical phenomena such as Hawking radiation. In particular, it is rigorously shown in the Thesis that the amplitude of the scattered wave decreases with the frequency as ω^{-1}, whereas in the experiment [155] it was only roughly estimated to be exponentially decreasing.

Whenever a wave passes over a bottom step, the amplitude and wave number of the transmitted wave may be significantly increased compared to the amplitude and wave number of the incident wave. To calculate the impact of a transmitted wave on offshore or coastal structures, one should closely analyse and take into account the parameters of the transmitted wave. The complex nature of these effects requires deep analytical modelling in addition to the numerical results. This research looked at four vital considerations: the transformation of long linear waves in an ocean with a variable depth; long wave scattering in a canal with a rapidly varying cross-section; long linear surface waves on stationary currents in a canal of constant depth and variable width; and the revision of the forced Korteweg–de Vries equation to describe a resonant interaction of a solitary wave with external pulse-type perturbations. White spaces in previous research will be noted.

In Chapter 2, it was considered and calculated the transformation of long linear waves in an ocean with a variable depth. Here, the transformation coefficients (the transmission and reflection coefficients) will be considered as the functions of frequency and the total depth drop for three typical models of the bottom profile: piecewise linear, piecewise quadratic and hyperbolic tangent profiles. We compare the influence of the different bottom profiles on the wave transformation and obtain exact analytical solutions for all three reference cases.

For all of these cases, exact solutions are obtained, analysed and graphically illustrated, allowing us to derive the transformation coefficients in the analytic form and compare them with the available data obtained for the particular models, either approximately or numerically. As will be shown, the results obtained are in good agreement with energy flux conservation and Lamb's formulae in the limiting case of zero frequency. We also study wave transformation (scattering) on the underwater barriers and trenches of different shapes whose slopes can be described by the similar functions (linear, piecewise quadratic, and tanh-functions). A comparison of the results obtained for these three cases will be presented and analysed.

In all cases we obtained qualitatively similar results which were in agreement with those earlier obtained by different authors for some particular cases by more approximate methods. In the limiting case, when the wave frequency goes to zero, we obtained the same transformation coefficients which are predicted by Lamb's theory (1932) [88] for a step-wise bottom.

However, some quantitative differences in the transformation coefficients for the different bottom profiles were found.

For the wave scattering on underwater barriers or tranches it has been shown that fewer oscillations in the transformation coefficients occur for barriers and tranches with linear slopes in comparison with barriers and tranches with piecewise quadratic or tanh-slopes.

More complicated real bottom profiles can be approximated with higher accuracy by the combination of linear, quadratic, and tanh-profiles similar to those used in the paper [129], where the bottom profile was approximated by a set of step-wise functions. The obtained results can be used, in particular, for the protection of beaches against storm surges, swells and tsunami waves.

In Chapter 3 it will be considered the case of long wave scattering in a canal with a rapidly varying cross-section, where the scattering coefficients will be calculated for all possible orientations of the incident wave, with respect to the background current (downstream and upstream propagation) and current type (subcritical, transcritical, and supercritical). It is shown that over-reflection or over-transmission can occur and the negative energy waves can appear. A spontaneous wave generation can happen in a transcritical accelerating flow, when the canal narrowing leads to the increase of the background current. This resembles a spontaneous wave generation on the horizon of an evaporating black hole due to the Hawking effect [27, 29, 47, 73, 126, 131, 152, 153].

In examining the classic problem of water wave transformation in a canal of a variable cross-section, we studied the coefficients of transformation of long linear waves in a canal of a rectangular cross-section with an abrupt change of geometrical parameters (width and depth). The transmission and reflection coefficients were found as functions of depth ratio and width ratio.

In the study of the subcritical and supercritical flows, we succeeded in calculating the transmission and reflection coefficients in explicit forms as functions of the depth drop and Froude number. The conditions for over-reflection and over-transmission have been found in terms of the relationships between the Froude number and canal geometric parameters X and Y, where $X = h_2/h_1$ is the ratio of the depths and $Y = b_2/b_1$ is the ratio of the widths of the duct.

In Chapter 4, we study analytically the scattering of long linear surface waves on stationary currents in a duct of a constant depth and variable width, assuming that the background velocity linearly increases or decreases with the longitudinal coordinate (gradual variation of duct width). This enabled us to arrive at an analytical solution, calculating the scattering coefficients as functions of incident wave frequency for all possible cases (sub-, super, and trans-critical currents). Both co-current and counter-current wave propagation in accelerating and decelerating currents were studied on a properly varying width to the canal, instead of the step-wise model considered Chapter 3.

The results obtained showed that the transformation coefficients can be found in the exact analytical forms both for co-current and counter-current wave propagation in gradually accelerating and decelerating currents. The results of this Chapter represent an interest as the hydrodynamic model of Hawking's effect, and are applicable to the real physical phenomena occurring in non-homogenous ducts with a water flow, at least at relatively small Froude numbers.

All problems describe above pertain to the dispersionless case when the wavelengths of all waves in the scattering process are far greater than the water depth h in the canal. However, the wavelengths can be comparable with or even less than the characteristic length l of current inhomogeneity. In the long-wave limit, the scattering coefficients were expressed through the simple algebraic formulae (in agreement with the formulae derived in the previous Chapter 2 for the case of abrupt change of canal cross-section).

The analysis undertaken is based on the fact that wavelengths of scattered waves drastically decrease in the vicinity of a critical point, where the speed of water flow $U(x)$ becomes equal to the speed of long waves: $U(x) = c$. Here, either the dispersion, or dissipation, or both these effects may play an important role. It was shown that in certain situations, viscosity can predominate over the dispersion. The influence of dissipation on Hawking radiation was considered in astrophysical application [132]. This chapter led to the finding of an exactly solvable model, enabling us to construct analytical solutions and calculate the scattering coefficients in the dispersionless limit.

In Chapter 5, it is considered the nonlinear models of waves transformation on localised moving obstacles. The asymptotic theory developed by Grimshaw and Pelinovsky with co-authors in the series of papers [62, 63, 64, 66, 121] is revised. While these authors described the dynamics of solitary waves in the KdV-like equations, their research was limited to the cases where the moving obstacles (representing a forcing for the incoming solitary wave) where either very narrow in comparison with the initial KdV soliton and could be approximated by the Dirac δ-function, or where the initial KdV soliton was very narrow (and approximated by the δ-function) in comparison with the localised forcing. In our research it was considered an arbitrary relationship between the width of the initial KdV soliton and external forcing. There were presented also several examples of forced KdV equation which admit exact analytical solutions both stationary and non-stationary.

For a small-amplitude forcing, we presented the asymptotic analysis based on the equations derived in the aforementioned papers and showed that in many cases solutions of approximate equations can be solved analytically, albeit the final formulae look rather cumbersome. In the limiting cases of a very narrow or a very wide forcing our results converge to those obtained by Grimshaw and Pelinovsky [66], but contain additional physically interesting regimes missed in their paper due to approximation of the soliton and forcing by the δ-function.

The results obtained are particularly important in view of their applications to physical phenomena occurring when external perturbations generate pressure fields capable of exciting and supporting solitary waves. Examples represent the cases where a moving atmospheric pressure or a slow-moving ship generates waves; where atmospheric waves are generated behind tall obstacles like a mountain ridge or where ocean currents flow around underwater obstacles, generating surface or internal waves. The results are also applicable to other areas of physics, such as plasma physics and Bose–Einstein condensate, where the highly universal forced Korteweg–de Vries equation is also used.

Within the Project, the traditional methods of theoretical and mathematical physics were used. They are based on the complex analysis technique, asymptotic methods, and classical and contemporary methods of mathematical physics. The numerical methods were used as the complementary tool to support theoretical findings. Within these methods the standard software Fortran, Matlab, Mathcad and Wolfram Mathematica were used.

Chapter 2

TRANSFORMATION OF LONG SURFACE WAVES IN THE OCEAN WITH A VARIABLE BATHYMETRY

In this chapter we consider transformation of long linear waves in an ocean with a variable depth. We calculate the transformation coefficients (the coefficients of transmission and reflection) as the functions of frequency and the total depth drop for three typical models of bottom profile variation: (i) piecewise linear, (ii) piecewise quadratic, and (iii) hyperbolic tangent profiles. For all these cases exact solutions are obtained, analysed and graphically illustrated. This allows us to derive the transformation coefficients in the analytic form and compare them with the available data obtained for the particular models either approximately or numerically. We show that the results obtained are in agreement with the energy flux conservation and Lamb's formulae in the limiting case of zero frequency. We also study wave transformation on the underwater barriers and trenches of different shapes and compare the results obtained. The results obtained in this Chapter have been published in Pure and Applied Geophysics [44].

2.1 Introduction

The problem of linear wave transformation on the bottom unevenness has a long history. The development of rigorous mathematical methods for the description of wave transformation in the coastal zone represents an important and topical problem both from the academic and practical points of view, especially in application to the protection of marine engineering constructions (platforms, gas and oil pipelines, etc.) [13] and coastlines against hazardous impacts of large oceanic waves including tsunami waves [48, 71]. As well-known (see, for example, [124]), tsunami waves in the open ocean can be treated as the linear waves in a shallow basin; their typical heights are about 0.5 m, and wavelengths are 300 – 500 km, whereas the average ocean depth is 4 – 5 km. Therefore, scattering of such waves on underwater mountain ranges or trenches can be studied within the framework of linear shallow water theory.

The problem of wave propagation in the fluid with a variable bathymetry has a general solution in two limiting cases. When the bottom smoothly varies with the distance so that the characteristic scale of bottom variation is much greater than the wavelength; then the traditional JWKB method can be used to calculate wave parameters (amplitude, wavelength, and other parameters) (see, e.g., [36, 105, 124]). In another limiting case when there is an underwater stepwise obstacle, the solution for a wave field can be obtained on both sides from the step and then the solution can be matched at the boundary of two homogeneous regions. This procedure is not so trivial as may seem at first glans, because in general one should take into account not only travelling waves, but also the infinite series of evanescent modes (see [87] and references therein). However, in the long-wave approximation the evanescent modes does not exist [36] and the situation becomes much simpler.

Besides these limiting cases the problem of long wave propagation can be solved analytically for some particular bottom profiles [31, 107] (see also [36]), moreover for the linear bottom profile there is an exact solution of linearised hydrodynamic equations for waves of *arbitrary* wavelength [142, 147]. It was also shown that in some particular cases exact solutions can be obtained for the reflectionless propagation of long linear and nonlinear waves in a fluid with a special bottom profiles (see [34, 35]) and references therein).

Here we revise the problem of linear wave transformation in a shallow water where $kh_{1,2} \ll 1$ with three particular bottom profiles: (i) piecewise linear, (ii) piecewise quadratic, and (iii) hyperbolic tangent (tanh-) profiles. We show that in these particular cases the basic equations can be solved analytically and solutions can be presented in general in terms of hypergeometric functions, which can be reduced to elementary functions in the particular cases. This allows us to derive the transformation coefficient and compare the results for all three profiles. Then we study wave transformation over underwater obstacles/trenches of finite width, present the results in the graphical forms and analyse them.

2.2 The piecewise linear bottom profile

Consider first long linear shallow water wave scattering when it propagates in a water with the piecewise linear bottom profile shown in Fig. 2.1. An exact analytical solution to this problem was obtained by Dean (1964) [31] as early as beginning of 60th of last century (see also the book by Dingemans (1997) [36] where other approached to this problem are described). We shall re-consider this problem and present the results obtained in the form suitable for the comparison with other results derived for the parabolic and tanh-profiles. In the long-wave approximation the basic hydrodynamic equations representing mass and momentum conservations are [20]:

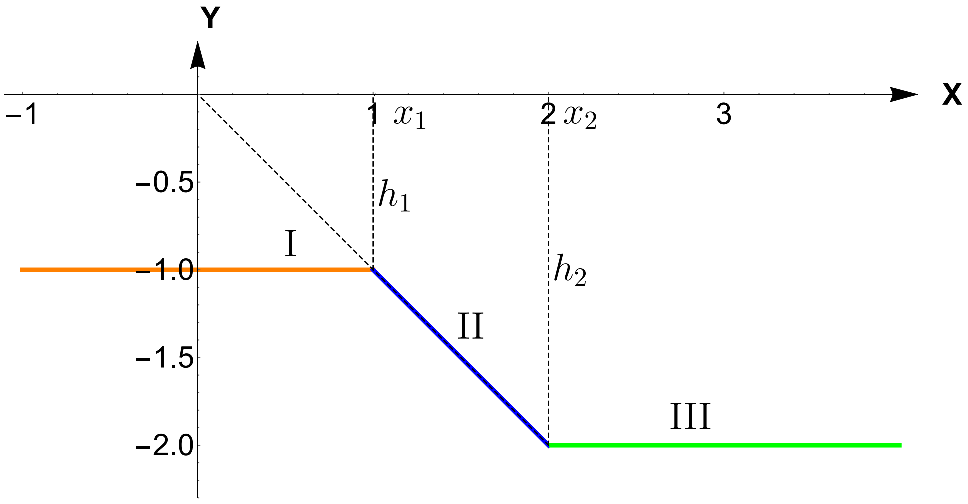

Figure 2.1: A basin with the piecewise linear bottom profile.

$$\eta^*_t + [U(\eta^* + h)]_x = 0, \tag{2.1}$$

$$\eta^*_x + U_t + UU_x = 0, \tag{2.2}$$

where U is the fluid velocity, η^* is the perturbation of a free surface, g is the acceleration due to gravity, and h is the water depth. We assume that the water depth is constant, $h = h_1$ when $x \leq x_1$ and $h = h_2$ when $x \geq x_2$; in the interval $x_1 \leq x \leq x_2$ the depth changes linearly $h = \alpha x$ (see Fig. 2.1).

For the further analysis it is convenient to present the set of equations (2.1) and (2.2) in the dimensionless form using the following change of variables:

$$V = \frac{U}{U_0}, \quad \eta = \frac{\eta^*}{\alpha l_0}, \quad \xi = \frac{x}{l_0}, \quad \hat{h} = \frac{h}{\alpha l_0} = \xi, \quad \hat{\omega} = \omega T_0, \quad \tau = \frac{t}{T_0}, \tag{2.3}$$

where $l_0 = x_2 - x_1$ (see Fig. 2.1), $T_0 = l_0/\alpha g$, and $U_0 = (\alpha g l_0)^{1/2}$

In the dimensionless variables the basic set of equations is:

$$\eta_\tau = -[V(\eta + h)]_\xi, \tag{2.4}$$

$$\eta_\xi = -V_\tau - V V_\xi. \tag{2.5}$$

Assuming that $\eta \ll h$, we obtain after linearisation and elimination of η the following wave equation:

$$V_{\tau\tau} - (Vh)_{\xi\xi} = 0 \tag{2.6}$$

In the intervals where the fluid depth is constant, i.e., for $x < x_1$ and $x > x_2$, an elementary solution to this equation can be sought in the form $V \sim e^{\mathrm{i}(\hat{\omega}\tau \pm k\xi)}$. However in the interval where the bottom linearly varies, i.e., when $x_1 < x < x_2$ and the depth $h = \xi$ in the dimensionless variables, the solution should be sought in the form: $V = \Psi(\xi) e^{\mathrm{i}\hat{\omega}\tau}$. After substitution this solution into Eq. (2.6) we obtain:

$$\xi \Psi_{\xi\xi} + 2\Psi_\xi + \hat{\omega}^2 \Psi = 0 \tag{2.7}$$

This is the standard Bessel equation whose solution is a linear combination of Bessel functions. Therefore for function $V(\xi, \tau)$ we obtain:

$$V(\xi) = \frac{1}{\hat{\omega}\sqrt{\xi}} \left[B_1 J_1(2\hat{\omega}\sqrt{\xi}) + B_2 Y_1(2\hat{\omega}\sqrt{\xi}) \right] e^{\mathrm{i}\hat{\omega}\tau}, \tag{2.8}$$

where $J_1(x)$ and $Y_1(x)$ are Bessel functions of the first and second kinds respectively. Then in the linear approximation we find from Eq. (2.4) for $\eta = \Phi(\xi) e^{\mathrm{i}\hat{\omega}\tau}$, where

$$\Phi(\xi) = \frac{\mathrm{i}}{\hat{\omega}} \left[B_1 J_0(2\hat{\omega}\sqrt{\xi}) + B_2 Y_0(2\hat{\omega}\sqrt{\xi}) \right]. \tag{2.9}$$

Here $J_0(x)$ and $Y_0(x)$ are Bessel functions of the first and second kinds, but with the zero indices. Now we can write down the general solutions for the perturbation of a free surface in three different domains shown in Fig. 2.1:

$$\Phi_l = A_1 \mathrm{e}^{-\mathrm{i}k_1(\xi - \xi_1)} + A_2 \mathrm{e}^{\mathrm{i}k_1(\xi - \xi_1)}, \qquad \xi \le \xi_1; \tag{2.10}$$

$$\Phi_c = \frac{\mathrm{i}}{\omega} \left[B_1 J_0(2\hat{\omega}\sqrt{\xi}) + B_2 Y_0(2\hat{\omega}\sqrt{\xi}) \right], \qquad \xi_1 \le \xi \le \xi_2; \tag{2.11}$$

$$\Phi_r = C_1 \mathrm{e}^{-\mathrm{i}k_2(\xi - \xi_2)} + C_2 \mathrm{e}^{\mathrm{i}k_2(\xi - \xi_2)}, \qquad \xi \ge \xi_2. \tag{2.12}$$

where the wavenumbers are

$$k_1 = \frac{\omega l_0}{\sqrt{gh_1}} = \frac{\hat{\omega}}{\sqrt{\xi_1}}, \quad k_2 = \frac{\omega l_0}{\sqrt{gh_2}} = \frac{\hat{\omega}}{\sqrt{\xi_2}} \tag{2.13}$$

and $A_{1,2}, B_{1,2}, C_{1,2}$ are arbitrary constants. Note that in stationary inhomogeneous media a wave frequency conserves in the process of wave transformation.

Solutions (2.10)–(2.12) can be matched at the boundaries of domains 1, 2, and 3 shown in Fig. 2.1 by means of the following boundary conditions reflecting the continuity of function $\Phi(\xi)$ and its first derivative:

$$\Phi_l(\xi_1) = \Phi_c(\xi_1),\ \Phi_c(\xi_2) = \Phi_r(\xi_2),\ \Phi_l'(\xi_1) = \Phi_c'(\xi_1),\ \Phi_c'(\xi_2) = \Phi_r'(\xi_2). \tag{2.14}$$

Using these boundary conditions, we consider below surface wave transformation on the bottom unevenness when the incident wave arrives from the left and from the right.

2.2.1 Wave transformation in the case of decreasing depth

This case corresponds to the situation when an incident wave arrives from the right in Fig. 2.1. Then we set the following coefficients in the solutions (2.10)–(2.12):

$$A_1 = 0, \quad A_2 = T_r, \quad C_1 = R, \quad C_2 = 1, \tag{2.15}$$

where C_2 is the amplitude of an incident wave, R is the reflection coefficient (the amplitude of reflected wave), and T_r is the transmission coefficient (the amplitude of transmitted wave).

By substitution solutions (2.10)–(2.12) with the coefficients (2.15) into the boundary conditions (2.14), we obtain for the transformation coefficients R and T, as well as for the amplitudes of waves B_1 and B_2 in the transient region II (see Fig. 2.1):

$$\begin{aligned}
R = \frac{1}{\Delta}\Big\{&\left[J_0\left(2\hat{\omega}\sqrt{\xi_2}\right) - \mathrm{i}J_1\left(2\hat{\omega}\sqrt{\xi_2}\right)\right]\left[Y_0\left(2\hat{\omega}\sqrt{\xi_1}\right) - \mathrm{i}Y_1\left(2\hat{\omega}\sqrt{\xi_1}\right)\right] \\
&- \left[J_0\left(2\hat{\omega}\sqrt{\xi_1}\right) - \mathrm{i}J_1\left(2\hat{\omega}\sqrt{\xi_1}\right)\right]\left[Y_0\left(2\hat{\omega}\sqrt{\xi_2}\right) - \mathrm{i}Y_1\left(2\hat{\omega}\sqrt{\xi_2}\right)\right]\Big\}, \quad (2.16)\\
T_r = \frac{2\,\mathrm{i}}{\Delta}&\left[J_1\left(2\hat{\omega}\sqrt{\xi_1}\right)Y_0\left(2\hat{\omega}\sqrt{\xi_1}\right) - J_0\left(2\hat{\omega}\sqrt{\xi_1}\right)Y_1\left(2\hat{\omega}\sqrt{\xi_1}\right)\right], \quad (2.17)\\
B_1 = -\frac{2\,\mathrm{i}\,\hat{\omega}}{\Delta}&\left[Y_0\left(2\hat{\omega}\sqrt{\xi_1}\right) - \mathrm{i}Y_1\left(2\hat{\omega}\sqrt{\xi_1}\right)\right], \quad (2.18)\\
B_2 = \frac{2\,\mathrm{i}\,\hat{\omega}}{\Delta}&\left[J_0\left(2\hat{\omega}\sqrt{\xi_1}\right) - \mathrm{i}J_1\left(2\hat{\omega}\sqrt{\xi_1}\right)\right], \quad (2.19)
\end{aligned}$$

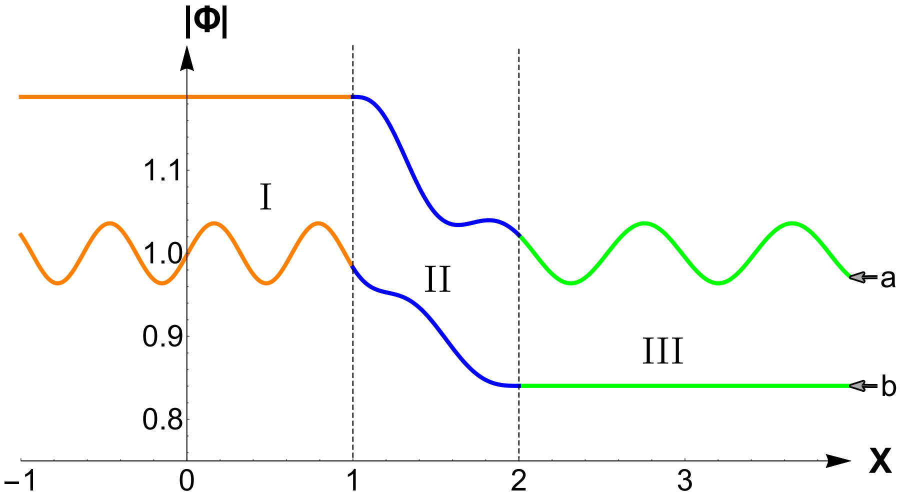

Figure 2.2: Solutions for the free surface perturbation (2.10)–(2.12) with the coefficients (2.16)–(2.19) in terms of $|\Phi(\xi)|$. Line a) pertains to the case when the incident wave arrives from the right where the depth $h_2 > h_1$, and line b) pertains to the case when the incident wave arrives from the left where the depth $h_1 > h_2$. The Roman numerals correspond to the domains shown in Fig. 2.1. The plot was generated for the particular set of parameters when $h_1 = 1$ and $h_2 = 2$, and wave frequency $\hat{\omega} = 5$; for other parameters h_1, h_2, and $\hat{\omega}$ the plots are similar to these.

where the determinant is:

$$\begin{aligned}\Delta = &\left[J_0\left(2\hat{\omega}\sqrt{\xi_2}\right) + \mathrm{i}J_1\left(2\hat{\omega}\sqrt{\xi_2}\right)\right]\left[Y_0\left(2\hat{\omega}\sqrt{\xi_1}\right) - \mathrm{i}Y_1\left(2\hat{\omega}\sqrt{\xi_1}\right)\right]\\ &-\left[J_0\left(2\hat{\omega}\sqrt{\xi_1}\right) - \mathrm{i}J_1\left(2\hat{\omega}\sqrt{\xi_1}\right)\right]\left[Y_0\left(2\hat{\omega}\sqrt{\xi_2}\right) + \mathrm{i}Y_1\left(2\hat{\omega}\sqrt{\xi_2}\right)\right]. \qquad (2.20)\end{aligned}$$

Solutions (2.10)–(2.12) with the coefficients (2.16)–(2.19) are shown in Fig. 2.2 for $|\Phi(\xi)|$ (see line a). A wavy dependence of function $|\Phi(\xi)|$ in the region III is caused by bits of incident and reflected waves, whereas in region I we have only one transmitted sinusoidal wave of a constant amplitude. Figure 2.3a) shows the reflection coefficient and Fig. 2.3b) the transmission coefficient as the functions of normalised frequency $\hat{\omega}$.

In the limiting case $\hat{\omega} \to 0$ the formulae for the transformation coefficients reduce to the well-known expressions derived by Lamb [88] for the step-wise bottom (see also [87, 105] and references therein):

$$R = \frac{1-\sqrt{k}}{1+\sqrt{k}}, \quad T = \frac{2}{1+\sqrt{k}}, \qquad (2.21)$$

where $k = h_1/h_2$. Such reduction is quite natural, because in the limit $\hat{\omega} \to 0$ the wave lengths of scattered waves become much greater than the length of transient

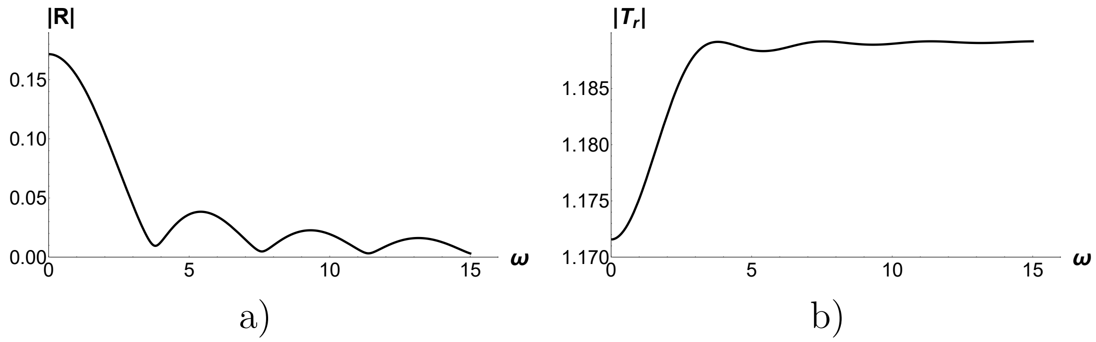

a)

b)

Figure 2.3: The reflection $|R|$ (a) and transmission $|T_r|$ (b) coefficients as the functions of normalised frequency $\hat{\omega}$ for the fixed value of $h_2/h_1 = 2$. The plots pertain to the case when the incident wave arrives from the right where the depth $h_2 > h_1$.

domain l_0.

The non-monotonic character of dependencies $|R|(\hat{\omega})$ and $|T|(\hat{\omega})$ is explained by the interference of waves within the transient zone $\xi_1 \leq \xi \leq \xi_2$ due to the reflections from the bottom edges at ξ_1 and ξ_2. However in the minima the reflection coefficient never vanishes (see Fig. 2.3), therefore the reflectionless propagation is impossible, although for some "quasi-resonant" frequencies the reflected wave can be very small.

As follows from Fig. 2.3, the amplitude of transmitted wave can be greater than the amplitude of an incident wave ($T > 1$); this is a usual effect when a wave travels from a deeper region to a shallower region, herewith its wavelength decreases and amplitude increases (no the over-transmission occurs). The energy flux conserves in this case and results in the relationship between R, T, and $h_{1,2}$. The energy flux can be determined as the density of wave energy (which is proportional to the squared wave amplitude) times wave speed (see, e.g., [36, 107]), which is in the dimensionless variables $c(x) = \sqrt{h(x)}$. Therefore, the energy flux conservation can be presented as:

$$c_1 T^2 = c_2(1 - R^2), \quad \text{or} \quad \sqrt{\frac{h_1}{h_2}} T^2 + R^2 = 1. \tag{2.22}$$

2.2.2 Wave transformation in the case of increasing depth

In this case when the incident wave arrives from the left we chose the coefficients of the system (2.10)–(2.12) as follows:

$$A_1 = 1, \quad A_2 = R, \quad C_1 = T_l, \quad C_2 = 0. \tag{2.23}$$

By substitution solutions (2.10)–(2.12) with the coefficients (2.23) into the boundary conditions (2.14), we obtain again for the transformation coefficients R and T_l, as well as for the amplitudes of waves in the transient domain 2 (see Fig. 2.1) B_1 and B_2:

$$\begin{aligned} R = {} & \frac{1}{\Delta}\left\{\left[J_0(2\hat{\omega}\sqrt{\xi_2}) + \mathrm{i}J_1(2\hat{\omega}\sqrt{\xi_2})\right]\left[Y_0(2\hat{\omega}\sqrt{\xi_1}) + \mathrm{i}Y_1(2\hat{\omega}\sqrt{\xi_1})\right]\right. \\ & \left. - \left[J_0(2\hat{\omega}\sqrt{\xi_1}) + \mathrm{i}J_1(2\hat{\omega}\sqrt{\xi_1})\right]\left[Y_0(2\hat{\omega}\sqrt{\xi_2}) + \mathrm{i}Y_1(2\hat{\omega}\sqrt{\xi_2})\right]\right\}, \qquad (2.24) \\ T_l = {} & \frac{2\mathrm{i}}{\Delta}\left[J_1(2\hat{\omega}\sqrt{\xi_2})Y_0(2\hat{\omega}\sqrt{\xi_2}) - J_0(2\hat{\omega}\sqrt{\xi_2})Y_1(2\hat{\omega}\sqrt{\xi_2})\right], \qquad (2.25) \\ B_1 = {} & \frac{2\hat{\omega}\mathrm{i}}{\Delta}\left[Y_0(2\hat{\omega}\sqrt{\xi_2}) + \mathrm{i}Y_1(2\hat{\omega}\sqrt{\xi_2})\right], \qquad (2.26) \\ B_2 = {} & -\frac{2\hat{\omega}\mathrm{i}}{\Delta}\left[J_0(2\hat{\omega}\sqrt{\xi_2}) + \mathrm{i}J_1(2\hat{\omega}\sqrt{\xi_2})\right], \qquad (2.27) \end{aligned}$$

where the determinant Δ is the same as in Eq. (2.20).

Solutions (2.10)–(2.12) with the coefficients (2.24)–(2.27) are shown in Fig. 2.2 for $|\Phi(\xi)|$ (see line b). Graphic of the reflection coefficient for the same depth ratio $h_2/h_1 = 2$ is the same as in Fig. 2.3a), and the graphic of transformation coefficient is similar to that shown in Fig. 2.3b), but with the additional multiplicative factor $\sqrt{h_2/h_1}$. Now the amplitude of transmitted wave is less than the amplitude of an incident wave ($T_l < 1$), but the energy flux still conserves and has the same form as in Eq. (2.22) with the depth interchange: $h_1 \longleftrightarrow h_2$. This is the direct consequence of the *reciprocity relationship* derived in [107]: $k_2h_2T_l = k_1h_1T_r$, where the wavenumbers k_1 and k_2 are determined in Eqs. (2.13).

2.3 The piecewise quadratic bottom profile

In this section we consider the case when the the bottom profile in the transient domain between two semi-infinite intervals with a constant depth can be approximated by a smooth conjugation of two quadratic functions as shown in Fig. 2.5 by line 1. A similar problem was considered by Kajiura (1961) [78] (see also [36]) for the model when one quadratic function in the transient domain connects two bottom levels with the discontinuities of derivatives at the boundaries (see line 2 in Fig. 2.5). Kajiura derived the reflection coefficient by means of JWKB method up to second order terms in the asymptotic expansion in small parameter $(kl_0)^{-1} \ll 1$, where k is the wavenumber and $l_0 = x_2 - x_1$ is the width of the transient domain. It has been shown that the reflection coefficient $R \sim \hat{\omega}^{-1}$ apart from an oscillatory structure of the dependence $R(\hat{\omega})$. This problem was re-considered later by Mei (1990) [107] who derived the exact solution for the transient domain with the quadratic bottom profile and obtained the transformation coefficients. Here we consider a similar problem, but with two quadratic functions representing smooth connection of two bottom levels as shown in Fig. 2.5. We show that the exact solutions can be constructed and the transformation coefficients can be derived in the analytic, although rather cumbersome form. We assume that the bottom profile can be presented by two parabolic functions

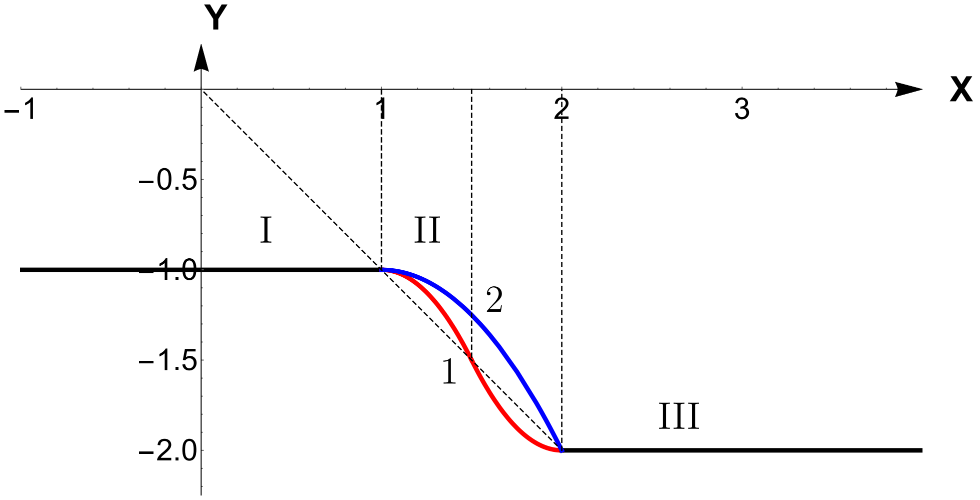

Figure 2.4: A basin with the piecewise quadratic bottom profile. Line 1 pertains to the case when two quadratic functions are conjugated at the middle of the transient zone ($\gamma = 0.5$ – see the text) with smooth conjugation at the boundaries shown by dashed vertical lines. Line 2 pertains to the quadratic profile connecting two constant bottom levels as considered by Kajiura (1961) [78] and Mei (1990) [107].

$h(\xi) = a\xi^2 + b\xi + c$ with different coefficients smoothly matched with each other within the transient domain (at the point ξ_c) and with the constant bottom levels at the edges ξ_1 and ξ_2 of the transient domain. This can be achieved by the following choice of parabolic functions:

$$h_L(\xi) = \xi_1 + \frac{(\xi - \xi_1)^2}{\gamma\,(\xi_2 - \xi_1)}, \qquad \xi_1 \le \xi \le \xi_c, \tag{2.28}$$

$$h_R(\xi) = \xi_2 - \frac{(\xi - \xi_2)^2}{(1 - \gamma)\,(\xi_2 - \xi_1)}, \qquad \xi_c \le \xi \le \xi_2, \tag{2.29}$$

where $\xi_c = \xi_2\gamma + (1 - \gamma)\xi_1$ and $0 < \gamma < 1$. Varying the parameter γ one can obtain a class of smooth parabolic profiles connecting two constant bottom levels at different points; this can be treated as the spline approximation of a bottom profile. For simplicity we show in Fig. 2.5 only one such profile with $\gamma = 0.5$ (see line 1). To construct a solution to the linearised set of equations (2.4), (2.5) it is convinient to reduce it to one equation for the perturbation of water surface

$\eta(\xi, \tau)$:

$$\eta_{\tau\tau} - \left(\eta_\xi h\right)_\xi = 0 \tag{2.30}$$

Substituting here a solution in the form: $\eta(\xi, \tau) = e^{\mathrm{i}\hat{\omega}\tau}\Phi(\xi)$ and the expressions for the bottom profile (2.28), (2.29), we obtain the Legendre equation for function $\Phi(\xi)$:

$$\left(a\xi^2 + b\xi + c\right)\Phi^{''} + (2a\xi + b)\,\Phi^{'} + \hat{\omega}^2\Phi = 0, \tag{2.31}$$

where a, b, and c are some real constants. Solution to this equation can be expressed in general in terms of the linear combination of Legendre functions:

$$\Phi(\xi) = B_1 P_\nu^0\left(\frac{2a\xi + b}{\sqrt{b^2 - 4ac}}\right) + B_2 Q_\nu^0\left(\frac{2a\xi + b}{\sqrt{b^2 - 4ac}}\right), \tag{2.32}$$

where P_ν^0 and Q_ν^0 are the Legendre functions of the first and second kinds with $\nu = \left(\sqrt{1 - 4\hat{\omega}^2/a} - 1\right)/2$ (Polyanin and Zaitsev 2003), and B_1 and B_2 are arbitrary constants. In the particular case when $a = -\hat{\omega}^2/n(n+1)$, where n is a positive integer, one of these functions reduces to the Legendre polynomial $P_n(\xi)$. Now solutions of Eq. (2.30) in all four domains shown in Fig. 2.5 can be presented as:

$$\Phi_l(\xi) = A_1 \mathrm{e}^{-\mathrm{i}k_1(\xi - \xi_1)} + A_2 \mathrm{e}^{\mathrm{i}k_1(\xi - \xi_1)}, \qquad \xi \le \xi_1, \tag{2.33}$$

$$\Phi_{p_1}(\xi) = B_1\bar{w}_1 + B_2\bar{w}_2, \qquad \xi_1 \le \xi \le \xi_c, \tag{2.34}$$

$$\Phi_{p_2}(\xi) = C_1\tilde{w}_1 + C_2\tilde{w}_2, \qquad \xi_c \le \xi \le \xi_2, \tag{2.35}$$

$$\Phi_r(\xi) = D_1 \mathrm{e}^{-\mathrm{i}k_2(\xi - \xi_2)} + D_2 \mathrm{e}^{\mathrm{i}k_2(\xi - \xi_2)}, \qquad \xi \ge \xi_2, \tag{2.36}$$

where $A_{1,2}, B_{1,2}, C_{1,2}$ and $D_{1,2}$ are arbitrary constants,

$$\bar{w}_1 = P_\nu^0\left[\frac{\xi - \xi_1}{\sqrt{\gamma\xi_1(\xi_1 - \xi_2)}}\right], \qquad \bar{w}_2 = Q_\nu^0\left[\frac{\xi - \xi_1}{\sqrt{\gamma\xi_1(\xi_1 - \xi_2)}}\right], \tag{2.37}$$

$$\tilde{w}_1 = P_\mu^0\left[\frac{\xi - \xi_2}{\sqrt{(1-\gamma)\,\xi_2\,(\xi_2 - \xi_1)}}\right], \quad \tilde{w}_2 = Q_\mu^0\left[\frac{\xi - \xi_2}{\sqrt{(1-\gamma)\,\xi_2\,(\xi_2 - \xi_1)}}\right], \tag{2.38}$$

and the indeces ν and μ are:

$$\nu = \frac{1}{2}\left[\sqrt{1 + 4\gamma\hat{\omega}^2\,(\xi_1 - \xi_2)} - 1\right], \; \mu = \frac{1}{2}\left[\sqrt{1 + 4\hat{\omega}^2\,(1-\gamma)\,(\xi_2 - \xi_1)} - 1\right]. \tag{2.39}$$

Solutions (2.33)–(2.36) can be matched at the boundaries of domains in the points $\xi = \xi_1, \xi_c$ and ξ_2 with the help of boundary conditions reflecting the continuity of function $\Phi(\xi)$ and its first derivative:

$$\Phi_l(\xi_1) = \Phi_{p_1}(\xi_1), \quad \Phi_{p_1}(\xi_c) = \Phi_{p_2}(\xi_c), \quad \Phi_{p_2}(\xi_2) = \Phi_r(\xi_2), \tag{2.40}$$

$$\Phi_l^{'}(\xi_1) = \Phi_{p_1}^{'}(\xi_1), \quad \Phi_{p_1}^{'}(\xi_c) = \Phi_{p_2}^{'}(\xi_c), \quad \Phi_{p_2}^{'}(\xi_2) = \Phi_r^{'}(\xi_2). \tag{2.41}$$

This gives a set of six linear algebraic equations for the coefficients $A_{1,2}, B_{1,2}, C_{1,2}$ and $D_{1,2}$.

Using these boundary conditions, we consider below surface wave transformation on the bottom unevenness when the incident wave arrives from the left and from the right. In the former case we set the following coefficients in the system (2.33)–(2.36):

$$A_1 = 0, \quad A_2 = T_l, \quad D_1 = R, \quad D_2 = 1 \tag{2.42}$$

and determine than R, T_l, as well as $B_{1,2}$ and $C_{1,2}$. In the later case we set the following coefficients in the system (2.33)–(2.36):

$$A_1 = 1, \quad A_2 = R, \quad D_1 = T_r, \quad D_2 = 0 \tag{2.43}$$

and determine than R, T_r, as well as $B_{1,2}$ and $C_{1,2}$. Omitting long and tedious calculations, we obtain the transformation coefficients $R(\hat{\omega})$ and $T_{l,r}(\hat{\omega})$ which are shown in Fig. 2.7 for three values of γ: $\gamma = 0.1$ (line 1), $\gamma = 0.5$ (line 2), and $\gamma = 0.9$ (line 3). The reflection coefficients are again the same for the left- and right-propagating incident waves. The transmission coefficients are different as in the previous model with the piecewise linear bottom profile, but proportional to each other, $|T_l| = |T_r|\sqrt{h_2/h_1}$, in accordance with the reciprocity theorem. Figure 2.7b) shows the coefficient T_r as the function of normalised wave frequency for the same three values of γ: $\gamma = 0.1$ (line 1), $\gamma = 0.5$ (line 5), and $\gamma = 0.9$ (line 3).
We do not present here formulae for the coefficients $B_{1,2}$ and $C_{1,2}$, as well as the explicit solutions (2.33)–(2.36), because they look very cumbersome. However in Fig. 2.6 we illustrate solutions obtained in terms of $|\Phi(\xi)|$ for the particular wave frequency and depths h_1 and h_2. In the limiting case $\hat{\omega} \to 0$ the formulae for the transformation coefficients reduce again to the well-known Lamb formulae for the step-wise bottom profile (2.21). The dependencies of transformation coefficients on frequency, $|R|(\hat{\omega})$ and $|T|(\hat{\omega})$, are still non-monotonic, but much smoother than in the former case of quasi-linear bottom profile (cf. graphics of Figs. 2.7 and 2.3), because in this case the bottom profile is much smoother having discontinuity only in the second derivative at the edge points ξ_1 and ξ_2. The energy flux conservation in the form of Eq. (2.22) has been tested and confirmed on the derived solutions.

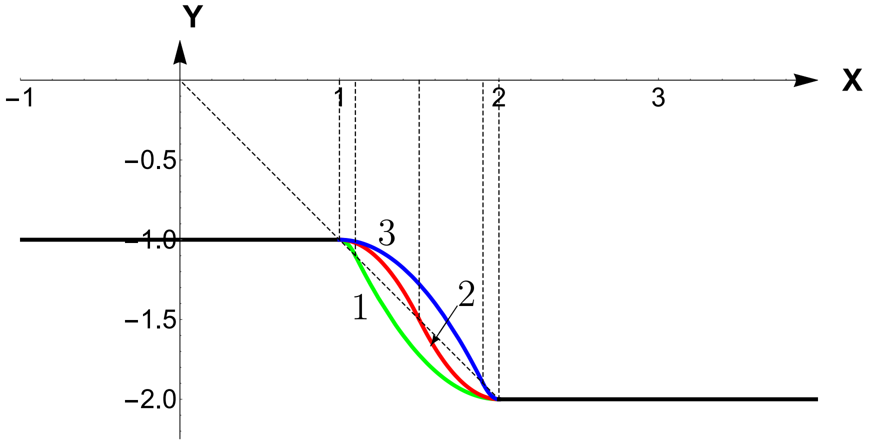

Figure 2.5: A basin with the piecewise quadratic bottom profile. Line 1 pertains to the case when quadratic functions are conjugated closer to the left edge of the transient zone ($\gamma = 0.1$); line 2 pertains to the case when two quadratic functions are conjugated at the middle of the transient zone ($\gamma = 0.5$ – see the text); and line 3 pertains to the case when quadratic functions are conjugated closer to the right edge of the transient zone ($\gamma = 0.9$).

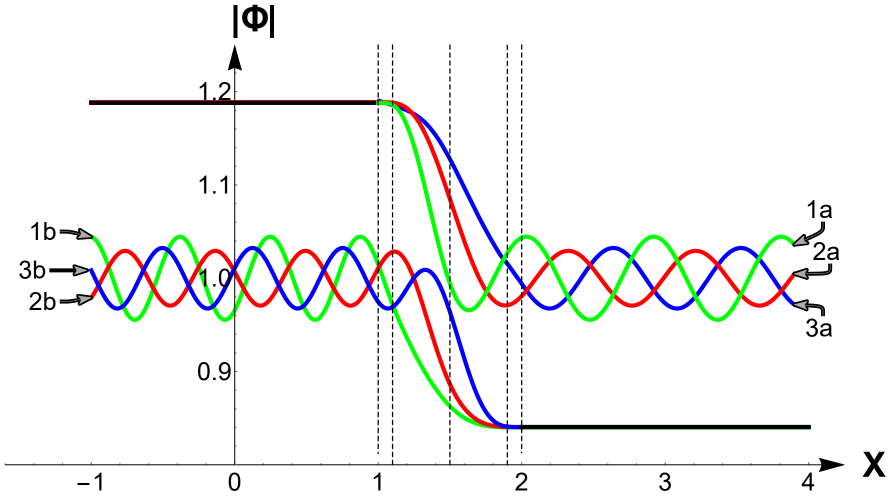

Figure 2.6: Graphics of solutions for the free surface perturbation in terms of $|\Phi(\xi)|$. Lines 1a, 2a, and 3a pertain to the case when the incident wave arrives from the right where the depth $h_2 > h_1$, and lines 1b, 2b, and 3b pertain to the case when the incident wave arrives from the left where the depth $h_1 > h_2$. The numbers 1, 2, 3 correspond to the cases when $\gamma = 0.1, 0.5, 0.9$ respectively. The plot was generated for the particular case when $h_1 = 1$ and $h_2 = 2$, and wave frequency $\hat{\omega} = 5$; for other parameters h_1, h_2, and $\hat{\omega}$ the plots are similar to these.

2.4 Hyperbolic tangent bottom profile

In this section we consider the bottom spatial variation that can be described by the tanh-function so that the fluid depth is: $h(\xi) = a\tanh(\xi) + b$, where $a = (h_2 - h_1)/2$ and $b = (h_2 + h_1)/2$. Figure 2.8 illustrates the tanh bottom

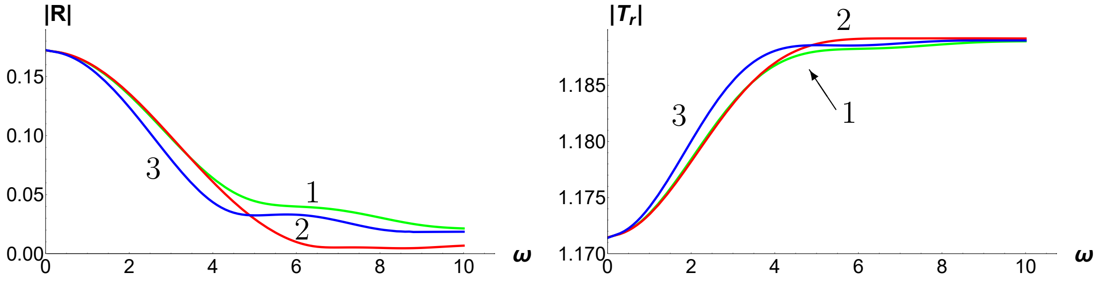

a) b)

Figure 2.7: The reflection R (frame a) and transmission T_r (frame b) coefficients as the functions of normalised frequency $\hat{\omega}$ for the fixed value of $h_2/h_1 = 2$ and $\hat{\omega} = 5$. Line 1 pertains to $\gamma = 0.5$, line 2 – to $\gamma = 0.1$, and line 3 – to $\gamma = 0.9$ (for the definition of γ see the text).

profile (line 1) in comparison with the quadratic profile (line 2) and linear profile (dashed line) considered in the previous sections. By substitution the depth

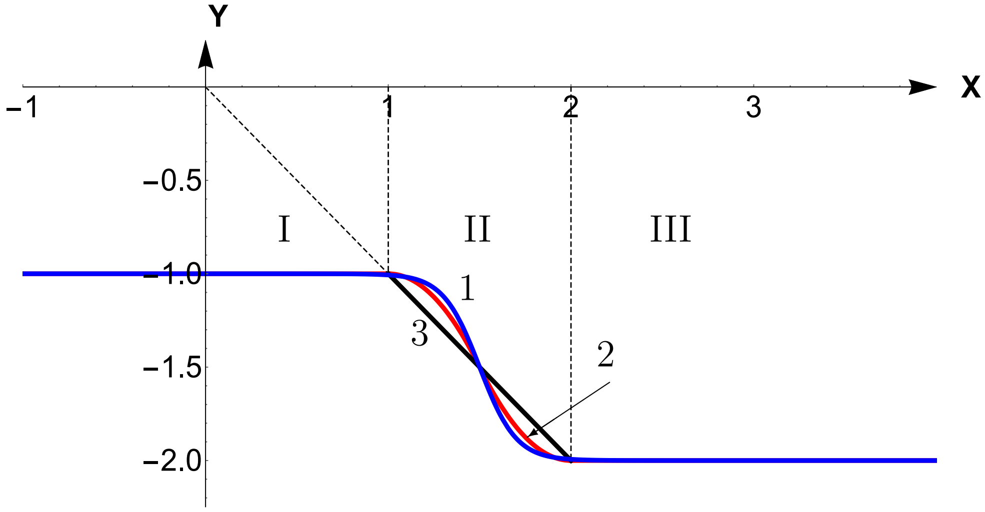

Figure 2.8: The tanh bottom profile (line 1), combined quadratic profile (line 2) and linear profile (line 3). In the domains I and III the bottom quickly becomes constant, whereas in the domain II the bottom profile experiences a significant transition from one level to another level.

profile into the equation for the velocity (2.6) we obtain:

$$[a\tanh(\xi) + b]\,\Psi_{\xi\xi} + 2a\,\mathrm{sech}^2(\xi)\Psi_\xi + \left[\hat{\omega}^2 - 2a\,\mathrm{sech}^2(\xi)\tanh(\xi)\right]\Psi = 0. \quad (2.44)$$

Solution to this equation can be presented in terms of hyper-geometric functions:

$$\Psi = \frac{(k^2-1)\left(1+\mathrm{e}^{2\xi}\right)}{2\left(1+\mathrm{e}^{2\xi}k^2\right)}\mathrm{e}^{\mathrm{i}\tilde{\omega}(\xi-\mathrm{i}\pi/2)}\times$$

$$\left\{C_1 \cdot {}_2F_1\left[\frac{\mathrm{i}\,(k-1)\,\tilde{\omega}}{2}, -\frac{\mathrm{i}\,(k+1)\,\tilde{\omega}}{2}, 1-\mathrm{i}\tilde{\omega}, -\frac{\mathrm{e}^{-2\xi}}{k^2}\right] + C_2\left(\frac{\mathrm{e}^{-\xi+\mathrm{i}\pi/2}}{-k^2}\right)^{\mathrm{i}\tilde{\omega}} \times \right.$$
$$\left. {}_2F_1\left[-\frac{\mathrm{i}\,(k-1)\,\tilde{\omega}}{2}, \frac{\mathrm{i}\,(k+1)\,\tilde{\omega}}{2}, 1+\mathrm{i}\tilde{\omega}, -\frac{\mathrm{e}^{-2\xi}}{k^2}\right]\right\}, \tag{2.45}$$

where $k=\sqrt{h_2/h_1}$, $\tilde{\omega}=\hat{\omega}/\sqrt{h_2}$ Substituting this solution into the equation (2.5), we obtain a solution for the perturbation of a free surface:

$$\begin{aligned}\Phi(\xi) = \frac{\sqrt{h_1}\,(k^2-1)\,\mathrm{e}^{\pi/2}}{2}&\left(C_1\left\{{}_2F_1\left[\frac{\mathrm{i}\,(k-1)\,\tilde{\omega}}{2}, -\frac{\mathrm{i}\,(k+1)\,\tilde{\omega}}{2}, 1-\mathrm{i}\tilde{\omega}, -\frac{\mathrm{e}^{-2\xi}}{k^2}\right]\right.\right. \\ &- \left.\frac{k+1}{k}{}_2F_1\left[\frac{\mathrm{i}\,(k-1)\,\tilde{\omega}}{2}, 1-\frac{\mathrm{i}\,(k+1)\,\tilde{\omega}}{2}, 1-\mathrm{i}\tilde{\omega}, -\frac{\mathrm{e}^{-2\xi}}{k^2}\right]\right\}\mathrm{e}^{\mathrm{i}\tilde{\omega}\xi} \\ &- C_2 k^{-2\mathrm{i}\tilde{\omega}}\left\{{}_2F_1\left[-\frac{\mathrm{i}\,(k-1)\,\tilde{\omega}}{2}, \frac{\mathrm{i}\,(k+1)\,\tilde{\omega}}{2}, 1+\mathrm{i}\tilde{\omega}, -\frac{\mathrm{e}^{-2\xi}}{k^2}\right]\right. \\ &- \left.\left.\frac{k+1}{k}{}_2F_1\left[-\frac{\mathrm{i}\,(k-1)\,\tilde{\omega}}{2}, 1+\frac{\mathrm{i}\,(k+1)\,\tilde{\omega}}{2}, 1+\mathrm{i}\tilde{\omega}, -\frac{\mathrm{e}^{-2\xi}}{k^2}\right]\right\}\mathrm{e}^{-\mathrm{i}\tilde{\omega}\xi}\right).\end{aligned} \tag{2.46}$$

The asymptotics of this solution when $\xi \to \pm\infty$ are: (1) $\xi \to +\infty$:

$$\Phi(\xi) = \frac{\sqrt{h_1}\,(k^2-1)}{2k}\left[-C_1\mathrm{e}^{\mathrm{i}\tilde{\omega}(\xi-\mathrm{i}\pi/2)} + C_2k^{-2\mathrm{i}\tilde{\omega}}\mathrm{e}^{-\mathrm{i}\tilde{\omega}(\xi-3\mathrm{i}\pi/2)}\right], \tag{2.47}$$

(2) $\xi \to -\infty$:

$$\begin{aligned}\Phi(\xi) = k^{\mathrm{i}(k-1)\tilde{\omega}}\sqrt{h_1}\Gamma\left(-\mathrm{i}k\tilde{\omega}\right)&\left\{C_2\left(k+1\right)\frac{\Gamma\left(\mathrm{i}\tilde{\omega}\right)}{\Gamma^2\left[-\frac{\mathrm{i}(k-1)\tilde{\omega}}{2}\right]}\right. \\ &- \left.C_1\left(k-1\right)\mathrm{e}^{2\pi\tilde{\omega}}\frac{\Gamma\left(-\mathrm{i}\tilde{\omega}\right)}{\Gamma^2\left[-\frac{\mathrm{i}(k+1)\tilde{\omega}}{2}\right]}\right\}\mathrm{e}^{\mathrm{i}\tilde{\omega}(k\xi+3\mathrm{i}\pi/2)} \\ &+ k^{-\mathrm{i}(k+1)\tilde{\omega}}\sqrt{h_1}\left\{C_2\left(k-1\right)\frac{\Gamma\left(\mathrm{i}\tilde{\omega}\right)\Gamma\left(\mathrm{i}k\tilde{\omega}\right)}{\Gamma^2\left[\frac{\mathrm{i}(1+k)\tilde{\omega}}{2}\right]}\right. \\ &- \left.C_1\mathrm{e}^{2\pi\tilde{\omega}}\frac{k^2-1}{2k}\frac{\Gamma\left(-\mathrm{i}\tilde{\omega}\right)\Gamma\left(1+\mathrm{i}k\tilde{\omega}\right)}{\Gamma\left[\frac{\mathrm{i}(k-1)\tilde{\omega}}{2}\right]\Gamma\left[1+\frac{\mathrm{i}(k-1)\tilde{\omega}}{2}\right]}\right\}\mathrm{e}^{-\mathrm{i}\tilde{\omega}(k\xi-3\mathrm{i}\pi/2)}.\end{aligned} \tag{2.48}$$

Thus, one can see that asymptotically solution (2.46) represents oppositely travelling waves which can be presented in the form:

$$\Phi\left(\xi\right) = A_1\mathrm{e}^{\mathrm{i}\tilde{\omega}\xi} + A_2\mathrm{e}^{-\mathrm{i}\tilde{\omega}\xi}, \qquad \xi \to +\infty \tag{2.49}$$

$$\Phi\left(\xi\right) = B_1\mathrm{e}^{\mathrm{i}k\tilde{\omega}\xi} + B_2\mathrm{e}^{-\mathrm{i}k\tilde{\omega}\xi}, \qquad \xi \to -\infty, \tag{2.50}$$

where $A_{1,2}$ and $B_{1,2}$ are the coefficients in front of corresponding exponential functions in Eqs. (2.47) and (2.48). Then, we can obtain the transformation coefficients of surface waves passing over such bottom unevenness. If an incident wave arrives from the right (from the deeper region as shown in Fig. 2.8), then we set:

$$A_1 = 1, \quad A_2 = R_r, \quad B_1 = T_r, \quad B_2 = 0 \tag{2.51}$$

and readily derive from Eqs. (2.47) and (2.48) the transformation coefficients:

$$R_r = -k^{-2\mathrm{i}\tilde{\omega}}\frac{k+1}{k-1}\frac{\Gamma\left(-\mathrm{i}\tilde{\omega}\right)\Gamma^2\left[\frac{1}{2}\mathrm{i}\left(k+1\right)\tilde{\omega}\right]}{\Gamma\left(\mathrm{i}\tilde{\omega}\right)\Gamma^2\left[\frac{1}{2}\mathrm{i}\left(k-1\right)\tilde{\omega}\right]}, \tag{2.52}$$

$$T_r = k^{\mathrm{i}(k-1)\tilde{\omega}}\frac{2k}{k+1}\frac{\Gamma\left(-\mathrm{i}\tilde{\omega}\right)\Gamma\left(-\mathrm{i}k\tilde{\omega}\right)}{\Gamma^2\left[-\frac{1}{2}\mathrm{i}\left(1+k\right)\tilde{\omega}\right]}\frac{\sinh\left(\pi\tilde{\omega}\right)\sinh\left(k\pi\tilde{\omega}\right)}{\mathrm{sech}^2\left[\frac{1}{2}\left(1+k\right)\pi\tilde{\omega}\right]}, \tag{2.53}$$

$$C_1 = \frac{-2\mathrm{e}^{-\pi\tilde{\omega}/2}k}{\sqrt{h_1}\left(k^2-1\right)}, \quad C_2 = \frac{-2\mathrm{e}^{3\pi\tilde{\omega}/2}k}{\sqrt{h_1}\left(k-1\right)^2}\frac{\Gamma\left(-\mathrm{i}\tilde{\omega}\right)\Gamma^2\left[\frac{1}{2}\mathrm{i}\left(k+1\right)\tilde{\omega}\right]}{\Gamma\left(\mathrm{i}\tilde{\omega}\right)\Gamma^2\left[\frac{1}{2}\mathrm{i}\left(k-1\right)\tilde{\omega}\right]}. \tag{2.54}$$

If an incident wave arrives from the left (from the shallower region), then we set:

$$A_1 = 0, \quad A_2 = T_l, \quad B_1 = R_l, \quad B_2 = 1 \tag{2.55}$$

and readily derive again from Eqs. (2.47) and (2.48) the transformation coefficients:

$$R_l = -k^{4\mathrm{i}\tilde{\omega}}R_r, \quad T_l = k^{\mathrm{i}(k-1)\tilde{\omega}}\frac{k+1}{2k}\frac{\Gamma^2\left[\frac{1}{2}\mathrm{i}\left(1+k\right)\tilde{\omega}\right]}{\Gamma\left(\mathrm{i}\tilde{\omega}\right)\Gamma\left(\mathrm{i}k\tilde{\omega}\right)}, \tag{2.56}$$

$$C_1 = 0, \qquad C_2 = \frac{\mathrm{e}^{\frac{3\pi\tilde{\omega}}{2}}k^{\mathrm{i}(1+k)\tilde{\omega}}\Gamma^2\left[\frac{1}{2}\mathrm{i}\left(1+k\right)\tilde{\omega}\right]}{\sqrt{h_1}\left(-1+k\right)\Gamma\left(\mathrm{i}\tilde{\omega}\right)\Gamma\left(\mathrm{i}k\tilde{\omega}\right)}. \tag{2.57}$$

Figure 2.9 illustrates solution (2.46) for the incident wave arriving from the right (line 1a) and from the left (line 1b) in comparison with the solutions derived for the piecewise quadratic bottom profile (lines 2a and 2b correspondingly). As one can see from this figure, the spatial periods of bits are shorter in the case of tanh bottom profile, whereas their amplitudes are a slightly greater then in the case of piece-parabolic bottom profile.

The moduli of transformation coefficients $|R_r|$ and $|T_r|$ are shown in Fig. 2.10 for the same two bottom profiles and for the case when the incident wave arrives from the right. In the case when the incident wave arrives from the left the modulus of reflection coefficient is the same as in the former case: $|R_l| = |R_r|$, and the transmission coefficient $|T_l|$ is related with the transmission coefficient $|T_r|$ by the reciprocity relationship: $|T_l| = |T_r|\sqrt{h_2/h_1}$.

The general conclusion which follows from the comparison of transformation coefficients for all three cases of piecewise linear, piecewise quadratic, and tanh bottom profiles is that the smoother the profile, the smaller oscillations in the dependencies of $|R(\hat{\omega})|$ and $|T(\hat{\omega})|$ (cf. lines 1 and 2 in Fig. 2.10 with the lines in Fig. 2.3). There are no oscillations in the dependencies $|R(\hat{\omega})|$ and $|T(\hat{\omega})|$ in the case of tanh-profile (see lines 1 in Fig. 2.10). In the case of piecewise quadratic bottom profile the oscillations in such dependencies are very small and almost invisible (see lines 2 in Fig. 2.10), whereas in the case of piecewise linear profile the oscillations are very well pronounced Fig. 2.3).

The conservation of energy flux in the form of Eq. (2.22) holds again, as expected. Having solutions for the wave propagation over uneven bottom with the piecewise linear, piecewise quadratic, and tanh bottom profiles, we can solve problems with the more complicated bottom profiles approximating them by sets of such functions for which exact solutions exist in the analytic forms. Below we present solutions for underwater trenches and barriers of different shapes. Similar problem was considered by Tokano (1960) [149], Newman (1965) [113], Kirby & Dalrymple (1983) [81], Devillard et al. (1988) [33] for a submerged rectangular bar and trench (see also (Massel 1989 [105]) and (Dingemans 1997 [36]) and references therein). In the paper by Rey et al. (1992) [129] this problem was studied experimentally in the laboratory wave tank.

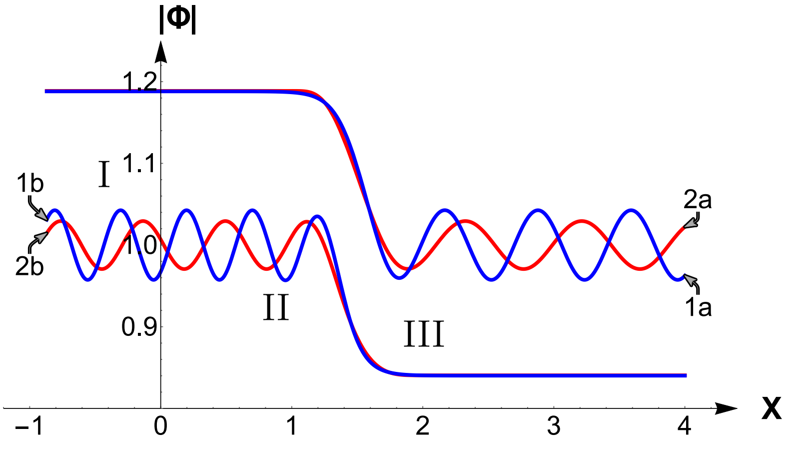

Figure 2.9: Graphics of solutions for the free surface perturbation in terms of $|\Phi(\xi)|$ for the tanh bottom profile (lines 1a and 1b) and for the piecewise quadratic bottom profile (lines 2a and 2b). Lines 1a and 2a pertain to incident waves arriving from the right, and lines 1b and 2b pertain to incident waves arrives from the left. The plot was generated for the particular case when $h_1 = 1$ and $h_2 = 2$, and wave frequency $\hat{\omega} = 5$; for other parameters h_1, h_2, and $\hat{\omega}$ the plots are similar to these.

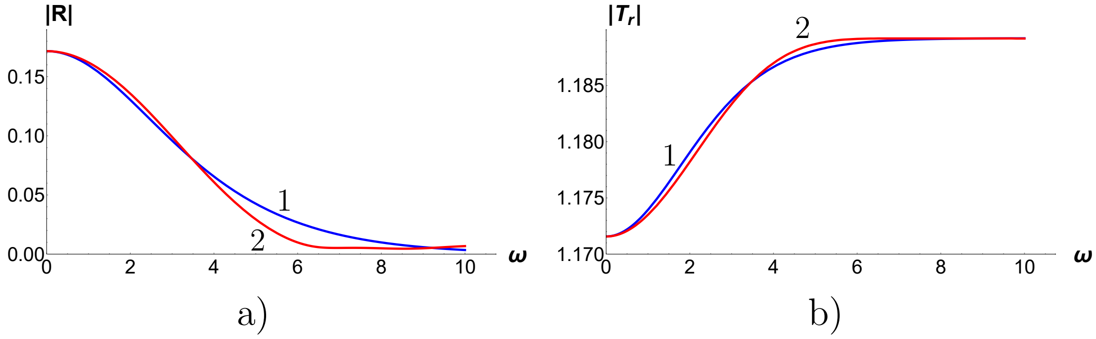

a) b)

Figure 2.10: The reflection (frame a) and transmission (frame b) coefficients for the tanh-profile (lines 1) and piecewise quadratic (lines 2) bottom profile for the cases when the incident waves arrives from the right. The plots were generated for the particular case when $h_1 = 1$ and $h_2 = 2$, and wave frequency $\hat{\omega} = 5$.

2.5 Wave scattering on an underwater trench and barrier with the linear slopes

Consider the bottom profiles shown in Fig. 2.11, which can be described by a set of linear functions $h(x) = ax + b$ with different parameters a and b. The left and right slopes of the trench/barrier can be described by the following parameters (see Fig. 2.11):

$$a_1 = \frac{h_2 - h_1}{x_2 - x_1}, \quad a_2 = \frac{h_2 - h_1}{x_3 - x_4}, \quad b_1 = \frac{h_1 x_2 - h_2 x_1}{x_2 - x_1}, \quad b_2 = \frac{h_1 x_3 - h_2 x_4}{x_3 - x_4}. \quad (2.58)$$

Solutions in the each interval of the piecewise linear bottom profile is:

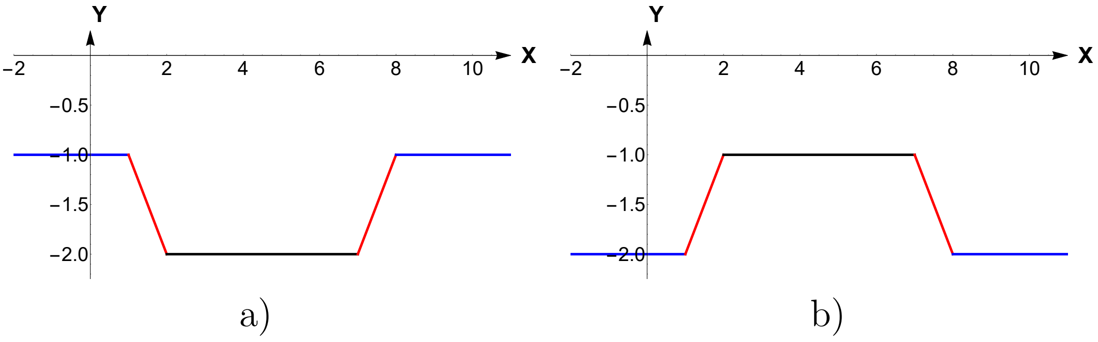

a) b)

Figure 2.11: Bottom profiles in the form of underwater trench (frame *a*) and barrier (frame *b*) with the linear slopes.

$$\Phi_L = A_1 e^{-\mathrm{i}k_1(x-x_1)} + A_2 e^{\mathrm{i}k_1(x-x_1)}, \qquad -\infty < x < x_1, \tag{2.59}$$

$$\Phi_{SL} = B_1 I_0\left(\frac{2\mathrm{i}\omega}{a_1}\sqrt{a_1x+b_1}\right) + B_2 K_0\left(\frac{2\mathrm{i}\omega}{a_1}\sqrt{a_1x+b_1}\right), \ x_1 < x < x_2, \tag{2.60}$$

$$\Phi_C = C_1 e^{-\mathrm{i}k_2x} + C_2 e^{\mathrm{i}k_2x}, \qquad x_2 < x < x_3, \tag{2.61}$$

$$\Phi_{SR} = D_1 I_0\left(\frac{2\mathrm{i}\omega}{a_2}\sqrt{a_2x+b_2}\right) + D_2 K_0\left(\frac{2\mathrm{i}\omega}{a_2}\sqrt{a_2x+b_2}\right), \ x_3 < x < x_4, \tag{2.62}$$

$$\Phi_R = E_1 e^{-\mathrm{i}k_1(x-x_4)} + E_2 e^{\mathrm{i}k_1(x-x_4)}, \qquad x_4 < x < \infty. \tag{2.63}$$

When the incident wave propagates from the left to right in the geometry shown in Fig. 2.11, then we set the following coefficients $A_{1,2}$ and $E_{1,2}$:

$$A_1 = 1, \quad A_2 = R, \quad E_1 = T, \quad E_2 = 0. \tag{2.64}$$

To match solutions (2.59)–(2.63) at the points x_1, x_2, x_3, and x_4, we use eight boundary conditions which reflect continuations of function $\Phi(\xi)$ and its first derivative:

$$\Phi_L(x_1) = \Phi_{SL}(x_1), \quad \Phi'_L(x_1) = \Phi'_{SL}(x_1), \tag{2.65}$$

$$\Phi_{SL}(x_2) = \Phi_C(x_2), \quad \Phi'_{SL}(x_2) = \Phi'_C(x_2), \tag{2.66}$$

$$\Phi_C(x_3) = \Phi_{SR}(x_3), \quad \Phi'_C(x_3) = \Phi'_{SR}(x_3), \tag{2.67}$$

$$\Phi_{SR}(x_4) = \Phi_R(x_4), \quad \Phi'_{SR}(x_4) = \Phi'_R(x_4). \tag{2.68}$$

This leads to the set of eight linear algebraic equations for eight unknown coefficients R, T, $B_{1,2}$, $C_{1,2}$, and $E_{1,2}$. The set can be readily solved, but solution looks very cumbersome, therefore we present below only a graphical illustration for the particular choices of parameters h_1, h_2, and $\hat{\omega} = 5$. Figure 2.12 shows wave filed amplitude $|\Phi(x)|$ for the trench with $h_2/h_1 = 2$ (frame a) and barrier with $h_1/h_2 = 2$ (frame b). In the both cases it is supposed that the incident wave arrives from the left. Figures 2.13 and 2.14 show the moduli of reflection and transmission coefficients respectively for the trench with $h_2/h_1 = 2$ (frames a) and barrier with $h_1/h_2 = 2$ (frames b). The oscillatory character of transformation coefficients as functions of wave frequency is the well-known phenomenon which has been noticed in many publications (see, e.g., [36, 78, 105, 107]). The reason of this is the interference of standing waves within the trench or barrier.

In this section we have considered wave scattering on a symmetric trench or barrier; similarly one can consider a scattering on non-symmetric obstacles with the linear slopes or even more complicated piecewise linear slopes.

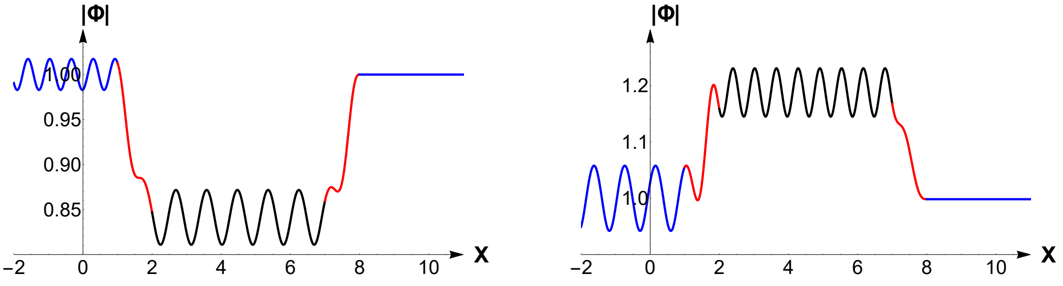

a) b)

Figure 2.12: Amplitude of surface wave field when an incident wave arrives from the left and scatters on the underwater trench $h_1 = 1$, $h_2 = 2$ (frame a) and barrier $h_1 = 2$, $h_2 = 1$ (frame b) with the linear slopes. In both cases the dimensionless frequency is $\hat{\omega} = 5$.

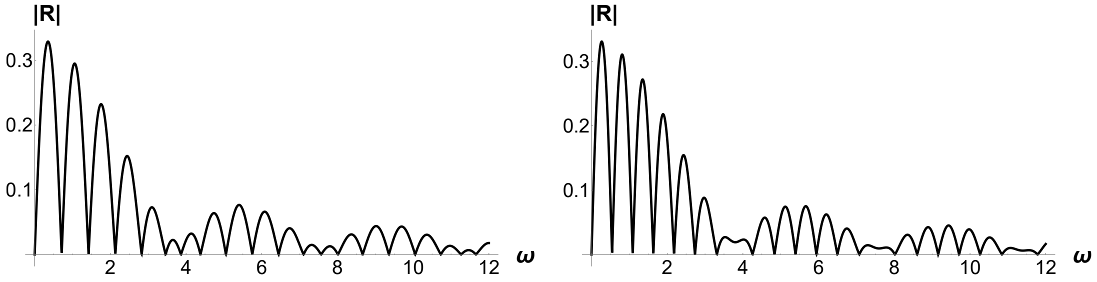

a) b)

Figure 2.13: The moduli of reflection coefficients for a surface wave of dimensionless frequency $\hat{\omega} = 5$ scattering at the underwater trench (frames a) and barrier (frames b) with the linear slopes shown in Fig. 2.11.

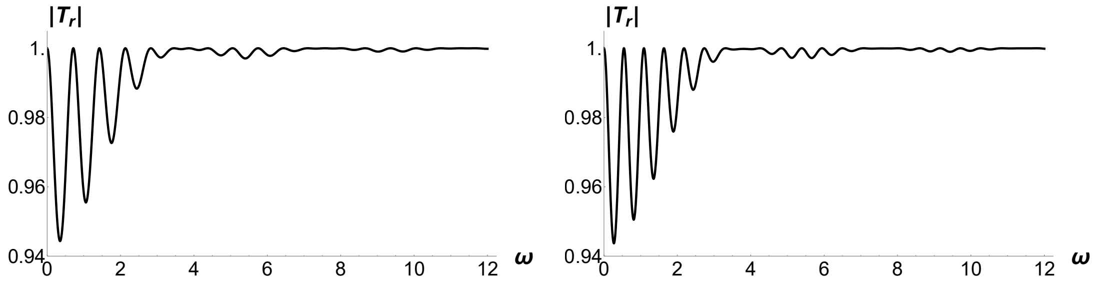

a) b)

Figure 2.14: The moduli of transmission coefficients for a surface wave of dimensionless frequency $\hat{\omega} = 5$ scattering at the underwater trench (frames a) and barrier (frames b) with the linear slopes shown in Fig. 2.11.

2.6 Wave scattering on an underwater trench and barrier with the piecewise quadratic slopes

Consider now a wave scattering on the underwater obstacles (trench or barrier) when the left and right slopes can be described by a smooth conjugation of quadratic functions. The water depth over the uneven bottom in this case can be presented as $h(\xi) = a\xi^2 + b\xi + c$ (see Fig. 2.15). The basic differential equation for the free surface perturbation over the uneven bottom is:

$$\left(a\xi^2 + b\xi + c\right)\Phi''(\xi) + (2a\xi + b)\Phi'(\xi) + \omega^2\Phi(\xi) = 0. \tag{2.69}$$

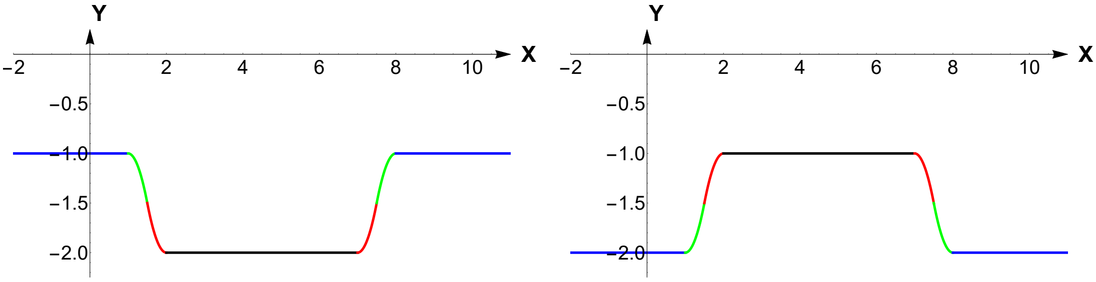

a) b)

Figure 2.15: Bottom profiles in the form of underwater trench (frame *a*) and barrier (frame *b*) with the piecewise quadratic slopes.

For the symmetric obstacles shown in Fig. 2.15 the coefficients of quadratic functions are:

$$\begin{aligned}
a_1 &= \frac{h_2 - h_1}{\left(\xi_2 - \xi_1\right)^2 \gamma}, & b_1 &= \frac{2\left(h_1 - h_2\right)\xi_1}{\left(\xi_2 - \xi_1\right)^2 \gamma}, & c_1 &= h_1 + \frac{\left(h_2 - h_1\right)\xi_1^2}{\left(\xi_2 - \xi_1\right)^2 \gamma}, \\
a_2 &= \frac{h_2 - h_1}{\left(\xi_2 - \xi_1\right)^2 (\gamma - 1)}, & b_2 &= \frac{2\left(h_1 - h_2\right)\xi_2}{\left(\xi_2 - \xi_1\right)^2 (\gamma - 1)}, & c_2 &= h_2 + \frac{\left(h_2 - h_1\right)\xi_2^2}{\left(\xi_2 - \xi_1\right)^2 (\gamma - 1)}, \\
a_3 &= \frac{h_1 - h_2}{\left(\xi_3 - \xi_4\right)^2 \gamma}, & b_3 &= \frac{2\left(h_2 - h_1\right)\xi_3}{\left(\xi_3 - \xi_4\right)^2 \gamma}, & c_3 &= h_2 + \frac{\left(h_1 - h_2\right)\xi_3^2}{\left(\xi_3 - \xi_4\right)^2 \gamma}, \\
a_4 &= \frac{h_1 - h_2}{\left(\xi_3 - \xi_4\right)^2 (\gamma - 1)}, & b_4 &= \frac{2\left(h_2 - h_1\right)\xi_4}{\left(\xi_3 - \xi_4\right)^2 (\gamma - 1)}, & c_4 &= h_1 + \frac{\left(h_1 - h_2\right)\xi_4^2}{\left(\xi_3 - \xi_4\right)^2 (\gamma - 1)}.
\end{aligned}$$

Here the parameter γ determines the positions of conjugation of quadratic functions in each slope:

$$\xi_{c1} = \xi_1 + \gamma\left(\xi_2 - \xi_1\right), \quad \xi_{c2} = \xi_3 + \gamma\left(\xi_4 - \xi_3\right). \tag{2.70}$$

Solutions to Eq. (2.69) can be presented in the dimensionless variables in terms of the Legendre polynomials $P_\nu(\xi)$ and $Q_\nu(\xi)$ (see Eqs. (2.34), (2.35)):

$$\Phi(\xi) = B_1 P_\nu\left(\frac{2a\xi + b}{\sqrt{b^2 - 4ac}}\right) + B_2 Q_\nu\left(\frac{2a\xi + b}{\sqrt{b^2 - 4ac}}\right), \tag{2.71}$$

where $\nu = \left(\sqrt{1 - 4\hat{\omega}^2/a} - 1\right)/2$. Wave perturbations in the each interval of ξ corresponding to different domains of bottom profile (see Fig. 2.15) can be presented as follows:

$$\begin{aligned}
\Phi_L(\xi) &= A_1 e^{-\mathrm{i}k_1(\xi-\xi_1)} + A_2 e^{\mathrm{i}k_1(\xi-\xi_1)}, && -\infty < \xi < \xi_1,\\
\Phi_{SL1}(\xi) &= B_1 P\left(a_1, b_1, c_1\right) + B_2 Q\left(a_1, b_1, c_1\right), && \xi_1 < \xi < \xi_{c1},\\
\Phi_{SL2}(\xi) &= C_1 P\left(a_2, b_2, c_2\right) + C_2 Q\left(a_2, b_2, c_2\right), && \xi_{c1} < \xi < \xi_2,\\
\Phi_C(\xi) &= D_1 e^{-\mathrm{i}k_2\xi} + D_2 e^{\mathrm{i}k_2\xi}, && \xi_2 < \xi < \xi_3,\\
\Phi_{SR1}(\xi) &= E_1 P\left(a_3, b_3, c_3\right) + E_2 Q\left(a_3, b_3, c_3\right), && \xi_3 < \xi < \xi_{c2},\\
\Phi_{SR2}(\xi) &= F_1 P\left(a_4, b_4, c_4\right) + F_2 Q\left(a_4, b_4, c_4\right), && \xi_{c2} < \xi < \xi_4,\\
\Phi_R(\xi) &= G_1 e^{-\mathrm{i}k_1(\xi-\xi_4)} + G_2 e^{\mathrm{i}k_1(\xi-\xi_4)}, && \xi_4 < \xi < \infty.
\end{aligned}$$

To match smoothly these functions we use the boundary conditions of continuity of function $\Phi(\xi)$ and its first derivatives at the boundaries of intervals like in Eqs. (2.14) above. As a result, we obtain a set of sixteen linear algebraic equations for the coefficients $A_{1,2}$, $B_{1,2}$, ..., $G_{1,2}$ that can be readily solved. Figure 2.16 shows wave filed amplitude $|\Phi(x)|$ for the trench with $h_2/h_1 = 2$ (frame a) and barrier with $h_1/h_2 = 2$ (frame b). In the both cases it is supposed that the incident wave arrives from the left. Figures 2.17 and 2.18 show the moduli of reflection

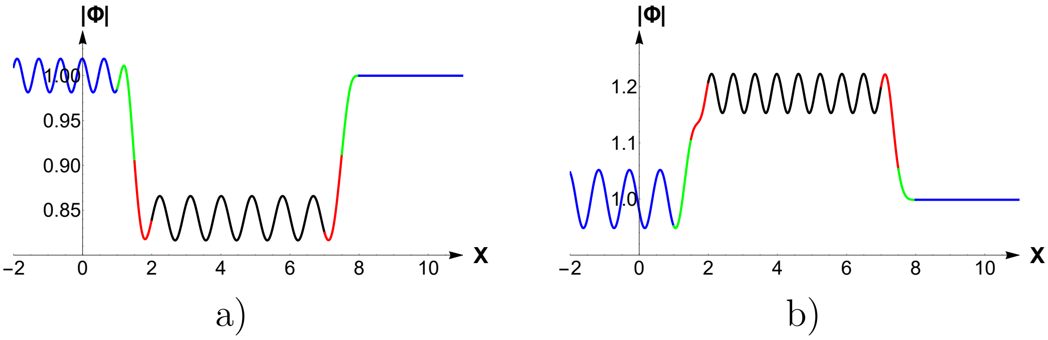

Figure 2.16: Amplitude of surface wave field when an incident wave arrives from the left and scatters on the underwater trench $h_1 = 1$, $h_2 = 2$ (frame a) and barrier $h_1 = 2$, $h_2 = 1$ (frame b) with the piecewise quadratic slopes (each pieces consist of two different parabolic slopes). In both cases the dimensionless frequency is $\hat{\omega} = 5$.

and transmission coefficients respectively for the trench with $h_2/h_1 = 2$ (frames a) and barrier with $h_1/h_2 = 2$ (frames b). It is interesting that in the case of an obstacle with the piecewise quadratic slopes the number of resonances in the low-frequency domain is greater than in the case of an obstacle of the same width, but with the linear slopes (cf. Figs. 2.13, 2.14 and Figs. 2.17, 2.18). The basic features of transmission coefficients including maxima of reflection coefficients are similar in both cases. In this section we considered again wave scattering on a symmetric trench or barrier; similarly one can consider a scattering on non-

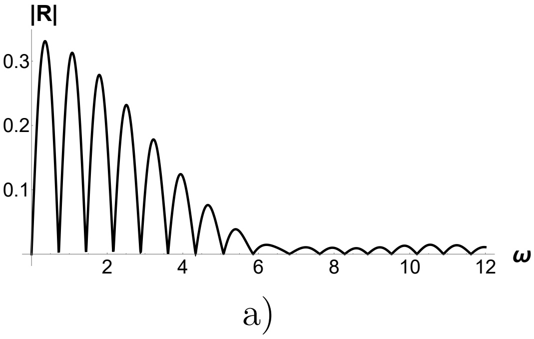

a) b)

Figure 2.17: The moduli of reflection coefficients for a surface wave of dimensionless frequency $\hat{\omega} = 5$ scattering at the underwater trench (frames a) and barrier (frames b) with the piecewise quadratic slopes shown in Fig. 2.15.

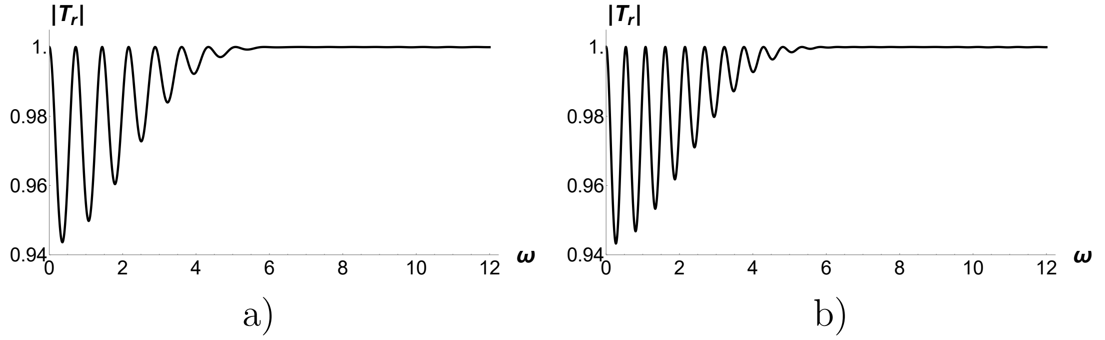

a) b)

Figure 2.18: The moduli of transmission coefficients for a surface wave of dimensionless frequency $\hat{\omega} = 5$ scattering at the underwater trench (frames a) and barrier (frames b) with the piecewise quadratic slopes shown in Fig. 2.15.

symmetric obstacles with the piecewise quadratic slopes or even more complicated combination of piecewise linear and piecewise quadratic slopes. This opens a wide possibilities to approximate real bottom profiles with the set of such functions.

2.7 Wave scattering on an underwater trench and barrier with the hyperbolic tangent profiles

In this section we consider wave transformation on the underwater obstacles with the slopes describing by tanh-functions. We assume that the characteristic width of each slope l_0 is much less than the distance L between them. The bottom profiles for the trench and barrier are very similar to those shown in Fig. 2.15; they are practically indistinguishable from their counterparts described by piecewise quadratic functions. When the obstacle slopes are far enough from each other so that $L \gg l_0$, then the wave fields at the big distances from the slopes can be considered in the form of travelling waves in a fluid of constant depth. (Note that in the considered case, the characteristic width of function $\tanh(\xi)$ is one – see the beginning of Section 2.4.) For the left slopes of obstacles centred around $\xi = 0$, a solution to the wave equation has the following asymptotics:

$$\begin{aligned}\Phi_0(\xi) &= w_1 e^{\mathrm{i}k\hat{\omega}\xi} + w_2 e^{-\mathrm{i}k\hat{\omega}\xi}, \quad && \xi \to -\infty,\\ \Phi_0(\xi) &= \tilde{w}_1 e^{\mathrm{i}\hat{\omega}\xi} + \tilde{w}_2 e^{-\mathrm{i}\hat{\omega}\xi}, && \xi \to +\infty\end{aligned}$$

where,

$$\begin{aligned}w_1 &= e^{-\pi\hat{\omega}/2}\sqrt{h_1}k^{\mathrm{i}(k-1)\hat{\omega}}\Gamma(-\mathrm{i}k\hat{\omega})\times\\ &\quad\left\{A_1\frac{e^{\pi\hat{\omega}}(1-k)\Gamma(-\mathrm{i}\hat{\omega})}{\Gamma^2\left[-\frac{1}{2}\mathrm{i}(k+1)\hat{\omega}\right]} + A_2\frac{e^{-\pi\hat{\omega}}(1+k)\Gamma(i\hat{\omega})}{\Gamma^2\left[-\frac{1}{2}\mathrm{i}(k-1)\hat{\omega}\right]}\right\},\\ w_2 &= e^{-\pi\hat{\omega}/2}\sqrt{h_1}k^{-\mathrm{i}(k+1)\hat{\omega}}\Gamma(\mathrm{i}k\hat{\omega})\times\\ &\quad\left\{-A_1\frac{e^{\pi\hat{\omega}}(1+k)\Gamma(-\mathrm{i}\hat{\omega})}{\Gamma^2\left[\frac{1}{2}\mathrm{i}(k-1)\hat{\omega}\right]} + A_2\frac{e^{-\pi\hat{\omega}}(k-1)\Gamma(\mathrm{i}\hat{\omega})}{\Gamma^2\left[\frac{1}{2}\mathrm{i}(1+k)\hat{\omega}\right]}\right\},\\ \tilde{w}_1 &= -\frac{A_1}{2k}\sqrt{h_1}\left(k^2-1\right)e^{\pi\hat{\omega}/2},\\ \tilde{w}_2 &= \frac{A_2}{2}\sqrt{h_1}k^{-1-2\mathrm{i}\hat{\omega}}\left(k^2-1\right)e^{-3\pi\hat{\omega}/2}.\end{aligned}$$

The asymptotics of a solution to the wave equation for the second slope centred around $\xi = L$ is:

$$\begin{aligned}\Phi_0(\xi) &= \hat{w}_1 e^{\mathrm{i}\hat{\omega}\xi} + \hat{w}_2 e^{-\mathrm{i}\hat{\omega}\xi}, \quad && \xi \to -\infty,\\ \Phi_0(\xi) &= \breve{w}_1 e^{\mathrm{i}k\hat{\omega}\xi} + \breve{w}_2 e^{-\mathrm{i}k\hat{\omega}\xi}, && \xi \to +\infty\end{aligned}$$

where

$$\begin{aligned}\breve{w}_1 &= e^{-\mathrm{i}L\hat{\omega}-k\pi\hat{\omega}/2}\sqrt{h_1}k^{\mathrm{i}(k-1)\hat{\omega}}\Gamma(-\mathrm{i}\hat{\omega})\times\\ &\quad\left\{B_1\frac{e^{k\pi\hat{\omega}}(k-1)\Gamma(-\mathrm{i}k\hat{\omega})}{\Gamma^2\left[-\frac{1}{2}\mathrm{i}(k+1)\hat{\omega}\right]} + B_2\frac{e^{-k\pi\hat{\omega}}(k+1)\Gamma(\mathrm{i}k\hat{\omega})}{\Gamma^2\left[\frac{1}{2}\mathrm{i}(k-1)\hat{\omega}\right]}\right\},\\ \breve{w}_2 &= \frac{1}{2}e^{\mathrm{i}L\hat{\omega}-k\pi\hat{\omega}/2}\sqrt{h_1}k^{\mathrm{i}(k+1)\hat{\omega}}(k-1)\times\\ &\quad\left\{B_1\frac{e^{k\pi\hat{\omega}}(k+1)\Gamma(1+\mathrm{i}\hat{\omega})\Gamma(-\mathrm{i}k\hat{\omega})}{\Gamma\left[-\frac{1}{2}\mathrm{i}(k-1)\hat{\omega}\right]\Gamma\left[1-\frac{1}{2}\mathrm{i}(k-1)\hat{\omega}\right]} - B_2\frac{2e^{-k\pi\hat{\omega}}\Gamma(i\hat{\omega})\Gamma(\mathrm{i}k\hat{\omega})}{\Gamma^2\left[\frac{1}{2}\mathrm{i}(k+1)\hat{\omega}\right]}\right\},\\ \hat{w}_1 &= \frac{1}{2}B_1 e^{k(-\mathrm{i}L+\pi/2)\hat{\omega}}\sqrt{h_1}\left(k^2-1\right),\\ \hat{w}_2 &= -\frac{1}{2}B_2 e^{\mathrm{i}kL\hat{\omega}-3k\pi\hat{\omega}/2}\sqrt{h_1}k^{2\mathrm{i}k\hat{\omega}}\left(k^2-1\right).\end{aligned}$$

For the incident wave arriving from the left we set the following coefficients:

$$w_2 = 1, \quad w_1 = R, \quad \tilde{w}_1 = \breve{w}_1, \quad \tilde{w}_2 = \breve{w}_2, \quad \hat{w}_1 = 0, \quad \hat{w}_2 = T. \tag{2.72}$$

Then we can solve the set of equations for R, T, as well as $\tilde{w}_1$, $\tilde{w}_1$ and obtain:

$$\begin{aligned} R = \frac{4\pi^2}{\Delta_1} k^{2\mathrm{i}k\hat{\omega}} \Gamma(-\mathrm{i}k\hat{\omega}) \times \Bigg\{ & e^{2\mathrm{i}L\hat{\omega}} (k-1)^2 k^{\mathrm{i}(k+3)\hat{\omega}} \frac{\Gamma^2(\mathrm{i}\hat{\omega}) \Gamma^4\left[\mathrm{i}(k-1)\hat{\omega}/2\right]}{\mathrm{sech}^2\left[(k+1)\pi\hat{\omega}/2\right]} \\ & - k^{\mathrm{i}(k-1)\hat{\omega}} (k+1)^2 \frac{\Gamma^2(-\mathrm{i}\hat{\omega}) \Gamma^4\left[\mathrm{i}(k+1)\hat{\omega}/2\right]}{\mathrm{sech}^2\left[(k-1)\pi\hat{\omega}/2\right]} \Bigg\}, \end{aligned} \tag{2.73}$$

$$T = \frac{\left(k^2-1\right)^2}{\Delta_2} e^{\mathrm{i}(k+1)L\hat{\omega}} k^{2\mathrm{i}(k+1)\hat{\omega}-1} \Gamma^4\left[\frac{\mathrm{i}}{2}(k-1)\hat{\omega}\right] \Gamma^4\left[\frac{\mathrm{i}}{2}(k+1)\hat{\omega}\right], \tag{2.74}$$

where

$$\begin{aligned} \Delta_1 = {} & k^{\mathrm{i}\hat{\omega}} \left(k^2-1\right) e^{\mathrm{i}L\hat{\omega}} \hat{\omega}^2 \Gamma(\mathrm{i}k\hat{\omega}) \Gamma^2\left[-\frac{\mathrm{i}}{2}(k-1)\hat{\omega}\right] \Gamma^2\left[-\frac{\mathrm{i}}{2}(k+1)\hat{\omega}\right] \times \\ & \Bigg\{ k^{\mathrm{i}(k+2)\hat{\omega}} (k-1)^2 e^{\mathrm{i}L\hat{\omega}} \Gamma^2(\mathrm{i}\hat{\omega}) \Gamma^4\left[\frac{\mathrm{i}}{2}(k-1)\hat{\omega}\right] \\ & - k^{\mathrm{i}(k-2)\hat{\omega}} (k+1)^2 e^{-\mathrm{i}L\hat{\omega}} \Gamma^2(-\mathrm{i}\hat{\omega}) \Gamma^4\left[\frac{\mathrm{i}}{2}(k+1)\hat{\omega}\right] \Bigg\} \\ \Delta_2 = {} & 4k^{2\mathrm{i}\hat{\omega}} e^{\mathrm{i}L\hat{\omega}} \Gamma^2(\mathrm{i}k\hat{\omega}) \Bigg\{ k^{2\mathrm{i}\hat{\omega}} e^{\mathrm{i}L\hat{\omega}} (k-1)^2 \Gamma^2(\mathrm{i}\hat{\omega}) \Gamma^4\left[\frac{\mathrm{i}}{2}(k-1)\hat{\omega}\right] \\ & - k^{-2\mathrm{i}\hat{\omega}} e^{-\mathrm{i}L\hat{\omega}} (k+1)^2 \Gamma^2(-\mathrm{i}\hat{\omega}) \Gamma^4\left[\frac{\mathrm{i}}{2}(k+1)\hat{\omega}\right] \Bigg\}. \end{aligned} \tag{2.75}$$

In Figs. 2.19 and 2.20 we show by lines 1 the moduli of reflection and transmission coefficients respectively for the trench with $h_2/h_1 = 2$ (frames a) and barrier with $h_1/h_2 = 2$ (frames b). For the comparison we show also by lines 2 similar coefficients derived in the previous section 2.7 for the trench an barrier with the piecewise quadratic slopes. As one can see from these figures, the qualitative character of dependencies of transformation coefficients on frequency are similar. Moreover, even the maximum and minimum vales of transformation coefficients are the same. However, there are some differences. In particular, the number of significant maxima and minima in the low-frequency domain is greater in the case of obstacles with the tanh-slopes. And in this case the maxima of reflection coefficients decay slower with the frequency.

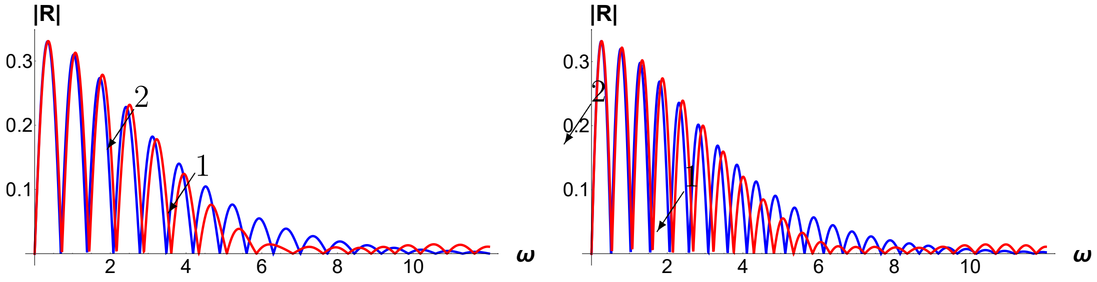

a) b)

Figure 2.19: The moduli of reflection coefficients for a surface wave of dimensionless frequency $\hat{\omega} = 5$ scattering at the underwater trench (frames a) and barrier (frames b). Lines 1 pertain to the obstacles with the tanh-slopes, and lines 2 – to the obstacles with the piecewise quadratic slopes shown in Fig. 2.15.

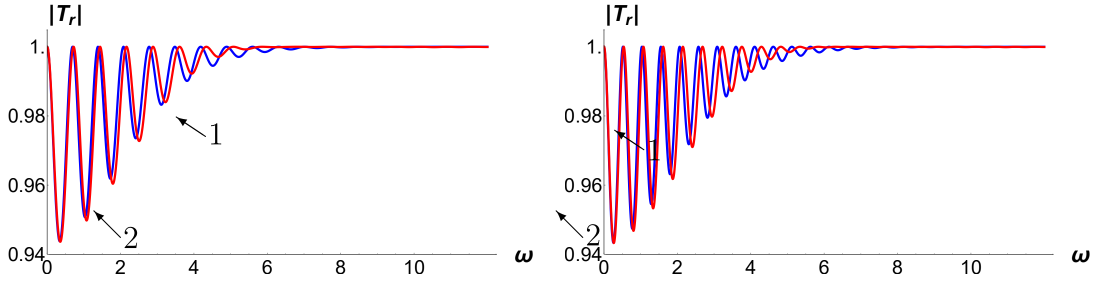

a) b)

Figure 2.20: The moduli of transmission coefficients for a surface wave of dimensionless frequency $\hat{\omega} = 5$ scattering at the underwater trench (frames a) and barrier (frames b). Lines 1 pertain to the obstacles with the tanh-slopes, and lines 2 – to the obstacles with the piecewise quadratic slopes shown in Fig. 2.15.

2.8 Conclusion

Thus, in this chapter we have studied surface wave transformation on bottom unevenness in a shallow basin. We have obtained exact analytical solutions for three reference cases of (i) linearly increasing or decreasing bottom on a finite spatial interval, (ii) piecewise quadratic transient bottom profile between two constant values, and (iii) a transient bottom profile described by the tanh-function. We have studied also wave scattering on underwater barriers and trenches whose slopes can be described by the similar functions (linear, piecewise quadratic, and tanh-functions). In all cases we obtained qualitatively similar results which are in agreement with the early obtained by different authors for some particular cases basically by approximate methods. In the limiting case when the wave frequency goes to zero we obtained the same transformation coefficients which are predicted by Lamb's theory (1932) [88] for step-wise bottom.

In the meantime, there are some quantitative differences in the transformation coefficients for the different bottom profiles. In particular, the smoother the bottom profile is, the smoother the dependencies of transformation coefficients on frequency – cf. Fig. 2.3 for the piecewise linear profile with Fig. 2.7 for the piecewise quadratic (line 2) and tanh (line 1) profiles. There are several well-pronounced oscillations in the dependence of $|R(\hat{\omega})|$ in Fig. 2.3. In particular, one can see that the reflection coefficient at some frequencies drops up to nearly zero. This provides almost reflectionless propagation [34, 35] of an incident wave at the corresponding frequencies.

The situation is opposite for the wave scattering on underwater barriers or tranches. In particular, one can see less oscillations in the transformation coefficients shown in Figs. 2.13 and 2.14 for the barriers and tranches with the linear slopes in comparison with the barriers and tranches with the piecewise quadratic or tanh-slopes (cf. with Figs. 2.19 and 2.20).

More complicated real bottom profiles can be approximated with the higher accuracy by the combination of considered here linear, quadratic, and tanh-profiles similar to what was used in [129], where the bottom profile was approximated by a set of step-wise functions. The results obtained can be used, in particular, for the protection of beaches against storm surges, swells, and tsunami waves.

Chapter 3

SCATTERING OF LONG WATER WAVES IN A CANAL WITH RAPIDLY VARYING CROSS-SECTION IN THE PRESENCE OF A CURRENT

In this Chapter we study analytically a long wave scattering in a canal with a rapidly varying cross-section. It is assumed that waves propagate on a stationary current with a given flow rate. Due to the fixed flow rate, the current speed is different in the different sections of the canal, upstream and downstream. The scattering coefficients (the transmission and reflection coefficients) are calculated for all possible orientations of incident wave with respect to the background current (downstream and upstream propagation) and for all possible regimes of current (subcritical, transcritical, and supercritical). It is shown that in some cases negative energy waves can appear in the process of waves scattering. The conditions are found when the over-reflection and over-transmission phenomena occur. In particular, it is shown that a spontaneous wave generation can arise in a transcritical accelerating flow, when the background current enhances due to the canal narrowing. This resembles a spontaneous wave generation on the horizon of an evaporating black hole due to the Hawking effect. The results obtained in this Chapter have been published in Physical Review Fluids [24].

3.1 Introduction

The problem of water wave transformation in a canal of a variable cross-section is one of the classic problems of theoretical and applied hydrodynamics. It has been studied in many books, reports, and journal papers starting from the first edition (1879) of the famous monograph by H. Lamb, *Hydrodynamics* (see the last lifetime publication [88]). In particular, the coefficients of transformation of long linear waves in a canal of a rectangular cross-section with an abrupt change of geometrical parameters (width and depth) were presented. The transmission and reflection coefficients were found as functions of depth ratio $X = h_2/h_1$ and width ratio $Y = b_2/b_1$, where h_1 and b_1 are the canal depth and width at that side from which the incident wave arrives, and h_2 and b_2 are the corresponding canal parameters at the opposite side where the transmitted wave goes to (see Fig. 3.1). The parameters X and Y can be both less than 1, and greater than 1. As explained in Ref. [88], the canal cross-section can vary smoothly, but if the wavelengths of all scattered waves are much greater than the characteristic scale of variation of the canal cross-section, then the canal model with the abrupt change of parameters is valid.

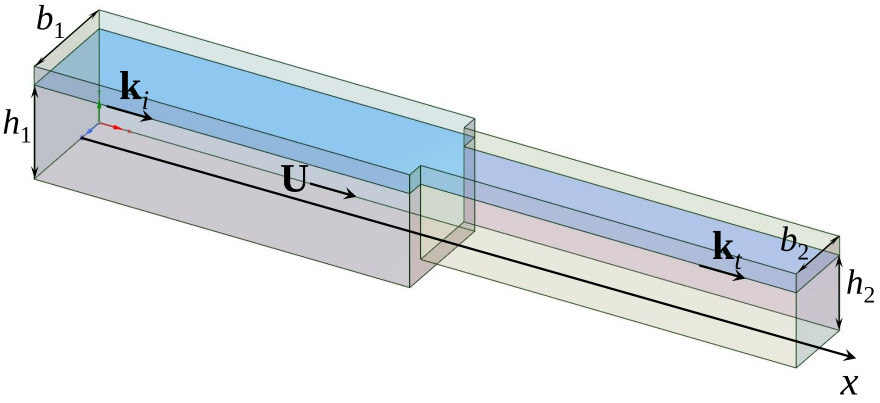

Figure 3.1: Sketch of a canal consisting of two sections of different rectangular cross-sections. The wavenumber of incident wave is $\mathbf{k}_i$, and the wavenumber of transmitted wave is $\mathbf{k}_t$ (a reflected wave is not shown). Water flow U is co-directed with the x-axis.

The Lamb model has been further generalised for waves of arbitrary wavelengths and applied to many practical problems. One of the typical applications of such a model is in the problem of oceanic wave transformation in the shelf zone; the numerous references can be found in the books and reviews [36, 86, 105]. In such applications the canal width is assumed to be either constant or infinitely long and only the water depth abruptly changes.

A similar problem was studied also in application to internal waves, but analytical results were obtained only for the transformation coefficients of long waves in a two-layer fluid [65], whereas for waves of arbitrary wavelength only the numerical results were obtained and the approximative formulae were suggested [22].

All aforementioned problems of wave transformation were studied for cases when there is no background current. However, there are many situations when there is a flow over an underwater step or in the canals or rivers with variable cross-sections. The presence of a current can dramatically affect the transformation coefficients due to the specific wave-current interaction (see, e.g., Ref. [12] and references therein). The amplitudes and energies of reflected and transmitted waves can significantly exceed the amplitude and energy of an incident wave. Such over-reflection and over-transmission phenomena are known in hydrodynamics and plasma physics (see, e.g., Ref. [77]); the wave energy in such cases can be extracted from the mean flow. Apparently, due to complexity of wave scattering problem in the presence of a background flow, no results were obtained thus far even for a relatively weak flow and small flow variation in a canal. There are, however, a number of works devoted to wave-current interactions and, in particular, wave scattering in spatially varying flows mainly on deep water (see, for instance, Refs. [12, 140, 146, 151] and references therein). In Ref. [12] the authors considered the surface wave scattering in two-dimensional geometry in (x, y)-plane for the various models of underwater obstacles and currents including vortices. In particular, they studied numerically wave passage over an underwater step in the shoaling zone in the presence of a current. However, the transformation coefficients were not obtained even in the plane geometry.

Here we study the problem of long wave scattering analytically for all possible configurations of the background flow and incident wave (downstream and upstream propagation) in the narrowing or widening canal (accelerating or decelerating flow) for the subcritical, transcritical, and supercritical regimes when the current speed is less or greater than the typical wave speed $c_0 = \sqrt{gh}$ in calm water in the corresponding canal section (g is the acceleration due to gravity, and h is the canal depth). Because we consider a limiting model case of very long waves when the variation of canal geometry is abrupt, the wave blocking phenomenon here has a specific character of reflection. Such a phenomenon has been studied in shallow-water limit in Ref. [140], but transformation coefficients were not obtained.

Notice also that in the last decade the problem of wave-current interaction in water with a spatially varying flow has attracted a great deal of attention from researchers due to application to the modelling of Hawking's radiation emitted by evaporating black holes [152] (see also Refs. [47, 73, 153]). Recent experiments in a water tank [45] have confirmed the main features of the Hawking radiation; however many interesting and important issues are still under investigation. In particular, it is topical to calculate the transformation coefficients of all possible modes generated in the process of incident mode conversion in the spatially varying flow. Several papers have been devoted to this problem both for the subcritical [29, 131] and transcritical [28, 130] flows. However, in all these papers the influence of wave dispersion was important, whereas there is no dispersion in the problem of black hole radiation. Our results for the dispersionless wave transformation can shed light on the problem of mode conversion in the relatively simple model considered in this Chapter.

3.2 Problem statement and dispersion relation

Consider a long surface gravity wave propagating on the background current in a canal consisting of two portions of different cross-section each as shown in Fig. 3.1. A similar problem with a minor modification can be considered for internal waves in two-layer fluid, but we focus here on the simplest model to gain an insight in the complex problem of wave-current interaction. We assume that both the canal width and depth abruptly change at the same place, at the juncture of two canal portions. The current is assumed to be uniform across the canal cross-section and flows from left to right accelerating, if the canal cross-section decreases, or decelerating, if it increases. In the presence of a current the water surface does not remain plane even if the canal depth is unchanged, but the width changes. According to the Bernoulli law, when the current accelerates due to the canal narrowing, the pressure in the water decreases and, as a result, the level of the free surface reduces. Therefore, asymptotically, when $x \to \infty$, the portion of canal cross-section occupied by water is $S_2 = b_2 h_2$. A similar variation in the water surface occurs in any case when the current accelerates due to decrease of the canal cross-section in general; this is shown schematically in Fig. 3.2 (this figure is presented not in scale, just for the sake of a vivid explanation of the wave scattering, whereas in fact, we consider periodic waves with the wavelengths much greater than the fluid depth).

The relationship between the water depth h_2, which asymptotically onsets at the infinity, and variations of canal width and depth at the juncture point is nontrivial. In particular, even in the case when the canal width is unchanged, and the canal cross-section changes only due to the presence of a bottom step of a height d, the water depth h_2 at the infinity is not equal to the difference $h_1 - d$ (see, e.g., Ref. [49]). As shown in the cited paper, variation of a free surface

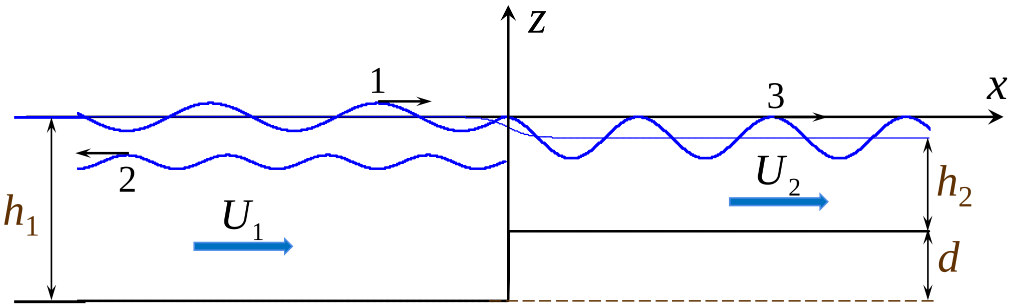

Figure 3.2: The side view of a flow in a canal with a variable cross-section. Wave 1 schematically represents an incident wave, wave 2 – a reflected wave, and wave 3 – a transmitted wave. The water surface slightly lowers when the background flow increases as shown schematically by thin line.

due to increase of water flow is smooth even in the case of abruptly changed depth, but in the long-wave approximation it can be considered as abrupt. In any case, we will parameterize the formulas for the transformation coefficients in terms of the real depth ratio at plus and minus infinity $X = h_2/h_1$ and canal width aspect ratio $Y = b_2/b_1$. The long-wave approximation allows us to neglect the dispersion assuming that the wavelength λ of any wave participating in the scattering is much greater than the canal depth h in the corresponding section.

In the linear approximation the main set of hydrodynamic equations for shallow-water waves in a perfect incompressible fluid is (see, e.g., Ref. [88]):

$$\frac{\partial u}{\partial t} + U\frac{\partial u}{\partial x} = -\,g\frac{\partial \eta}{\partial x}, \tag{3.1}$$

$$\frac{\partial \eta}{\partial t} + U\frac{\partial \eta}{\partial x} = -\,h\frac{\partial u}{\partial x}. \tag{3.2}$$

Here $u(x,t)$ is a wave induced perturbation of a horizontal velocity, U is the velocity of background flow which is equal to U_1 at minus infinity and U_2 at plus infinity, $\eta(x,t)$ is the perturbation of a free surface due to the wave motion, and h is the canal depth which is equal to h_1 at minus infinity and h_2 at plus infinity – see Fig. 3.2.

For the incident harmonic wave of the form $\sim \mathrm{e}^{\mathrm{i}(\omega t - kx)}$ co-propagating with the background flow we obtain from Eq. (3.2)

$$(\omega - U_1 k_i)\,\eta_i = h_1 k_i u_i, \tag{3.3}$$

where index i pertains to incident wave (in what follows indices t and r will be used for the transmitted and reflected waves respectively).

Combining this with Eq. (3.1), we derive the dispersion relation for the incident wave

$$\omega = (U_1 + c_{01})\, k_i, \tag{3.4}$$

where $c_{01} = \sqrt{gh_1}$.

Similarly for the transmitted wave we have $(\omega - U_2 k_t)\,\eta_t = h_2 k_t u_t$ and the dispersion relation $\omega = (U_2 + c_{02})\, k_t$, where $c_{02} = \sqrt{gh_2}$. Notice that the wave frequency remains unchanged in the process of wave transformation in a stationary, but spatially varying medium. Then, equating the frequencies for the incident and transmitted waves, we obtain $k_t/k_i = (U_1 + c_{01}) / (U_2 + c_{02})$.

From the mass conservation for the background flow we have $U_1 h_1 b_1 = U_2 h_2 b_2$ or $U_1/U_2 = XY$. Using this relationship, we obtain for the wavenumber of the transmitted wave

$$\frac{k_t}{k_i} = XY \frac{1 + \mathrm{Fr}}{X^{3/2} Y + \mathrm{Fr}}, \tag{3.5}$$

where $\mathrm{Fr} = U_1/c_{01}$ is the Froude number. The relationship between the wavenumbers of incident and transmitted waves as functions of the depth drop X is shown in Fig. 3.3 for several values of Fr and $Y = 1$. As one can see, the ratio of wavenumbers k_t/k_i non-monotonically depends on X; it has a maximum at $X_m = (2\mathrm{Fr}/Y)^{2/3}$. The maximum value $(k_t/k_i)_{max} = \sqrt[3]{4Y}\,(1 + \mathrm{Fr}) / \left(3\sqrt[3]{\mathrm{Fr}}\right)$ is also a non-monotonic function of the Froude number; it has a minimum at

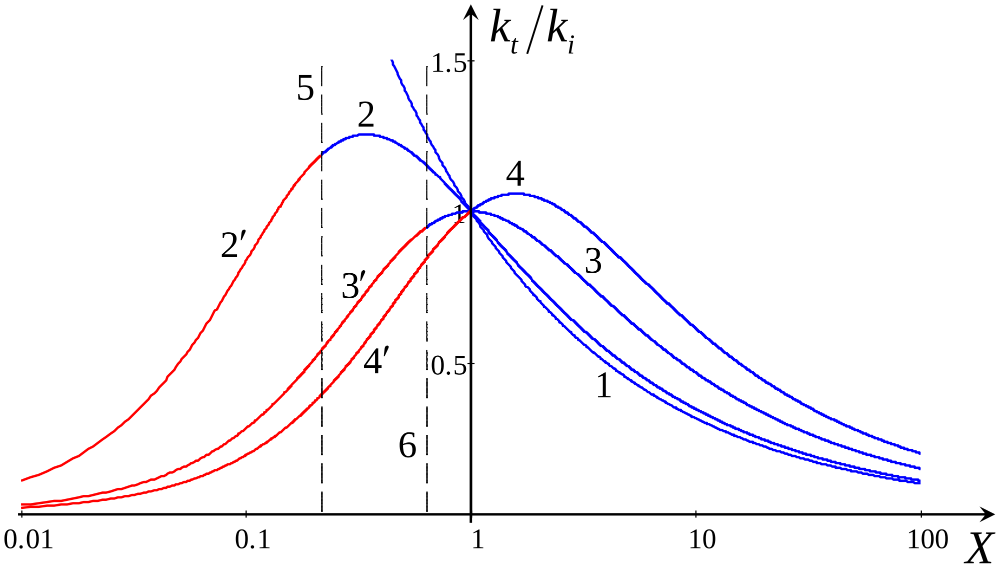

Figure 3.3: The dependence of wavenumber ratio on the depth drop $X = h_2/h_1$ for different Froude numbers and $Y = 1$. Line 1 pertains to the reference case when $\mathrm{Fr} = 0$, lines 2 and 2′ – to $\mathrm{Fr} = 0.1$, lines 3 and 3′ – to $\mathrm{Fr} = 0.5$, line 4 and 4′ – to $\mathrm{Fr} = 1$. Dashed vertical lines 5 and 6 show the boundaries between the subcritical and supercritical regimes in the downstream domain for $\mathrm{Fr} = 0.1$, line 5, and $\mathrm{Fr} = 0.5$, line 6.

$\mathrm{Fr} = 0.5$ where $(k_t/k_i)_{max} = \sqrt[3]{Y}$. In the limiting case, when there is no current ($\mathrm{Fr} = 0$), $k_t/k_i = X^{-1/2}$ independently of Y (see line 1 in Fig. 3.3). The current with the Froude number $\mathrm{Fr} < 1$ remains subcritical in the downstream domain, if $X > (\mathrm{Fr}/Y)^{2/3}$. Otherwise it becomes supercritical. Dashed lines 5 and 6 in Fig. 3.3 show the boundaries between the subcritical and supercritical regimes in the downstream domains for two values of the Froude number, $\mathrm{Fr} = 0.1$ and $\mathrm{Fr} = 0.5$ respectively.

For the upstream propagating reflected wave the harmonic dependencies of free surface and velocity perturbations are $\{\eta, u\} \sim \mathrm{e}^{\mathrm{i}(\omega t + k_r x)}$. Then from Eq. (3.2) we obtain $(\omega + U_1 k_r)\,\eta_r = -h_1 k_r u_r$, and combining this with Eq. (3.1), we derive the dispersion relation for the reflected wave with $k_r < 0$

$$\omega = (c_{01} - U_1)\,|k_r|. \tag{3.6}$$

Equating the frequencies of the incident and reflected waves, we obtain from the dispersion relations the relationship between the wavenumbers:

$$\frac{|k_r|}{k_i} = \frac{1 + \mathrm{Fr}}{1 - \mathrm{Fr}}. \tag{3.7}$$

Notice that the ratio of wavenumbers $|k_r|/k_i$ depends only on Fr, but does not depend on X and Y. The dispersion relations for long surface waves on a constant current are shown in Fig. 3.4. Lines 1 and 2 show the dispersion dependencies for the downstream and upstream propagating waves, respectively, in the upstream domain, if the background current is subcritical, i.e., when $\mathrm{Fr} < 1$. Lines 3 and 4

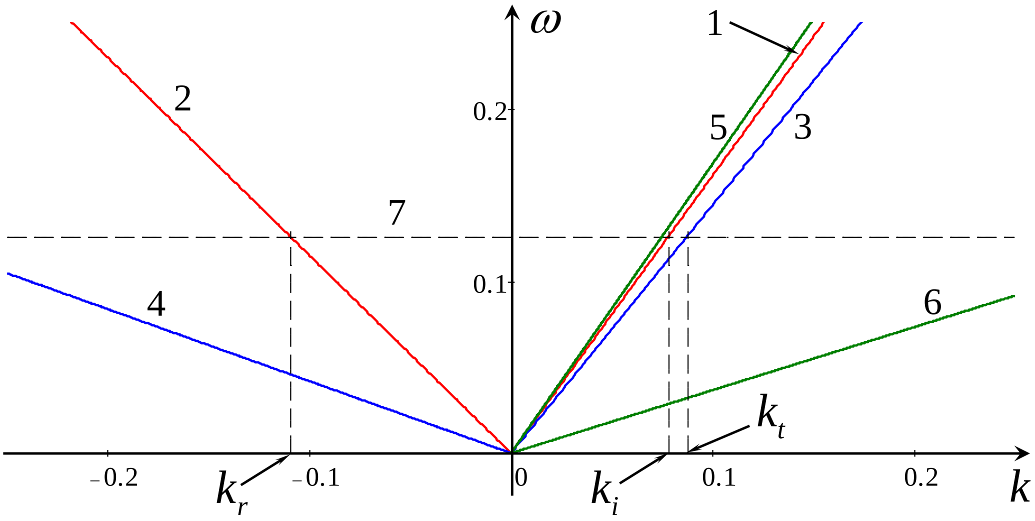

Figure 3.4: Qualitative sketch of dispersion lines for long surface waves on a uniform background flow in a canal. For details see the text.

show the dispersion dependencies for the downstream and upstream propagating waves, respectively, which can potentially exist in the downstream domain, if the background current remains subcritical in this domain too, i.e. when $U_2/c_{02} \equiv \mathrm{Fr}/\left(X^{3/2}Y\right) < 1$. If there is a source generating an incident wave of frequency ω and wavenumber k_i at minus infinity, then after scattering at the canal juncture the reflected wave appears in the upstream domain with the same frequency and wavenumber k_r. Dashed horizontal line 7 in Fig. 3.4 shows the given frequency ω. In the downstream domain with a subcritical flow the incident wave generates only one transmitted wave with the wavenumber k_t. If the flow in one of the domains becomes faster and faster so that $\mathrm{Fr} \to 1_-$, then the dispersion line corresponding to the upstream propagating waves tilts to the negative portion of horizontal axis k in Fig. 3.4 (cf. lines 2 and 4), and its intersection with the horizontal dashed line 7 shifts to the minus infinity. In the case of a supercritical flow, $\mathrm{Fr} > 1$, the dispersion line corresponding to the upstream propagating waves is line 6 in Fig. 3.4. Its intersection with the horizontal dashed line 7 originates at the plus infinity (as the continuation of the intersection point of line 4 with line 7 disappeared at the minus infinity) and moves to the left when the flow velocity increases. The speeds of such waves in a calm water are smaller than the speed of a current, therefore despite the waves propagate counter current, the current traps them and pulls downstream. In the immovable laboratory coordinate frame they look like waves propagating to the right jointly with the current. As shown in Refs. [46, 98], such waves possess a negative energy. This means that the total energy of a medium when waves are excited is less then the energy of a medium without waves. Obviously, this can occur only in the non-equilibrium media, for example, in hydrodynamical flows possessing kinetic energy. In the equilibrium media, wave excitation makes the total energy greater than the energy of the non-perturbed media (more detailed discussion of the negative energy concept one can find in the citations presented above and references therein). In Appendix 6.2 we present the direct calculation of wave energy for the dispersionless case considered here and show when it become negative. With the help of dispersion relations, the links between the perturbations of fluid velocity and free surface in the incident, reflected and transmitted waves can be presented as

$$u_i = c_{01}\eta_i/h_1; \quad u_r = -c_{01}\eta_r/h_1; \quad u_t = c_{02}\eta_t/h_2. \tag{3.8}$$

Using these relationships, we calculate in the next sections the transformation coefficients for all possible flow regimes and wave-current configurations.

3.3 Subcritical flow in both the upstream and downstream domains

3.3.1 Downstream propagating incident wave

Consider first the case when the current is co-directed with the x-axis (see Fig. 3.2) and the incident wave travels in the same direction. Then, the transmitted wave is also co-directed with the current, but the reflected wave travels against the current. We assume that the current is subcritical in both left domain and right domains, i.e. its speed $U_1 < c_{01}$ and $U_2 < c_{02}$. This can be presented alternatively in terms of the Froude number and canal specific ratios, viz $\mathrm{Fr} < 1$ and $\mathrm{Fr} < X^{3/2}Y$.

To derive the transformation coefficients, we use the boundary conditions at the juncture point $x = 0$. These conditions physically imply the continuity of pressure and continuity of horizontal mass flux induced by a surface wave. The total pressure in the moving fluid consists of hydrostatic pressure $\rho g(h + \eta)$ and kinetic pressure $\rho(U + u)^2/2$. The condition of pressure continuity in the linear approximation reduces to

$$g\eta_1 + U_1 u_1 = g\eta_2 + U_2 u_2, \tag{3.9}$$

where indices 1 and 2 pertain to the left and right domains respectively far enough from the juncture point $x = 0$. In the left domain we have $\{\eta_1, u_1\} = \{\eta_i + \eta_r, u_i + u_r\}$, whereas in the right domain $\{\eta_2, u_2\} = \{\eta_t, u_t\}$.

Using the relationships between $u_{i,r,t}$ and $\eta_{i,r,t}$ as per Eq. (3.8) and assuming that the incident wave has a unit amplitude in terms of η, we obtain from Eq. (3.9)

$$g\left(1 + R_\eta\right) + U_1 \frac{c_{01}}{h_1}\left(1 - R_\eta\right) = gT_\eta + U_2 \frac{c_{02}}{h_2} T_\eta, \tag{3.10}$$

where R_η and T_η are amplitudes of reflected and transmitted waves respectively. In the dimensionless form this equations reads

$$1 + \mathrm{Fr} + \left(1 - \mathrm{Fr}\right) R_\eta = T_\eta \left(1 + \frac{\mathrm{Fr}}{X^{3/2}Y}\right). \tag{3.11}$$

The condition of mass flux continuity leads to the equation

$$\rho b_1 \left(h_1 + \eta_1\right)\left(U_1 + u_1\right) = \rho b_2 \left(h_2 + \eta_2\right)\left(U_2 + u_2\right). \tag{3.12}$$

In the linear approximation and dimensionless form this gives:

$$1 + \mathrm{Fr} - (1 - \mathrm{Fr})\, R_\eta = T_\eta \sqrt{X} Y \left(1 + \frac{\mathrm{Fr}}{X^{3/2} Y}\right). \tag{3.13}$$

After that we derive the transformation coefficients R_η and T_η from Eqs. (3.11) and (3.13):

$$R_\eta = \frac{1 + \mathrm{Fr}}{1 - \mathrm{Fr}} \frac{1 - \sqrt{X} Y}{1 + \sqrt{X} Y}, \quad T_\eta = \frac{1 + \mathrm{Fr}}{X^{3/2} Y + \mathrm{Fr}} \frac{2 X^{3/2} Y}{1 + \sqrt{X} Y}. \tag{3.14}$$

These formulas naturally reduce to the well-known Lamb formulas [88] when Fr → 0. Graphics of T_η and R_η as functions of depth drop X are shown in Fig. 3.5 for the particular value of Froude number $\mathrm{Fr} = 0.5$ and $Y = 1$.

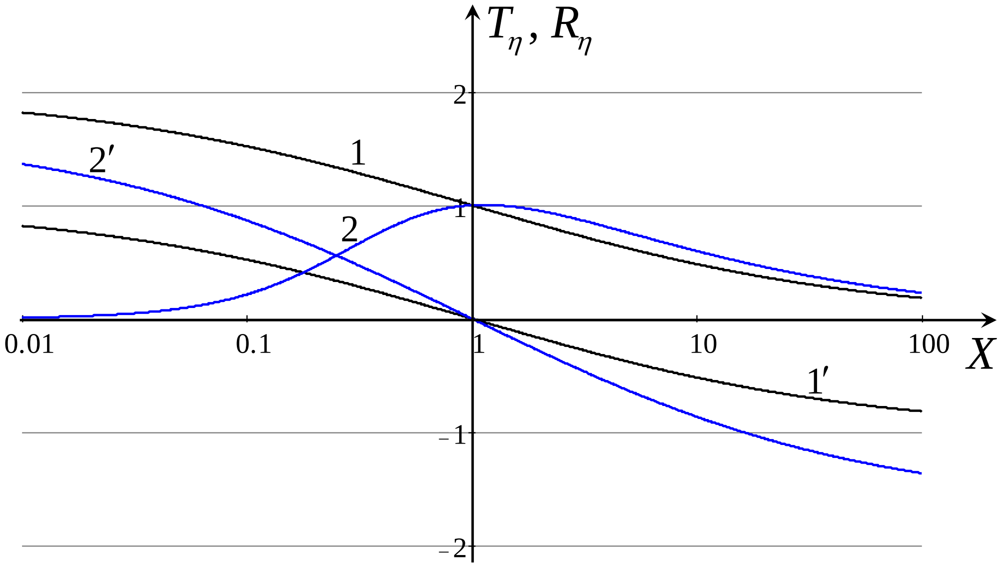

Figure 3.5: The transformation coefficients of surface waves on a uniform subcritical current in a canal with flat walls, $Y = 1$, as functions of the depth drop X. Line 1 for T_η and line 1′ for R_η pertain to the reference case given by the Lamb formulas with $\mathrm{Fr} = 0$; lines 2 (for T_η) and 2′ (for R_η) pertain to the flow with $\mathrm{Fr} = 0.5$.

As follows from the formula for R_η, the reflection coefficient increases uniformly in absolute value, when the Froude number increases from 0 to 1, provided that $\sqrt{X} Y \neq 1$. It is important to notice that the reflectionless propagation can occur in the case, when $\sqrt{X} Y = 1$, whereas neither X, nor Y are equal to one. The transmission coefficient in this case $T_\eta = (1 + \mathrm{Fr}) / (1 + Y^2 \mathrm{Fr}) \neq 1$ in general, except the case when $\mathrm{Fr} = 0$. The reflection coefficient is negative when $\sqrt{X} Y > 1$, which means that the reflected wave is in anti-phase with respect to the incident wave.

The dependence of T_η on the Froude number is more complicated and non-monotonic in X. However, in general $T_\eta \to 0$ in two limiting cases, when $X \to 0$, then $T_\eta \approx 2X^{3/2}Y\,(1 + 1/\mathrm{Fr})$, and when $X \to \infty$, then $T_\eta \approx 2\,(1 + \mathrm{Fr})\,/\left(\sqrt{X}Y\right)$ (see Fig. 3.5).

It is appropriate to mention here the nature of singularity of the reflection coefficient R_η and wavenumber k_r of the reflected wave as per Eq. (3.7) when $\mathrm{Fr} \to 1$. In such case, the dispersion line 2 in Fig. 3.4 approaches negative half-axis of k, and the point of intersection of line 2 with the dashed horizontal line 7 shifts to the minus infinity, i.e. $k_r \to -\infty$, and the wavelength of reflected wave $\lambda_r = 2\pi/|k_r| \to 0$. Thus, we see that when $\mathrm{Fr} \to 1$, then the amplitude of the reflected wave R_η infinitely increases, and its wavelength vanishes. It will be shown below that the wave energy flux associated with the reflected wave remains finite even when $\mathrm{Fr} = 1$.

The results obtained for the transformation coefficients are in consistency with the wave energy flux conservation in an inhomogeneous stationary moving fluid (see, e.g., Ref. [93]), $W \equiv V_g E = \mathrm{const.}$, where $V_g \equiv d\omega/dk$ is the group speed in the moving fluid, and E is the density of wave energy. In the case of long waves in shallow water we have $(V_g)_{1,2} = (c_0)_{1,2} \pm U_{1,2}$. As shown in Appendix 6.2 (see also Refs. [41, 98]), the period-averaged energy density in the long-wave limit is $E = gA^2b\,(1 \pm \mathrm{Fr})\,/2$, where A is the amplitude of free surface perturbation, b is the canal width, sign plus pertains to waves co-propagating with the background flow, and sign minus – to waves propagating against the flow. Taking into account that the energy fluxes in the incident and transmitted waves are directed to the right, and the energy flux in the reflected wave is directed to the left, we obtain

$$(1 + \mathrm{Fr})^2 - (1 - \mathrm{Fr})^2 R_\eta^2 = \sqrt{X}Y \left(1 + \frac{\mathrm{Fr}}{X^{3/2}Y}\right)^2 T_\eta^2, \tag{3.15}$$

where the factor $\sqrt{X}Y$ accounts for the change of the cross-sectional area of the canal.

Substituting here the expressions for the transformation coefficients Eq. (3.14), we confirm that Eq. (3.15) reduces to the identity. Notice that the second term in the left-hand side of Eq. (3.15), which represents the energy flux induced by the reflected wave, remains finite even at $\mathrm{Fr} = 1$.

The gain of energy densities in the reflected and transmitted waves can be presented as the ratios E_r/E_i and E_t/E_i. Using the formulas for the transformation coefficients and expression for the wave energy in a moving fluid (see above), we obtain

$$\frac{E_r}{E_i} = \frac{1+\mathrm{Fr}}{1-\mathrm{Fr}}\left(\frac{1-\sqrt{X}Y}{1+\sqrt{X}Y}\right)^2, \quad \frac{E_t}{E_i} = \frac{4Y}{\left(1+\sqrt{X}Y\right)^2}\frac{1+\mathrm{Fr}}{1+\mathrm{Fr}/X^{3/2}Y}. \tag{3.16}$$

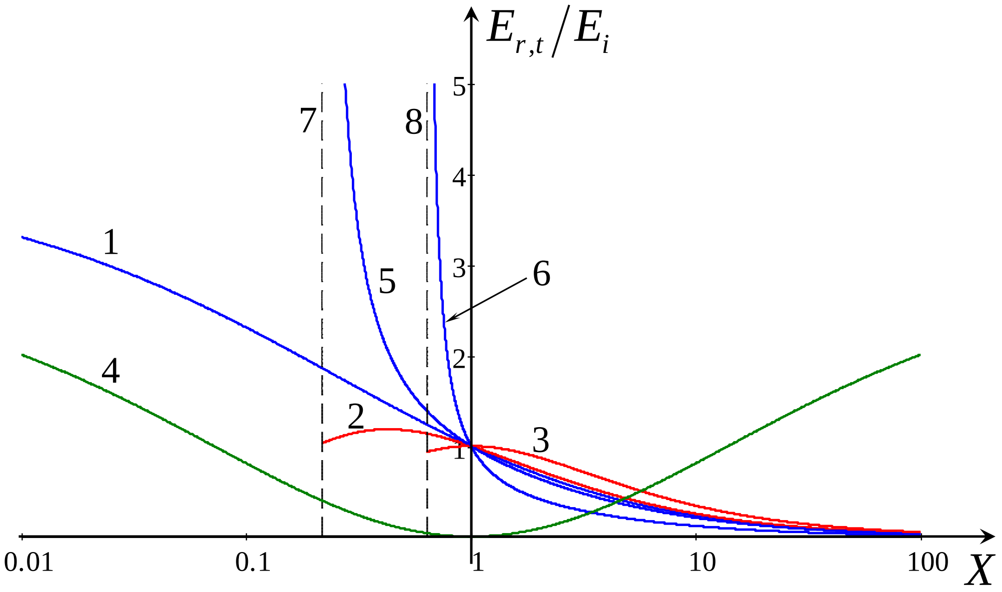

Figure 3.6: The gain of energy density in the transmitted wave for several Froude numbers and $Y = 1$ as functions of the depth drop X. Line 1 pertains to the reference case when $\mathrm{Fr} = 0$; lines 2 and 3 pertain to the downstream propagating waves in the subcritical flows with $\mathrm{Fr} = 0.1$ and 0.5 respectively; and lines 5 and 6 pertain to the upstream propagating waves in the same flows. Line 4 shows the typical dependence of energy density gain in the upstream propagating reflected wave with $\mathrm{Fr} = 0.5$. Lines 7 and 8 show the boundaries of subcritical regimes for $\mathrm{Fr} = 0.1$ and 0.5 respectively.

As follows from the first of these expressions, the density of wave energy in the reflected wave is enhanced uniformly by the current at any Froude number ranging from 0 to 1 regardless of X and Y, whereas the density of wave energy in the transmitted wave can be slightly enhanced by the current only if $X^{3/2}Y > 1$; otherwise, it is less than that in the incident wave. Figure 3.6 illustrates the gain of energy density in the transmitted wave for several Froude numbers and $Y = 1$. Line 4 in that figure shows the typical dependence of E_r/E_i on X for $\mathrm{Fr} = 0.5$ and $Y = 1$. When $\mathrm{Fr} \to 1$ the gain of wave energy in the reflected wave infinitely increases within the framework of a linear model considered here (in reality the nonlinear, viscous, or dispersive effects can restrict infinite growth). In this case the typical over-reflection phenomenon [77] occurs in the scattering of downstream propagating wave, when the energy density in the reflected wave becomes greater than the energy density in the incident wave. This can occur due to the wave energy extraction from the mean flow.

3.3.2 Upstream propagating incident wave

Consider now the case when the current is still co-directed with the x axis (see Fig. 3.2) and the incident wave travels in the opposite direction from plus infinity. Then, the transmitted wave in the left domain propagates counter current, and the reflected wave in the right domain is co-directed with the current. In the dispersion diagram shown in Fig. 3.4 the incident wave now corresponds to the intersection of line 2 with the dashed horizontal line 7 (with the wavenumber k_r replaced by k_i), the reflected wave corresponds to intersection of line 1 with line 7 (with the wavenumber k_i replaced by k_r), and the transmitted wave corresponds to the intersection of line 4 with line 7 (not visible in the figure).

To derive the transformation coefficients, we use the same boundary conditions at the juncture point $x = 0$ and after simple manipulations similar to those presented in the previous subsection we obtain essentially the same formulas for the wave numbers of transmitted and reflected waves as in Eqs. (3.5) and (3.7), as well as the transformation coefficients as in Eqs. (3.14) with the only difference that the sign of the Froude number should be changed everywhere to the opposite, $\mathrm{Fr} \to -\mathrm{Fr}$. However, the change of sign in the Froude number leads to singularities in both the wavenumber of the transmitted wave and the transmission coefficient. Therefore for the wave numbers of scattered waves we obtain:

$$\frac{k_r}{k_i} = \frac{1-\mathrm{Fr}}{1+\mathrm{Fr}}, \quad \frac{k_t}{k_i} = XY\frac{1-\mathrm{Fr}}{X^{3/2}Y-\mathrm{Fr}}. \tag{3.17}$$

In Fig. 3.7, lines 1 – 3 show the dependencies of normalized wavenumbers of transmitted waves on the depth drop X for $Y = 1$ and several particular values of the Froude number. Line 1 pertains to the reference case studied by [88] when there is no flow ($\mathrm{Fr} = 0$). As one can see, when the depth drop decreases and approaches the critical value, $X \to X_c = (\mathrm{Fr}/Y)^{2/3}$, the wavenumber of the transmitted wave becomes infinitely big (and the corresponding wavelength vanishes). This means that the current in the left domain becomes very strong and supercritical; the transmitted wave cannot propagate against it and the blocking phenomenon occurs (see, e.g., Refs. [10, 99] and references therein).

The transformation coefficients for this case are

$$R_\eta = \frac{1-\mathrm{Fr}}{1+\mathrm{Fr}}\frac{1-\sqrt{X}Y}{1+\sqrt{X}Y}, \quad T_\eta = \frac{1-\mathrm{Fr}}{X^{3/2}Y-\mathrm{Fr}}\frac{2X^{3/2}Y}{1+\sqrt{X}Y}. \tag{3.18}$$

They are as shown in Fig. 3.8 in the domains where the subcritical regime

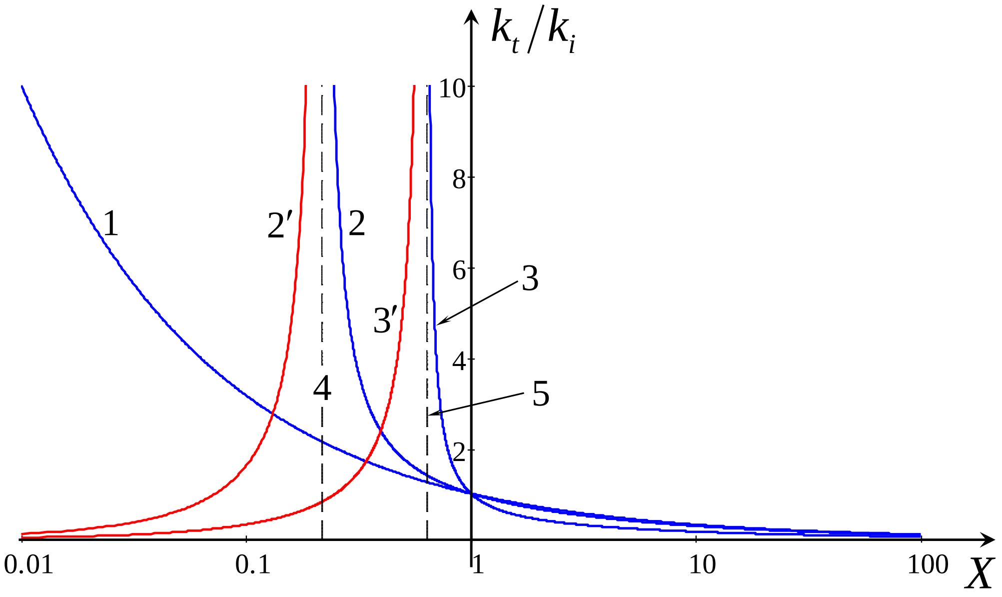

Figure 3.7: The dependencies of normalized wave numbers of transmitted waves on the depth drop X for $Y = 1$ and several particular values of the Froude number. Line 1 pertains to the reference case when there is no flow (Fr = 0); other lines pertain to the subcritical cases (line 2 – Fr = 0.1; line 3 – Fr = 0.5) and supercritical cases (line 2′ – Fr = 0.1; line 3′ – Fr = 0.5). Dashed vertical lines 4 and 5 show the boundaries between the subcritical and supercritical cases for Fr = 0.1 and 0.5, respectively.

occurs, $X > (\mathrm{Fr}/Y)^{2/3}$ as the functions of depth drop X for $Y = 1$ and two values of the Froude number. When depth drop decreases and approaches the critical value X_c, the transmission coefficient infinitely increases, and the over-transmission phenomenon occurs. However, it can be readily shown that the energy flux remains finite, and the law of energy flux conservation Eq. (3.15) with $\mathrm{Fr} \to -\mathrm{Fr}$ holds true in this case too.

The gain of energy densities in the reflected and transmitted waves follows from Eq. (3.16) if we replace Fr by −Fr (see lines 4 and 5 in Fig. 3.6):

$$\frac{E_r}{E_i} = \frac{1-\mathrm{Fr}}{1+\mathrm{Fr}}\left(\frac{1-\sqrt{X}Y}{1+\sqrt{X}Y}\right)^2, \quad \frac{E_t}{E_i} = \frac{4Y}{\left(1+\sqrt{X}Y\right)^2}\frac{1-\mathrm{Fr}}{1-\mathrm{Fr}/X^{3/2}Y}. \tag{3.19}$$

The presence of a subcritical current leads to uniform decrease of wave energy density in the reflected wave regardless of X and Y. Moreover, the wave density in this wave vanishes when $\mathrm{Fr} \to 1$. However, in the transmitted wave the density of wave energy quickly increases when $X \to X_c$ being greater than X_c (see lines 5 and 6 in Fig. 3.6). Thus, the typical over-transmission phenomenon occurs in the scattering of upstream propagating wave (cf. with the over-reflection phenomenon

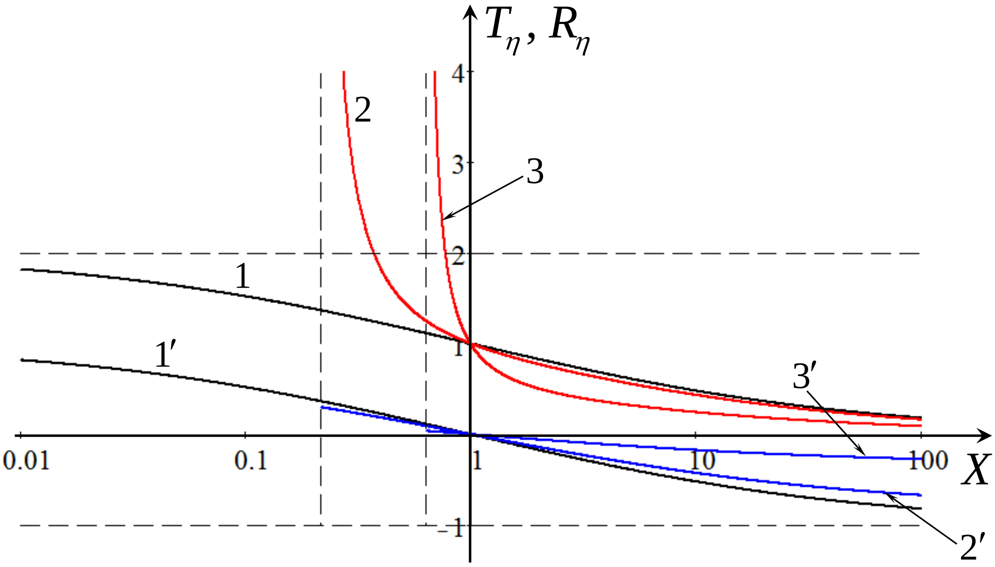

Figure 3.8: The transformation coefficients for the upstream propagating incident waves in a canal with flat walls, $Y = 1$, as functions of depth drop X. Line 1 for T_η and line 1′ for R_η pertain to the reference case when Fr = 0; lines 2 (for T_η) and 2′ (for R_η) pertain to Fr = 0.1, and lines 3 (for T_η) and 3′ (for R_η) pertain to Fr = 0.5.

described at the end of the previous subsection).

3.4 Subcritical flow in the upstream domain, but supercritical in the downstream domain

In such a case an incident wave can propagate only along the current. In the downstream domain where the current is supercritical no one wave can propagate against it. Therefore, we consider here a scattering of only a downstream propagating incident wave which arrives from minus infinity in Fig. 3.1. We assume that the Froude number and geometric parameters of a canal are such that $X^{3/2}Y < \mathrm{Fr} < 1$.

In the upstream domain two waves of frequency ω can propagate in the subcritical flow. One of them is an incident wave with the unit amplitude and wavenumber $k_i = \omega/(c_{01} + U_1)$ and another one is the reflected wave with the amplitude R_η and wavenumber $k_r = \omega/(c_{01} - U_1)$. In the downstream domain two waves can exist too. One of them is the transmitted wave of positive energy with the amplitude T_p and wavenumber $k_{t1} = \omega/(U_2 + c_{02})$ and another one is the transmitted wave of negative energy (see the Appendix) with the amplitude T_n and wavenumber $k_{t2} = \omega/(U_2 - c_{02})$.

The relationships between the wavenumbers of scattered waves follows from the frequency conservation. For the transmitted wave of positive energy and reflected wave we obtain the same formulas as in Eqs. (3.5) and (3.7), whereas for the transmitted wave of negative energy we obtain

$$\frac{k_{t2}}{k_i} = XY\frac{\mathrm{Fr} + 1}{\mathrm{Fr} - X^{3/2}Y}. \tag{3.20}$$

As follows from this formula, the wavenumber k_{t2} infinitely increases when $X \to X_c$ being less than X_c. The dependencies of k_{t1}/k_i are shown in Fig. 3.3 by lines 2′, 3′, and 4′ for Fr = 0.1, 0.5, and 1, respectively, whereas the dependencies of k_{t2}/k_i are shown in Fig. 3.7 by lines 2′ and 3′ for Fr = 0.1 and 0.5 respectively.

To find the transformation coefficients we use the same boundary conditions as in Eqs. (3.10) and (3.12), but now they provide the following set of equations:

$$1 + \mathrm{Fr} + (1 - \mathrm{Fr})\,R_\eta = T_p\left(1 + \frac{\mathrm{Fr}}{X^{3/2}Y}\right) + T_n\left(1 - \frac{\mathrm{Fr}}{X^{3/2}Y}\right), \tag{3.21}$$

$$1 + \mathrm{Fr} - (1 - \mathrm{Fr})\,R_\eta = \sqrt{X}Y\left[T_p\left(1 + \frac{\mathrm{Fr}}{X^{3/2}Y}\right) - T_n\left(1 - \frac{\mathrm{Fr}}{X^{3/2}Y}\right)\right]. \tag{3.22}$$

This set relates three unknown quantities, R_η, T_p, and T_n. We can express, for example, amplitudes of transmitted waves T_p and T_n in terms of unit amplitude of incident wave and amplitude of reflected wave R_η:

$$T_p = \frac{X}{2\left(X^{3/2}Y + \mathrm{Fr}\right)}\left[(1 + \mathrm{Fr})\left(\sqrt{X}Y + 1\right) + (1 - \mathrm{Fr})\left(\sqrt{X}Y - 1\right)R_\eta\right], \tag{3.23}$$

$$T_n = \frac{X}{2\left(X^{3/2}Y - \mathrm{Fr}\right)}\left[(1 + \mathrm{Fr})\left(\sqrt{X}Y - 1\right) + (1 - \mathrm{Fr})\left(\sqrt{X}Y + 1\right)R_\eta\right], \tag{3.24}$$

whereas the reflection coefficient R_η remains unknown.

It can be noticed a particular case when the background flow could, probably, spontaneously generate waves to the both sides of a juncture where the background flow abruptly changes from the subcritical to supercritical value. Bearing in mind that the transformation coefficients are normalized on the amplitude of an incident wave, $R_\eta \equiv A_r/A_i$, $T_p \equiv A_p/A_i$, $T_n \equiv A_n/A_i$, and considering a limit when $A_i \to 0$, we obtain from Eqs. (3.23) and (3.24):

$$\frac{A_r}{A_p} = \frac{2}{X\,(1 - \mathrm{Fr})}\frac{X^{3/2} + \mathrm{Fr}}{\sqrt{X}Y - 1}, \qquad \frac{A_n}{A_p} = \frac{\sqrt{X}Y + 1}{\sqrt{X}Y - 1}\frac{X^{3/2} + \mathrm{Fr}}{X^{3/2} - \mathrm{Fr}}. \tag{3.25}$$

The conservation of wave energy flux in general is

$$(1+\mathrm{Fr})^2-(1-\mathrm{Fr})^2R_\eta^2=\frac{1}{X^{5/2}Y}\left[\left(X^{3/2}Y+\mathrm{Fr}\right)^2T_p^2-\left(X^{3/2}Y-\mathrm{Fr}\right)^2T_n^2\right]. \tag{3.26}$$

After substitution here of the transmission coefficients Eqs. (3.23) and (3.24) we obtain the identity regardless of R_η. In the case of spontaneous wave generation when there is no incident wave, Eq. (3.26) turns to the identity too after its re-normalization and substitution of Eqs. (3.25). This resembles a spontaneous wave generation due to Hawking's effect [47, 152, 153]) at the horizon of an evaporating black hole, when a positive energy wave propagates towards our space (the upstream propagating wave A_r in our case), whereas a negative energy wave together with a positive energy wave propagates towards the black hole (the downstream propagating waves A_n and A_p).

Thus, within the model with an abrupt change of canal cross-section the complete solution for the wave scattering cannot be obtained in general. One needs to discard from the approximation when the current speed abruptly increases at the juncture and consider a smooth current transition from one value U_1 to another one U_2 (this problem was recently studied in Ref. [23]).

3.5 Supercritical flow in both the upstream and downstream domains

Now let us consider a wave scattering in the case when the flow is supercritical both in upstream and downstream domain, $U_1 > c_{01}$ and $U_2 > c_{02}$. In terms of the Froude number we have Fr > 1 and Fr $> X^{3/2}Y$. It is clear that in such a situation, similar to the previous subsection, only a downstream propagating incident wave can be considered.

In the upstream supercritical flow there is no reflected wave. In the dispersion diagram of Fig. 3.4 the downstream propagating incident wave of frequency ω can be either the wave on the intersection of line 5 with the dashed horizontal line, or on the intersection of line 6 with the dashed horizontal line (the intersection point is off the figure), or even both. The former wave is the wave of positive energy and has the wavenumber $k_{i1} = \omega/(U_1 + c_{01})$, whereas the latter is the wave of negative energy (see the Appendix) and has the wavenumber $k_{i2} = \omega/(U_1 - c_{01})$.

In the downstream domain where we assume that the flow is supercritical too, two waves appear as the result of scattering of incident waves. As in the upstream domain, one of the transmitted waves has positive energy and the wavenumber $k_{t1} = \omega/(U_2 + c_{02})$, and the other has negative energy and the wavenumber

$k_{t2} = \omega/(U_2 - c_{02})$.

Let us assume that there is a wavemaker at minus infinity that generates a sinusoidal surface perturbation of frequency ω. Then, two waves of positive and negative energies with the amplitudes A_p and A_n, respectively, can jointly propagate. In the process of wave scattering at the canal juncture two transmitted waves with opposite energies will appear with the amplitudes T_p and T_n. Their amplitudes can be found from the boundary conditions Eqs. (3.10) and (3.12). Then, after simple manipulations similar to those in Secs. 3.3 and 3.4 we obtain:

$$T_p = \frac{X}{2\left(X^{3/2}Y + \mathrm{Fr}\right)} \left[(\mathrm{Fr}+1)\left(\sqrt{X}Y + 1\right)A_p - (\mathrm{Fr}-1)\left(\sqrt{X}Y - 1\right)A_n\right], \tag{3.27}$$

$$T_n = \frac{X}{2\left(X^{3/2}Y - \mathrm{Fr}\right)} \left[(\mathrm{Fr}+1)\left(\sqrt{X}Y - 1\right)A_p - (\mathrm{Fr}-1)\left(\sqrt{X}Y + 1\right)A_n\right]. \tag{3.28}$$

At certain relationships between the amplitudes A_p and A_n it may happen that there is only one transmitted wave, either of positive energy ($T_n = 0$), when

$$A_n = A_p \frac{\mathrm{Fr}+1}{\mathrm{Fr}-1} \frac{\sqrt{X}Y - 1}{\sqrt{X}Y + 1}, \tag{3.29}$$

or of negative energy ($T_p = 0$), when

$$A_n = A_p \frac{\mathrm{Fr}+1}{\mathrm{Fr}-1} \frac{\sqrt{X}Y + 1}{\sqrt{X}Y - 1}. \tag{3.30}$$

From the law of wave energy flux conservation we obtain

$$(\mathrm{Fr}+1)^2 A_p^2 - (\mathrm{Fr}-1)^2 A_n^2 = \sqrt{X}Y \left[\left(\frac{\mathrm{Fr}}{X^{3/2}Y} + 1\right)^2 T_p^2 - \left(\frac{\mathrm{Fr}}{X^{3/2}Y} - 1\right)^2 T_n^2\right]. \tag{3.31}$$

Substituting here the expressions for T_p and T_n as per Eqs. (3.27) and (3.28), we see that Eq. (3.31) becomes an identity regardless of amplitudes of incoming waves A_p and A_n, including the cases when they are related by Eqs. (3.29) or (3.30). In the particular cases one of the incident waves can be suppressed, ether the wave of negative energy or wave of positive energy. In the former case we set $A_n = 0$ and $A_p = 1$, and in the latter case we set $A_p = 0$ and $A_n = 1$.

When there is only one incident wave of *positive energy* with the amplitude $A_p = 1$ and there is no wave of negative energy ($A_n = 0$), then the transmission coefficients Eqs. (3.27) and (3.28) reduce to

$$T_p = \frac{X}{2}\frac{\mathrm{Fr}+1}{\mathrm{Fr}+X^{3/2}Y}\left(1+\sqrt{X}Y\right), \quad T_n = \frac{X}{2}\frac{\mathrm{Fr}+1}{\mathrm{Fr}-X^{3/2}Y}\left(1-\sqrt{X}Y\right). \tag{3.32}$$

Recall that these formulas are valid for supercritical flows when $\mathrm{Fr} > 1$ and $\mathrm{Fr} > X^{3/2}Y$. In the limiting case when $X \to 0$ and $Y = \mathrm{const.}$, we obtain

$$T_p \approx T_n \approx X\frac{\mathrm{Fr}+1}{2\mathrm{Fr}}. \tag{3.33}$$

In another limiting case when $X^{3/2}Y \to \mathrm{Fr}$ the transmission coefficient for the positive energy wave remains constant, whereas the transmission coefficient for the negative energy wave within the framework of linear theory goes to plus or minus infinity depending on the value of Y. Figure 3.9(a) illustrates the transmission coefficients T_p and T_n as functions of X for $Y = 1$ and two particular values of the Froude number.

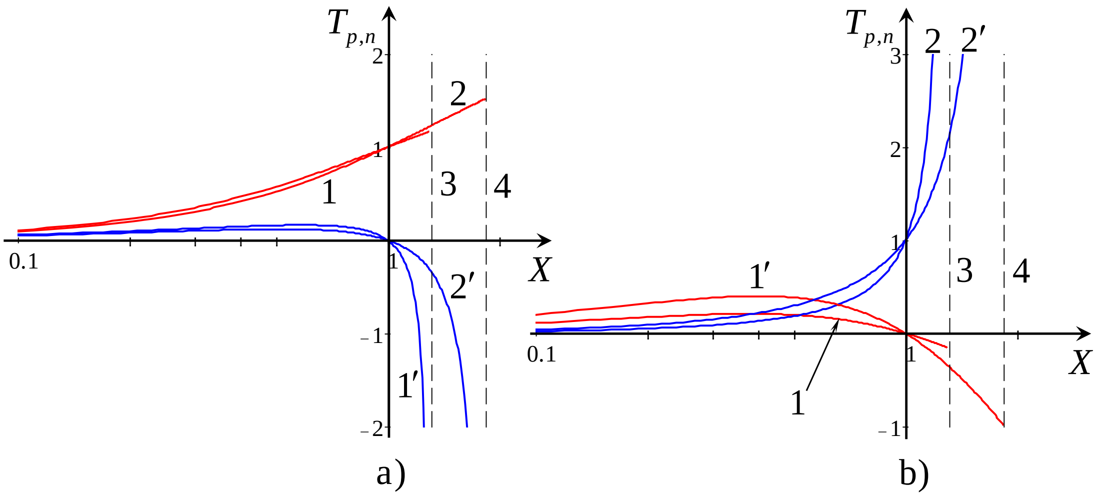

Figure 3.9: The transmission coefficients for the downstream propagating incident waves of positive energy (frame a) and negative energy (frame b) in a canal with the flat walls, $Y = 1$, as functions of the depth drop X. Line 1 for T_p and line 1′ for T_n pertain to $\mathrm{Fr} = 1.5$, and lines 2 (for T_p) and 2′ (for T_n) pertain to $\mathrm{Fr} = 2.5$. Data for lines 1 and 2 in frame (b) were multiplied by a factor of ten to make the graphics clearly visible.

When there is only one incident wave of *negative energy* with the amplitude $A_n = 1$ and there is no wave of positive energy ($A_p = 0$), then the transmission coefficients Eqs. (3.27) and (3.28) reduce to

$$T_p = \frac{X}{2}\frac{\mathrm{Fr}-1}{\mathrm{Fr}+X^{3/2}Y}\left(1-\sqrt{X}Y\right), \quad T_n = \frac{X}{2}\frac{\mathrm{Fr}-1}{\mathrm{Fr}-X^{3/2}Y}\left(1+\sqrt{X}Y\right). \tag{3.34}$$

In the limiting case when $X \to 0$, and $Y = \mathrm{const.}$, we obtain

$$T_p \approx T_n \approx X\frac{\mathrm{Fr}-1}{2\mathrm{Fr}}. \tag{3.35}$$

In another limiting case when $X^{3/2}Y \to \mathrm{Fr}$, the transmission coefficient for the positive energy wave remains finite, whereas, the transmission coefficient for the negative energy wave within the framework of linear theory goes to plus infinity. Figure 3.9(b) shows the transmission coefficients T_p and T_n as functions of X for $Y = 1$ for two particular values of the Froude number.

3.6 Supercritical flow in the upstream and subcritical in the downstream domain

Let us consider, at last, the case when the flow is supercritical in the upstream domain, where $U_1 > c_{01}$, but due to canal widening becomes subcritical in the downstream domain, where $U_2 < c_{02}$. Thus, the flow is decelerating and in terms of the Froude number we have $1 < \mathrm{Fr} < X^{3/2}Y$. Assume first that the incident wave propagates downstream.

3.6.1 Downstream propagating incident wave

As was mentioned in the previous section, two waves with the amplitudes A_p and A_n can propagate simultaneously from minus infinity, if they are generated by the same wavemaker with the frequency ω. In the downstream domain potentially two waves of positive energy can exist, but only one of them propagating downstream can appear as the transmitted wave with the amplitude T_η as the result of wave scattering at the juncture.

The amplitudes of scattered waves can be found from the boundary conditions Eqs. (3.10) and (3.12). This gives, after simple manipulations:

$$\begin{aligned}(1+\mathrm{Fr})\,A_p + (1-\mathrm{Fr})\,A_n =& T_\eta\left(1+\frac{\mathrm{Fr}}{X^{3/2}Y}\right), \qquad (3.36)\\ (1+\mathrm{Fr})\,A_p - (1-\mathrm{Fr})\,A_n =& \sqrt{X}YT_\eta\left(1+\frac{\mathrm{Fr}}{X^{3/2}Y}\right). \qquad (3.37)\end{aligned}$$

This set of equations provides a unique solution for the transmission coefficient T_η only in the case when the amplitudes of incoming waves are related:

$$A_n = \frac{1+\mathrm{Fr}}{1-\mathrm{Fr}}\frac{1-\sqrt{X}Y}{1+\sqrt{X}Y}A_p, \quad T_\eta = \frac{1+\mathrm{Fr}}{X^{3/2}Y+\mathrm{Fr}}\frac{2X^{3/2}Y}{1+\sqrt{X}Y}A_p. \qquad (3.38)$$

If one of the incident waves is absent ($A_n = 0$ or $A_p = 0$) or amplitudes of incoming waves are not related by Eq. (3.38), then the set of Eqs. (3.36) and (3.37) is inconsistent. In such cases the problem of wave scattering in the canal does not have a solution within the framework of a model with a sharp change of the cross-section.

If the amplitudes of incident waves A_p and A_n are related by Eq. (3.38), then the conservation of wave energy flux holds and takes the form

$$\left(\mathrm{Fr}+1\right)^2 A_p^2 - \left(\mathrm{Fr}-1\right)^2 A_n^2 = \sqrt{X}Y\left(\frac{\mathrm{Fr}}{X^{3/2}Y}+1\right)^2 T_\eta^2. \qquad (3.39)$$

Substituting here A_n and T_η from Eq. (3.38), we see that it becomes just the identity.

3.6.2 Upstream propagating incident wave

For the incident wave arriving from the plus infinity and propagating upstream in the subcritical domain of the flow, the problem of wave scattering within the model with a sharp change of a current is undefined. The incoming wave cannot penetrate from the domain with a subcritical flow into the domain with a supercritical flow, therefore one can say that formally the reflection coefficient in this case $R_\eta = 1$, and the transmission coefficients $T_\eta = 0$. However such a problem should be considered within a more complicated model with a smooth transcritical flow; this has been done in Ref. [23].

3.7 Conclusion

In this Chapter within the linear approximation we have studied a scattering of long surface waves at the canal juncture when its width and depth abruptly change at a certain place. We have calculated the transformation coefficients for the reflected and transmitted waves in the presence of a background flow whose speed changes from U_1 to U_2 in accordance with the mass flux conservation. The calculated coefficients represent the effectiveness of the conversion of the incident wave into the other wave modes – reflected and transmitted of either positive or negative energy. Our consideration generalizes the classical problem studied by Ref. [88] when the background flow is absent. It was assumed that the characteristic scale of current variation in space is much less than the wavelengths of scattered waves. Such a simplified model allows one to gain insight into the complex problem of wave-current interaction and find the conditions for the over-reflection and over-transmission of water waves. We have analyzed all possible orientations of the incident wave with respect to flow and studied all possible regimes of water flow (subcritical, supercritical, and transcritical).

In the study of the subcritical and supercritical flows (see Secs. 3.3 and 3.5) we have succeeded in calculating the transmission and reflection coefficients in the explicit forms as functions of the depth drop $X = h_2/h_1$, specific width ratio

$Y = b_2/b_1$, and Froude number Fr. Based on these, the conditions for the over-reflection and over-transmission have been found in terms of the relationships between the Froude number and canal geometric parameters X and Y. It appears that it is not possible to do the same for the transcritical flows, at least within the framework of the simplified model considered in this Chapter (see Secs. 3.4 and 3.6). The reason for that is in the critical point where $\mathrm{Fr} = 1$ which appears in the smooth transient domain between two portions of a canal with the different cross-sections. The transition through the critical point is a rather complex problem which was recently studied on the basis of a model with a continuously varying flow speed in a duct of smoothly varying width [23]. The summary of results obtained is presented in Table I.

The problem studied can be further generalized for waves of arbitrary length taking into account the effect of dispersion. Similar works in this direction were published recently for relatively smooth current variation in the canal with the finite-length bottom obstacles [29, 131]. It is worthwhile to notice that in the dispersive case for purely gravity waves there is always one wave of negative energy for which the flow is supercritical. This negative energy mode smoothly transforms into the dispersionless mode when the flow increases. In such cases two other upstream propagating modes disappear, and the dispersion relations reduces to one of considered in this Chapter. It will be a challenge to compare the theoretical results obtained in this Chapter with the numerical and experimental data; this may be a matter of future study.

I. Subcritical flow in the upstream and downstream domains			
$\mathbf{k}_i$, U	**Reflect. coeff.**	**Transmiss. coeff.**	**Peculiarity of a scattering**
$k_i \uparrow\uparrow U$	R_η see Eq. (3.14)	T_η see Eq. (3.14)	Regular scattering
$k_i \downarrow\uparrow U$	R_η see Eq. (3.18)	T_η see Eq. (3.18)	Regular scattering
II. Subcritical flow in the upstream domain and supercritical in the downstream domain. PEW and NEW appear downstream.			
$\mathbf{k}_i$, U	**Reflect. coeff.**	**Transmiss. coeff.**	**Peculiarity of a scattering**
$k_i \uparrow\uparrow U$	R_η is undetermined, according to [23], $R_\eta = 1$	T_p see Eq. (3.23) T_n see Eq. (3.24)	Undefined problem statement, according to [23], $T_p = -T_n = 1$
$k_i \downarrow\uparrow U$	Impossible situation		
III. Supercritical flow in the upstream and downstream domains			
$\mathbf{k}_i$, U	**Reflect. coeff.**	**Transmiss. coeff.**	**Peculiarity of a scattering**
$k_i \uparrow\uparrow U$	No reflected wave	T_p see Eq. (3.27) T_n see Eq. (3.28)	Incident wave can be PEW or NEW, or both. See Eqs. (3.32), (3.34).
$k_i \downarrow\uparrow U$	Impossible situation		
IV. Supercritical flow in the upstream and subcritical in the downstream domain			
$\mathbf{k}_i$, U	**Reflect. coeff.**	**Transmiss. coeff.**	**Peculiarity of a scattering**
$k_i \uparrow\uparrow U$	No reflected wave	T_η provided that $A_n \sim A_p$, Eq. (3.38)	Over-determined problem if there is only one incident wave
$k_i \downarrow\uparrow U$	Formally $R_\eta = 1$	Formally $T_\eta = 0$	See Ref. [23]

Table 3.1: The summary of considered cases.

A cocurrent propagating incident waves is denoted by $k_i \uparrow\uparrow U$, whereas a countercurrent propagating incident waves is denoted by $k_i \downarrow\uparrow U$. The acronyms PEW and NEW pertain to positive and negative energy waves, correspondingly.

Chapter 4

WAVE SCATTERING IN SPATIALLY INHOMOGENEOUS CURRENTS

In this Chapter we study analytically a scattering of long linear surface waves on stationary currents in a duct (canal) of a constant depth and variable width. It is assumed that the background velocity linearly increases or decreases with the longitudinal coordinate due to the gradual variation of duct width. Such a model admits analytical solution of the problem in hand, and we calculate the scattering coefficients as functions of incident wave frequency for all possible cases of sub-, super, and trans-critical currents. For completeness we study both co-current and counter-current wave propagation in accelerating and decelerating currents. The results obtained are analysed in application to recent analog gravity experiments [45, 135, 136, 155] and can shed light on the problem of hydrodynamic modelling of Hawking radiation. The results obtained in this Chapter have been published in Physical Review D [23].

4.1 Introduction

Since 1981 when Unruh established the analogy in wave transformation occurring at the horizon of a black hole and at a critical point of a hydrodynamic flow [152] there have been many attempts to calculate the transformation coefficients and find the analytical expression for the excitation coefficient of a negative energy mode (see, for instance, [27, 29, 126, 131] and references therein). In parallel with theoretical study there were several attempts to model the wave scattering in spatially inhomogeneous currents experimentally and determine this coefficient through the measurement data [45, 155] (similar experiments were performed or suggested in other media, for example, in the atomic Bose—Einstein condensate – see [143] and numerous references therein). In particular, the dependence of amplitude of a negative energy mode on frequency of incident wave in a water tank was determined experimentally [155]; however several aspects of the results obtained in this paper were subject to criticism.

The problem of water wave transformation in spatially inhomogeneous currents is of significant interest itself and there is a vast number of publications devoted to theoretical and experimental study of this problem. However in applying to the modelling of Hawking's effect, the majority of these publications suffer a drawback which is related to the parasitic effect of dispersion, whereas the dispersion is absent in the pure gravitational Hawking effect.

Below we consider a model which describes a propagation of small-amplitude long surface water waves in a duct (canal) of constant depth but variable width. The dispersion is absent, and the model is relevant to the analytical study of the Hawking effect. We show that the transformation coefficients can be found in the exact analytical forms both for co-current and counter-current wave propagation in gradually accelerating and decelerating currents.

We believe that the results obtained can be of wider interest, not only as a model of Hawking's effect, but in application to real physical phenomena occurring in currents in non-homogenous ducts, at least at relatively small Froude numbers. We consider all possible configurations of the background current and incident wave.

4.2 Derivation of the Governing Equation

Let us consider the set of equations for water waves on the surface of a perfect fluid of a constant density ρ and depth h. Assume that the water moves along the x-axis with a stationary velocity $U(x)$ which can be either an increasing or a decreasing function of x. Physically such a current can be thought as a model of water flow in a horizontal duct with a properly varying width $b(x)$. We will bear in mind such a model, although we do not pretend here to consider a current in a real duct, but rather to investigate an idealized hydrodynamic model which is described by the equation analogous to that appearing in the context of black hole evaporation due to Hocking radiation [27, 29, 47, 73, 126, 131, 152, 153].

In contrast to other papers also dealing with the surface waves on a spatially varying current (see, e.g., [27, 29, 126, 131]), we consider here the case of shallow-water waves when there is no dispersion, assuming that the wavelengths $\lambda \gg h$.

In the hydrostatic approximation, which is relevant to long waves in shallow water [89], the pressure can be presented in the form $p = p_0 + \rho g(\eta - z)$, where p_0 is the atmospheric pressure, g is the acceleration due to gravity, z is the vertical coordinate, and $\eta(x,t)$ is the perturbation of free surface ($-h \le z \le \eta$). Then the linearized Euler equation for small perturbations having also only one velocity component $u(x,t)$ takes the form:

$$\frac{\partial u}{\partial t} + \frac{\partial (Uu)}{\partial x} = -g\frac{\partial \eta}{\partial x}. \tag{4.1}$$

The second equation is the continuity equation which is equivalent to the mass conservation equation for shallow-water waves:

$$\frac{\partial S}{\partial t} + \frac{\partial}{\partial x}\left[S\left(U+u\right)\right] = 0, \tag{4.2}$$

where $S(x,t)$ is the portion of the cross-section of a duct occupied by water, $S(x,t) = b(x)[h + \eta(x,t)]$, where $b(x)$ is the width of the duct.

For the background current Eq. (4.2) gives the mass flux conservation $Q \equiv \rho U(x)S(x) = \rho U(x)b(x)h = \text{const}$. Inasmuch as $h = \text{const}$, we have $U(x)b(x) = Q/\rho h = \text{const}$, and Eq. (4.2) in the linear approximation reduces to:

$$b(x)\frac{\partial \eta}{\partial t} + \frac{\partial}{\partial x}\left[b(x)\left(U\eta + uh\right)\right] = 0. \tag{4.3}$$

Thus, the complete set of equations for shallow water waves in a duct of a variable width consists of Eqs. (4.1) and (4.3). This set can be reduced to one equation of the second order. To this end let us divide first Eq. (4.3) by $b(x)$ and rewrite it in the equivalent form:

$$\frac{\partial \eta}{\partial t} + U\frac{\partial \eta}{\partial x} = -hU\frac{\partial}{\partial x}\frac{u}{U}. \tag{4.4}$$

Expressing now the velocity component u in terms of the velocity potential φ, $u = \partial\varphi/\partial x$, and combining Eqs. (4.1) and (4.4), we derive

$$\left(\frac{\partial}{\partial t} + U\frac{\partial}{\partial x}\right)\left(\frac{\partial \varphi}{\partial t} + U\frac{\partial \varphi}{\partial x}\right) = c_0^2 U\frac{\partial}{\partial x}\left(\frac{1}{U}\frac{\partial \varphi}{\partial x}\right), \tag{4.5}$$

where $c_0 = \sqrt{gh}$ is the speed of linear long waves in shallow water without a background current.

As this equation describes wave propagation on the stationary moving current of perfect fluid, it provides the law of wave energy conservation which can be presented in the form (its derivation is given in Appendix 6.2):

$$\frac{\partial \mathcal{E}}{\partial t} + \frac{\partial J}{\partial x} = 0, \tag{4.6}$$

where

$$\mathcal{E} = \frac{\mathrm{i}}{U}\left[\overline{\varphi}\left(\frac{\partial \varphi}{\partial t} + U\frac{\partial \varphi}{\partial x}\right) - \varphi\left(\frac{\partial \overline{\varphi}}{\partial t} + U\frac{\partial \overline{\varphi}}{\partial x}\right)\right], \quad J = \mathcal{E}U - \frac{\mathrm{i}\, c_0^2}{U}\left(\overline{\varphi}\frac{\partial \varphi}{\partial x} - \varphi\frac{\partial \overline{\varphi}}{\partial x}\right),$$

and the over-bar denotes complex conjugation.

Solution of the linear equation (4.5) can be sought in the form $\varphi(x,t) = \Phi(x)\mathrm{e}^{-\mathrm{i}\,\omega t}$, then it reduces to the ODE for the function $\Phi(x)$:

$$\left(-\mathrm{i}\,\omega + U\frac{d}{dx}\right)\left(-\mathrm{i}\,\omega\Phi + U\frac{d\Phi}{dx}\right) = c_0^2 U\frac{d}{dx}\left(\frac{1}{U}\frac{d\Phi}{dx}\right). \tag{4.7}$$

If we normalize the variables such that $U/c_0 = V$, $x/L = \xi$, and $\omega L/c_0 = \hat{\omega}$, where L is the characteristic spatial scale of the basic current, then we can present the main equation in the final form:

$$V\left(1 - V^2\right)\frac{d^2\Phi}{d\xi^2} - \left[\left(1 + V^2\right)V' - 2\,\mathrm{i}\,\hat{\omega}V^2\right]\frac{d\Phi}{d\xi} + V\hat{\omega}^2\Phi = 0, \tag{4.8}$$

where the prime stands for here and below differentiation with respect to the entire function argument (in this particular case with respect to ξ). If the perturbations are monochromatic in time, as above, then the wave energy $\mathcal{E}$ and energy flux J do not depend on time, therefore, as follows from Eq. (4.6), the energy flux does not depend on x too, so $J = \text{const}$.

For the concrete calculations we chose the piecewise linear velocity profile, assuming that the current varies linearly within a finite interval of x and remains constant out of this interval (see Fig. 4.1):

$$\begin{aligned}
V_a(\xi) &= \begin{cases} V_1 \equiv \xi_1, & \xi \le \xi_1, \\ \xi, & 0 < \xi_1 < \xi < \xi_2, \\ V_2 \equiv \xi_2, & \xi \ge \xi_2; \end{cases} \\
V_d(\xi) &= \begin{cases} V_1 \equiv -\xi_1, & \xi \le \xi_1, \\ -\xi, & \xi_1 < \xi < \xi_2 < 0, \\ V_2 \equiv -\xi_2, & \xi \ge \xi_2, \end{cases}
\end{aligned} \tag{4.9}$$

where $V_a(\xi)$ pertains to the accelerating current, and $V_d(\xi)$ – to the decelerating current. To simplify further calculations, we have chosen, without the loss of generality, the origin of the coordinate frame such that the velocity profile is directly proportional to $\pm\xi$ in the interval $\xi_1 \le \xi \le \xi_2$ as shown in Fig. 4.1). For such velocity configurations it is convenient to set $L = (x_2 - x_1)c_0/(U_2 - U_1) = (x_2 - x_1)/|V_2 - V_1|$. The choice of piecewise linear velocity profile allows us to reduce the governing equation (4.8) to the analytically solvable equation and obtain exact solutions. The corresponding water flow can be realized in a duct with a variable width, which is constant, $b = b_1$, when $\xi \le \xi_1$, then gradually varies along the ξ-axis as $b(\xi) = b_1\xi_1/\xi$ in the interval $\xi_1 \le \xi \le \xi_2$, and after that remains constant again, $b_2 = b_1\xi_1/\xi_2$ when $\xi \ge \xi_2$. Schematically the sketch of a duct with gradually decreasing width that provides an accelerating current is shown in Fig. 4.2. Equation (4.8) should be augmented by the boundary conditions at $\xi \to \pm\infty$ which specify the scattering problem, as well as by the

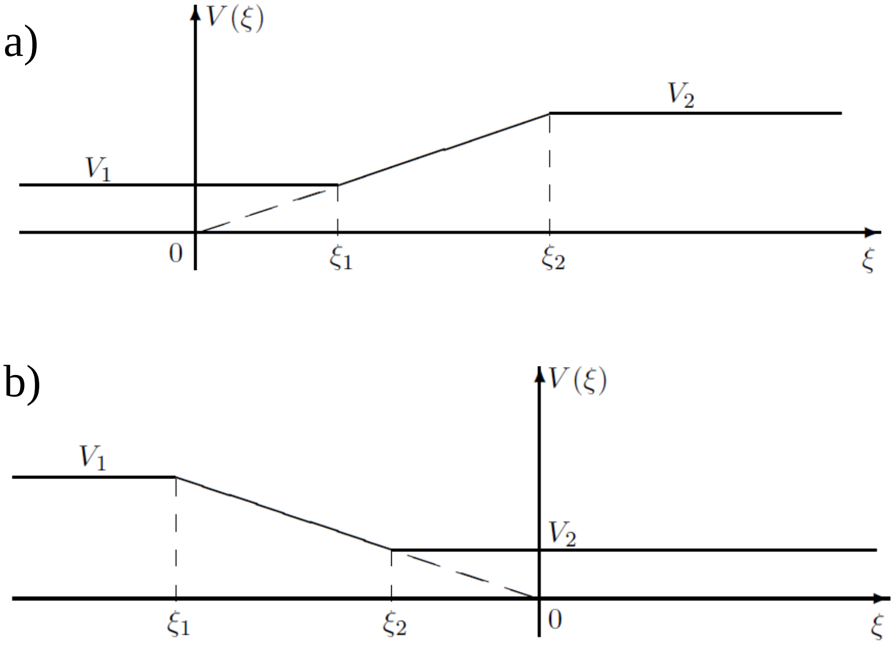

Figure 4.1: Sketch of accelerating (a) and decelerating (b) background currents.

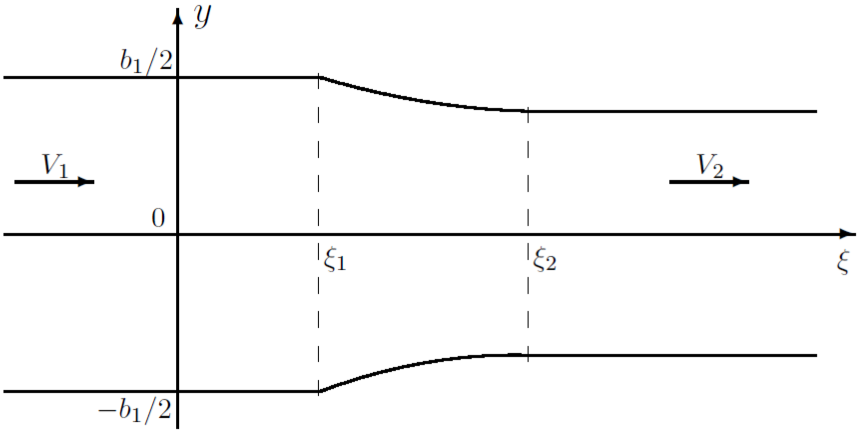

Figure 4.2: The sketch of a duct with the decreasing width that provides spatially accelerating background current.

matching conditions at $\xi = \xi_1$ and $\xi = \xi_2$. The latter conditions reduce to the continuity of the function $\Phi(\xi)$ and its derivative $\Phi'(\xi)$ (see Appendix 6.2 for the derivation):

$$\Phi(\xi_{1,2} + 0) = \Phi(\xi_{1,2} - 0), \qquad \Phi'(\xi_{1,2} + 0) = \Phi'(\xi_{1,2} - 0). \tag{4.10}$$

On the basis of Eq. (4.8) and matching conditions (4.10), we are able to study analytically all possible cases of orientation of an incident wave and a current, assuming that the current can be sub-critical ($V_{1,2} < 1$), trans-critical ($V_1 > 1$, $V_2 < 1$ or vice versa $V_1 < 1$, $V_2 > 1$), or super-critical ($V_{1,2} > 1$).

4.3 Qualitative analysis of the problem based on the JWKB approximation

Before the construction of an exact solution for wave scattering in currents with the piecewise linear velocity profiles, it seems reasonable to consider the problem qualitatively to reveal its specific features which will help in the interpretation of results obtained.

Consider first a long sinusoidal wave propagating on a current with constant U. Assume, in accordance with the shallow-water approximation, that the wavelength $\lambda \gg h$. The dispersion relation for such waves is

$$(\omega - \mathbf{kU})^2 = c_0^2 k^2, \tag{4.11}$$

where $\mathbf{k} = (k, 0, 0)$ is a wave vector related with a wavelength $\lambda = 2\pi/|\mathbf{k}|$.

A graphic of the dispersion relation is shown in Fig. 4.3 for two values of the current speed, sub-critical, $U < c_0$, and super-critical, $U > c_0$. Since we consider dispersionless shallow-water waves, graphics of the dependencies $\omega(k)$ are straight lines formally extending from minus to plus infinity. We suppose, however, that the frequency ω is a non-negative quantity which is inversely proportional to the wave period; therefore, without loss of generality, we can ignore those portions of dispersion lines which correspond to negative frequencies (in Fig. 4.3 they are shown by inclined dashed lines). The dashed horizontal line in Fig. 4.3 shows a particular fixed frequency of all waves participating in the scattering process. For co-current propagating waves with $\boldsymbol{k} \uparrow\uparrow \mathbf{U}$ the dispersion relation (4.11) reduces to $\omega = (U + c_0)|\mathbf{k}|$, whereas for counter-current propagating waves with $\boldsymbol{k} \downarrow\uparrow \mathbf{U}$ it is $\omega = |U - c_0||\mathbf{k}|$. Thus, the dispersion lines for surface waves on a current are not symmetrical with respect to the vertical axis $k = 0$. When the current speed U increases, the right branch 1 turns toward the vertical axis (cf. lines 1 and

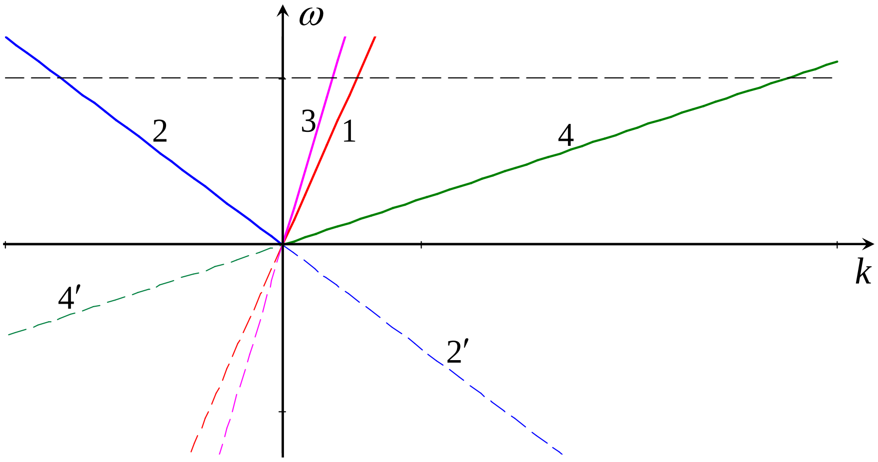

Figure 4.3: The dispersion dependencies for surface waves on uniformly moving shallow water. Lines 1 and 2 pertain to co-current and counter-current propagating waves respectively in a sub-critical current ($U < c_0$). Lines 3 and 4 pertain to positive- and negative-energy waves respectively in a super-critical current ($U > c_0$) both propagating downstream.

3 in Fig. 4.3). The left branch 2 in this case tilts toward the negative half-axis k; coincides with it when $U = c_0$, and then, when $U > c_0$, it goes to the lower half-plane and becomes negative. However, its negative portion $2'$ goes up, passes through the axis k and appears in the upper half-plane as the dispersion line 4. Thus, waves corresponding to lines 3 and 4 are downstream propagating waves, whereas there are no upstream propagating waves, if $U > c_0$. From the physical point of view this means that the current is so strong that it pulls downstream even counter-current propagating waves. As was shown, for instance, in Refs. [24, 46, 98], in a such strong current, waves on branch 3 have positive energy, whereas waves on branch 4 have negative energy.

To consider wave propagation on a spatially variable current when it accelerates or decelerates along x-axis, let us use the JWKB method, which physically presumes that the wavelengths are much less than the characteristic scale of inhomogeneity, $\lambda \ll L$ (whereas still $\lambda \gg h$ and the shallow-water approximation is valid). This condition can be presented in the form $L/\lambda = L/(c_0 T) = L\omega/(2\pi c_0) = \hat{\omega}/2\pi \gg 1$ (where $T = 2\pi/\omega$ is the wave period) and if it is fulfilled, the JWKB solution of Eq. (4.8) can be sought in the form (see, e.g., [37, 117]):

$$\Phi(\xi) = \exp\left[\mathrm{i}\,\hat{\omega}\int q(\xi)\,d\xi\right], \quad q(\xi) = q_0(\xi) + \hat{\omega}^{-1}q_1(\xi) + \hat{\omega}^{-2}q_2(\xi) + \ldots \tag{4.12}$$

Substitution of these expressions into Eq. (4.8) gives two linearly independent solutions:

$$\Phi^{(\pm)}(\xi) = \sqrt{V(\xi)}\exp\left[\mathrm{i}\,\hat{\omega}\int \frac{d\xi}{V(\xi) \pm 1} + O(\hat{\omega}^{-1})\right], \tag{4.13}$$

and the general solution of Eq. (4.8) is the linear combination of these two particular solutions:

$$\Phi(x) = A_F\,\Phi^{(+)}(x) + A_B\,\Phi^{(-)}(x), \tag{4.14}$$

where A_F and A_B are amplitudes of co-current propagating F-wave and counter-current propagating B-wave, respectively.

In the current with a spatially varying velocity $V(\xi)$, wave propagation and transformation has a regular character, if $V(\xi) \neq 1$ (i.e., if $U(x) \neq c_0$); then Eq. (4.8) does not contain critical points.

In sub-critical currents, when $0 < V_{1,2} < 1$ everywhere, an incident wave arriving from the left (F-wave) or from the right (B-wave) partially transmits through the domain of inhomogeneity and partially transforms into the reflected wave of B- or F-type respectively. Notice that in this case waves of both types have positive energy.

In super-critical currents, when $V_{1,2} > 1$ is everywhere, as was mentioned above, both F-wave and B-wave can propagate only in the direction of the current; however F-wave has positive energy whereas B-wave has negative energy. An incident wave of any type propagating from left to right partially transforms into the wave of another type, so that at the infinity, $\xi \to \infty$, waves of both types appear.

In contrast to these cases, in a trans-critical current there is a critical point where $V(\xi) = 1$. The existence of such a point has only a minor influence on the co-current propagating F-wave, but exerts a crucial action on the B-wave, because its "wave number" $q_0^{(-)} \to \infty$ when $V(\xi) \to 1$. Due to this, an arbitrarily small but finite viscosity leads to dissipation of a B-wave that attains a neighborhood of the critical point. As the result of this the energy flux J does not conserve, in general, when waves pass through this critical point. However, as will be shown below, the energy flux conserves in spatially accelerating trans-critical currents, but does not conserve in decelerating currents.

Indeed, in an accelerating current where $0 < V_1 < 1 < V_2$, an incident wave can arrive only from the left as the F-type wave only. In the sub-critical domain ($\xi < 1$) it transforms into the B-wave that runs backwards, towards $\xi = -\infty$. After passing the critical point, being in the supercritical domain ($\xi > 1$) it transforms into the B-wave that runs forward towards $\xi = +\infty$. As a result, there is no B-wave that attains the critical point; hence, there is no dissipation, and energy flux conserves. On the contrary, in decelerating currents (where $V_1 > 1 > V_2 > 0$) B-waves, no matter incident or "reflected", run to the critical point and dissipate there; therefore the energy flux does not conserve in this case.

A specific situation occurs when the incident B-wave propagates from plus infinity in the sub-critical current towards the critical point and generates an F-wave on the current inhomogeneity. If the current is super-critical on the left of the critical point, then no one wave can penetrate into that domain. Thus, the wave energy of incident B-wave partially converts into a reflected F-wave and partially absorbs in the vicinity of the critical point due to vanishingly small viscosity. We will come to the discussion of these issues in Section 4.5 when we construct exact solutions of scattering problem for Eq. (4.8) where it is possible.

A qualitative analysis presented above demonstrates that the most interesting results can be obtained for the trans-critical currents and that the critical points play a crucial role in such currents. However, in the vicinity of a critical point the velocity of arbitrary type $U(x)$ can be generally approximated by a linear function, $U(x) \sim x$. This makes an additional argument in favor of studying wave scattering in currents with piecewise linear velocity profiles.

4.4 Wave scattering in inhomogeneous currents with a piecewise linear velocity profile

Consider now exact solutions of the problem on surface wave scattering in inhomogeneous currents with piecewise linear velocity profiles described by Eqs. (4.9) and shown in Fig. 4.1. The basic equation (4.8) has constant coefficients out of the interval $\xi_1 < \xi < \xi_2$, where the current velocity linearly varies with ξ (either increasing or decreasing). Therefore out of this interval, solutions to this equation can be presented in terms of exponential functions with the purely imaginary exponents describing sinusoidal travelling waves.

Within the interval $\xi_1 < \xi < \xi_2$ Eq. (4.8) with the help of change of variable $\zeta = \xi^2$ reduces to one of the hypergeometric equations:

$$\zeta(1-\zeta)\frac{d^2\Phi}{d\zeta^2} - (1 \mp \mathrm{i}\,\hat{\omega})\zeta\,\frac{d\Phi}{d\zeta} + \frac{\hat{\omega}^2}{4}\,\Phi = 0, \tag{4.15}$$

where upper sign pertains to the case of accelerating current, and lower sign – to the case of decelerating current.

The matching conditions at $\xi = \xi_1$ and $\xi = \xi_2$ are given by Eqs. (4.10).

4.4.1 Wave transformation in sub-critical currents

Assume first that an incident wave propagates from left to right parallel to the main current which is sub-critical in all domains, $V_1 < V_2 < 1$. As mentioned above, in the left ($\xi < \xi_1$) and right ($\xi > \xi_2$) domains Eq. (4.8) has constant coefficients, and in the intermediate domain ($\xi_1 < \xi < \xi_2$), where $V(\xi) = \xi$, this equation reduces to one of hypergeometric equations (4.15). These equations are regular in the sub-critical case, and their coefficients do not turn to zero. Two linearly independent solutions can be expressed in terms of Gauss hypergeometric function ${}_2F_1(a, b; c; \zeta)$ (see §6.4 in book [95]). Thus, the general solution of Eq. (4.8) for the accelerating current in three different domains can be presented as follows:

$$\Phi(\xi) = A_1 \mathrm{e}^{\mathrm{i}\kappa_1(\xi-\xi_1)} + A_2 \mathrm{e}^{-\mathrm{i}\kappa_2(\xi-\xi_1)}, \qquad \xi \le \xi_1, \tag{4.16}$$

$$\Phi(\xi) = B_1 w_2(\xi^2) + B_2 w_3(\xi^2), \qquad \xi_1 \le \xi \le \xi_2, \tag{4.17}$$

$$\Phi(\xi) = C_1 \mathrm{e}^{\mathrm{i}\kappa_3(\xi-\xi_2)} + C_2 \mathrm{e}^{-\mathrm{i}\kappa_4(\xi-\xi_2)}, \qquad \xi \ge \xi_2, \tag{4.18}$$

where $\kappa_1 = \hat{\omega}/(1+V_1)$, $\kappa_2 = \hat{\omega}/(1-V_1)$, $\kappa_3 = \hat{\omega}/(1+V_2)$, $\kappa_4 = \hat{\omega}/(1-V_2)$, $A_{1,2}$, $B_{1,2}$, $C_{1,2}$ are arbitrary constants, and

$$w_2(\zeta) = \zeta\, {}_2F_1(1-\mathrm{i}\,\hat{\omega}/2,\, 1-\mathrm{i}\,\hat{\omega}/2;\, 2; \zeta), w_3(\zeta) = {}_2F_1(-\mathrm{i}\hat{\omega}/2, -\mathrm{i}\,\hat{\omega}/2; 1-\mathrm{i}\,\hat{\omega}; 1-\zeta). \tag{4.19}$$

The Wronskian of these linearly independent functions is [95]:

$$W = w_2'(\zeta) w_3(\zeta) - w_2(\zeta) w_3'(\zeta) = \frac{\Gamma(1-\mathrm{i}\,\hat{\omega})}{\Gamma^2(1-\mathrm{i}\,\hat{\omega}/2)} (1-\zeta)^{\mathrm{i}\,\hat{\omega}-1}. \tag{4.20}$$

Similarly the general solution of Eq. (4.8) for the decelerating current can be presented. In the domains $\xi < \xi_1$ and $\xi > \xi_2$ solutions are the same as above, whereas in the intermediate domain $\xi_1 < \xi < \xi_2$ the general solution is:

$$\Phi(\xi) = B_1 \tilde{w}_2(\xi^2) + B_2 \tilde{w}_3(\xi^2), \tag{4.21}$$

where the linearly independent functions are

$$\tilde{w}_2(\zeta) = \zeta\, {}_2F_1(1+\mathrm{i}\,\hat{\omega}/2,\, 1+\mathrm{i}\,\hat{\omega}/2;\, 2; \zeta), \quad \tilde{w}_3(\zeta) = {}_2F_1(\mathrm{i}\hat{\omega}/2, \mathrm{i}\,\hat{\omega}/2; 1+\mathrm{i}\,\hat{\omega}; 1-\zeta). \tag{4.22}$$

with the Wronskian:

$$\tilde{W} = \tilde{w}_2'(\zeta) \tilde{w}_3(\zeta) - \tilde{w}_2(\zeta) \tilde{w}_3'(\zeta) = \frac{\Gamma(1+\mathrm{i}\,\hat{\omega})}{\Gamma^2(1+\mathrm{i}\,\hat{\omega}/2)} (1-\zeta)^{-\mathrm{i}\,\hat{\omega}-1}. \tag{4.23}$$

4.4.1.1 Accelerating currents. Transformation of downstream propagating incident wave

Assume that the incident wave has a unit amplitude $A_1 = 1$ and calculate the transformation coefficients, setting $C_2 = 0$ and denoting the amplitudes of the reflected wave by $R \equiv A_2$ and the transmitted wave by $T \equiv C_1$ (R and T play a role of transformation coefficients, as they are usually determined in hydrodynamics – see, e.g. [86, 105] and references therein).

Using the matching conditions at the boundaries of domains (see Appendix 6.2), we find:

$$\begin{aligned}
B_1\, w_2(V_1^2) + B_2\, w_3(V_1^2) =& R + 1, && (4.24)\\
B_1\, w_2'(V_1^2) + B_2\, w_3'(V_1^2) =& \frac{\mathrm{i}\,\hat{\omega}}{2V_1}\left(\frac{1}{1+V_1} - \frac{R}{1-V_1}\right), && (4.25)\\
B_1\, w_2(V_2^2) + B_2\, w_3(V_2^2) =& T, && (4.26)\\
B_1\, w_2'(V_2^2) + B_2\, w_3'(V_2^2) =& \frac{\mathrm{i}\,\hat{\omega}}{2V_2}\frac{T}{1+V_2}. && (4.27)
\end{aligned}$$

From these equations we derive the transformation coefficients:

$$\begin{aligned}
R =& \frac{1}{\Delta}\left\{\frac{\hat{\omega}^2\left[w_2(V_1^2)w_3(V_2^2) - w_2(V_2^2)w_3(V_1^2)\right]}{4V_1V_2(1+V_1)(1+V_2)} - w_2'(V_1^2)w_3'(V_2^2) + \right.\\
& w_2'(V_2^2)w_3'(V_1^2) + \frac{\mathrm{i}\,\hat{\omega}}{2}\left[\frac{w_2(V_1^2)w_3'(V_2^2) - w_2'(V_2^2)w_3(V_1^2)}{V_1(1+V_1)} - \right.\\
& \left.\left.\frac{w_2(V_2^2)w_3'(V_1^2) - w_2'(V_1^2)w_3(V_2^2)}{V_2(1+V_2)}\right]\right\}, && (4.28)\\
T =& -\frac{\mathrm{i}\,\hat{\omega}}{\Delta}\frac{(1-V_2^2)^{\mathrm{i}\,\hat{\omega}-1}}{V_1(1-V_1^2)}\,\frac{\Gamma(1-\mathrm{i}\,\hat{\omega})}{\Gamma^2(1-\mathrm{i}\,\hat{\omega}/2)}, && (4.29)\\
B_1 =& -\frac{\mathrm{i}\,\hat{\omega}}{\Delta}\frac{1}{V_1(1-V_1^2)}\left[\frac{\mathrm{i}\,\hat{\omega}}{2V_2(1+V_2)}\,w_3(V_2^2) - w_3'(V_2^2)\right], && (4.30)\\
B_2 =& \frac{\mathrm{i}\,\hat{\omega}}{\Delta}\frac{1}{V_1(1-V_1^2)}\left[\frac{\mathrm{i}\,\hat{\omega}}{2V_2(1+V_2)}\,w_2(V_2^2) - w_2'(V_2^2)\right], && (4.31)
\end{aligned}$$

where

$$\begin{aligned}
\Delta =& w_2'(V_1^2)w_3'(V_2^2) - w_2'(V_2^2)w_3'(V_1^2) + \frac{\hat{\omega}^2\left[w_2(V_1^2)w_3(V_2^2) - w_2(V_2^2)w_3(V_1^2)\right]}{4V_1V_2(1-V_1)(1+V_2)}\\
& \frac{\mathrm{i}\,\hat{\omega}}{2}\left[\frac{w_2(V_1^2)w_3'(V_2^2) - w_2'(V_2^2)w_3(V_1^2)}{V_1(1-V_1)} + \frac{w_2(V_2^2)w_3'(V_1^2) - w_2'(V_1^2)w_3(V_2^2)}{V_2(1+V_2)}\right]. && (4.32)
\end{aligned}$$

The modules of transformation coefficients $|T|$ and $|R|$, as well as modules of intermediate coefficients of wave excitation in the transient domain, $|B_1|$ and $|B_2|$, are shown in Fig. 4.4 as functions of dimensionless frequency $\hat{\omega}$ for the particular values of $V_1 = 0.1$ and $V_2 = 0.9$. Qualitatively similar graphics were obtained for other values of V_1 and V_2. In the long-wave approximation, when $\hat{\omega} \to 0$, the hypergeometric function ${}_2F_1(a, b; c; d)$ degenerates (see Appendix 6.2), then the

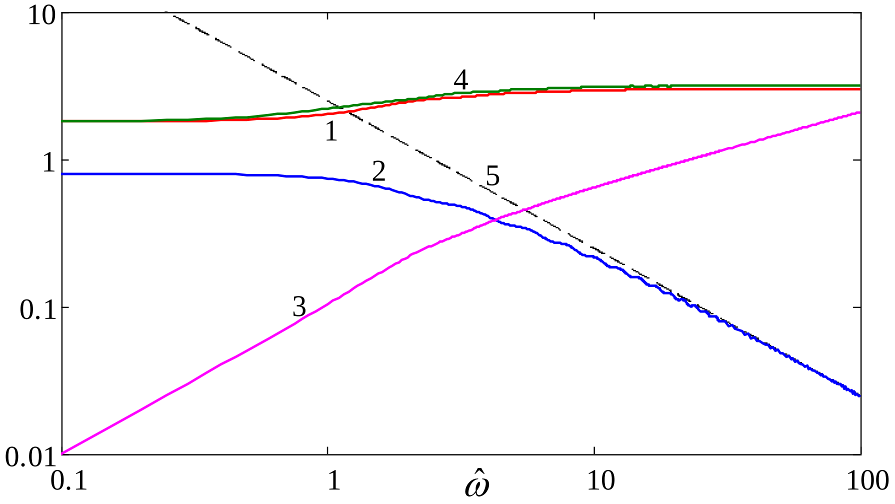

Figure 4.4: Modules of transformation coefficient as functions of dimensionless frequency $\hat{\omega}$ for $V_1 = 0.1$, $V_2 = 0.9$. Line 1 – $|T|$, line 2 – $|R|$, line 3 – $|B_1|$, line 4 – $|B_2|$ Dashed line 5 represents the asymptotic for the reflection coefficient $R \sim \hat{\omega}^{-1}$.

transformation coefficients reduce to

$$R = \frac{1 - V_1/V_2}{1 + V_1/V_2}, \quad T = 1 + R = \frac{2}{1 + V_1/V_2}. \tag{4.33}$$

These values are purely real and agree with the transformation coefficients derived in Ref. [24] for surface waves in a duct with the stepwise change of cross-section and velocity profile, and such an agreement takes place also for other wave-current configurations considered below. Notice only that here the transformation coefficients are presented in terms of velocity potential φ, whereas in Ref. [24] they are presented in terms of free surface elevation η. The relationship between these quantities is given in the end of Appendix 6.2).

In Fig. 4.5a) we present the graphic of $|\Phi(\xi)|$ (see line 1) as per Eqs. (4.16)–(4.18) with $A_1 = 1$ and other determined transformation coefficients $A_2 = R$ as per Eq. (4.28), $C_1 = T$ as per Eq. (4.29), and $C_2 = 0$. Coefficients B_1 and B_2 are given by Eqs. (4.30) and (4.31). The plot was generated for the particular value of $\hat{\omega} = 1$; for other values of $\hat{\omega}$ the graphics are qualitatively similar. The solution obtained should be in consistency with the energy flux conservation [24, 98], which is derived in Appendix 6.2 in terms of the velocity potential φ:

$$V_2\left(1 - |R|^2\right) = V_1|T|^2. \tag{4.34}$$

Substituting here the transformation coefficients R and T from Eqs. (4.28) and (4.29), we confirm that Eq. (4.34) reduces to the identity.

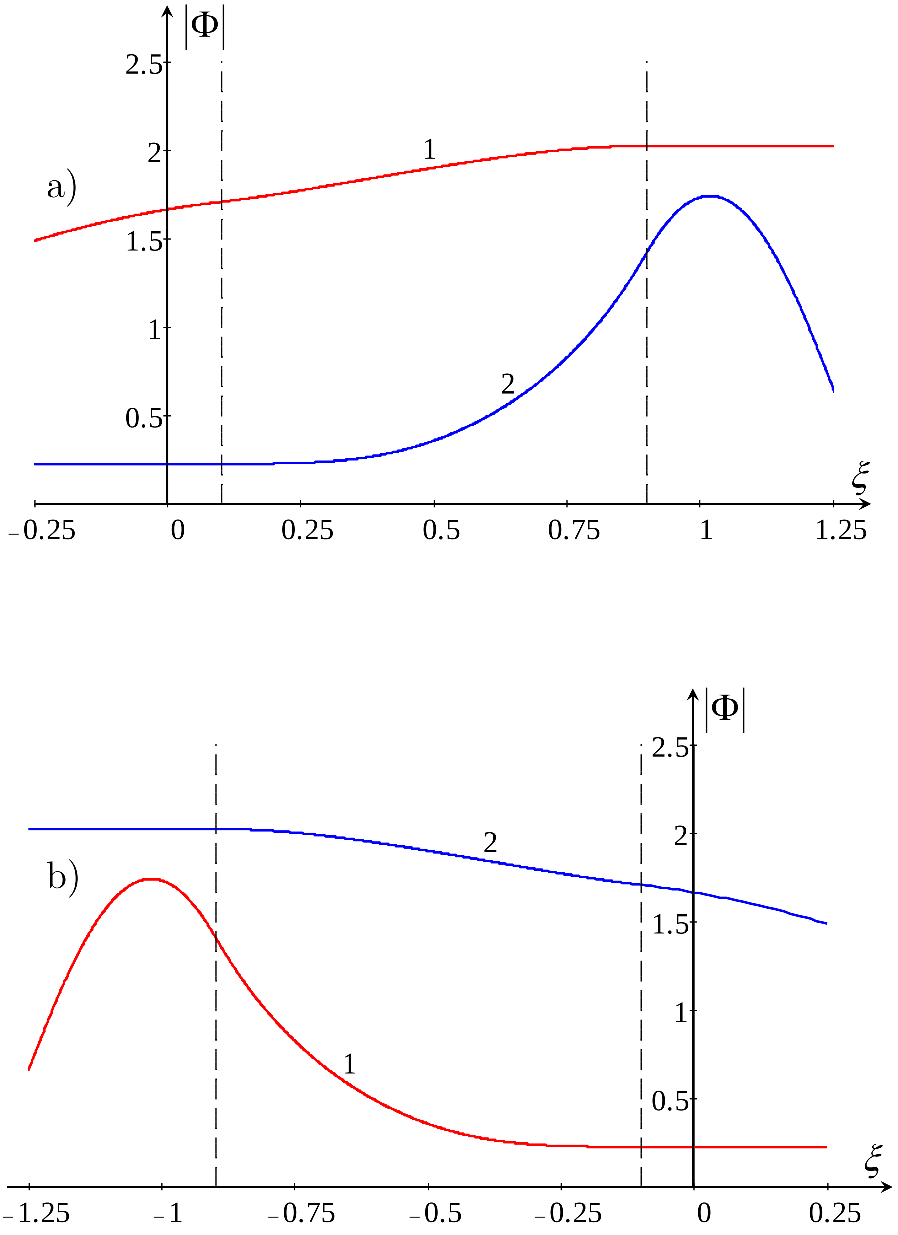

Figure 4.5: Modules of function $\Phi(\xi)$ for wave scattering in accelerating (a) and decelerating (b) sub-critical currents with $V_1 = 0.1$ and $V_2 = 0.9$ in the former case and $V_1 = 0.9$ and $V_2 = 0.1$ in the latter case. Line 1 in each frame pertains to the co-current propagating incident wave, and line 2 – to the counter-current propagating incident wave. Dashed vertical lines show the boundaries of the transient domain ξ_1 and ξ_2 where the speed of the background current linearly changes.

To characterize the rate of energy flux transmission, one can introduce the energy transmission factor

$$K_T = \frac{V_1}{V_2}\,|T|^2 \quad \xrightarrow{\hat{\omega}\to 0} \quad \frac{4V_1/V_2}{(1+V_1/V_2)^2}. \tag{4.35}$$

Then one can see that although the modulus of the transmission coefficient is greater than one (see line 1 in Fig. 4.4) the total energy flux (4.34) through the duct cross-section conserves because the cross-section decreases in the transition from the left to right domain, and the transmitted energy flux is less than the incident one ($K_T < 1$).

4.4.1.2 Accelerating currents. Transformation of upstream propagating incident wave

If the incident wave arrives from plus infinity, then we set in Eqs. (4.16) and (4.18) its amplitude $C_2 = 1$, the amplitude of reflected wave $C_1 = R$, and the amplitude of transmitted wave $A_2 = T$, whereas $A_1 = 0$. Then from the matching conditions we obtain

$$
\begin{aligned}
B_1\, w_2(V_1^2) + B_2\, w_3(V_1^2) =& T, && (4.36)\\
B_1\, w_2'(V_1^2) + B_2\, w_3'(V_1^2) =& -\frac{\mathrm{i}\,\hat{\omega}}{2V_1}\frac{T}{1-V_1}, && (4.37)\\
B_1\, w_2(V_2^2) + B_2\, w_3(V_2^2) =& 1 + R, && (4.38)\\
B_1\, w_2'(V_2^2) + B_2\, w_3'(V_2^2) =& -\frac{\mathrm{i}\,\hat{\omega}}{2V_2}\left(\frac{1}{1-V_2} - \frac{R}{1+V_2}\right). && (4.39)
\end{aligned}
$$

Solution of this set of equations is:

$$
\begin{aligned}
R =& \frac{1}{\Delta}\left\{\frac{\hat{\omega}^2\left[w_2(V_1^2)w_3(V_2^2) - w_2(V_2^2)w_3(V_1^2)\right]}{4V_1V_2(1-V_1)(1-V_2)} - w_2'(V_1^2)w_3'(V_2^2) + \right.\\
& w_2'(V_2^2)w_3'(V_1^2) - \frac{\mathrm{i}\,\hat{\omega}}{2}\left[\frac{w_2(V_1^2)w_3'(V_2^2) - w_2'(V_2^2)w_3(V_1^2)}{V_1(1-V_1)} - \right.\\
& \left.\left.\frac{w_2(V_2^2)w_3'(V_1^2) - w_2'(V_1^2)w_3(V_2^2)}{V_2(1-V_2)}\right]\right\}, && (4.40)\\
T =& -\frac{\mathrm{i}\,\hat{\omega}}{\Delta}\frac{(1-V_1^2)^{\mathrm{i}\,\hat{\omega}-1}}{V_2(1-V_2^2)}\,\frac{\Gamma(1-\mathrm{i}\,\hat{\omega})}{\Gamma^2(1-\mathrm{i}\,\hat{\omega}/2)}, && (4.41)\\
B_1 =& \frac{\mathrm{i}\,\hat{\omega}}{\Delta}\frac{1}{V_2(1-V_2^2)}\left[\frac{\mathrm{i}\,\hat{\omega}}{2V_1(1-V_1)}\,w_3(V_1^2) + w_3'(V_1^2)\right], && (4.42)\\
B_2 =& -\frac{\mathrm{i}\,\hat{\omega}}{\Delta}\frac{1}{V_2(1-V_2^2)}\left[\frac{\mathrm{i}\,\hat{\omega}}{2V_1(1-V_1)}\,w_2(V_1^2) + w_2'(V_1^2)\right], && (4.43)
\end{aligned}
$$

where Δ is the same as in Eq. (4.32).

In the long-wave approximation, $\hat{\omega} \to 0$, we obtain the limiting values of transformation coefficients

$$
R = \frac{1 - V_2/V_1}{1 + V_2/V_1}, \quad T = 1 + R = \frac{2}{1 + V_2/V_1}. \tag{4.44}
$$

These values again are purely real and agree with the transformation coefficients derived in Ref. [24] for surface waves in a duct with the stepwise change of cross-section and velocity profile.

This solution is also in consistency with the energy flux conservation, which now takes the form:

$$V_1\left(1 - |R|^2\right) = V_2|T|^2. \tag{4.45}$$

Substituting here the expressions for the transformation coefficients, (4.40) and (4.41), we confirm that Eq. (4.45) reduces to the identity. The energy transmission factor K_T in the limit $\hat{\omega} \to 0$ remains the same as in Eq. (4.35).

The graphic of $|\Phi(\xi)|$ is presented in Fig. 4.5a) by line 2. The plot was generated on the basis of solution (4.16)–(4.18) with $C_2 = 1$, $A_1 = 0$ and other determined transformation coefficients $C_1 = R$ as per Eq. (4.40) and $A_2 = T$ as per Eq. (4.41). Coefficients B_1 and B_2 are given by Eqs. (4.42) and (4.43).

4.4.1.3 Wave transformation in a decelerating sub-critical current

The decelerating current can occur, for example, in a widening duct. To calculate the transformation coefficients of waves in a decelerating current with a piecewise linear profile it is convenient to choose the origin of coordinate frame such as shown in Fig. 4.1b).

The general solutions of the basic equation (4.8) in the left and right domains beyond the interval $\xi_1 < \xi < \xi_2$ are the same as in Eqs. (4.16) and (4.18), whereas in the transient domain the solution is given by Eq. (4.21).

To calculate the transformation coefficients one can repeat the simple, but tedious calculations similar to the presented above. The result shows that the expressions for the transformation coefficients remain the same as in Eqs. (4.28)–(4.32) for the co-current propagating incident wave and Eqs. (4.40)–(4.43), and (4.32) for the counter-current propagating incident wave, but in both these cases $\hat{\omega}$ should be replaced by $-\hat{\omega}$ and w_i by $\tilde{w}_i$. The energy flux Eq. (4.34) for the co-current propagating incident wave or Eq. (4.45) for the counter-current propagating incident wave conserves in these cases too.

The graphics of $|\Phi(\xi)|$ are presented in Fig. 4.5b) by line 1 for co-current propagating incident wave, and by line 2 for counter-current propagating incident wave.

4.4.2 Wave transformation in a super-critical current

Assume now that the main current is super-critical everywhere, $V_2 > V_1 > 1$. In this case, there are no upstream propagating waves. Indeed in such strong current even waves propagating with the speed $-c_0$ in the frame moving with the water are pulled downstream by the current whose speed $U > c_0$, therefore in the immovable laboratory frame the speed of such "counter-current" propagating waves is $U - c_0 > 0$. Such waves possess a negative energy (see, for instance, [24, 46, 98]). Thus, the problem statement can contain an incident sinusoidal wave propagating only downstream from the $\xi < \xi_1$ domain; the wave can be of either positive energy with $\hat{\omega} = (V_1 + 1)\kappa_1$ or negative energy with $\hat{\omega} = (V_1 - 1)\kappa_2$. After transformation on the inhomogeneous current in the interval $\xi_1 < \xi < \xi_2$ these waves produce two transmitted waves in the right domain, $\xi > \xi_2$ one of positive energy and another of negative energy. Below we consider such transformation in detail.

In the super-critical case the basic equation (4.8) is also regular and its coefficients do not turn to zero. To construct its solutions in the intermediate domain $\xi_1 \le \xi \le \xi_2$ it is convenient to re-write the equation in slightly different form:

$$\eta(1-\eta)\frac{d^2\Psi}{d\eta^2} + [1 - (2 \mp \mathrm{i}\,\hat{\omega})\eta]\frac{d\Psi}{d\eta} \pm \frac{\mathrm{i}\,\hat{\omega}}{2}\left(1 \mp \frac{\mathrm{i}\,\hat{\omega}}{2}\right)\Psi = 0, \tag{4.46}$$

where $\eta = 1/\zeta$, $\Psi(\eta) = \eta^{\pm \mathrm{i}\,\hat{\omega}/2}\Phi$, upper signs pertain to the accelerating current, and lower signs – to the decelerating currents.

Solutions of Eq. (4.8) in the domains where the current speed is constant are

$$\Phi(\xi) = A_1 \mathrm{e}^{\mathrm{i}\kappa_1(\xi - \xi_1)} + A_2 \mathrm{e}^{\mathrm{i}\kappa_2(\xi - \xi_1)}, \qquad \xi \le \xi_1, \tag{4.47}$$

$$\Phi(\xi) = C_1 \mathrm{e}^{\mathrm{i}\kappa_3(\xi - \xi_2)} + C_2 \mathrm{e}^{\mathrm{i}\kappa_4(\xi - \xi_2)}, \qquad \xi \ge \xi_2, \tag{4.48}$$

were $\kappa_1 = \hat{\omega}/(V_1 + 1)$, $\kappa_2 = \hat{\omega}/(V_1 - 1)$, $\kappa_3 = \hat{\omega}/(V_2 + 1)$, $\kappa_4 = \hat{\omega}/(V_2 - 1)$.

In the intermediate domain $\xi_1 \le \xi \le \xi_2$ the solution of hypergeometric Eq. (4.46) in the case of accelerating current is

$$\Phi(\xi) = \xi^{\mathrm{i}\,\hat{\omega}}\left[B_1 \breve{w}_1\left(\xi^{-2}\right) + B_2 \breve{w}_3\left(\xi^{-2}\right)\right], \tag{4.49}$$

where two linearly independent solutions of Eq. (4.46) can be chosen in the form (see §6.4 in the book [95]):

$$\breve{w}_1(\eta) = {}_2F_1(-\mathrm{i}\,\hat{\omega}/2,\, 1-\mathrm{i}\,\hat{\omega}/2;\, 1; \eta), \quad \breve{w}_3(\eta) = {}_2F_1(-\mathrm{i}\hat{\omega}/2, 1-\mathrm{i}\,\hat{\omega}/2; 1-\mathrm{i}\,\hat{\omega}; 1-\eta) \tag{4.50}$$

with the Wronskian

$$\breve{W} = \breve{w}_1'(\eta)\breve{w}_3(\eta) - \breve{w}_1(\eta)\breve{w}_3'(\eta) = \frac{(1-\eta)^{\mathrm{i}\,\hat{\omega}-1}}{\eta}\frac{\Gamma(1-\mathrm{i}\,\hat{\omega})}{\Gamma(-\mathrm{i}\,\hat{\omega}/2)\Gamma(1-\mathrm{i}\,\hat{\omega}/2)}. \tag{4.51}$$

In the case of decelerating current the solution of hypergeometric Eq. (4.46) is

$$\Phi(\xi) = (-\xi)^{-\mathrm{i}\hat\omega}\left[B_1\hat w_1\left(\xi^{-2}\right) + B_2\hat w_3\left(\xi^{-2}\right)\right], \tag{4.52}$$

and linearly independent solutions can be chosen in the form:

$$\hat w_1(\eta) = {}_2F_1(\mathrm{i}\,\hat\omega/2,\, 1+\mathrm{i}\,\hat\omega/2;\, 1; \eta), \quad \hat w_3(\eta) = {}_2F_1(\mathrm{i}\hat\omega/2, 1+\mathrm{i}\,\hat\omega/2; 1+\mathrm{i}\,\hat\omega; 1-\eta) \tag{4.53}$$

with the Wronskian

$$\hat W = \hat w_1'(\eta)\hat w_3(\eta) - \hat w_1(\eta)\hat w_3'(\eta) = \frac{(1-\eta)^{-\mathrm{i}\,\hat\omega-1}}{\eta}\frac{\Gamma(1+\mathrm{i}\,\hat\omega)}{\Gamma(\mathrm{i}\,\hat\omega/2)\Gamma(1+\mathrm{i}\,\hat\omega/2)}. \tag{4.54}$$

4.4.2.1 Transformation of a positive-energy wave in an accelerating current

Consider first transformation of a positive energy incident wave (see line 3 in Fig. 4.3) with the unit amplitude ($A_1 = 1$, $A_2 = 0$). Matching the solutions in different current domains and using the chain rule $d/d\xi = -2\xi^{-3}d/d\eta$, we obtain at $\xi = \xi_1$:

$$B_1\,\breve w_1(V_1^{-2}) + B_2\,\breve w_3(V_1^{-2}) = V_1^{-\mathrm{i}\,\hat\omega}, \tag{4.55}$$

$$B_1\,\breve w_1'(V_1^{-2}) + B_2\,\breve w_3'(V_1^{-2}) = \frac{\mathrm{i}\,\hat\omega}{2}\frac{V_1^{2-\mathrm{i}\,\hat\omega}}{V_1+1}, \tag{4.56}$$

where prime stands for a derivative of a corresponding function with respect to its entire argument.

Similarly from the matching conditions at $\xi = \xi_2$ we obtain:

$$C_1 + C_2 = V_2^{\mathrm{i}\,\hat\omega}\left[B_1\,\breve w_1(V_2^{-2}) + B_2\,\breve w_3(V_2^{-2})\right], \tag{4.57}$$

$$(V_2-1)C_1-(V_2+1)C_2 = -\frac{2\mathrm{i}}{\hat\omega}\,V_2^{\mathrm{i}\,\hat\omega-2}(V_2^2-1)\left[B_1\,\breve w_1'(V_2^{-2}) + B_2\,\breve w_3'(V_2^{-2})\right]. \tag{4.58}$$

From Eqs. (4.55) and (4.56) we find

$$B_1 = -\frac{\Gamma(-\mathrm{i}\,\hat\omega/2)\,\Gamma(1-\mathrm{i}\,\hat\omega/2)}{\Gamma(1-\mathrm{i}\,\hat\omega)}\,V_1^{\mathrm{i}\,\hat\omega-2}\left(V_1^2-1\right)^{1-\mathrm{i}\,\hat\omega}\left[\frac{\breve w_3'(V_1^{-2})}{V_1^2} - \frac{\mathrm{i}\,\hat\omega\,\breve w_3(V_1^{-2})}{2(V_1+1)}\right], \tag{4.59}$$

$$B_2 = \frac{\Gamma(-\mathrm{i}\,\hat\omega/2)\,\Gamma(1-\mathrm{i}\,\hat\omega/2)}{\Gamma(1-\mathrm{i}\,\hat\omega)}\,V_1^{\mathrm{i}\,\hat\omega-2}\left(V_1^2-1\right)^{1-\mathrm{i}\,\hat\omega}\left[\frac{\breve w_1'(V_1^{-2})}{V_1^2} - \frac{\mathrm{i}\,\hat\omega\,\breve w_1(V_1^{-2})}{2(V_1+1)}\right]. \tag{4.60}$$

Substituting these in Eqs. (4.57) and (4.58), we find the transmission coefficients for the positive energy mode $T_p \equiv C_1$ and negative energy mode $T_n \equiv C_2$:

$$
\begin{aligned}
T_p = -\frac{\Gamma^2(-\mathrm{i}\,\hat{\omega}/2)}{2\Gamma(1-\mathrm{i}\,\hat{\omega})}\, V_1^{\mathrm{i}\,\hat{\omega}-2} V_2^{\mathrm{i}\,\hat{\omega}-1} \left(V_1^2-1\right)^{1-\mathrm{i}\,\hat{\omega}} \left(V_2^2-1\right) \times \\
\left\{ \frac{\breve{w}_1'(V_1^{-2})\breve{w}_3'(V_2^{-2}) - \breve{w}_1'(V_2^{-2})\breve{w}_3'(V_1^{-2})}{V_1^2 V_2^2} + \frac{\hat{\omega}^2}{4}\, \frac{\breve{w}_1(V_1^{-2})\breve{w}_3(V_2^{-2}) - \breve{w}_1(V_2^{-2})\breve{w}_3(V_1^{-2})}{(V_1+1)(V_2-1)} + \right. \\
\left. \frac{\mathrm{i}\,\hat{\omega}}{2} \left[\frac{\breve{w}_1'(V_1^{-2})\breve{w}_3(V_2^{-2}) - \breve{w}_1(V_2^{-2})\breve{w}_3'(V_1^{-2})}{V_1^2(V_2-1)} - \frac{\breve{w}_1(V_1^{-2})\breve{w}_3'(V_2^{-2}) - \breve{w}_1'(V_2^{-2})\breve{w}_3(V_1^{-2})}{V_2^2(V_1+1)} \right] \right\},
\end{aligned}
\tag{4.61}
$$

$$
\begin{aligned}
T_n = \frac{\Gamma^2(-\mathrm{i}\,\hat{\omega}/2)}{2\Gamma(1-\mathrm{i}\,\hat{\omega})}\, V_1^{\mathrm{i}\,\hat{\omega}-2} V_2^{\mathrm{i}\,\hat{\omega}-1} \left(V_1^2-1\right)^{1-\mathrm{i}\,\hat{\omega}} \left(V_2^2-1\right) \times \\
\left\{ \frac{\breve{w}_1'(V_1^{-2})\breve{w}_3'(V_2^{-2}) - \breve{w}_1'(V_2^{-2})\breve{w}_3'(V_1^{-2})}{V_1^2 V_2^2} - \frac{\hat{\omega}^2}{4}\, \frac{\breve{w}_1(V_1^{-2})\breve{w}_3(V_2^{-2}) - \breve{w}_1(V_2^{-2})\breve{w}_3(V_1^{-2})}{(V_1+1)(V_2+1)} - \right. \\
\left. \frac{\mathrm{i}\,\hat{\omega}}{2} \left[\frac{\breve{w}_1'(V_1^{-2})\breve{w}_3(V_2^{-2}) - \breve{w}_1(V_2^{-2})\breve{w}_3'(V_1^{-2})}{V_1^2(V_2+1)} + \frac{\breve{w}_1(V_1^{-2})\breve{w}_3'(V_2^{-2}) - \breve{w}_1'(V_2^{-2})\breve{w}_3(V_1^{-2})}{V_2^2(V_1+1)} \right] \right\}.
\end{aligned}
\tag{4.62}
$$

The modules of transformation coefficients $|T_p|$ and $|T_n|$ together with the intermediate coefficients of wave excitation in the transient zone $|B_1|$ and $|B_2|$ are shown below in Fig. 4.6a) as functions of dimensionless frequency $\hat{\omega}$ for the particular values of $V_1 = 1.1$ and $V_2 = 1.9$. Qualitatively similar graphics were obtained for other values of V_1 and V_2. In Fig. 4.7a) we present graphics of $|\Phi(\xi)|$ as per Eqs. (4.47)–(4.49) for $A_1 = 1$, $A_2 = 0$, $C_1 = T_p$ as per Eq. (4.61), and $C_2 = T_n$ as per Eq. (4.62). Coefficients B_1 and B_2 are given by Eqs. (4.59) and (4.60). The plot was generated for two particular values of frequency, $\hat{\omega} = 1$ (line 1), and $\hat{\omega} = 100$ (line 2). The transmission coefficients are in consistency with the energy flux conservation law which has the following form:

$$
J = \frac{2\hat{\omega}}{V_1} = \frac{2\hat{\omega}}{V_2}\left(|T_p|^2 - |T_n|^2\right) \quad \text{or} \quad |T_p|^2 - |T_n|^2 = \frac{V_2}{V_1}. \tag{4.63}
$$

If we introduce two energy transmission factors, for positive- and negative-energy waves,

$$
K_{Tp} = \frac{V_1}{V_2}\,|T_p|^2 \quad \text{and} \quad K_{Tn} = \frac{V_1}{V_2}\,|T_n|^2, \tag{4.64}
$$

then we can see that both waves grow in such a manner that $K_{Tp} - K_{Tn} = 1$. This means that the positive-energy wave not only dominates in the right domain (cf. lines 1 and 2 in Fig. 4.6a), but it also carries a greater energy flux than the incident one. Moreover, with a proper choice of V_1 and V_2 even the energy flux of negative-energy wave can become greater by modulus than that of incident wave, $K_{Tn} > 1$. Then we have $K_{Tp} > K_{Tn} > 1$. Figure 4.8 illustrates the

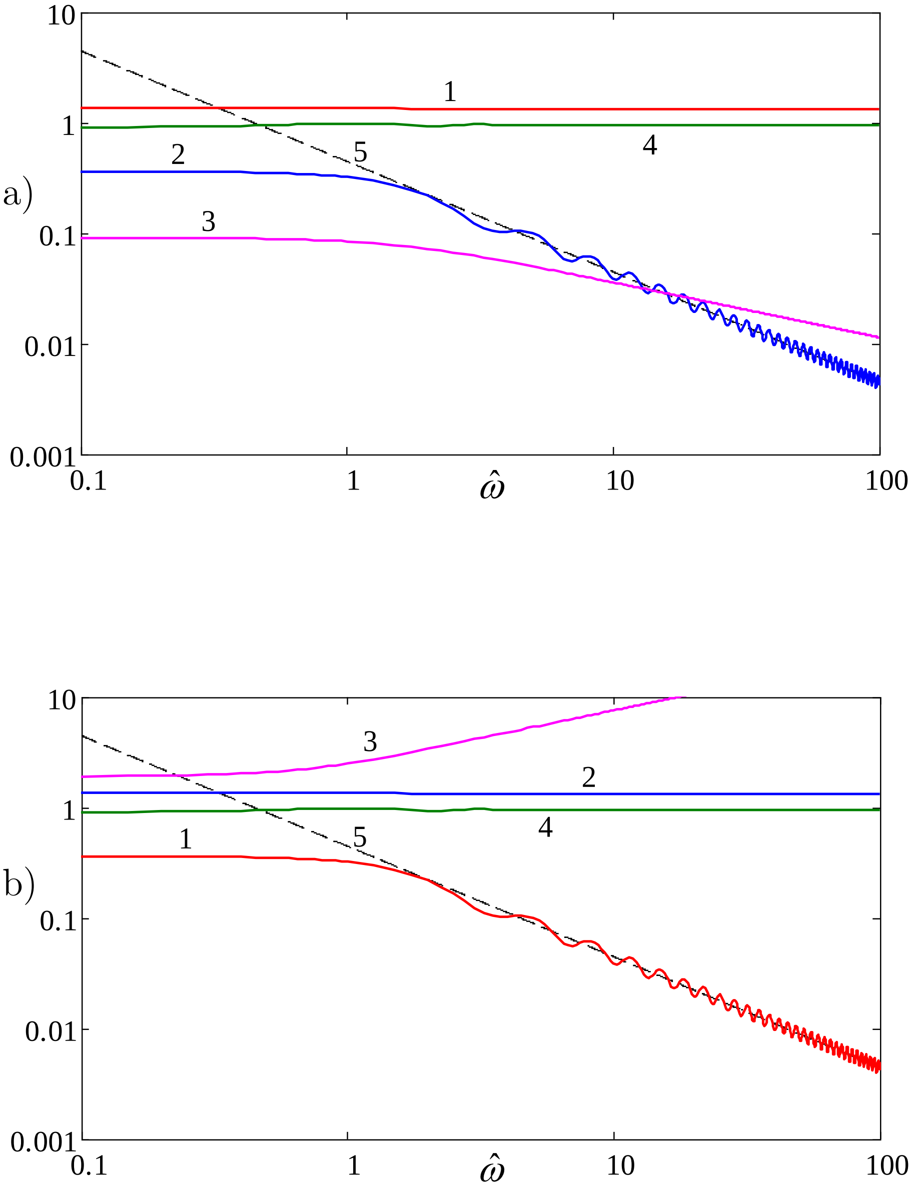

Figure 4.6: Modules of transformation coefficient as functions of dimensionless frequency $\hat{\omega}$ when a positive energy wave scatters (panel a) and negative energy wave scatters (panel b) in the current with $V_1 = 1.1$, $V_2 = 1.9$. Line 1 – $|T_p|$, line 2 – $|T_n|$, line 3 – $|B_1|$, line 4 – $|B_2|$. Dashed lines 5 represent the asymptotics for $|T_n| \sim \hat{\omega}^{-1}$ in panel a) and for $|T_p| \sim \hat{\omega}^{-1}$ in panel b).

dependencies of energy transmission factors on the frequency for relatively small increase of current speed ($V_1 = 1.1$, $V_2 = 1.9$) and big increase of current speed ($V_1 = 1.1$, $V_2 = 8.0$). In the latter case both K_{Tp} and K_{Tn} are greater than 1 in a certain range of frequencies $\hat{\omega} < \hat{\omega}_c$. In the long-wave approximation, $\hat{\omega} \to 0$ (see Appendix 6.2) we obtain (cf. [24]):

$$T_p = \frac{1 + V_1/V_2}{2V_1/V_2},\ T_n = -\frac{1 - V_1/V_2}{2V_1/V_2},\ K_{Tp} = \frac{(1 + V_1/V_2)^2}{4V_1/V_2},\ K_{Tn} = \frac{(1 - V_1/V_2)^2}{4V_1/V_2}. \tag{4.65}$$

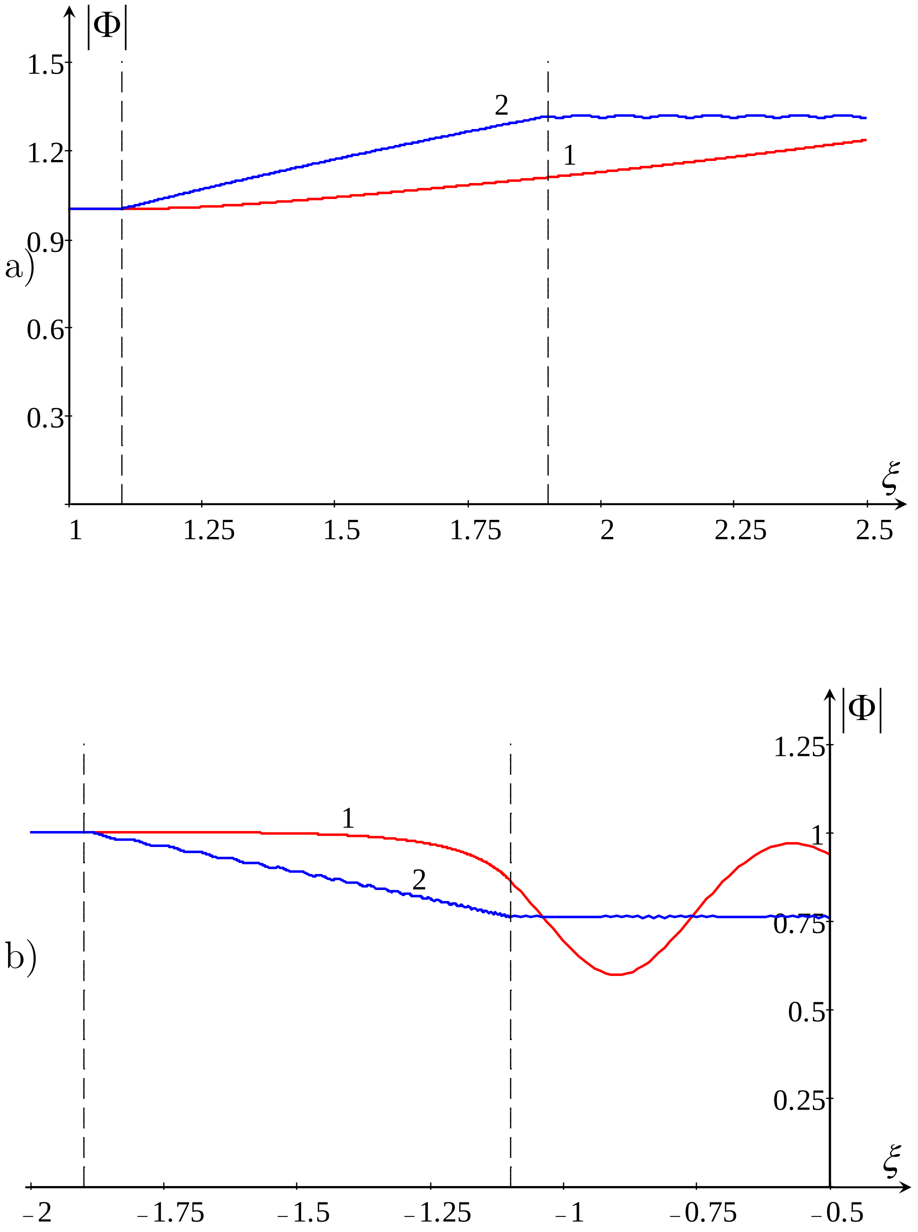

Figure 4.7: Module of function $\Phi(\xi)$ for the scattering of positive- and negative-energy waves in accelerating with $V_1 = 1.1$ and $V_2 = 1.9$ (frame a) and decelerating with $V_1 = 1.9$ and $V_2 = 1.1$ (frame b) super-critical currents for two particular values of frequency, $\hat{\omega} = 1$ (line 1), and $\hat{\omega} = 100$ (line 2).

4.4.2.2 Transformation of negative-energy wave in an accelerating current

Consider now transformation of a negative energy incident wave (see line 4 in Fig. 4.3) with unit amplitude ($A_1 = 0$, $A_2 = 1$). From the matching conditions

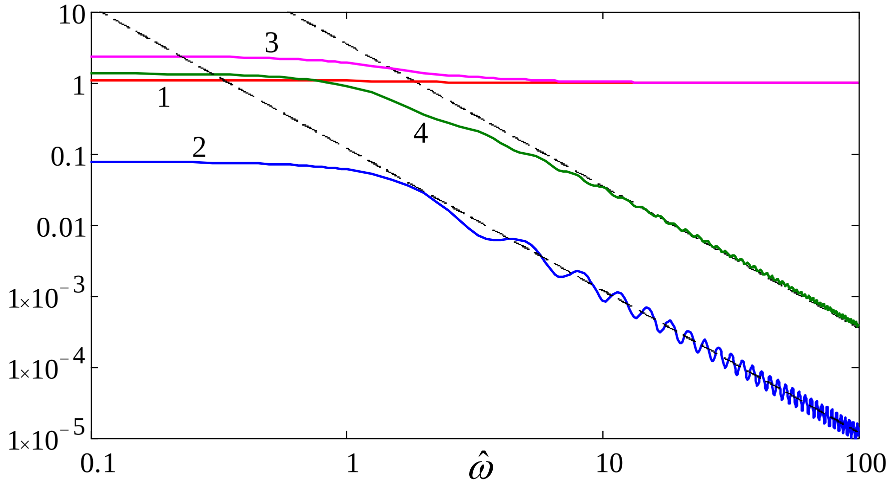

Figure 4.8: The dependencies of energy transmission factors K_{Tp} and K_{Tn} on the frequency for a relatively small increase of current speed ($V_1 = 1.1$, $V_2 = 1.9$), lines 1 and 2 respectively, and a large increase of current speed ($V_1 = 1.1$, $V_2 = 8.0$), lines 3 and 4 respectively. Inclined dashed lines show the asymptotic dependencies $K_{Tn} \sim \hat{\omega}^{-2}$.

at $\xi = \xi_1$ we obtain:

$$B_1\,\breve{w}_1(V_1^{-2}) + B_2\,\breve{w}_3(V_1^{-2}) = V_1^{-\mathrm{i}\,\hat{\omega}}, \tag{4.66}$$

$$B_1\,\breve{w}_1'(V_1^{-2}) + B_2\,\breve{w}_3'(V_1^{-2}) = -\frac{\mathrm{i}\,\hat{\omega}}{2}\frac{V_1^{2-\mathrm{i}\,\hat{\omega}}}{V_1 - 1}. \tag{4.67}$$

The matching conditions at $\xi = \xi_2$ remain the same as in Eqs. (4.57) and (4.58).

From Eqs. (4.66) and (4.67) we find

$$B_1 = -\frac{\Gamma(-\mathrm{i}\,\hat{\omega}/2)\,\Gamma(1-\mathrm{i}\,\hat{\omega}/2)}{\Gamma(1-\mathrm{i}\,\hat{\omega})}\,V_1^{\mathrm{i}\,\hat{\omega}-2}\left(V_1^2-1\right)^{1-\mathrm{i}\,\hat{\omega}}\left[\frac{\breve{w}_3'(V_1^{-2})}{V_1^2} + \frac{\mathrm{i}\,\hat{\omega}\,\breve{w}_3(V_1^{-2})}{2(V_1-1)}\right], \tag{4.68}$$

$$B_2 = \frac{\Gamma(-\mathrm{i}\,\hat{\omega}/2)\,\Gamma(1-\mathrm{i}\,\hat{\omega}/2)}{\Gamma(1-\mathrm{i}\,\hat{\omega})}\,V_1^{\mathrm{i}\,\hat{\omega}-2}\left(V_1^2-1\right)^{1-\mathrm{i}\,\hat{\omega}}\left[\frac{\breve{w}_1'(V_1^{-2})}{V_1^2} + \frac{\mathrm{i}\,\hat{\omega}\,\breve{w}_1(V_1^{-2})}{2(V_1-1)}\right]. \tag{4.69}$$

Substituting these in Eqs. (4.57) and (4.58), we find the transmission coefficients for the positive energy mode $T_p \equiv C_1$ and negative energy mode $T_n \equiv C_2$:

$$\begin{aligned} T_p = -\frac{\Gamma^2(-\mathrm{i}\,\hat{\omega}/2)}{2\Gamma(1-\mathrm{i}\,\hat{\omega})}\,V_1^{\mathrm{i}\,\hat{\omega}-2}V_2^{\mathrm{i}\,\hat{\omega}-1}\left(V_1^2-1\right)^{1-\mathrm{i}\,\hat{\omega}}\left(V_2^2-1\right)\times \\ \left\{\frac{\breve{w}_1'(V_1^{-2})\breve{w}_3'(V_2^{-2}) - \breve{w}_1'(V_2^{-2})\breve{w}_3'(V_1^{-2})}{V_1^2V_2^2} - \frac{\hat{\omega}^2}{4}\,\frac{\breve{w}_1(V_1^{-2})\breve{w}_3(V_2^{-2}) - \breve{w}_1(V_2^{-2})\breve{w}_3(V_1^{-2})}{(V_1-1)(V_2-1)} + \right. \\ \left.\frac{\mathrm{i}\,\hat{\omega}}{2}\left[\frac{\breve{w}_1'(V_1^{-2})\breve{w}_3(V_2^{-2}) - \breve{w}_1(V_2^{-2})\breve{w}_3'(V_1^{-2})}{V_1^2(V_2-1)} + \frac{\breve{w}_1(V_1^{-2})\breve{w}_3'(V_2^{-2}) - \breve{w}_1'(V_2^{-2})\breve{w}_3(V_1^{-2})}{V_2^2(V_1-1)}\right]\right\}, \end{aligned} \tag{4.70}$$

$$T_n = \frac{\Gamma^2(-\mathrm{i}\,\hat{\omega}/2)}{2\Gamma(1-\mathrm{i}\,\hat{\omega})}\, V_1^{\mathrm{i}\,\hat{\omega}-2} V_2^{\mathrm{i}\,\hat{\omega}-1}\left(V_1^2-1\right)^{1-\mathrm{i}\,\hat{\omega}}\left(V_2^2-1\right)\times$$
$$\left\{\frac{\breve{w}_1'(V_1^{-2})\breve{w}_3'(V_2^{-2})-\breve{w}_1'(V_2^{-2})\breve{w}_3'(V_1^{-2})}{V_1^2V_2^2}+\frac{\hat{\omega}^2}{4}\,\frac{\breve{w}_1(V_1^{-2})\breve{w}_3(V_2^{-2})-\breve{w}_1(V_2^{-2})\breve{w}_3(V_1^{-2})}{(V_1-1)(V_2+1)}-\right.$$
$$\left.\frac{\mathrm{i}\,\hat{\omega}}{2}\left[\frac{\breve{w}_1'(V_1^{-2})\breve{w}_3(V_2^{-2})-\breve{w}_1(V_2^{-2})\breve{w}_3'(V_1^{-2})}{V_1^2(V_2+1)}-\frac{\breve{w}_1(V_1^{-2})\breve{w}_3'(V_2^{-2})-\breve{w}_1'(V_2^{-2})\breve{w}_3(V_1^{-2})}{V_2^2(V_1-1)}\right]\right\}. \tag{4.71}$$

The modules of transformation coefficients $|T_p|$ and $|T_n|$ together with the intermediate coefficients of wave excitation in the transient zone $|B_1|$ and $|B_2|$ are shown in Fig. 4.6b) as functions of dimensionless frequency $\hat{\omega}$ for the particular values of $V_1 = 1.1$ and $V_2 = 1.9$. Qualitatively similar graphics were obtained for other values of V_1 and V_2. The graphic of $|\Phi(\xi)|$ is the same as the graphic shown in Fig. 4.7a) for the case of scattering of positive-energy incident wave.

The transmission coefficients are again in consistency with the energy flux conservation law which now has the following form:

$$J = -\frac{2\hat{\omega}}{V_1} = -\frac{2\hat{\omega}}{V_2}\left(|T_n|^2 - |T_p|^2\right) \quad \text{or} \quad |T_n|^2 - |T_p|^2 = \frac{V_2}{V_1}. \tag{4.72}$$

As follows from this equation, the energy flux J is negative everywhere, and the negative energy wave dominates in the right domain (cf. lines 1 and 2 in Fig. 4.6b). Both transmitted waves grow in a such manner that the energy transmission factors (see Eq. (4.64)) obey the equality $K_{Tn} - K_{Tp} = 1$. Thus, the negative-energy wave not only dominates in the right domain, but also carries a greater energy flux than the incident wave. At a certain relationship between V_1 and V_2 the energy fluxes of positive- and negative-energy waves can be greater on absolute value than that of incident wave, then we have $K_{Tn} > K_{Tp} > 1$.

In the long-wave approximation, $\hat{\omega} \to 0$, we obtain (see Appendix 6.2):

$$T_p = -\frac{1 - V_1/V_2}{2V_1/V_2},\; T_n = \frac{1 + V_1/V_2}{2V_1/V_2},\; K_{Tp} = \frac{(1 - V_1/V_2)^2}{4V_1/V_2},\; K_{Tn} = \frac{(1 + V_1/V_2)^2}{4V_1/V_2}, \tag{4.73}$$

i.e., in comparison with Eqs. (4.65), the energy transmission factors are interchanged. The values of transmission coefficients are purely real, but now $T_p < 0$ and $T_n > 0$; they are in agreement with results derived in Ref. [24].

4.4.2.3 Wave transformation in a decelerating super-critical current

In the case of decelerating super-critical current ($V_1 > V_2 > 1$) the configuration of the incident wave and current is the same as above in this subsection. Again there is no reflected wave in the left domain $\xi < \xi_1$ and there are two transmitted waves in the right domain $\xi > \xi_2$.

The main equation describing wave propagation is the same as Eq. (4.46) with only formal replacement of $\hat{\omega}$ by $-\hat{\omega}$. The general solutions of the basic equation (4.8) in the left and right domains beyond the interval $\xi_1 < \xi < \xi_2$ are the same as in Eqs. (4.47) and (4.48), whereas in the transient domain the solution is given by Eq. (4.52).

To calculate the transformation coefficients one can repeat the simple, but tedious calculations similar to those presented above. The result shows that the expressions for the transformation coefficients remain the same as in Eqs. (4.61) and (4.62) for the incident wave of positive energy and Eqs. (4.70) and (4.71) for the incident wave of negative energy, but in both these cases $\hat{\omega}$ should be replaced by $-\hat{\omega}$ and $\breve{w}_i$ by $\hat{w}_i$. The corresponding energy fluxes for the incident waves of positive and negative energies conserve, and Eqs. (4.63) and Eq. (4.72) remain the same in these cases too.

The graphics of $|\Phi(\xi)|$ for the scattering of positive- and negative-energy waves are also the same in the decelerating currents. They are shown in Fig. 4.7b) in the subsubsection 4.4.2.1 for two particular values of frequency, $\hat{\omega} = 1$ (line 1), and $\hat{\omega} = 100$ (line 2).

4.4.3 Wave transformation in trans-critical accelerating currents $0 < V_1 < 1 < V_2$

The specific feature of a trans-critical current is the transition of the background current speed $U(x)$ through the critical wave speed c_0. In this case the basic equation (4.8) contains a singular point where $V = 1$, therefore the behavior of solutions in the vicinity of this point should be thoroughly investigated.

The general solution of Eq. (4.8) in different intervals of ξ-axis can be presented in the form:

$$\Phi(\xi) = A_1 e^{\mathrm{i}\,\kappa_1(\xi-\xi_1)} + A_2 e^{-\mathrm{i}\,\kappa_2(\xi-\xi_1)}, \qquad \xi < \xi_1, \tag{4.74}$$

$$\Phi(\xi) = B_1 w_2(\xi^2) + B_2 w_3(\xi^2), \qquad \xi_1 < \xi < 1, \tag{4.75}$$

$$\Phi(\xi) = \xi^{\mathrm{i}\,\hat{\omega}} \left[\breve{B}_1\, \breve{w}_1(\xi^{-2}) + \breve{B}_2\, \breve{w}_3(\xi^{-2})\right], \quad 1 < \xi < \xi_2, \tag{4.76}$$

$$\Phi(\xi) = C_1\, e^{\mathrm{i}\,\kappa_3(\xi-\xi_2)} + C_2\, e^{-\mathrm{i}\,\kappa_4(\xi-\xi_2)}, \qquad \xi > \xi_2, \tag{4.77}$$

where $\kappa_1 = \hat{\omega}/(1 + V_1)$, $\kappa_2 = \hat{\omega}/(1 - V_1)$, $\kappa_3 = \hat{\omega}/(V_2 + 1)$, and $\kappa_4 = \hat{\omega}/(V_2 - 1)$.

To pass through the singular point where $V(\xi) = 1$, let us consider asymptotic behavior of solution $\Phi(\xi)$ in the vicinity of the point $\xi = 1$. To this end we use the formula valid for $|\arg(1-x)| < \pi$ (see [52], formula 9.131.2.):

$$
{}_2F_1(a,b;c;x) = \frac{\Gamma(c)\,\Gamma(c-a-b)}{\Gamma(c-a)\,\Gamma(c-b)}\,{}_2F_1(a,b;a+b-c+1;1-x)+ \tag{4.78}
$$

$$
\frac{\Gamma(c)\,\Gamma(a+b-c)}{\Gamma(a)\,\Gamma(b)}\,(1-x)^{c-a-b}\,{}_2F_1(c-a,c-b;c-a-b+1;1-x). \tag{4.79}
$$

With the help of this formula let us present the asymptotic expansion of functions (4.75) and (4.76), keeping only the leading terms:

$$
\Phi(\xi) = B_2 + \frac{\Gamma(\mathrm{i}\,\hat{\omega})\,B_1}{\Gamma^2(1+\mathrm{i}\,\hat{\omega}/2)} + \frac{\Gamma(-\mathrm{i}\,\hat{\omega})\,B_1}{\Gamma^2(1-\mathrm{i}\,\hat{\omega}/2)}\,(1-\xi^2)^{\mathrm{i}\,\hat{\omega}} + O(1-\xi^2), \quad \xi^2 \to 1_{-0}, \tag{4.80}
$$

$$
\Phi(\xi) = \breve{B}_2 + \frac{\Gamma(1+\mathrm{i}\,\hat{\omega})\,\breve{B}_1}{2\Gamma^2(1+\mathrm{i}\,\hat{\omega}/2)} + \frac{\Gamma(1-\mathrm{i}\,\hat{\omega})\,\breve{B}_1}{2\Gamma^2(1-\mathrm{i}\,\hat{\omega}/2)}\,(\xi^2-1)^{\mathrm{i}\,\hat{\omega}} + O(\xi^2-1), \quad \xi^2 \to 1_{+0}. \tag{4.81}
$$

As one can see from these formulae, for real $\hat{\omega}$ solutions contain fast oscillating functions from both sides of a singular point $\xi^2 = 1$, which correspond to B-waves, propagating against the current; these functions, however, remain finite. To match the solutions across the singular point let us take into consideration a small viscosity in Eq. (4.1):

$$
\frac{\partial u}{\partial t} + \frac{\partial (Uu)}{\partial x} = -g\frac{\partial \eta}{\partial x} + \nu\frac{\partial^2 u}{\partial x^2}, \tag{4.82}
$$

where ν is the coefficient of kinematic viscosity.

Due to this correction to Eq. (4.1) we obtain the modified Eq. (4.8) for $\Phi(\xi)$:

$$
\nu V^2\frac{d^3\Phi}{d\xi^3} + V\left(1 - V^2 - \mathrm{i}\,\nu\hat{\omega}\right)\frac{d^2\Phi}{d\xi^2} - \left[\left(1+V^2\right)V' - 2\,\mathrm{i}\,\hat{\omega}V^2\right]\frac{d\Phi}{d\xi} + V\hat{\omega}^2\Phi = 0. \tag{4.83}
$$

Introducing a new variable $\zeta = \xi^2$ and bearing in mind that $V(\xi) = \xi$ for the accelerating current, we re-write Eq. (4.83):

$$
2\nu\zeta^2\frac{d^3\Phi}{d\zeta^3} + \zeta\left[1 - \zeta + (3-\mathrm{i}\,\hat{\omega})\,\nu\right]\frac{d^2\Phi}{d\zeta^2} - \left[\frac{\mathrm{i}\,\nu\hat{\omega}}{2} + (1-\mathrm{i}\,\hat{\omega})\,\zeta\right]\frac{d\Phi}{d\zeta} + \frac{\hat{\omega}^2}{4}\Phi = 0. \tag{4.84}
$$

From this equation one can see that in the vicinity of the critical point, where $|\zeta - 1| \sim \varepsilon \ll 1$, the viscosity plays an important role, if $\nu \sim \varepsilon^2$. Setting $\nu = \varepsilon^2/2$

and $\zeta = 1 + \varepsilon z$, we obtain an equation containing the terms up to ε^2:

$$(1+\varepsilon z)^2 \frac{d^3\Phi}{dz^3} - (1+\varepsilon z)\left(z - \frac{3 - \mathrm{i}\,\hat{\omega}}{2}\varepsilon\right)\frac{d^2\Phi}{dz^2} - \\ \left[(1-\mathrm{i}\,\hat{\omega})(1+\varepsilon z) + \frac{\mathrm{i}\,\hat{\omega}}{4}\varepsilon^2\right]\frac{d\Phi}{dz} + \frac{\varepsilon\hat{\omega}^2}{4}\Phi = 0. \tag{4.85}$$

Looking for a solution to this equation in the form of asymptotic series with respect to parameter ε, $\Phi(z) = \Phi_0(z) + \varepsilon\Phi_1(z) + \ldots$, we obtain in the leading order

$$\frac{d}{dz}\left(\frac{d^2\Phi_0}{dz^2} - z\frac{d\Phi_0}{dz} + \mathrm{i}\,\hat{\omega}\Phi_0\right) = 0. \tag{4.86}$$

Integration of this equation gives the second order equation

$$\frac{d^2\Phi_0}{dz^2} - z\frac{d\Phi_0}{dz} + \mathrm{i}\,\hat{\omega}\,(\Phi_0 - D_0) = 0, \tag{4.87}$$

where D_0 is a constant of integration.

This equation reduces to the equation of a parabolic cylinder with the help of ansatz $\Phi_0(z) = e^{z^2/4}G(z) + D_0$:

$$\frac{d^2G}{dz^2} + \left(\mathrm{i}\,\hat{\omega} + \frac{1}{2} - \frac{z^2}{4}\right)G = 0. \tag{4.88}$$

Two linearly independent solutions of this equation can be constructed from the following four functions $\mathcal{D}_{\mathrm{i}\,\hat{\omega}}(\pm z)$ and $\mathcal{D}_{-\mathrm{i}\,\hat{\omega}-1}(\pm \mathrm{i}z)$ (see [52], 9.255.1). Thus, in the vicinity of the critical point $\xi = 1$ the solution can be presented in the form

$$\Phi_0(z) = D_0 + e^{z^2/4}\left[D_1\mathcal{D}_{\mathrm{i}\,\hat{\omega}}(z) + D_2\mathcal{D}_{\mathrm{i}\,\hat{\omega}}(-z)\right], \tag{4.89}$$

where D_0, D_1, and D_2 are arbitrary constants.

This solution should be matched with the asymptotic expansions (4.80) and (4.81) using the following asymptotics of functions of the parabolic cylinder when $|s| \gg 1$ (see [52], 9.246):

$$\mathcal{D}_p(s) \sim s^p\, e^{-s^2/4}{}_2F_0\left(-\frac{p}{2}, \frac{1-p}{2}; -\frac{2}{s^2}\right), \quad |\arg s| < \frac{3\pi}{4}, \tag{4.90}$$

$$\mathcal{D}_p(s) \sim s^p e^{-s^2/4}{}_2F_0\left(-\frac{p}{2}, \frac{1-p}{2}; -\frac{2}{s^2}\right) - \frac{\sqrt{2\pi}e^{\mathrm{i}\pi p}}{\Gamma(-p)}s^{-p-1}e^{s^2/4}{}_2F_0\left(\frac{p}{2}, \frac{1+p}{2}; \frac{2}{s^2}\right), \tag{4.91}$$

$$\mathcal{D}_p(s) \sim s^p e^{-s^2/4}{}_2F_0\left(-\frac{p}{2}, \frac{1-p}{2}; -\frac{2}{s^2}\right) - \frac{\sqrt{2\pi}e^{-\mathrm{i}\pi p}}{\Gamma(-p)}s^{-p-1}e^{s^2/4}{}_2F_0\left(\frac{p}{2}, \frac{1+p}{2}; \frac{2}{s^2}\right) \tag{4.92}$$

where Eq. (4.91) is valid for $\pi/4 < \arg s < 5\pi/4$, and Eq. (4.92) is valid for $-5\pi/4 < \arg s < -\pi/4$.

With the help of these formulae it is easy to see that the oscillating terms in expansions (4.80) and (4.81) should be matched with the last two terms in Eq. (4.89) which, however, grow infinitely (the former grows, when $z \to -\infty$, and the latter, when $z \to +\infty$). To remove infinitely growing terms from the solution, we need to set $D_1 = D_2 = 0$ in Eq. (4.89), then after the matching, we obtain in Eqs. (4.80), (4.81) and (4.75), (4.76)

$$B_1 = \breve{B}_1 = 0, \quad \text{and} \quad B_2 = \breve{B}_2 = D_0. \tag{4.93}$$

Notice that from the physical point of view the former equality, $B_1 = \breve{B}_1 = 0$, is just a consequence of the fact mentioned in Sec. 4.3 that in the trans-critical accelerating current the B-waves (i.e., counter-current propagating waves on the left of critical point and negative-energy waves on the right of it) cannot reach the critical point.

After that assuming that the incident wave arriving from minus infinity has a unit amplitude $A_1 = 1$, using matching conditions (4.10) and putting $T_p \equiv C_1$, $T_n \equiv C_2$, we obtain

$$\begin{aligned}
B_2\, w_3\left(V_1^2\right) &= R + 1, \qquad \qquad (4.94)\\
B_2\, w_3'(V_1^2) &= \frac{-\mathrm{i}\,\hat{\omega} R}{2V_1(1 - V_1)} + \frac{\mathrm{i}\,\hat{\omega}}{2V_1(1 + V_1)}, \qquad \qquad (4.95)\\
T_n + T_p &= V_2^{\mathrm{i}\,\hat{\omega}} \breve{w}_3\left(V_2^{-2}\right) \breve{B}_2, \qquad \qquad (4.96)\\
(V_2 + 1)T_n - (V_2 - 1)T_p &= \frac{2\mathrm{i}}{\hat{\omega}}\, V_2^{\mathrm{i}\,\hat{\omega}-2}\left(V_2^2 - 1\right) \breve{w}_3'\left(V_2^{-2}\right) \breve{B}_2. \qquad \qquad (4.97)
\end{aligned}$$

This set can be readily solved yielding the following transformation coefficients:

$$\begin{aligned}
R &= -\frac{w_3'\left(V_1^2\right) - \dfrac{\mathrm{i}\,\hat{\omega}\, w_3\left(V_1^2\right)}{2V_1(1 + V_1)}}{w_3'\left(V_1^2\right) + \dfrac{\mathrm{i}\,\hat{\omega}\, w_3\left(V_1^2\right)}{2V_1(1 - V_1)}}, \qquad \qquad (4.98)\\
B_2 &= \breve{B}_2 = \frac{R + 1}{w_3\left(V_1^2\right)}, \qquad \qquad (4.99)\\
T_n &= \frac{\mathrm{i}}{\hat{\omega}}\, V_2^{\mathrm{i}\,\hat{\omega}-1}\left(V_2^2 - 1\right)\left[\frac{\breve{w}_3'\left(V_2^{-2}\right)}{V_2^2} - \frac{\mathrm{i}\,\hat{\omega}}{2}\frac{\breve{w}_3\left(V_2^{-2}\right)}{V_2 + 1}\right] B_2, \qquad \qquad (4.100)\\
T_p &= -\frac{\mathrm{i}}{\hat{\omega}}\, V_2^{\mathrm{i}\,\hat{\omega}-1}\left(V_2^2 - 1\right)\left[\frac{\breve{w}_3'\left(V_2^{-2}\right)}{V_2^2} + \frac{\mathrm{i}\,\hat{\omega}}{2}\frac{\breve{w}_3\left(V_2^{-2}\right)}{V_2 - 1}\right] B_2. \qquad \qquad (4.101)
\end{aligned}$$

In the long-wave approximation, $\hat{\omega} \to 0$, we obtain (see Appendix 6.2):

$$R = \frac{1 - V_1}{1 + V_1}, \quad T_p = \frac{V_2 + 1}{V_1 + 1}, \quad T_n = -\frac{V_2 - 1}{V_1 + 1}, \quad K_{Tp,n} = \frac{V_1}{V_2}\left(\frac{V_2 \pm 1}{V_1 + 1}\right)^2, \tag{4.102}$$

where in the last formula sign plus pertains to the positive- and sign minus – to the negative-energy transmitted wave.

These values are purely real, $R > 0$ and $T_p > 0$, whereas $T_n < 0$. The problem of surface wave transformation in a duct with the stepwise change of cross-section and velocity profile is undetermined for such current, therefore in Ref. [24] one of the parameters, R_η – the reflection coefficient in terms of free surface perturbation, was undefined. Now from Eq. (4.102) it follows that the transformation coefficients in terms of free surface perturbation in Ref. [24] are $R_\eta = T_{p\eta} = -T_{n\eta} = 1$ (for the relationships between the transformation coefficients in terms of velocity potential and free surface perturbation see Appendix 6.2).

Because of the relationships between the coefficients (4.93), the solution in the domain $\xi_1 < \xi < \xi_2$ is described by the same analytical function $w_3\left(\xi^2\right) \equiv \xi^{\mathrm{i}\hat{\omega}}\breve{w}_3\left(\xi^{-2}\right)$ (see Eqs. (9) and (11) in §6.4 of the book [95]). In the result, the energy flux is still conserved despite a small viscosity in the vicinity of the critical point $\xi = 1$:

$$J = \frac{2\hat{\omega}}{V_1}\left(1 - |R|^2\right) = \frac{2\hat{\omega}}{V_2}\left(|T_p|^2 - |T_n|^2\right) > 0 \text{ or } V_2\left(1 - |R|^2\right) = V_1\left(|T_p|^2 - |T_n|^2\right). \tag{4.103}$$

As one can see from these expressions, the energy flux in the reflected wave by modulus is always less than in the incident wave, therefore over-reflection here is not possible. In the meantime the energy transmission factors $K_{Tp,n}$ can be greater than 1; this implies that the over-transmission can occur with respect to both positive- and negative-energy waves.

The transformation coefficients $|R|$, $|T_p|$ and $|T_n|$ together with the intermediate coefficients of wave excitation in the transient zone, $|B_2| = |\breve{B}_2|$, are presented in Fig. 4.9 as functions of dimensionless frequency $\hat{\omega}$ for the particular values of speed, $V_1 = 0.1$ and $V_2 = 1.9$. Qualitatively similar graphics were obtained for other values of V_1 and V_2. Notice that both the transmission coefficient of negative energy wave $|T_n|$ and reflection coefficient of positive energy wave $|R|$ decay asymptotically with the same rate $\sim \hat{\omega}^{-1}$.

Figure 4.10 illustrates the dependencies of energy transmission factors on the frequency for two cases: (i) when both $K_{Tp,n} < 1$ ($V_1 = 0.1$, $V_2 = 1.9$) and (ii) when both $K_{Tp,n} > 1$ in a certain range of frequencies $\hat{\omega} < \hat{\omega}_c$ ($V_1 = 0.9$, $V_2 = 8.0$). In Fig. 4.11 we present graphics of $|\Phi(\xi)|$ as per Eqs. (4.74)–(4.77)

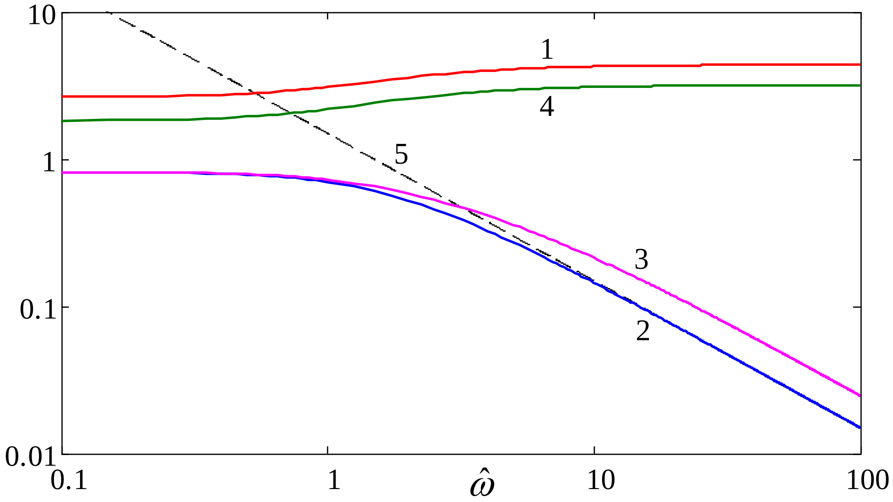

Figure 4.9: Modules of the transformation coefficient as functions of dimensionless frequency $\hat{\omega}$ for $V_1 = 0.1$, $V_2 = 1.9$. Line 1 – $|T_p|$, line 2 – $|T_n|$, line 3 – $|R|$, line 4 – $|B_2| = |\breve{B}_2|$. Dashed line 5 represents the asymptotic for $|T_n| \sim \hat{\omega}^{-1}$.

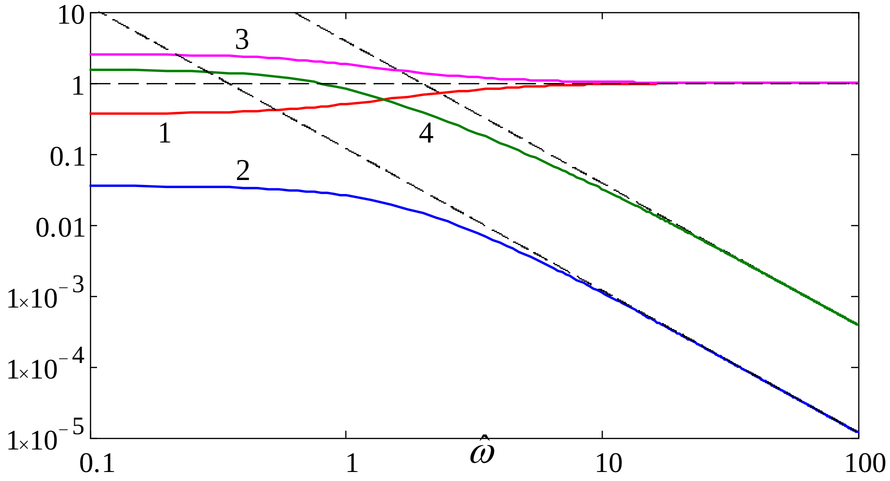

Figure 4.10: The dependencies of energy transmission factors on the frequency (i) when both $K_{Tp} < 1$ (line 1) and $K_{Tn} < 1$ (line 2) (here $V_1 = 0.1$, $V_2 = 1.9$); and (ii) when both $K_{Tp} > 1$ (line 3) and $K_{Tn} > 1$ (line 4) in a certain range of frequencies $\hat{\omega} < \hat{\omega}_c$ (here $V_1 = 0.9$, $V_2 = 8.0$). Inclined dashed lines show the asymptotic dependencies $K_{Tn} \sim \hat{\omega}^{-2}$.

for $A_1 = 1$, $A_2 = R$ as per Eq. (4.98), $D_1 = T_n$ as per Eq. (4.100), and $D_2 = T_p$ as per Eq. (4.101). Coefficients $B_1 = \breve{B}_1 = 0$ as per Eq. (4.93), and $B_2 = \breve{B}_2$ are given by Eq. (4.99). Line 1 in this figure pertains to the case when $V_1 = 0.1$, $V_2 = 1.9$, and line 2 – to the case when $V_1 = 0.9$, $V_2 = 8.0$.

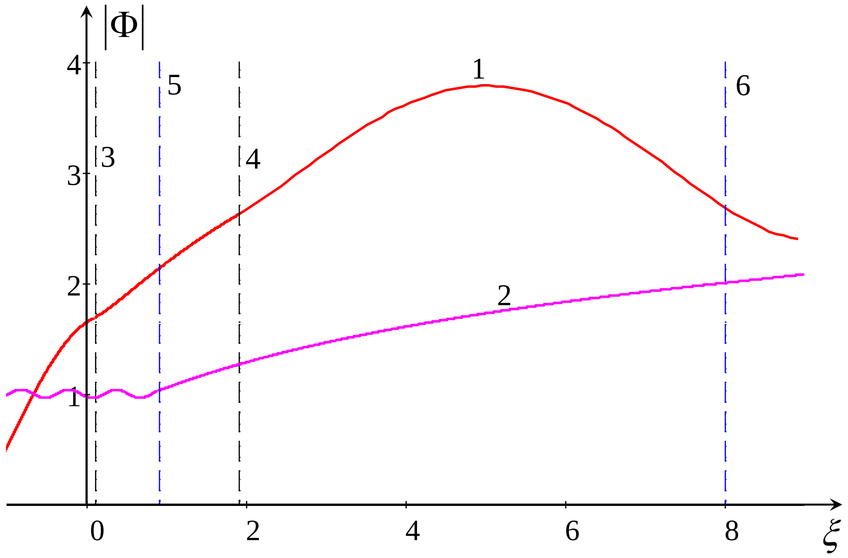

Figure 4.11: Modules of function $\Phi(\xi)$ for wave scattering in accelerating trans-critical current with $V_1 = 0.1$ and $V_2 = 1.9$ (line 1) and $V_1 = 0.9$ and $V_2 = 8.0$ (line 2). Dashed vertical lines 3 and 4 show the transition zone where the current accelerates from $V_1 = 0.1$ to $V_2 = 1.9$, and dashed vertical lines 5 and 6 show the transition zone where the current accelerates from $V_1 = 0.9$ to $V_2 = 8.0$. The plot was generated for $\hat{\omega} = 1$.

4.4.4 Wave transformation in trans-critical decelerating currents $V_1 > 1 > V_2 > 0$

In this subsection we consider the wave transformation in gradually decelerating background current assuming that the current is super-critical in the left domain and sub-critical in the right domain. For the sake of simplification of hypergeometric functions used below we chose again the coordinate frame such as shown in Fig. 4.1b). In such a current the transition through the critical point, where $V(\xi) = 1$, occurs at $\xi = -1$.

In the left domain, where the current is super-critical, only downstream propagating waves can exist, with the positive or negative energy. In contrast to that, in the right domain, where the background current is sub-critical, two waves of positive energy can coexist; one of them is co-current propagating and another one is counter-current propagating.

The general solution of Eq. (4.8) in the different domains can be formally presented with the help of functions $\tilde{w}$ as per Eq. (4.22) and $\hat{w}$ as per Eq. (4.53):

$$\Phi(\xi) = A_1 e^{\mathrm{i}\kappa_1(\xi-\xi_1)} + A_2 e^{\mathrm{i}\kappa_2(\xi-\xi_1)}, \qquad \xi < \xi_1, \tag{4.104}$$

$$\Phi(\xi) = (-\xi)^{-\mathrm{i}\hat{\omega}} \left[\hat{B}_1\, \hat{w}_1\left(\xi^{-2}\right) + \hat{B}_2\, \hat{w}_3\left(\xi^{-2}\right)\right], \quad \xi_1 < \xi < -1, \tag{4.105}$$

$$\Phi(\xi) = B_1\, \tilde{w}_2\left(\xi^2\right) + B_2\, \tilde{w}_3\left(\xi^2\right), \qquad -1 < \xi < \xi_2 < 0, \tag{4.106}$$

$$\Phi(\xi) = C_1\, e^{\mathrm{i}\kappa_3(\xi-\xi_2)} + C_2\, e^{-\mathrm{i}\kappa_4(\xi-\xi_2)}, \qquad \xi > \xi_2, \tag{4.107}$$

where $\kappa_1 = \hat{\omega}/(V_1+1)$, $\kappa_2 = \hat{\omega}/(V_1-1)$, $\kappa_3 = \hat{\omega}/(1+V_2)$, $\kappa_4 = \hat{\omega}/(1-V_2)$.

The matching conditions at $\xi = \xi_1$ provide (cf. Eqs. (4.55)and (4.56)):

$$A_1 + A_2 = V_1^{-\mathrm{i}\hat{\omega}} \left[\hat{B}_1\, \hat{w}_1\left(V_1^{-2}\right) + \hat{B}_2\, \hat{w}_3\left(V_1^{-2}\right)\right], \tag{4.108}$$

$$(V_1-1)A_1 - (V_1+1)A_2 = \frac{2\mathrm{i}}{\hat{\omega}}\, V_1^{-\mathrm{i}\hat{\omega}-2}\left(V_1^2-1\right)\left[\hat{B}_1\, \hat{w}_1'\left(V_1^{-2}\right) + \hat{B}_2\, \hat{w}_3'\left(V_1^{-2}\right)\right], \tag{4.109}$$

And similarly the matching conditions at $\xi = \xi_2$ provide:

$$C_1 + C_2 = B_1\, \tilde{w}_2\left(V_2^2\right) + B_2\, \tilde{w}_3\left(V_2^2\right), \tag{4.110}$$

$$(1-V_2)C_1 - (1+V_2)C_2 = \frac{2\mathrm{i}}{\hat{\omega}}\, V_2\left(1-V_2^2\right)\left[B_1\, \tilde{w}_2'\left(V_2^2\right) + B_2\, \tilde{w}_3'\left(V_2^2\right)\right]. \tag{4.111}$$

With the help of Eq. (4.79) we find the asymptotic expansions when $\xi \to -1_{\pm 0}$

$$\Phi(\xi) = \hat{B}_2 + \frac{\Gamma(1-\mathrm{i}\hat{\omega})\hat{B}_1}{2\Gamma^2(1-\mathrm{i}\hat{\omega}/2)} + \frac{\Gamma(1+\mathrm{i}\hat{\omega})\hat{B}_1}{2\Gamma^2(1+\mathrm{i}\hat{\omega}/2)}\left(\xi^2-1\right)^{-\mathrm{i}\hat{\omega}} + O\left(\xi^2-1\right), \ \xi \to -1_{-0}, \tag{4.112}$$

$$\Phi(\xi) = B_2 + \frac{\Gamma(-\mathrm{i}\hat{\omega})B_1}{\Gamma^2(1-\mathrm{i}\hat{\omega}/2)} + \frac{\Gamma\left(\mathrm{i}\hat{\omega}\right)B_1}{\Gamma^2(1+\mathrm{i}\hat{\omega}/2)}\left(1-\xi^2\right)^{-\mathrm{i}\hat{\omega}} + O\left(1-\xi^2\right), \ \xi \to -1_{+0}. \tag{4.113}$$

which are similar to Eqs. (4.80) and (4.81), and contain fast oscillating terms corresponding to counter-current propagating B-waves as well.

To match solutions in the vicinity of critical point $\xi = -1$, we again take into consideration a small viscosity. Bearing in mind that $V(\xi) = -\xi$ (see Fig. 4.1b)) and setting $\zeta = \xi^2 = 1 + \varepsilon z$, $\nu = \varepsilon^2/2$, we arrive at the equation similar to

Eq. (4.85):

$$
\begin{aligned}
&(1+\varepsilon z)^2\,\frac{d^3\Phi}{dz^3} + (1+\varepsilon z)\left(z + \frac{3+\mathrm{i}\,\hat{\omega}}{2}\varepsilon\right)\frac{d^2\Phi}{dz^2} + \\
&\left[(1+\mathrm{i}\,\hat{\omega})(1+\varepsilon z) + \frac{\mathrm{i}\,\hat{\omega}}{4}\varepsilon^2\right]\frac{d\Phi}{dz} - \frac{\varepsilon\hat{\omega}^2}{4}\Phi = 0. \qquad (4.114)
\end{aligned}
$$

This equation in the leading order on the small parameter $\varepsilon \ll 1$ reduces to (cf. Eq. (4.86)):

$$
\frac{d}{dz}\left(\frac{d^2\Phi_0}{dz^2} + z\frac{d\Phi_0}{dz} + \mathrm{i}\,\hat{\omega}\Phi_0\right) = 0. \qquad (4.115)
$$

Integrating this equation and substituting $\Phi_0(z) = D_0 + e^{-z^2/4}G(z)$, we obtain again the equation of a parabolic cylinder in the form (cf. Eq. (4.116)):

$$
\frac{d^2G}{dz^2} + \left(\mathrm{i}\,\hat{\omega} - \frac{1}{2} - \frac{z^2}{4}\right)G = 0. \qquad (4.116)
$$

Thus, the general solution to Eq. (4.115) in the vicinity of critical point $\xi = -1$ can be presented as:

$$
\Phi_0(z) = D_0 + e^{-z^2/4}\left[D_1\mathcal{D}_{\mathrm{i}\,\hat{\omega}-1}(z) + D_2\mathcal{D}_{\mathrm{i}\,\hat{\omega}-1}(-z)\right],
$$

where D_0, D_1 and D_2 are arbitrary constants.

The asymptotic expansions (4.90)–(4.92) show that this solution remains limited for any arbitrary constants. Moreover, the oscillatory terms in Eqs. (4.112) and (4.113) become exponentially small after transition through the critical point $\xi = -1$. As was explained in Sec. 4.3, this means that the B-waves running toward the critical point both from the left (negative-energy waves) and from the right (counter-current propagating positive-energy waves) dissipate in the vicinity of the critical point. For this reason the wave energy flux does not conserve in the decelerating trans-critical currents (see Eqs. (4.128) and (4.135) below). Taking this fact into account, one can match solutions (4.112) and (4.113):

$$
D_0 = \frac{\Gamma(-\mathrm{i}\,\hat{\omega})}{\Gamma^2(1-\mathrm{i}\,\hat{\omega}/2)}B_1 + B_2 = \frac{\Gamma(1-\mathrm{i}\,\hat{\omega})}{2\Gamma^2(1-\mathrm{i}\,\hat{\omega}/2)}\hat{B}_1 + \hat{B}_2. \qquad (4.117)
$$

After that using the identity $\Gamma(x)\Gamma(1-x) = \pi/\sin\pi x$, we find for the constants D_1 and D_2 the following expressions:

$$
D_1 = \frac{-\mathrm{i}\sqrt{\pi/2}}{\Gamma^2(1+\mathrm{i}\hat{\omega}/2)}\frac{e^{-\mathrm{i}\hat{\omega}\ln\varepsilon}}{\sinh\pi\hat{\omega}}B_1, \quad D_2 = \frac{\hat{\omega}\sqrt{\pi/2}}{2\Gamma^2(1+\mathrm{i}\hat{\omega}/2)}\frac{e^{-\mathrm{i}\hat{\omega}\ln\varepsilon}}{\sinh\pi\hat{\omega}}\hat{B}_1. \qquad (4.118)
$$

Using the prepared formulae we can now calculate the transformation coefficients for incident waves of either positive or negative energy travelling in the duct from the minus to plus infinity.

4.4.4.1 Transformation of downstream propagating positive-energy wave

Assume first that the incident wave of unit amplitude has positive energy and let us set in Eqs. (4.104) and (4.107) $A_1 = 1$, $A_2 = 0$, $C_1 \equiv T_1$, and $C_2 = 0$. Then from Eqs. (4.108) and (4.109) we obtain (cf. Eqs. (4.55) and (4.56)):

$$\hat{B}_1\,\hat{w}_1\left(V_1^{-2}\right) + \hat{B}_2\,\hat{w}_3\left(V_1^{-2}\right) = V_1^{\mathrm{i}\,\hat{\omega}}, \tag{4.119}$$

$$\hat{B}_1\,\hat{w}_1'\left(V_1^{-2}\right) + \hat{B}_2\,\hat{w}_3'\left(V_1^{-2}\right) = -\frac{\mathrm{i}\,\hat{\omega}}{2}\frac{V_1^{\mathrm{i}\,\hat{\omega}+2}}{V_1+1}. \tag{4.120}$$

From this set of equations using the Wronskian (4.54), one can find

$$\hat{B}_1 = -\frac{\Gamma(\mathrm{i}\,\hat{\omega}/2)\,\Gamma(1+\mathrm{i}\,\hat{\omega}/2)}{\Gamma(1+\mathrm{i}\,\hat{\omega})}\,V_1^{-\mathrm{i}\,\hat{\omega}-2}\left(V_1^2-1\right)^{\mathrm{i}\,\hat{\omega}+1}\left[\frac{\hat{w}_3'\left(V_1^{-2}\right)}{V_1^2} + \frac{\mathrm{i}\,\hat{\omega}}{2}\frac{\hat{w}_3\left(V_1^{-2}\right)}{V_1+1}\right], \tag{4.121}$$

$$\hat{B}_2 = \frac{\Gamma(\mathrm{i}\,\hat{\omega}/2)\,\Gamma(1+\mathrm{i}\,\hat{\omega}/2)}{\Gamma(1+\mathrm{i}\,\hat{\omega})}\,V_1^{-\mathrm{i}\,\hat{\omega}-2}\left(V_1^2-1\right)^{\mathrm{i}\,\hat{\omega}+1}\left[\frac{\hat{w}_1'\left(V_1^{-2}\right)}{V_1^2} + \frac{\mathrm{i}\,\hat{\omega}}{2}\frac{\hat{w}_1\left(V_1^{-2}\right)}{V_1+1}\right]. \tag{4.122}$$

Similarly from the matching conditions (4.110) and (4.111) we obtain

$$B_1\,\tilde{w}_2\left(V_2^2\right) + B_2\,\tilde{w}_3\left(V_2^2\right) = T_1, \tag{4.123}$$

$$B_1\,\tilde{w}_2'\left(V_2^2\right) + B_2\,\tilde{w}_3'\left(V_2^2\right) = \frac{-\mathrm{i}\,\hat{\omega}T_1}{2V_2(1+V_2)}. \tag{4.124}$$

Using the Wronskian (4.23), we derive from these equations

$$B_1 = -\frac{\Gamma^2(1+\mathrm{i}\,\hat{\omega}/2)}{\Gamma(1+\mathrm{i}\,\hat{\omega})}\left(1-V_2^2\right)^{\mathrm{i}\,\hat{\omega}+1}\left[\tilde{w}_3'\left(V_2^2\right) + \frac{\mathrm{i}\,\hat{\omega}}{2}\frac{\tilde{w}_3\left(V_2^2\right)}{V_2(1+V_2)}\right]T_1, \tag{4.125}$$

$$B_2 = \frac{\Gamma^2(1+\mathrm{i}\,\hat{\omega}/2)}{\Gamma(1+\mathrm{i}\,\hat{\omega})}\left(1-V_2^2\right)^{\mathrm{i}\,\hat{\omega}+1}\left[\tilde{w}_2'\left(V_2^2\right) + \frac{\mathrm{i}\,\hat{\omega}}{2}\frac{\tilde{w}_2\left(V_2^2\right)}{V_2(1+V_2)}\right]T_1. \tag{4.126}$$

Substituting B_1 and B_2, as well as $\hat{B}_1$ and $\hat{B}_2$, in Eq. (4.117), we obtain the transmission coefficient

$$T_1 = -\frac{2\mathrm{i}}{\hat{\omega}}\,V_1^{-\mathrm{i}\,\hat{\omega}-2}\left(\frac{V_1^2-1}{1-V_2^2}\right)^{\mathrm{i}\,\hat{\omega}+1} \times$$

$$\frac{\dfrac{\hat{w}_1'\left(V_1^{-2}\right)}{V_1^2} + \dfrac{\mathrm{i}\,\hat{\omega}}{2}\dfrac{\hat{w}_1\left(V_1^{-2}\right)}{V_1+1} - \dfrac{\Gamma(1-\mathrm{i}\,\hat{\omega})}{2\Gamma^2(1-\mathrm{i}\,\hat{\omega}/2)}\left[\dfrac{\hat{w}_3'(V_1^{-2})}{V_1^2} + \dfrac{\mathrm{i}\,\hat{\omega}}{2}\dfrac{\hat{w}_3\left(V_1^{-2}\right)}{V_1+1}\right]}{\tilde{w}_2'\left(V_2^2\right) + \dfrac{\mathrm{i}\,\hat{\omega}}{2}\dfrac{\tilde{w}_2\left(V_2^2\right)}{V_2(1+V_2)} - \dfrac{\Gamma(-\mathrm{i}\,\hat{\omega})}{\Gamma^2(1-\mathrm{i}\,\hat{\omega}/2)}\left[\tilde{w}_3'\left(V_2^2\right) + \dfrac{\mathrm{i}\,\hat{\omega}}{2}\dfrac{\tilde{w}_3\left(V_2^2\right)}{V_2(1+V_2)}\right]}. \quad (4.127)$$

Calculations of the energy fluxes on each side of the transient domain show that they are both positive, but generally different, i.e., the energy flux does not conserve,

$$J_1 = J(\xi < -1) = \frac{2\hat{\omega}}{V_1} \neq J_2 = J(\xi > -1) = \frac{2\hat{\omega}}{V_2}\,|T_1|^2. \quad (4.128)$$

This interesting fact can be explained by the partial wave absorption in the critical point due to viscosity. The detailed explanation of this is given in Section 4.5. The difference in the energy flux in the incident and transmitted waves is independent of the viscosity, when $\nu \to 0$:

$$\Delta J \equiv J_1 - J_2 = 2\hat{\omega}\left(1/V_1 - |T_1|^2/V_2\right) \overset{\hat{\omega}\to 0}{\longrightarrow} \frac{1 - V_1V_2}{V_1(1+V_2)^2}(V_1 - V_2)J_1, \quad (4.129)$$

and it is easily seen that it can be both positive and negative.

In Fig. 4.12a) we present the transmission coefficient $|T_1|$ together with the intermediate coefficients of wave excitation in the transient domain, $|B_1|$, $|B_2|$, $|\hat{B}_1|$, and $|\hat{B}_2|$, as functions of dimensionless frequency $\hat{\omega}$ for the particular values of current speed $V_1 = 1.9$ and $V_2 = 0.1$. As one can see from this figure, the transmission coefficient gradually increases with the frequency.

The graphic of $|\Phi(\xi)|$ is shown in Fig. 4.13 by lines 1 and 2. The plot was generated for $\hat{\omega} = 1$ on the basis of solution Eqs. (4.104)–(4.107) with $A_1 = 1$, $A_2 = 0$, $D_1 = T_1$ as per Eq. (4.127), and $D_2 = 0$. Coefficients B_1 and B_2 are given by Eqs. (4.125) and (4.126), and coefficients $\hat{B}_1$ and $\hat{B}_2$ are given by Eqs. (4.121) and (4.122). The module of function $\Phi(\xi)$ is discontinuous only in the critical point $\xi = -1$, and the phase of function $\Phi(\xi)$ quickly changes in the small vicinity of this point.

4.4.4.2 Transformation of downstream propagating negative-energy wave

Assume now that the incident wave is a unit amplitude wave of negative energy and correspondingly set $A_1 = 0$, $A_2 = 1$, $C_1 = 0$, and $C_2 \equiv T_2$. Then from Eqs.

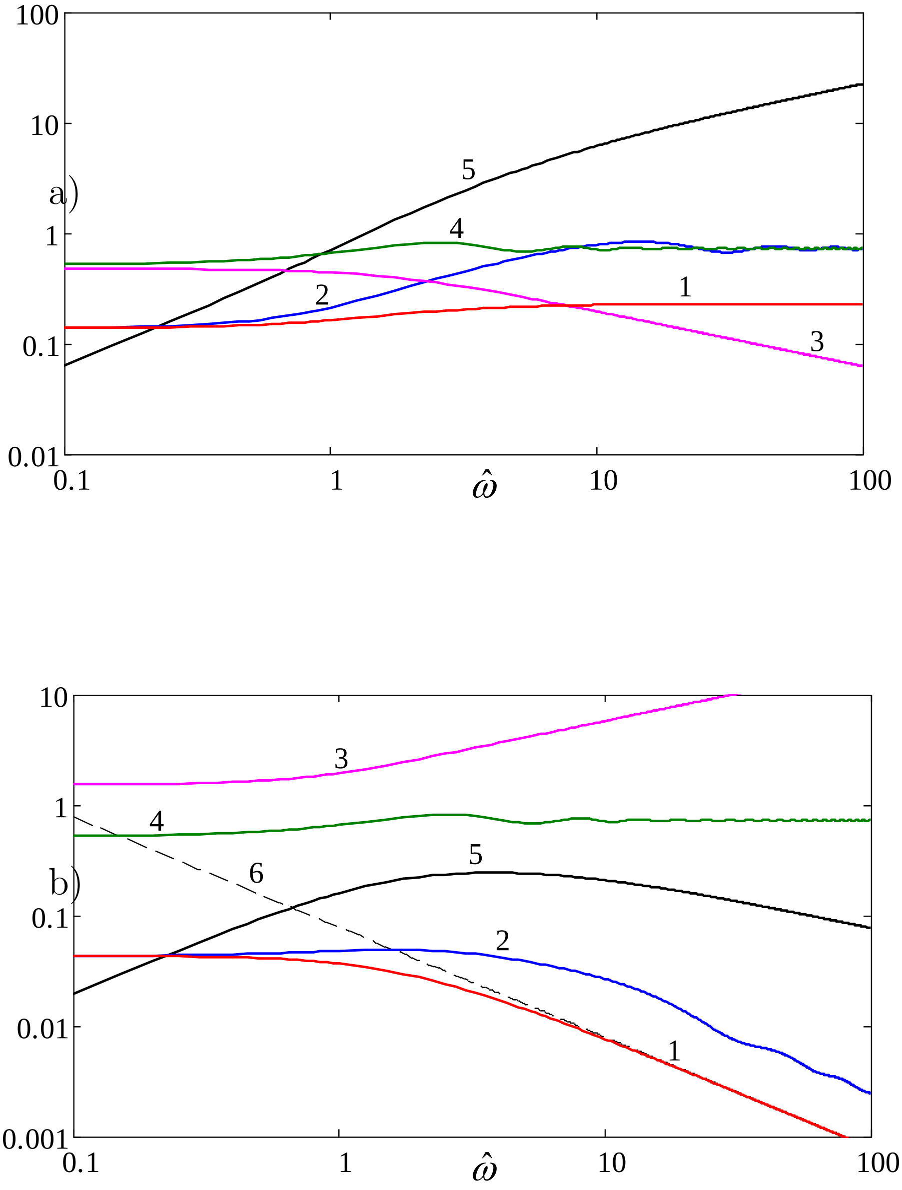

Figure 4.12: Modules of the transmission coefficients $|T_1|$ (line 1 in panel a) and $|T_2|$ (line 1 in panel b), as well as coefficients of wave excitation in the transient domain, $|B_1|$ (line 2), $|B_2|$ (line 3), $|\hat{B}_1|$ (line 4), and $|\hat{B}_2|$ (line 5), for the scattering of positive energy wave (panel a) and negative energy wave (panel b) as functions of dimensionless frequency $\hat{\omega}$ for $V_1 = 1.9$, $V_2 = 0.1$. Dashed line 6 in panel (b) represents the high-frequency asymptotic for $|T_2| \sim \hat{\omega}^{-1}$.

(4.108) and (4.109) we obtain:

$$\hat{B}_1\,\hat{w}_1\left(V_1^{-2}\right) + \hat{B}_2\,\hat{w}_3\left(V_1^{-2}\right) = V_1^{\mathrm{i}\,\hat{\omega}}, \tag{4.130}$$

$$\hat{B}_1\,\hat{w}_1'\left(V_1^{-2}\right) + \hat{B}_2\,\hat{w}_3'\left(V_1^{-2}\right) = \frac{\mathrm{i}\,\hat{\omega}}{2}\frac{V_1^{\mathrm{i}\,\hat{\omega}+2}}{V_1 - 1}. \tag{4.131}$$

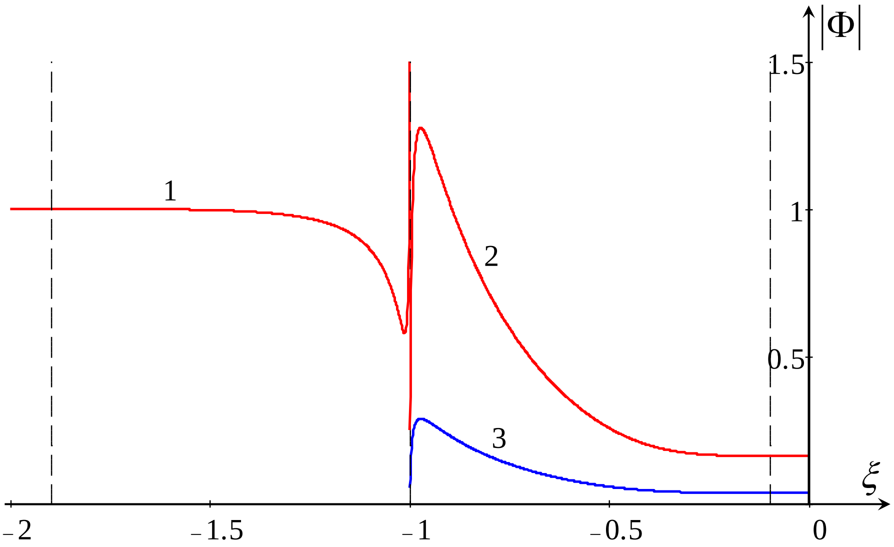

Figure 4.13: Modules of function $\Phi(\xi)$ for wave scattering in decelerating transcritical current with $V_1 = 1.9$ and $V_2 = 0.1$ for $\hat{\omega} = 1$. Lines 1 and 2 pertain to the scattering of a positive-energy incident wave, and lines 1 and 3 pertain to the scattering of a negative-energy incident wave (line 1 is the same both for positive- and negative-energy waves).

From this set we find

$$\hat{B}_1 = -\frac{\Gamma(\mathrm{i}\,\hat{\omega}/2)\,\Gamma(1+\mathrm{i}\,\hat{\omega}/2)}{\Gamma(1+\mathrm{i}\,\hat{\omega})}\,V_1^{-\mathrm{i}\,\hat{\omega}-2}\left(V_1^2-1\right)^{\mathrm{i}\,\hat{\omega}+1}\left[\frac{\hat{w}_3'\left(V_1^{-2}\right)}{V_1^2}-\frac{\mathrm{i}\,\hat{\omega}}{2}\frac{\hat{w}_3\left(V_1^{-2}\right)}{V_1-1)}\right], \tag{4.132}$$

$$\hat{B}_2 = \frac{\Gamma(\mathrm{i}\,\hat{\omega}/2)\,\Gamma(1+\mathrm{i}\,\hat{\omega}/2)}{\Gamma(1+\mathrm{i}\,\hat{\omega})}\,V_1^{-\mathrm{i}\,\hat{\omega}-2}\left(V_1^2-1\right)^{\mathrm{i}\,\hat{\omega}+1}\left[\frac{\hat{w}_1'\left(V_1^{-2}\right)}{V_1^2}-\frac{\mathrm{i}\,\hat{\omega}}{2}\frac{\hat{w}_1\left(V_1^{-2}\right)}{V_1-1)}\right]. \tag{4.133}$$

From the matching conditions at $\xi = \xi_2$ (see Eqs. (4.110) and (4.111)) we obtain the similar expressions for the coefficients B_1 and B_2 as in Eqs. (4.125) and (4.126) with the only replacement of T_1 by T_2. Substituting then all four coefficients B_1, B_2, $\hat{B}_1$, and $\hat{B}_2$ in Eq. (4.117), we obtain the transmission coefficient T_2:

$$T_2 = -\frac{2\mathrm{i}}{\hat{\omega}}\,V_1^{-\mathrm{i}\,\hat{\omega}-2}\left(\frac{V_1^2-1}{1-V_2^2}\right)^{\mathrm{i}\,\hat{\omega}+1}\times$$

$$\frac{\dfrac{\hat{w}_1'\left(V_1^{-2}\right)}{V_1^2}-\dfrac{\mathrm{i}\,\hat{\omega}}{2}\dfrac{\hat{w}_1\left(V_1^{-2}\right)}{V_1-1}-\dfrac{\Gamma(1-\mathrm{i}\,\hat{\omega})}{2\Gamma^2(1-\mathrm{i}\,\hat{\omega}/2)}\left[\dfrac{\hat{w}_3'(V_1^{-2})}{V_1^2}-\dfrac{\mathrm{i}\,\hat{\omega}\,\hat{w}_3\left(V_1^{-2}\right)}{2(V_1-1)}\right]}{\tilde{w}_2'\left(V_2^2\right)+\dfrac{\mathrm{i}\,\hat{\omega}}{2}\dfrac{\tilde{w}_2\left(V_2^2\right)}{V_2(1+V_2)}-\dfrac{\Gamma(-\mathrm{i}\,\hat{\omega})}{\Gamma^2(1-\mathrm{i}\,\hat{\omega}/2)}\left[\tilde{w}_3'\left(V_2^2\right)+\dfrac{\mathrm{i}\,\hat{\omega}\,\tilde{w}_3\left(V_2^2\right)}{2V_2(1+V_2)}\right]}. \tag{4.134}$$

Calculations of the energy fluxes on each side of the transient domain show that they are not equal again, moreover, they have opposite signs in the left and right domains:

$$J_1 = J(\xi < -1) = -\frac{2\hat{\omega}}{V_1} < 0, \quad J_2 = J(\xi > -1) = \frac{2\hat{\omega}}{V_2}\left|T_2\right|^2 > 0. \tag{4.135}$$

The wave of negative energy in the left domain propagates to the right, its group velocity V_g is positive, but because it has a negative energy E, its energy flux, $J = EV_g$ is negative.

In the long-wave approximation, $\hat{\omega} \to 0$ we obtain (see Appendix 6.2):

$$T_1 = \frac{V_2(V_1+1)}{V_1(V_2+1)}, \quad T_2 = \frac{V_2(V_1-1)}{V_1(V_2+1)}, \quad K_{T1,T2} = \frac{V_2}{V_1}\left(\frac{V_1 \pm 1}{V_2+1}\right)^2, \tag{4.136}$$

where in the last formula sign plus pertains to the positive- and sign minus – to the negative-energy wave. As one can see, the transmission coefficients are purely real and positive, $T_{1,2} > 0$, in both cases.

The problem of surface wave transformation in a duct with the stepwise change of cross-section and velocity profile is undetermined for such current too; however from the results obtained it follows that in terms of free surface perturbation the transformation coefficients are

$$T_{1\eta} = \frac{V_2}{V_1}\left(\frac{V_1+1}{V_2+1}\right)^2, \quad T_{2\eta} = \frac{V_2}{V_1}\frac{V_1^2-1}{(V_2+1)^2} \tag{4.137}$$

(for the relationships between the transformation coefficients in terms of velocity potential and free surface perturbation see Appendix 6.2).

In Fig. 4.12b) we present the transmission coefficient $|T_2|$ together with the coefficients of wave excitation in the intermediate domain, $|B_1|$, $|B_2|$, $|\hat{B}_1|$, and $|\hat{B}_2|$, as functions of dimensionless frequency $\hat{\omega}$ for the particular values of current speed $V_1 = 1.9$ and $V_2 = 0.1$. As one can see from this figure, the transmission coefficient remains almost constant for small frequencies when $\hat{\omega} < 1$, then it decreases with the frequency and asymptotically vanishes as $|T_2| \sim \hat{\omega}^{-1}$ when $\hat{\omega} \to \infty$.

The graphic of $|\Phi(\xi)|$ is shown in Fig. 4.13 by lines 1 and 3 (the left branch of function $|\Phi(\xi)|$ for the incident negative- and positive-energy waves are the same). The plot was generated for $\hat{\omega} = 1$ on the basis of solution Eqs. (4.104)–(4.107) with $A_1 = 0$, $A_2 = 1$, $D_1 = 0$, and $D_2 = T_2$ as per Eq. (4.134). Coefficients B_1 and B_2 are given by Eqs. (4.125) and (4.126), and coefficients $\hat{B}_1$ and $\hat{B}_2$ are given by Eqs. (4.132) and (4.133). The module of function $\Phi(\xi)$ is discontinuous only in the critical point $\xi = -1$, but the phase of function $\Phi(\xi)$ quickly changes in the small vicinity of this point.

4.4.4.3 Transformation of a counter-current propagating wave

Consider now the case when the incident wave propagates against the mean current in the spatially variable current from the right domain where the background current is sub-critical. There are no waves capable to propagate against in the $\xi < -1$ domain where $V > 1$, therefore there is no transmitted wave in this case. However, the incident wave can propagate against the current and even penetrate into the transient zone $\xi_1 < \xi < \xi_2$ up to the critical point $\xi = -1$ until the current remains subcritical.

Because there are no waves in the domain $\xi < -1$, we should set in Eqs. (4.104)–(4.107) $A_1 = A_2 = \hat{B}_1 = \hat{B}_2 = 0$, $C_1 \equiv R$, and $C_2 = 1$. Then the matching condition (4.117) yields

$$B_2 = -\frac{\Gamma(-\mathrm{i}\,\hat{\omega})}{\Gamma^2(1-\mathrm{i}\,\hat{\omega}/2)}B_1, \tag{4.138}$$

and from Eqs. (4.110) and (4.111) we obtain for the reflection coefficient

$$R = -\frac{\tilde{w}_2'\left(V_2^2\right) - \dfrac{\mathrm{i}\,\hat{\omega}}{2}\dfrac{\tilde{w}_2\left(V_2^2\right)}{V_2(1-V_2)} - \dfrac{\Gamma(-\mathrm{i}\,\hat{\omega})}{\Gamma^2(1-\mathrm{i}\,\hat{\omega}/2)}\left[\tilde{w}_3'(V_2^2) - \dfrac{\mathrm{i}\,\hat{\omega}}{2}\dfrac{\tilde{w}_3\left(V_2^2\right)}{V_2(1-V_2)}\right]}{\tilde{w}_2'\left(V_2^2\right) + \dfrac{\mathrm{i}\,\hat{\omega}}{2}\dfrac{\tilde{w}_2\left(V_2^2\right)}{V_2(1+V_2)} - \dfrac{\Gamma(-\mathrm{i}\,\hat{\omega})}{\Gamma^2(1-\mathrm{i}\,\hat{\omega}/2)}\left[\tilde{w}_3'\left(V_2^2\right) + \dfrac{\mathrm{i}\,\hat{\omega}}{2}\dfrac{\tilde{w}_3\left(V_2^2\right)}{V_2(1+V_2)}\right]}. \tag{4.139}$$

Then, from Eqs. (4.110) and (4.138) we find B_1 and B_2; in particular for B_1 we obtain:

$$B_1 = \frac{1+R}{\tilde{w}_2\left(V_2^2\right) - \dfrac{\Gamma(-\mathrm{i}\,\hat{\omega})}{\Gamma^2(1-\mathrm{i}\,\hat{\omega}/2)}\tilde{w}_3\left(V_2^2\right)}. \tag{4.140}$$

Graphics of modulus of reflection coefficient $|R|$ as well as coefficients $|B_1|$ and $|B_2|$ are shown in Fig. 4.14 as functions of dimensionless frequency $\hat{\omega}$ for the particular values of $V_1 = 1.9$ and $V_2 = 0.1$. In the long-wave approximation, $\hat{\omega} \to 0$, using the asymptotics of hypergeometric function ${}_2F_1(a,b;c;d)$ (see Appendix 6.2), we obtain the limiting value of the reflection coefficient

$$R = \frac{1-V_2}{1+V_2}. \tag{4.141}$$

In terms of free surface perturbation this value corresponds to $R_\eta = 1$ (for the relationships between the transformation coefficients in terms of velocity potential and free surface perturbation see Appendix 6.2). This formally agrees with the solution found in Ref. [24].

In Fig. 4.15 we present graphics of $|\Phi(\xi)|$ as per Eqs. (4.104)–(4.107) for $A_1 = A_2 = 0$, $D_1 = 1$, and $D_2 = R$ as per Eq. (4.139). Coefficients B_1 and B_2

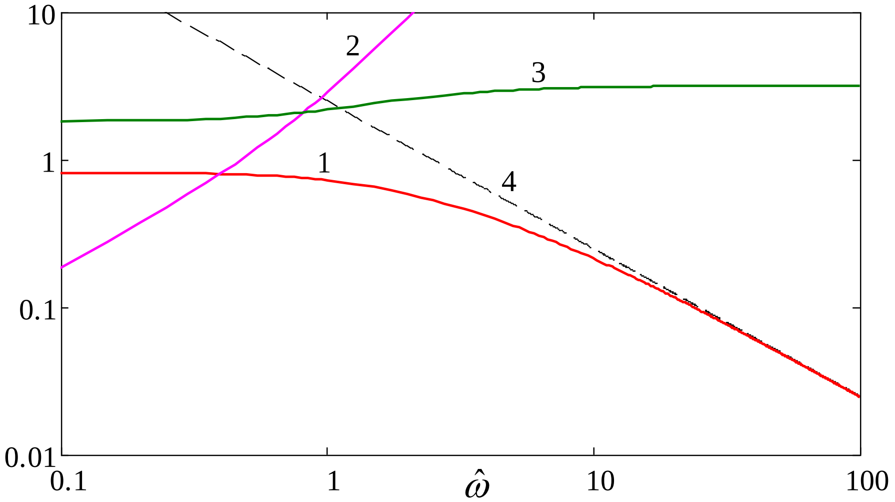

Figure 4.14: Modulus of the reflection coefficients $|R|$ (line 1) and coefficients of wave excitation in the transient domain, $|B_1|$ (line 2) and $|B_2|$ (line 3), as functions of dimensionless frequency $\hat{\omega}$ for $V_1 = 1.9$, $V_2 = 0.1$. Dashed line 4 represents the high-frequency asymptotic for $|R| \sim \hat{\omega}^{-1}$.

are given by Eqs. (4.140) and (4.138), and coefficients $\hat{B}_1 = \hat{B}_2 = 0$. A plot was generated for three dimensionless frequencies: line 1 – for $\hat{\omega} = 0.1$, line 2 – for $\hat{\omega} = 1$, and line 3 – for $\hat{\omega} = 100$. The phase of function $\Phi(\xi)$ infinitely increases when the incident wave approaches the critical point $\xi = -1$. The energy fluxes

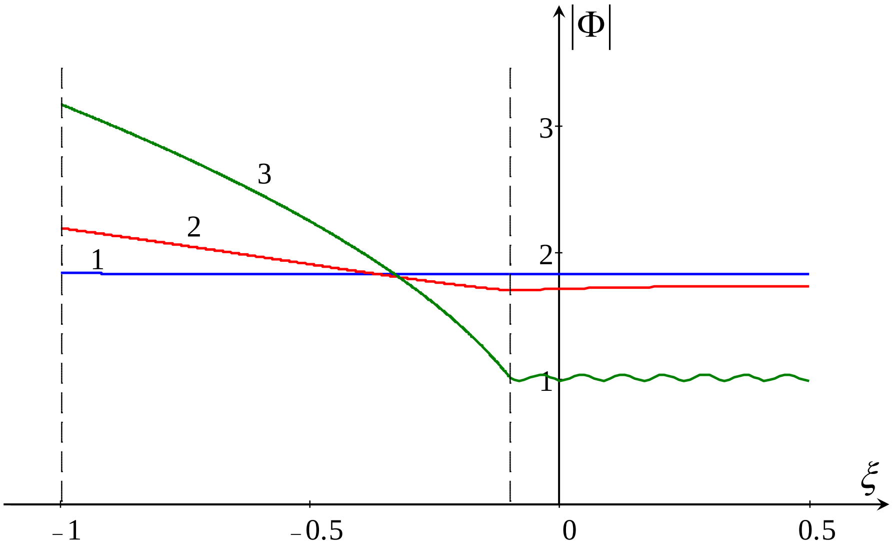

Figure 4.15: Module of function $\Phi(\xi)$ for a counter-current propagating incident wave which scatters in the decelerating trans-critical current with $V_1 = 1.9$ and $V_2 = 0.1$ for the particular values of $\hat{\omega}$: line 1 – $\hat{\omega} = 0.1$, line 2 – $\hat{\omega} = 1$, and line 3 – $\hat{\omega} = 100$.

in the incident J_i and reflected J_r waves in the right domain ($\xi > \xi_2$) are

$$J_i = -\frac{2\hat{\omega}}{V_2} < 0, \quad J_r = \frac{2\hat{\omega}}{V_2}|R|^2 > 0. \tag{4.142}$$

Thus, the total energy flux in the right domain $\Delta J \equiv J_i - J_r = -\left(2\hat{\omega}/V_2\right)\left(1 - |R|^2\right) < 0$ is negative; it transfers towards the critical point, where it is absorbed by the viscosity.

4.5 Discussion and conclusion

In this Chapter we have calculated the transformation coefficients of shallow water gravity waves propagating on a longitudinally varying quasi-one-dimensional current. Owing to the choice of a piecewise linear velocity profile $U(x)$ (or, in the dimensionless variables, $V(\xi)$, see Fig. 4.1) we were able to calculate analytically the scattering coefficients as functions of incident wave frequency $\hat{\omega}$ for accelerating and decelerating sub-, super-, and trans-critical currents, as well as for all possible types of incident wave.

Presented analysis pertains to the dispersionless case when the wavelengths of all waves participating in the scattering process are much greater than the water depth in the canal. However, the wavelengths λ can be comparable with or even less than the characteristic length of current inhomogeneity L. In the long-wave limit $\lambda \gg L$, the scattering coefficients are expressed through the simple algebraic formulae which are in agreement with the formulae derived in [24] for the case of abrupt change of canal cross-section.

The most important property of scattering processes in sub-, super-, and accelerating trans-critical currents is that the wave energy flux conserves, $J =$ const, (see Eq. (4.6) and the text below Eq. (4.8)). This law provides a highly convenient and physically transparent basis for the analysis of wave scattering.

In the simplest case of sub-critical currents ($U(x) < c_0$, or $V(\xi) < 1$), both accelerating and decelerating, all participating waves possess a positive energy, and the energy flux of the unit amplitude incident wave (no matter whether running from the left or from the right) is divided between reflected and transmitted waves in a such manner that $|R|^2 + K_T = 1$ (see Eqs. (4.34) and (4.33) for the wave running from the left, and Eqs. (4.45) and (4.44) for the wave running from the right).

In super-critical currents ($V(\xi) > 1$) there are positive- and negative-energy waves both propagating downstream but carrying energy fluxes of opposite signs. Propagating through the inhomogeneity domain $\xi_1 < \xi < \xi_2$, they transform into each other in a such way that the energy flux of each wave grows in absolute value to the greater extent the greater the velocity ratio is. As a result, at $\xi > \xi_2$ the energy flux of each transmitted wave can become greater (in absolute value) than that of the incident wave (see Fig. 4.8). Quantitatively the increase of wave-energy fluxes can be easily estimated in the low-frequency limit using Eqs. (4.65) and (4.73).

The scattering process in accelerating trans-critical currents ($V_1 < 1 < V_2$) looks like a hybrid with respect to those in sub- and super-critical currents. The incident wave can be the only co-current propagating wave of positive energy. Initially, at $\xi < \xi_1$, its energy flux (at unit amplitude) $J_0 = 2\hat{\omega}/V_1$, but in the domain $\xi_1 < \xi < 1$ it partially transforms into the counter-current propagating reflected wave, and at $\xi = 1$ its energy flux is only $J_0(1 - |R|^2)$ (see Eq. (4.103)). Further, in the super-critical domain $1 < \xi < \xi_2$, it generates a negative-energy wave, and the energy fluxes of both waves grow in absolute value to the greater extent the greater V_2 is. And again this process can be better understand in the low-frequency limit by means of Eqs. (4.102).

The most interesting scattering processes takes place in decelerating trans-critical currents ($V_1 > 1 > V_2$) where B-waves (which are either counter-current propagating positive-energy waves or downstream propagating negative energy waves, see Sec. 4.3) run to the critical point (where $V(\xi) = 1$) and become highly-oscillating in its vicinity. For this reason we are forced to give up the model of ideal fluid and to take into account an infinitesimal viscosity in the neighborhood of the critical point. As a result, the energy flux continues to conserve on the left and right of the critical point, but changes in its small vicinity. Let us illuminate the details of this phenomenon.

Consider first an incident positive-energy F-wave arriving from the left. In the transient domain $\xi_1 < \xi < -1$ it partially transforms into the negative-energy B-wave. The total wave flux conserves, whereas the energy flux of each individual wave increases in absolute value up to the critical point (to the more greater extent the greater V_1 is). As follows from the qualitative consideration on the basis of JWKB method (see Section 4.3) and from exact analytical solutions (see Subsection 4.4.4), near the critical point the B-wave becomes highly oscillating in space. This causes its absorption due to viscosity; as will be shown below, the absorption is proportional to ν/λ^2. In contrast to that, the wavelength of the co-current propagating F-wave does not change significantly in the process of transition through the critical point (see Section 4.3), therefore the effect of viscosity onto this wave is negligible. After transition this wave runs through the non-unform subcritical domain $-1 < \xi < \xi_2$ and partially transforms into another B-wave – a counter-current propagating wave of positive energy. This wave approaching the critical point also becomes highly oscillating and therefore absorbs in the vicinity of that point. The energy flux of transmitted F-wave decreases proportional to V_2. The total change of energy flux in transition from the incident to the transmitted wave is described by Eqs. (4.129), and in the limit $\hat{\omega} \to 0$ is determined by the product $V_1 V_2$.

If the incident wave arriving from minus infinity is the B-wave of negative energy carrying a negative energy flux (see J_1 in Eq. (4.135)), then in the transient zone, $\xi_1 < \xi < -1$, it generates due to scattering on inhomogeneous current the F-wave of positive energy, so that the wave fluxes of both waves grow in absolute value. The B-wave absorbs due to viscosity in the vicinity of the critical point $\xi = -1$, whereas the F-wave freely passes through this point with an insignificant change of its wavelength. After passing through the critical point the F-wave generates in the domain $-1 < \xi < \xi_2$ a new B-wave of positive energy, which propagates a counter-current towards the critical point and absorbs in its vicinity due to viscosity. Therefore, the energy flux of the F-wave increases first from zero at $\xi = \xi_1$ up to some maximal value at $\xi = -1$, then it decreases due to transformation of wave energy into the B-wave to some value at $\xi = \xi_2$ (see J_2 in Eq. (4.135)), and then remains constant. In the long-wave approximation, $\hat{\omega} \to 0$, we obtain

$$\begin{aligned}\Delta J \equiv & |J_2| - |J_1| = \left(\frac{V_1}{V_2}|T_2|^2 - 1\right)|J_1| = \\ & \frac{V_2\,|J_1|}{V_1(1+V_2)^2}\left[V_1^2 - V_1\left(4 + V_2 + \frac{1}{V_2}\right) + 1\right]. \end{aligned} \tag{4.143}$$

Analysis of this expression shows that because $V_2 + 1/V_2 \geq 2$, then ΔJ can be positive (i.e., the energy flux of transmitted wave can be greater than the energy flux of incident wave by absolute value), if $V_1 > 3 + 2\sqrt{2} \approx 5.83$.

If there are two incident waves arriving simultaneously from minus infinity so that one of them has positive energy and another one – negative energy, then at some relationships between their amplitudes and phases it may happen that in the transient zone in front of the critical point the superposition of these waves and scattered waves generated by them can annihilate either the positive-energy F-wave or negative-energy B-wave. In the former case it will not be a transmitted wave behind the critical point, because the B-wave in its vicinity completely absorbs (the “opacity” phenomena occurs). In the latter case there is no negative-energy B-wave on the left of the critical point and therefore there is nothing to absorb, and the F-wave passes through this point without loss of energy (we assume that the viscosity is negligible). Further, the F-wave spends some portion of its energy transforming into the counter-current propagating B-wave of positive energy which ultimately dissipates in the vicinity of the critical point. Nevertheless, the residual energy flux of transmitted wave at $\xi > \xi_2$ turns to be equal to the total energy flux of two incident waves at $\xi < \xi_1$, and in such a very particular case the energy flux conserves.

Finally, if an incident B-wave of positive energy arrives from plus infinity, then in the inhomogeneous zone, $-1 < \xi < \xi_2$, it generates a co-current propagating F-wave of positive energy. The energy fluxes of both these waves have opposite signs and decrease in absolute value as one approaches the critical point. In the critical point the energy flux of F-wave vanishes, and the remainder of the B-wave absorbs. In this case the less the V_2 the higher the reflection coefficient $|R|$ is, and this is especially clear in the low-frequency approximation, see Eq. (4.141).

The analysis presented above is based on the fact that the wavelengths of scattered waves drastically decrease in the vicinity of a critical point, where $V(\xi) = 1$. In such case either the dispersion, or dissipation, or both these effects may enter into play. We will show here that at certain situations the viscosity can predominate over the dispersion. Considering the harmonic solution $\sim e^{i\kappa\xi}$ of Eq. (4.83) in the vicinity of a critical point and neglecting the term $\sim V'$, we obtain the dispersion relation extending (4.11). In the dimensional form it is:

$$(\omega - \mathbf{kU})^2 = c_0^2 k^2 - i\nu k^2 (\omega - \mathbf{kU}). \tag{4.144}$$

The solution to this equation for small a viscosity $\nu k \ll c_0$ is

$$\omega = |c_0 \pm U||\mathbf{k}| - i\nu k^2/2. \tag{4.145}$$

The viscosity effect becomes significant when the imaginary and real parts of frequency become of the same order of magnitude. This gives $|\mathbf{k}| \sim 2|c_0 \pm U|/\nu$. Multiplying both sides of this relationship by h, we obtain $|\mathbf{k}|h \sim 2h|c_0 \pm U|/\nu$. For the counter-current propagating B-wave $|c_0 - U| \to 0$, therefore the product $|\mathbf{k}|h$ can be small despite of smallness on ν. So, the condition $|\mathbf{k}|h \sim 2h|c_0 - U|/\nu \ll 1$ allows us to consider the influence of viscosity in the vicinity of a critical point, whereas the dispersion remains negligibly small. In the meantime, the wavelength of co-current propagating F-wave does not change dramatically in the process of transition through the critical point (see Section 4.3). For such wave the viscosity is significant when $|\mathbf{k}|h \sim 2h(c_0 + U)/\nu \gg 1$ which corresponds to the deep-water approximation.

Notice in the conclusion that the wave-current interaction in recent years became a very hot topic due to applications both to the natural processes occurring in the oceans and as a model of physical phenomena closely related with the Hawking radiation in astrophysics [27, 29, 47, 73, 126, 131, 152, 153]. The influence of high-momentum dissipation on the Hawking radiation was considered in astrophysical application [132] (see also [2] where the dissipative fields in de Sitter and black hole spacetimes metrics were studied with application to the quantum entanglement due to pair production and dissipation). The peculiarity of this Chapter is in the finding of exactly solvable model which enabled us to construct analytical solutions and calculate the scattering coefficients in the dispersionless limit. We have shown, in particular, that in the case of accelerating trans-critical current both the reflection coefficient of positive-energy wave and transmission coefficient of negative-energy wave decrease asymptotically with the frequency as $|R| \sim T_n \sim \hat{\omega}^{-1}$. This can be presented in terms of the Hawking temperature $T_H = (1/2\pi)(dU/dx)$ (see, e.g., [131, 153]) and dimensional frequency ω as $|R| \sim T_n \sim 2\pi T_H/\omega$.

Chapter 5

SOLITON INTERACTION WITH EXTERNAL FORCING WITHIN THE KORTEWEG–DE VRIES EQUATION

In this Chapter we revise the solutions of the forced Korteweg–de Vries equation describing a resonant interaction of a solitary wave with external pulse-type perturbations. In contrast to previous works where only the limiting cases of a very narrow forcing in comparison with the initial soliton or a very narrow soliton in comparison with the width of external perturbation were studied, we consider here an arbitrary relationship between the widths of soliton and external perturbation of a relatively small amplitude. In many particular cases, exact solutions of the forced Korteweg–de Vries equation can be obtained for the specific forcings of arbitrary amplitude. We use the earlier developed asymptotic method to derive an approximate set of equations up to the second-order on a small parameter characterising the amplitude of external force. The analysis of exact solutions of the derived equations is presented and illustrated graphically. It is shown that the theoretical outcomes obtained by asymptotic method are in a good agreement with the results of direct numerical modelling within the framework of forced Korteweg–de Vries equation. The results obtained in this Chapter have been published in Chaos: An Interdisciplinary Journal of Nonlinear Science [43].

5.1 Introduction

The forced Korteweg–de Vries (fKdV) equation is a canonical model for the description of resonant excitation of weakly nonlinear waves by moving perturbations. Such an equation was derived by many authors for atmospheric internal waves over a local topography [14, 120], surface and internal water waves generated by moving atmospheric perturbations or in a flow over bottom obstacles [3, 25, 26, 38, 58, 67, 69, 75, 79, 80, 82, 83, 90, 109, 112, 116, 125, 137, 141, 157], internal waves in a rotating fluid with a current over an obstacle [57]. The number of publications on this topic is so huge that it is impossible to mention all of them in this thesis. In addition to the papers mentioned above we will only add a review paper [59] and relatively recent publication [60] where a reader can find some more references.

An effective method of asymptotic analysis of fKdV equation, when the amplitude of external force acting on a KdV soliton is relatively small, was developed in the series of papers by Grimshaw and Pelinovsky with co-authors [62, 63, 64, 66, 121]. Two limiting cases were analysed in those papers: (i) when the width of external force is very small in comparison with the width of a soliton and can be approximated by the Dirac delta-function and (ii) when a soliton width is very small in comparison with the width of external perturbation. Similar approach was used in Ref. [100] where the forcing term was approximated by the derivative of Dirac delta-function.

In the meantime, in the natural conditions a relationship between the widths of solitary wave and external forcing can be arbitrary, therefore it is of interest to generalise the analysis of those authors and consider a resonance between the solitary waves and external forces of arbitrary width. For such arrangements we have found few physically interesting regimes, which were missed in the previous studies. In addition to that, we show that for some special external forces exact solutions of fKdV equation can be obtained even when the amplitude of external force is not small. We compare our solutions derived by means of asymptotic method with the results of direct numerical modelling within the framework of fKdV equation and show that there is a good agreement between two approaches. In the meantime, the numerical simulation demonstrates that there are some effects, which are not caught by the asymptotic theory.

Below we briefly describe the basic model and asymptotic method developed in the papers [62, 63, 64, 66, 121] for the analysis of soliton interaction with external forcing, and then we apply the basic set of approximate equations to the particular cases of stationary and periodic forcing. In Sect. 5.7 we present the results of numerical modelling and comparison of theoretical outcomes with the numerical data. In the Conclusion, we discuss the results obtained in this Chapter.

5.2 The basic model equation and perturbation scheme

In this Chapter we follow the asymptotic method developed in the aforementioned papers [62, 63, 64, 66, 121] and apply it to the fKdV equation in the form:

$$\frac{\partial u}{\partial t}+c\frac{\partial u}{\partial x}+\alpha u\frac{\partial u}{\partial x}+\beta\frac{\partial^3 u}{\partial x^3}=\varepsilon\frac{\partial f}{\partial x}, \tag{5.1}$$

where c, α and β are constant coefficients, and $f(x,t)$ describes the external perturbation of amplitude ε moving with the constant speed V.

Introducing new variables $\hat{x}=x-Vt$, $\hat{t}=t$, we can transform Eq. (5.1) to the following form (the symbol ˆ is further omitted):

$$\frac{\partial u}{\partial t}+(c-V)\frac{\partial u}{\partial x}+\alpha u\frac{\partial u}{\partial x}+\beta\frac{\partial^3 u}{\partial x^3}=\varepsilon\frac{\partial f}{\partial x}. \tag{5.2}$$

This form corresponds to the moving coordinate frame where the external force is stationary and depends only on spatial coordinate x.

In the absence of external force, i.e., when $f(x,t)\equiv 0$, Eq. (5.2) reduces to the well-known KdV equation which has stationary solutions in the form of periodic and solitary waves. We study here the dynamics of a solitary wave under the action of an external force of small amplitude $\varepsilon \ll 1$ assuming that in the zero approximation (when $\varepsilon=V=0$) the solution is

$$u_0=A_0\,\mathrm{sech}^2(\gamma_0\Phi), \tag{5.3}$$

where the inverse half-width of a soliton $\gamma_0=\sqrt{\alpha A_0/12\beta}$ and its speed $\upsilon_0=c+\alpha A_0/3$ depend on the amplitude A_0, $\Phi=x-x_0-\upsilon_0 t$ is the total phase of the soliton, and x_0 is an arbitrary constant determining the initial soliton position at $t=0$.

In the presence of external force of a small amplitude the solitary wave solution (5.3) is no longer valid, but one can assume that under the action of external perturbation it will gradually vary so that its amplitude and other parameters can be considered as functions of “slow time” $\mathrm{T} = \varepsilon t$, so that

$$\upsilon(\mathrm{T}) = c - V + \frac{\alpha A(\mathrm{T})}{3}, \tag{5.4}$$

$$\Psi(\mathrm{T}) = x_0 + \frac{1}{\varepsilon}\int\limits_0^T \upsilon(\tau)\,d\tau. \tag{5.5}$$

Now we have to define functions $A(\mathrm{T})$ and $\upsilon(\mathrm{T})$. This can be done by means of the asymptotic method developed, in particular, in Refs. [61, 66]. Following these papers, we seek for a solution of the perturbed KdV equation (5.2) in the form of the expansion series:

$$\begin{aligned} u &= u_0 + \varepsilon u_1 + \varepsilon^2 u_2 + \ldots \\ \upsilon &= \upsilon_0 + \varepsilon \upsilon_1 + \varepsilon^2 \upsilon_2 + \ldots \end{aligned} \tag{5.6}$$

In the leading order of perturbation method (in the zero approximation), when $\varepsilon = 0$, we obtain the solitary wave solution (5.3) for u_0 and υ_0. In the next approximation we obtain the same solution, but with slowly varying parameters in time. The dependence of soliton amplitude A on T can be found from the energy balance equation [66], which follows from Eq. (5.2) after multiplication by $u(x,t)$ and integration over x:

$$\frac{d}{d\mathrm{T}}\int\limits_{-\infty}^{\infty} \frac{u^2(\Phi)}{2}d\Phi = \int\limits_{-\infty}^{\infty} u(\Phi)\frac{df(\Phi)}{d\Phi}d\Phi. \tag{5.7}$$

Substituting here solution (5.3), we obtain the equations for $A(\mathrm{T})$:

$$\frac{dA}{d\mathrm{T}} = \gamma\int\limits_{-\infty}^{\infty} \operatorname{sech}^2(\gamma\Phi)\frac{df(\Phi+\Psi)}{d\Phi}d\Phi, \tag{5.8}$$

The second equation for $\Psi(T)$ in this approximation represents just a kinematic condition: the time derivative of soliton phase is equal to the instant soliton speed in the moving coordinate frame:

$$\frac{d\Psi}{d\mathrm{T}} = \Delta V + \frac{\alpha A(\mathrm{T})}{3}, \tag{5.9}$$

where $\Delta V = c - V$.

In the second order of asymptotic theory, a correction to the wave speed υ_1 (see Eq. (5.6)) should be taken into account. Leaving aside the derivation of the corrected equation (5.9) (the details can be found in [66]), we present here the final equation:

$$\frac{d\Psi}{d\mathrm{T}} = \Delta V + \frac{\alpha A(\mathrm{T})}{3} + \frac{\varepsilon\alpha}{24\beta\gamma^2}\int\limits_{-\infty}^{\infty}\left[\tanh\gamma\Phi + (\gamma\Phi - 1)\,\mathrm{sech}^2\,\gamma\Phi\right]\frac{\partial f(\Phi+\Psi)}{\partial\Phi}d\Phi. \tag{5.10}$$

Thus, the set of equations in the first approximation consists of Eqs. (5.8) and (5.9), whereas in the second approximation it consists of Eqs. (5.8) and (5.10). However, as has been shown in Ref. [66], the last term in Eq. (5.10) containing small parameter ε dramatically changes the behaviour of the system and makes the result realistic, whereas Eq. (5.9) provides just a rough approximation to the real solution valid at fairly small time interval in the vicinity of a forcing. This difference between the solutions in the first and second approximations will be illustrated in the next Section, and then we will analyse only solutions corresponding to the second approximation described by Eqs. (5.8) and (5.10) for different kinds of external force $f(x)$.

5.3 The KdV-type forcing

Let us consider first the case when

$$f(x) = \mathrm{sech}^2\,\frac{x}{\Delta_f}, \quad V = c + \frac{4\beta}{\Delta_f^2} - \frac{\varepsilon\alpha\Delta_f^2}{12\beta}, \tag{5.11}$$

where Δ_f is a free parameter characterising the half-width of external force.

With this function $f(x)$ one can find an exact solution of Eq. (5.2) in the form of a KdV soliton (5.3) synchronously moving with the external force, $\upsilon_s = V$, and having the amplitude $A_s = 12\beta/\alpha\Delta_f^2$ and half-width $\gamma_s^{-1} = \Delta_f$. This solution represents a particular case of a family of exact solutions to the class of forced generalised KdV equations constructed in Ref. [92]. Note that here the parameters ε and Δ_f are arbitrary, and the amplitude A_s of a soliton is determined only by the width of external force Δ_f, whereas the soliton speed V is determined both by the width Δ_f and amplitude ε of external force.

Let us assume now that the parameter ε is small, and we have the initial condition for Eq. (5.2) in the form of KdV soliton shifted from the centre of forcing and moving with its own velocity υ_0 with the initial amplitude $A_0 \neq A_s$. By substitution of function $f(x)$ from Eq. (5.11) in Eq. (5.8), we obtain for the parameter $\gamma(\mathrm{T})$ the following equation:

$$\frac{d\gamma}{d\mathrm{T}} = -\frac{2\varepsilon\alpha}{3\beta}e^{2\theta}\int\limits_{0}^{\infty}\frac{q^K}{\left(e^{2\theta}+q^K\right)^2}\frac{q-1}{(q+1)^3}dq, \tag{5.12}$$

where $q = \exp{(2\Phi/\Delta_f)}$, $\theta = \gamma\Psi$, and $K = \gamma_0\Delta_f$ is the ratio of half-widths of external force and initial soliton. The parameter K can be also presented in terms of the half-distance D_f between the extrema of forcing function $f(x)$: $K = 2\gamma_0 D_f / \ln{(2+\sqrt{3})}$ (see the distance between maximum and minimum of f'_x in Fig. 5.1).

Equation (5.9) of the first approximation in terms of $\theta = \gamma\Psi$ reads (cf. [66]):

$$\frac{d\theta}{dT} = \Delta V\gamma + 4\beta\gamma^3. \tag{5.13}$$

According to the asymptotic theory, soliton velocity should be close to the forcing velocity. If we assume that at the initial instant of time they are equal, $\upsilon_0 = V$, then we obtain that the forcing amplitude ε is linked with the initial soliton amplitude A_0 through the formula:

$$\varepsilon = \frac{\alpha A_0^2\left(1-K^2\right)}{3K^4}. \tag{5.14}$$

This formula shows that the polarity of forcing depends on the sign of its amplitude ε and is determined by the parameter K: it is positive, if $K < 1$, and negative otherwise.

Dividing Eq. (5.12) by Eq. (5.13), we obtain:

$$\frac{d\gamma}{d\theta} = -\frac{2\varepsilon\alpha e^{2\theta}}{3\beta\gamma\left(\Delta V + 4\beta\gamma^2\right)}\int\limits_0^\infty \frac{q^K}{\left(e^{2\theta}+q^K\right)^2}\frac{q-1}{(q+1)^3}dq. \tag{5.15}$$

This is the first-order separable equation whose general solution can be presented in the form:

$$\Gamma^2 + 2\Gamma = 32\frac{K^2-1}{K^4}\int\int\limits_0^\infty \left[\frac{q^K}{\left(e^{2\theta}+q^K\right)^2}\frac{q-1}{(q+1)^3}dq\right] e^{2\theta}d\theta + C, \tag{5.16}$$

where $\Gamma = A/A_0$ is the dimensionless amplitude of a solitary wave, and C is a constant of integration.

The integrals in the right-hand side of Eq. (5.16) can be evaluated analytically; however we do not present here the results of integration as they are very cumbersome. After evaluation of the integrals in Eq. (5.16), the phase portrait of the dynamical system (5.12)–(5.13) in terms of the dependence $\Gamma(\theta)$ can be plotted for any value of the parameter K.

In the case when the width of initial solitary wave is the same as the width of external force, i.e., $K = 1$, we obtain $\Gamma = 1$ and $C = 3$.

When K varies in the range $0 < K < 1$, then the forcing is positive, $\varepsilon f(x) >$

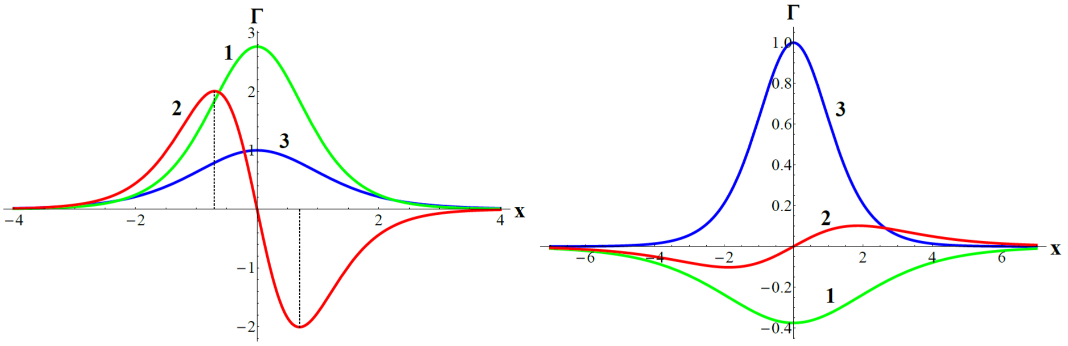

a) b)

Figure 5.1: The shape and polarity of forcing function $f(x)$ (green lines 1) as per Eqs. (5.11) and (5.14) for $K = 0.75$ (a) and $K = 2$ (b), red lines 2 represent the derivatives $f'_x(x)$, and blue lines 3 show the initial KdV solitons of unit amplitudes.

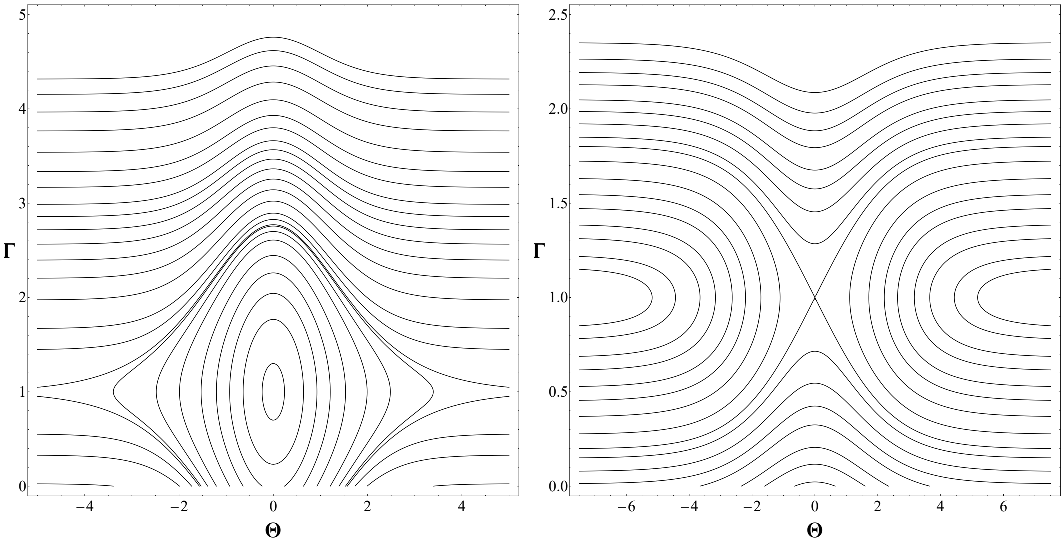

a) b)

Figure 5.2: The phase portraits of the dynamical system (5.12)–(5.13) as per Eq. (5.16) in the first approximation on the parameter ε for $K = 0.75$ (a) and $K = 2$ (b).

0 (see Fig. 5.1a), and the right-hand side of Eq. (5.16) is positive too; then the equilibrium state with $\Gamma = 1$ and $\theta = 0$ is of the centre-type in the phase plane. Therefore, if soliton parameters are such that it is slightly shifted from the equilibrium position, then it will oscillate around this position as shown in the phase plane of Fig. 5.2a). This formally corresponds to the trapping regime when a solitary wave is trapped in the neighbourhood of centre of external force.

If the amplitude and speed of initial soliton are big enough, then the soliton simply passes through the external perturbation and moves away. Such a regime of motion corresponds to the transient trajectories shown in the phase plane of (Fig. 5.2b) above the separatrix (the line dividing trapped and transient

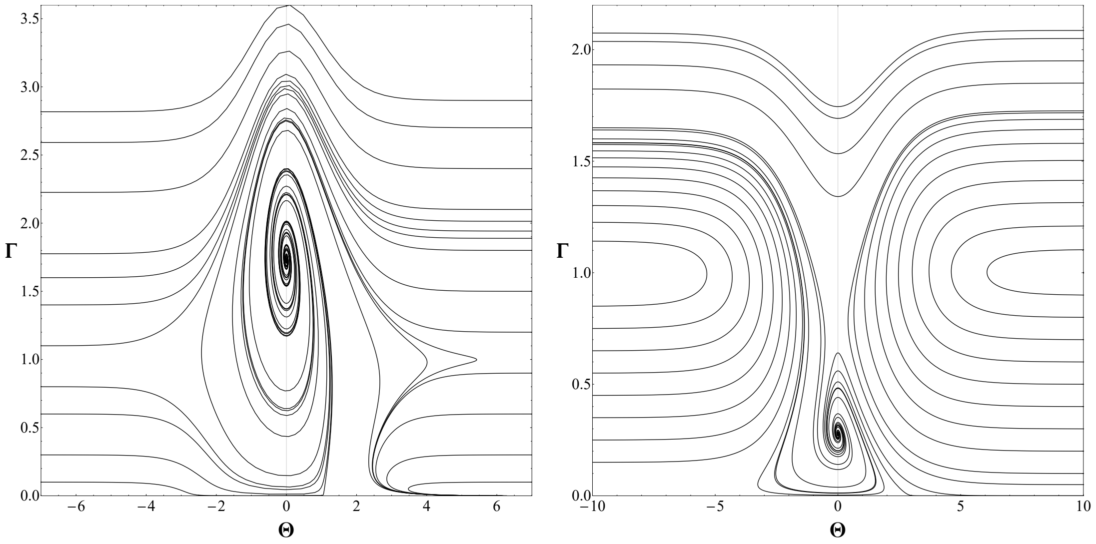

a) b)

Figure 5.3: The phase portraits of the dynamical system (5.12), (5.17) in the second approximation on the parameter ε for $K = 0.75$ (a) and $K = 2$ (b).

trajectories).

There are also trajectories in the lower part of the phase plane which either bury into the horizontal axes with $\Gamma = 0$, or originate from this axis. Such trajectories correspond to decay of solitons of certain amplitudes or birth of solitons from small perturbations, which however appear for a while, but then decay. Some of these trajectory types, which appear within the separatrix, correspond to the "virtual solitons" (see unclosed trajectories within the separatrix in Fig. 5.2a). The "virtual solitons" are generated in the neighbourhood of forcing maximum, then increase, but after a while completely disappear.

When $K > 1$, then the forcing is negative, $\varepsilon f(x) < 0$ (see Fig. 5.1b), the right-hand side of Eq. (5.16) is negative too, and the equilibrium state with $\Gamma = 1$ and $\theta = 0$ is of the saddle-type, as shown in Fig. 5.2b). In this case there are repulsive regimes, where solitary waves approach the forcing either from the left or from the right and bounce back. There are also the transient regimes above and below separatrices, where solitons of big or small amplitudes simply pass through the forcing. There are regimes corresponding to the "virtual solitons", which arise for a while from small perturbations and then disappear (see the trajectories originating at the line $\Gamma = 0$ in Fig. 5.2b).

In this approximation our results are qualitatively similar to the results obtained in Ref. [66], but in contrast to that paper, as well as subsequent papers [62, 63, 64, 121], we do not use here the approximation of soliton or forcing by the Dirac delta-function. In the limiting cases, when the width of one of these entities becomes very small, our results completely reduce to those derived in Ref. [66].

As was already noted in Ref. [66], asymptotic equations of the first approximation actually do not provide physically realistic description of soliton dynamics. Only in the second approximation the dynamical system for Γ and θ reflects a realistic description. In this approximation, Eq. (5.12) remains the same, and Eq. (5.13) should be replaced by a more complex equation, which follows from Eq. (5.10) and in terms of function θ reads:

$$\frac{d\theta}{dT} = \Delta V \gamma + 4\beta\gamma^3 - \frac{\Delta V^2}{\beta\gamma}\frac{K^2-1}{K^4}\int\limits_0^\infty \frac{e^{2\theta}\left(1+2\theta-K\ln q\right)-q^K}{\left(e^{2\theta}+q^K\right)^2}\frac{q-1}{\left(q+1\right)^3}q^K dq. \tag{5.17}$$

The integral on the right-hand side of this equation can be calculated analytically, but the result is very cumbersome. Combining Eq. (5.17) with Eq. (5.12), one can plot the improved phase portrait of the dynamical system; it is shown in Fig. 5.3. It is evident that the phase portrait in the second approximation dramatically differs from the phase portrait of the first approximation. First of all, the equilibrium state of the centre-type in Fig. 5.2a) maps into the unstable focus, alias spiral (see Fig. 5.3a); this has been noticed already in Ref. [66]. Secondly, the equilibrium amplitude Γ in the second approximation is greater than in the first approximation. Thirdly, on the transient trajectories of Fig. 5.3a) soliton amplitudes do not return back to their initial values (cf. asymptotics of transient trajectories above the focus, when $\theta \to \pm\infty$). There are some other important features which were missed in Ref. [66] because of additional approximation of soliton or forcing by the Dirac delta-function. In particular, when $K < 1$, there is a repulsive regime clearly visible in the right lower corner of Fig. 5.3a). Similarly, there are differences in the phase portraits of first and second approximation when $K > 1$. In particular, a new equilibrium state of a stable focus appears below the saddle (which is not visible in Fig. 5.3b) due to rarefaction of trajectories, but clearly implied as a separator between the transient and captured trajectories). Note that in Ref. [66] the focus was mistakenly identified with the centre-type equilibrium state. This equilibrium state corresponds to the small-amplitude soliton trapped by the negative forcing shown in 5.1b). Meanwhile, it is clear from the physical point of view and confirmed through the analysis of dynamical system in the second approximation that a positive forcing, such as shown in Fig. 5.1a), cannot trap and confine a soliton.

5.4 The KdVB-type forcing

In this section we consider Eq. (5.2) with the different and non-symmetric forcing function of the form:

$$f\left(x\right)=\left(\pm 1-\tanh\frac{x}{\Delta_f}\right)\operatorname{sech}^2\frac{x}{\Delta_f}. \tag{5.18}$$

Equation (5.2) with this forcing function can be derived from the Korteweg–de Vries–Burgers (KdVB) equation and has the exact solution for any parameter Δ_f in the form of a shock wave [154]:

$$u\left(x\right)=\varepsilon\Delta_f\left(1\pm\tanh\frac{x}{\Delta_f}+\frac{1}{2}\operatorname{sech}^2\frac{x}{\Delta_f}\right), \tag{5.19}$$

whereas the forcing amplitude ε and speed V are determined by the forcing width Δ_f:

$$\varepsilon=\frac{24\beta}{\alpha\Delta_f^3};\qquad V=c+\frac{24\beta^2}{\Delta_f^2}.$$

The forcing function (5.18) and its derivative f'_x are shown in Fig. 5.4. In the same figure one can see the exact solutions (5.19) for the shock wave (black line in frame a) and "anti-shock wave" (black line in frame b). As follows from the exact solutions, a localised external force can produce a non-localised perturbation for $u(x)$ in the fKdV equation (5.1). Two different forcing functions corresponding to the upper and lower signs in Eq. (5.18) are mirror symmetric with respect to the vertical axis, therefore we illustrate below the solutions generated by only one of them shown in Fig. 5.4a), but for the sake of generality, below we present

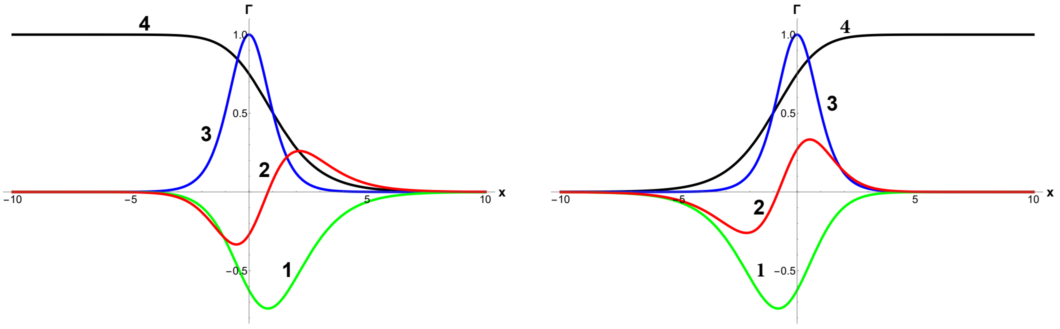

a) b)

Figure 5.4: The forcing function with $K=2$. Frame (a) pertains to the upper sign in Eq. (5.18), and frame (b) – to the lower sign. Green lines (1) illustrate forcing functions $f(x)$, red lines (2) – its derivatives $f'(x)$, blue lines 3 represent the KdV solitons at the initial instant of time, and black lines 4 represent the exact solutions of KdVB equation (5.19) in the forms of shock wave (in frame a) and "anti-shock wave" (in frame b).

solutions for both signs in Eq. (5.18). Note that the forcing function (5.18) of any sign always represents only a negative potential shifted from the centre either to the right or to the left (see green lines 1 in the figure). If the initial perturbation is chosen in the form of a KdV soliton (5.3) and the amplitude of external force is small, $\varepsilon \ll 1$, then we can apply again the asymptotic theory presented in Sect. 5.2 to describe the evolution of a soliton under the influence of external force (5.18). In this case Eq. (5.8) after substitution soliton solution and the forcing function (5.18) reduces to the following equation:

$$\frac{d}{dT}\left(\frac{2A^2}{3\gamma}\right) = \pm\frac{10\beta\varepsilon}{\Delta_f^2}\int\limits_{-\infty}^{\infty} A\,\mathrm{sech}^2(\gamma\Phi)\,\mathrm{sech}^4\left(\frac{\Phi+\Psi}{\Delta_f}\right)\left[2 - e^{\pm\frac{2(\Phi+\Psi)}{\Delta_f}}\right]d\Phi. \quad (5.20)$$

Introducing the parameters $q = e^{2\Phi/\Delta_f}$ and $K = 2\gamma_0 D_f/\ln\left[(7+\sqrt{33})/4\right]$, where D_f as above, is the half-distance between the extrema of forcing derivative f'_x (see Fig. 5.4) and skipping Eq. (5.9) of the first approximation, we present the set of equations (5.8) and (5.10) in the second approximation on the parameter ε as:

$$\frac{d\gamma}{dT} = \mp\frac{320\beta}{\Delta_f^4}e^{2\theta}\int\limits_0^{\infty}\frac{q^{K+1}}{\left(e^{2\theta}+q^K\right)^2}\frac{q^{\pm 1}-2}{(q+1)^4}dq, \quad (5.21)$$

$$\frac{d\theta}{dT} = \Delta V\gamma + 4\beta\gamma^3 \mp \frac{10\Delta V^2}{27\beta\gamma K^4}\int\limits_0^{\infty}\frac{e^{2\theta}\left(1+2\theta-K\ln q\right)-q^K}{\left(e^{2\theta}+q^K\right)^2}\frac{q^{\pm 1}-2}{(q+1)^4}q^{K+1}\,dq, \quad (5.22)$$

where the upper and lower signs correspond to the upper and lower signs in the forcing function (5.18). The set of equations (5.21) and (5.22) does not have equilibrium states for relatively small width of the forcing $K \leq 3$ as shown in Fig. 5.5a). In the phase plane there are either transient trajectories or bouncing trajectories in this case. If the forcing width increases and becomes greater than $K > 3$, then the equilibrium state of a stable focus appears, which corresponds to the trapped KdV soliton of a small amplitude within the potential well as shown in Fig. 5.5b). But when the forcing width further increases and becomes greater than $K > 5$, then the equilibrium state disappears again, and the phase portrait of the system (5.21) and (5.22) becomes qualitatively similar to that shown in Fig. 5.2b).

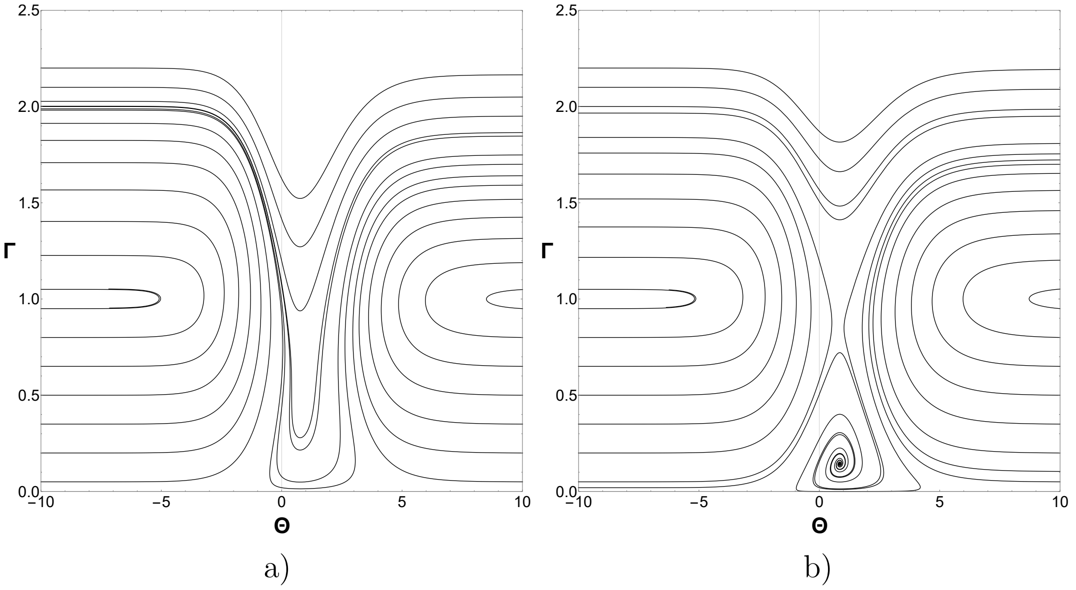

Figure 5.5: The phase portraits of the dynamical system (5.21) and (5.22) with $K = 2$ (frame a) and $K = 3.5$ (frame b).

5.5 The Gardner-type forcing

Consider now the forcing function in the form:

$$f(x) = \frac{1}{\left[1 + B\cosh\left(x/\Delta_f\right)\right]^3}, \tag{5.23}$$

where B, and Δ_f are constant parameters. Its derivative is:

$$f'_x(x) = -\frac{3B(1+B)^3\sinh\left(x/\Delta_f\right)}{\Delta_f\left[1 + B\cosh\left(x/\Delta_f\right)\right]^4}, \tag{5.24}$$

For any parameters ε and Δ_f this forcing provides the exact solution to the fKdV Eq. (5.2) in the form of Gardner soliton (see, e.g., Ref. [118]):

$$u\left(x\right) = \frac{A_f}{1 + B\cosh\left(x/\Delta_f\right)}, \tag{5.25}$$

where $A_f = 6\beta/\alpha\Delta_f^2$, $V = c + \beta/\Delta_f^2$. The parameters B and Δ_f determine the amplitude of external force ε by means of the formula:

$$\varepsilon = -\frac{12\beta^2(B-1)}{\alpha(B+1)^2{\Delta_f}^4}. \tag{5.26}$$

Real nonsingular soliton solutions exist only for $B > 0$ and $B < -1$. When B ranges from 0 to 1, we have a family of solitons varying from a KdV soliton, when $B \to 1_-$, to a table-top soliton, when $B \to 0_+$. When $1 \le B < \infty$, we obtain a family of bell-shaped solitons of positive polarity, and when $-\infty < B < -1$, – a family of bell-shaped solitons of negative polarity (see, e.g., Ref. [118]). The half-width of forcing (5.23), i.e. half-distance between the extrema of function f'_x, is determined by the parameter B:

$$D_f = \Delta_f \ln \left[\frac{1 \pm R \pm \sqrt{2\,(R + R^2 - 42B^2)}}{6B} \right], \qquad (5.27)$$

where $R = \sqrt{1 + 48B^2}$, upper signs pertain to $B > 0$, and lower signs – to $B < 0$. Figure 5.6 shows the parameter $K = \gamma_0 D_f$ as the function of B.

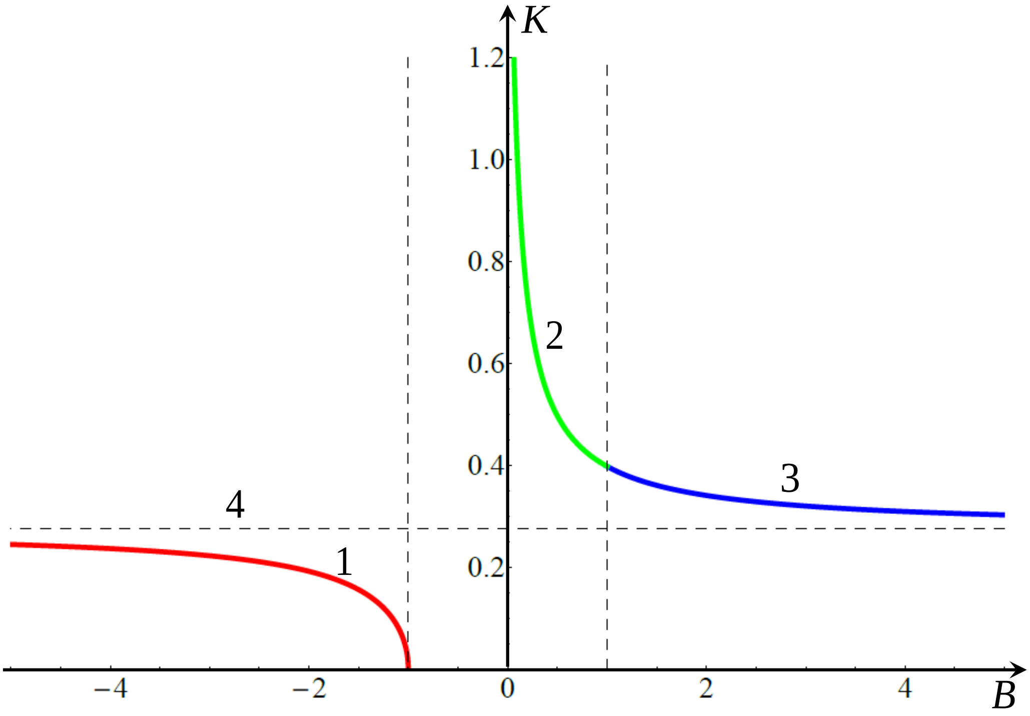

Figure 5.6: The dependence of parameter K characterising the relative width of forcing (5.23) as function of parameter B. Horizontal line 4 shows the asymptotic value of $K = \ln 3/4 \approx 0.275$ when $B \to \pm\infty$.

In the interval $-\infty < B < -1$ the forcing is narrow, $K < 1$ (see line 1 in Fig. 5.6), and function $f(x)$ is positive (see green line 1 in Fig. 5.7a). In the interval $1 < B < \infty$ the forcing is narrow too (see line 3 in Fig. 5.6), but function $f(x)$ is negative (see green line 1 in Fig. 5.11a). In the interval $0 < B < 1$ (see line 2 in Fig. 5.6) the forcing can be both wide, $K > 1$, when B is very close to zero, and narrow, $K < 1$, in the rest of this interval; the forcing function is positive within the entire interval $0 < B \leq 1$ (see green lines 1 in Fig. 5.9. Note that as follows from Eq. (5.26), the amplitude of forcing vanishes when $B \to \pm\infty$, and we have a KdV soliton of arbitrary amplitude freely moving without external action. When $B \to -1_-$, the forcing width becomes zero, but its amplitude goes to infinity; the forcing looks like the Dirac δ-function.

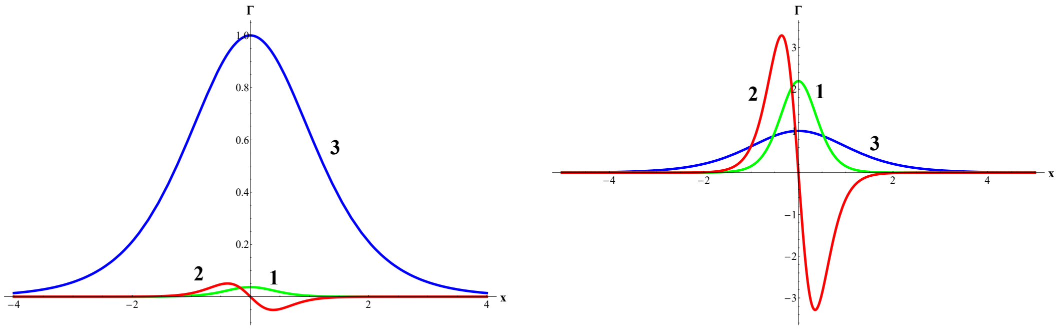

a) b)

Figure 5.7: Green lines 1 represent the forcing function $f(x)$ as per Eq. (5.23), red lines 2 represent its derivatives $f'(x)$, and blue lines 3 show the initial KdV soliton (5.3). In frame a) $K = 0.274$, $B = -221.23$; in frame b) $K = 0.25$, $B = -6.08$.

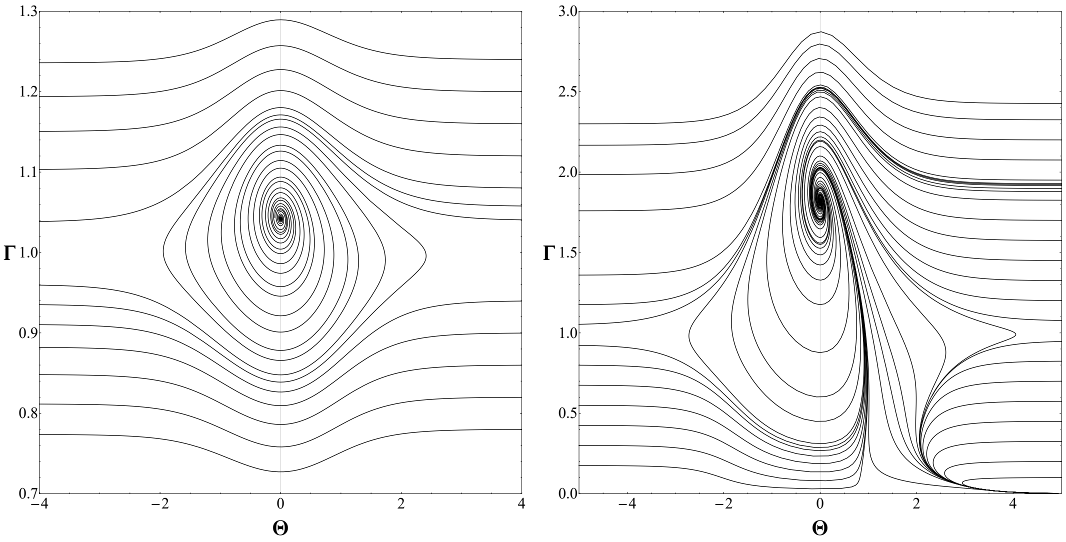

a) b)

Figure 5.8: Phase portraits of the dynamical system (5.28) and (5.29) for $K = 0.274$ (frame a); and $K = 0.25$ (frame b).

When $B \to 0_+$, the forcing becomes infinitely wide. These two limiting cases have been studied in Ref. [66], and our purpose here is to study the situations when K is of the order of unity.

Assume again that the amplitude of external force is small $\varepsilon \ll 1$ and the initial perturbation has the form of KdV soliton (5.3) moving with the initial velocity $v_0 = V$. This gives $\gamma_0 \Delta_f = 1/2$. After substitution of function $f'_x(x)$

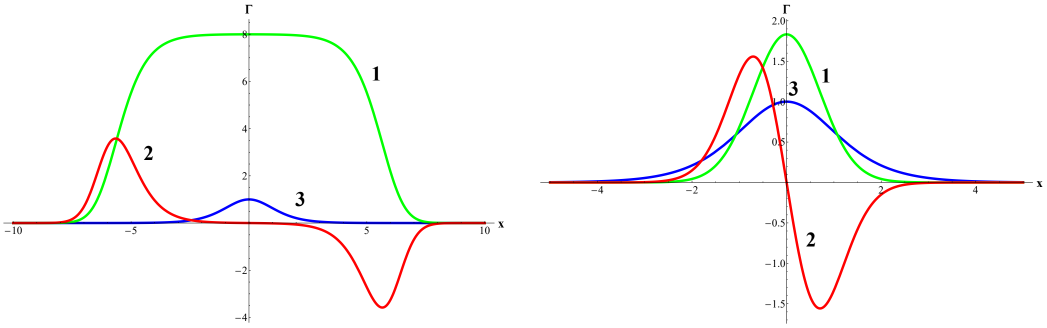

a) b)

Figure 5.9: Green lines 1 represent the forcing function $f(x)$ as per Eq. (5.23), red lines 2 are its derivatives $f'(x)$, and blue lines 3 are the initial KdV soliton (5.3). In frame a) $K = 2$, $B = 0.012$; in frame b) $K = 0.5$, $B = 0.49$.

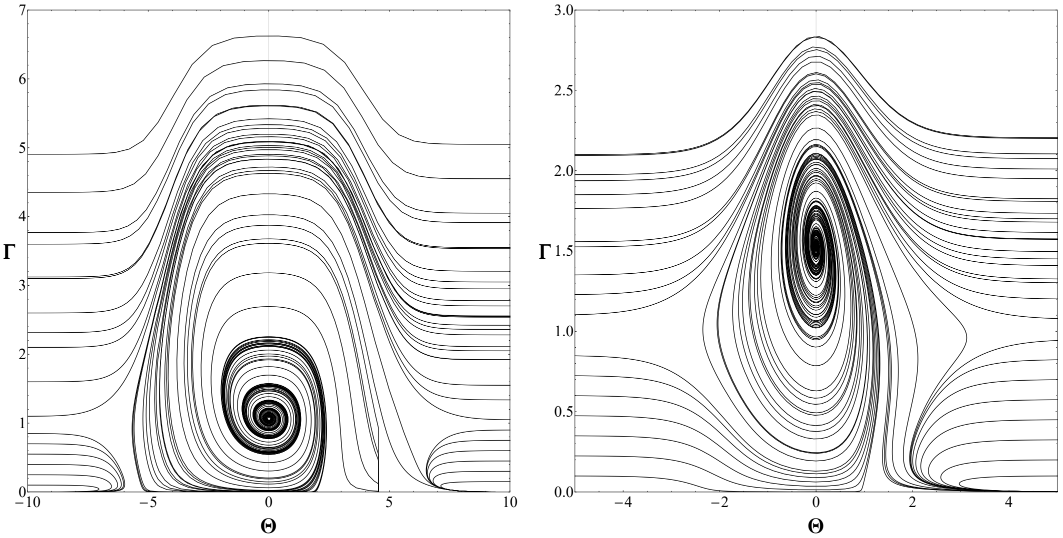

a) b)

Figure 5.10: Phase portraits of the dynamical system (5.28) and (5.29) for $K = 2$ (frame a); and $K = 0.5$ (frame b).

from Eq. (5.24) and soliton solution (5.3) into Eqs. (5.8) and (5.10) and denoting $p = e^{\Phi/\Delta_f}$, we obtain in the second approximation the following set of equations:

$$\frac{d\gamma}{dT} = \frac{48(B^2-1)\Delta V^2}{\beta B^3} e^{2\theta} \int\limits_0^\infty \frac{p^3\left(p^2-1\right)dp}{\left(e^{2\theta}+p\right)^2\left(p^2+2p/B+1\right)^4}, \tag{5.28}$$

$$\frac{d\theta}{dT} = \Delta V\gamma + 4\beta\gamma^3 - \frac{24\Delta V^2}{\beta\gamma}\frac{B^2-1}{B^3}\int\limits_0^\infty \frac{e^{2\theta}\left(1+2\theta-\ln p\right)-p}{\left(e^{2\theta}+p\right)^2}\frac{p^3\left(p^2-1\right)dp}{\left(p^2+2p/B+1\right)^4}. \tag{5.29}$$

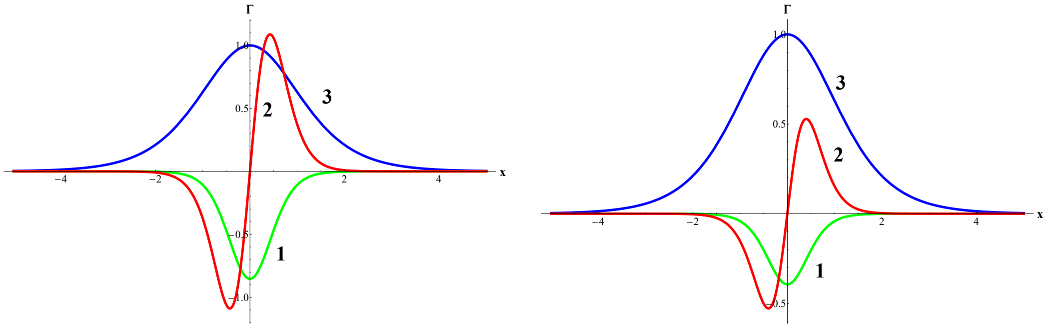

a) b)

Figure 5.11: Green lines 1 are the forcing functions $f(x)$ as per Eq. (5.23), red lines 2 are their derivatives $f'(x)$, and blue lines 3 are the initial KdV solitons (5.3). In frame a) $K = 0.3$, $B = 5.5$; in frame b) $K = 0.283$, $B = 17$.

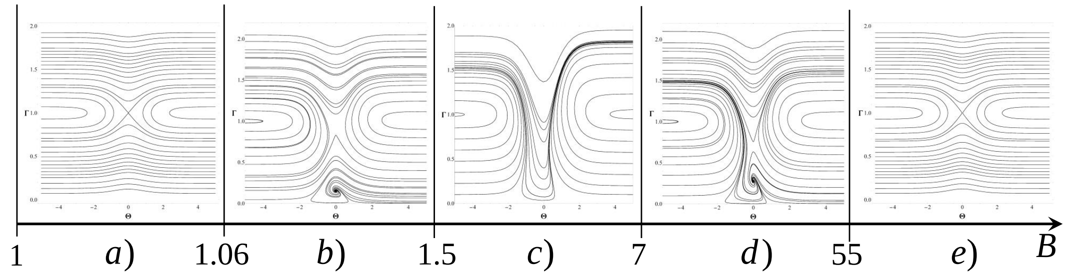

Figure 5.12: Phase portraits of the system (5.28) and (5.29) in the different interval of parameter $B \geq 1$ corresponding to the narrow forcing ($0.275 < K < 0.397$), of a negative polarity. The portraits were generated for the following parameters: frame a): $B = 1.05$, $K = 0.392$; frame b): $B = 1.2$, $K = 0.379$; frame c): $B = 3$, $K = 0.32$; frame d): $B = 12.5$, $K = 0.288$; frame e): $B = 60$, $K = 0.277$.

Below we describe the changes in the phase portraits of the dynamical system (5.28) and (5.29) when the parameter B varies from minus to plus infinity. When this parameter is negative, $-\infty < B < -1$, the forcing is narrow $K < 1$ and positive (see lines 1 in Fig. 5.7). Such forcing with a hump cannot trap a soliton, therefore there is only one equilibrium state, the unstable focus (alias the unstable spiral), which implies that a soliton placed at this state escapes it under the action of infinitely small perturbations (see Fig. 5.8). The only difference between the portraits shown in Figs. 5.8a) and 5.8b) is that there are no transient trajectories in the latter figure below the equilibrium point, but instead the bouncing trajectories appear in the right lower corner.

When the parameter B varies in the range $0 < B \leq 1$, the forcing can be both wide, $K > 1$, and narrow, $K < 1$, but in both cases the potential function is positive (see lines 1 in Fig. 5.9). Again, due to the positive hump-type forcing incapable to trap a soliton, the only one equilibrium state on the phase plane is possible, the unstable focus. The typical phase portraits in this case are qualitatively similar both for the wide and narrow forcing (cf. Figs. 5.10a) and 5.10b) for $K = 2$, $B = 0.012$ and $K = 0.5$, $B = 0.49$ respectively).

When $B > 1$, the forcing is narrow $0.275 < K < 1$, but now negative (see lines 1 in Fig. 5.11). Such forcing with a well can trap a soliton of a very small amplitude in the certain intervals of parameter B. In the interval $1 \leq B < B_1(\approx 1.06)$, there is only one unstable equilibrium state of a saddle type; the typical phase portrait is shown in Fig. 5.12a). Then, in the interval $B_1 < B < B_2(\approx 1.5)$ there is an equilibrium state of the stable focus type; the corresponding phase portrait is shown in frame b). In the next interval $B_2 \leq B < B_3(\approx 7)$ the equilibrium state disappears, and the typical phase portrait is shown in frame c). In the interval $B_3 < B < B_4(\approx 55)$ an equilibrium state of the stable focus type appears again; the corresponding phase portrait is shown in frame d). And at last, in the interval $B > B_4$ the unstable equilibrium state of a saddle type like in the frame a) arises again (see frame e). In the latter case forcing amplitude becomes very small (it asymptotically vanishes when $B \to \infty$), therefore it is incapable to retain a soliton.

5.6 A periodic forcing

Consider now soliton dynamics in the nonstationary external field periodically varying in time and space. A similar problem has been studied in Refs. [19, 30, 64, 68]. As has been shown in those papers, a periodic forcing can lead to both dynamic and chaotic regimes of wave motion. Here we consider a model of forcing which generalises the model studied in Ref. [64] and admits exact solutions. In contrast with the Ref. [64], we do not use here again the approximation of either soliton or external forcing by the Dirac delta-function and study only the dynamic behaviour of a soliton in a periodically varying forcing.

Let us assume that in Eq. (5.1) the forcing function has the form:

$$f(x,t) = \sigma F(t)\,\mathrm{sech}^2\left[\frac{x - \int S(t)dt}{\Delta_f}\right], \tag{5.30}$$

where $F(t)$ and $S(t)$ are arbitrary functions of their argument, and σ is a real parameter.

As has been shown in Ref. [92], the fKdV equation (5.1) with such forcing function has the exact solution for any parameters ε and Δ_f in the form of a soliton moving with the variable velocity $S(t)$:

$$u(x,t) = \frac{12\beta}{\alpha\Delta_f^2}\,\mathrm{sech}^2\left[\frac{x - \int S(t)dt}{\Delta_f}\right], \tag{5.31}$$

where $\sigma = 12\beta/\left(\varepsilon\alpha\Delta_f^2\right)$, and $S(t) = c + 4\beta/\Delta_f^2 - F(t)$.

Let us choose, in particular,

$$F(t) = \frac{\varepsilon\alpha}{12\beta}\Delta_f^2\left(1 + \tilde{V}\sin\varepsilon\omega t\right), \tag{5.32}$$

where $\tilde{V}$ and ω are arbitrary real parameters; then solution (5.31) represents a soliton moving with the mean velocity V as per Eq. (5.11) and periodically varying component proportional to $\tilde{V}\cos(\varepsilon\omega t)$:

$$V_{tot} = c + \frac{4\beta}{\Delta_f^2} - \frac{\varepsilon\alpha\Delta_f^2}{12\beta}\left(1 + \tilde{V}\sin\varepsilon\omega t\right). \tag{5.33}$$

With the choice of $F(t)$ as above, the forcing function has the same shape as in Fig. 5.1, but now the amplitude of forcing function $f(x,t)$ periodically varies in time and the forcing moves with periodically varying speed. Note that in Ref. [64] the authors considered variation of only forcing phase, whereas in our case both the forcing amplitude and phase vary in time.

If $\varepsilon \ll 1$ is a small parameter as above and the initial perturbation has the form of a KdV soliton (5.3), then from the slightly modified asymptotic theory described in Section 5.3 we obtain very similar equations for the first- and second-order approximations. To show this, let us make the transformation of independent variables in Eq. (5.1) $\hat{x} = x - \int S(t)dt$, $\hat{t} = t$, then Eq. (5.1) reduces to the form similar to Eq. (5.2) (the symbol $\hat{}$ is further omitted):

$$\frac{\partial u}{\partial t} + [c - S(t)]\frac{\partial u}{\partial x} + \alpha u\frac{\partial u}{\partial x} + \beta\frac{\partial^3 u}{\partial x^3} = \varepsilon\frac{df(x)}{dx}. \tag{5.34}$$

In the presence of small external perturbation solitary wave solution (5.3) gradually varies, and its amplitude, half-width γ^{-1}, and velocity become slow functions of time $T = \varepsilon t$, so that the soliton phase can be determined as in Section 5.2: $\Phi = x - \Psi(T)$ (cf. Eq. (5.4)), but with the periodically varying speed:

$$v(T) = \frac{\alpha A(T)}{3} - \frac{4\beta}{\Delta_f^2} + \frac{\varepsilon\alpha}{12\beta}\Delta_f^2\left(1 + \tilde{V}\sin\omega T\right). \tag{5.35}$$

The time dependence of soliton amplitude follows from the energy balance equation (5.7). Then carrying out the asymptotic analysis up to the second order on the parameter ε, we eventually obtain the set of equations similar to Eqs. (5.12) and (5.17) with the only modifications caused by the periodic factor in front of integrals:

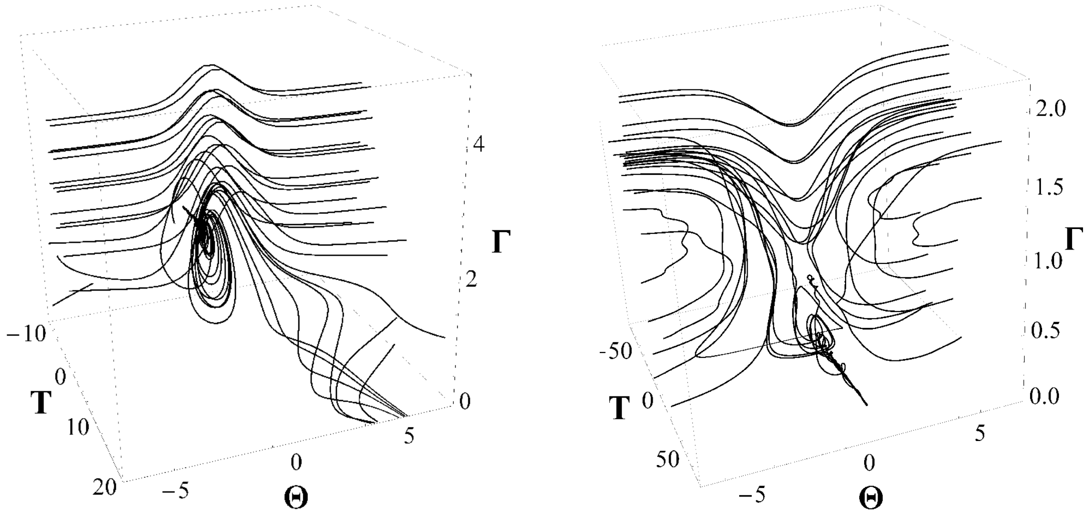

a) b)

Figure 5.13: The phase space θ, Γ, T of the non-stationary dynamical system (5.36), (5.37).

$$\frac{d\gamma}{dT} = \frac{2\varepsilon\alpha}{3\beta}\left(1 + \tilde{V}\sin\omega T\right) e^{2\theta} \int\limits_0^\infty \frac{q^K}{\left(e^{2\theta} + q^K\right)^2} \frac{q-1}{(q+1)^3} dq, \tag{5.36}$$

$$\frac{d\theta}{dT} = \Delta V(T)\gamma + 4\beta\gamma^3 - \frac{\varepsilon\alpha}{3\beta\gamma}\left(1 + \tilde{V}\sin\omega T\right) \cdot \int\limits_0^\infty \frac{e^{2\theta}\left(1 + 2\theta - K\ln q\right) - q^K}{\left(e^{2\theta} + q^K\right)^2} \frac{q-1}{(q+1)^3} q^K dq, \tag{5.37}$$

where now

$$\Delta V(T) = c - V_{tot} = -\frac{4\beta}{\Delta_f^2} + \frac{\varepsilon\alpha}{12\beta}\Delta_f^2\left(1 + \tilde{V}\sin\omega T\right).$$

There are no analytical solutions to this set of equations, but it can be solved numerically, and a qualitative character of solutions can be illustrated by means of three-dimensional phase space, where the third coordinate is the T-axis. Few typical phase trajectories are shown in Fig. 5.13 for the positive and negative forcing functions (cf. with the phase plane shown in Fig. 5.3). Due to oscillations of forcing functions, the phase trajectories revolve around the unstable (frame a) or stable (frame b) focus-type equilibria and displace along the T-axis. Trajectories in frame (a) eventually become parallel to the T-axis; this corresponds to solitary waves escaping from the forcing and uniformly moving with the constant amplitudes and speeds. Trajectories in frame (b), in contrast, eventually converge to the equilibrium point corresponding to the solitary wave trapped by the negative forcing. Such solitary wave ultimately moves synchronously with the forcing having periodically varying amplitude and speed.

5.7 Results of numerical study

To validate the theoretical results obtained on the basis of asymptotic theory, we undertook direct numerical calculations within the framework of original forced KdV equation (5.1) with the different shapes of forcing $f(x,t)$. Below we present the most typical examples for the Gardner-type forcing considered in Section 5.5. In other cases the results obtained were qualitatively similar to presented here. Numerical solutions were obtained by means of the finite-difference code described in [115] and realised in Fortran.

First of all, it was confirmed that in all cases when the forcing is of positive polarity, there is no trapped soliton moving synchronously with the forcing. Even when a KdV soliton was placed initially at the centre of the hump-type forcing, it eventually escaped from the forcing and moved independently. A hump-type narrow forcing was capable to retain a KdV soliton only for while in agreement with the analytical prediction – see the phase planes shown in Figs. 5.3a), 5.8, and 5.10b). In the case of a wide forcing the situation becomes more complicated and leads to the permanent generation of solitary waves at the rear slope of the forcing. Below we describe in detail soliton interaction with the wide and narrow forcing using as an example the Gardner-type forcing.

We considered solutions for $B > 0$ starting from small $B = 0.012$ when the forcing represents a Π-shaped pulse as shown in Fig. 5.9a). According to the asymptotic theory, such forcing leads to the unstable node/spiral on the phase plane (see Fig. 5.10a), which corresponds to the generation of solitons escaping from the forcing zone and moving to the right. However, when a soliton emerging from a small perturbation escapes from the forcing zone, another soliton is created, and the process is repeated many times. Moreover, because the forcing is wide for such parameter B, several solitons can coexist within the forcing zone; then some of them leave this zone while new solitons are generated on the left slope of the forcing function. This was indeed observed, and results obtained are shown in Fig. 5.14. As one can see from this figure, the initial small-amplitude bell-shaped soliton at $t = 0$ starts to grow, but at the same time another perturbation generates on the left slope of the forcing function. Very quickly the number of solitons within the forcing reaches three, then one of them leaves the forcing zone at $t = 140$ and simultaneously one more small soliton is generated at the left slope of forcing. Then the second soliton leaves the forcing zone at $t = 280$ and

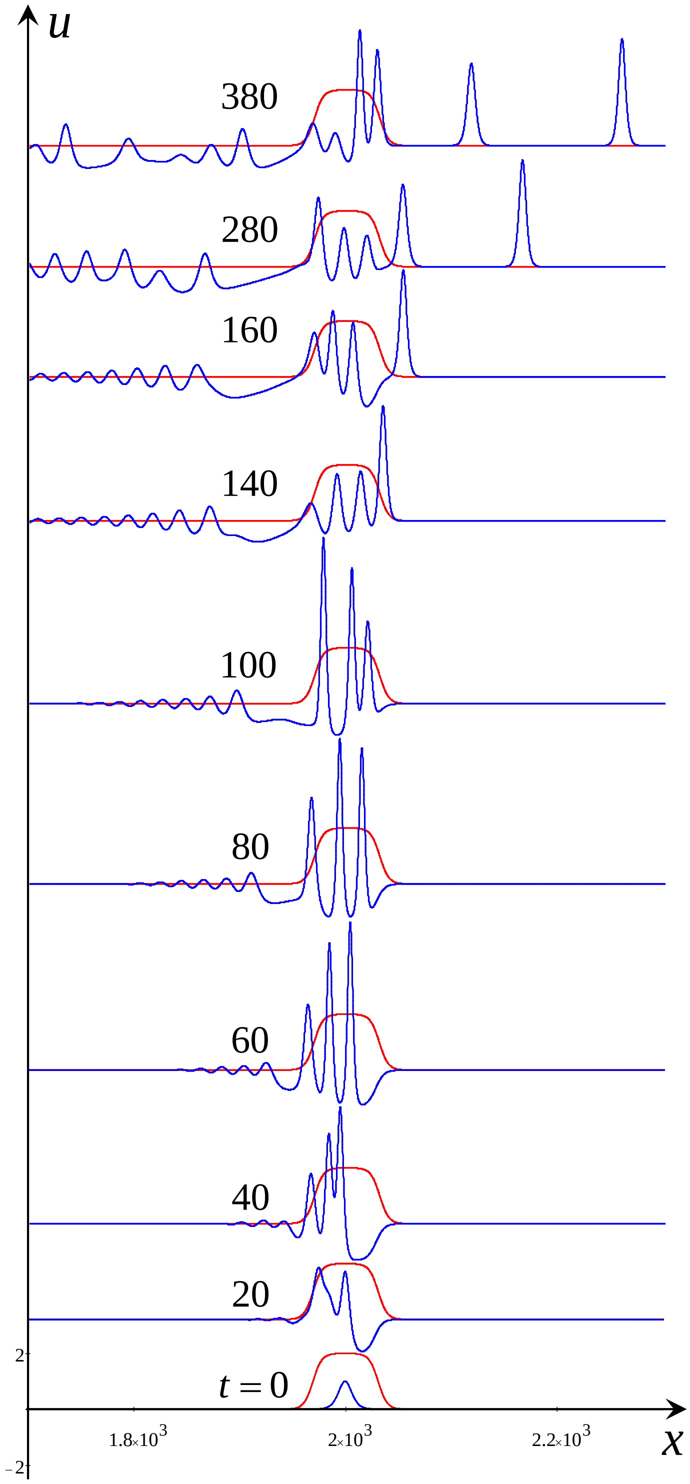

Figure 5.14: Generation of solitons (blue lines) by wide forcing (red lines) in the case of Gardner-type forcing (only a fragment of the spatial domain of total length 4000 is shown). The numerical solution of Eq. 5.1 was obtained with the following parameters $\alpha = 1$, $\alpha_1 = -0.5$, $\beta = 6$, $B = 0.012$.

the process repeats. Thus, the forcing acts as a generator of infinite series of random-amplitude solitons. The details of this and all subsequent processes can been seen in the videos available at the website [42]. The analysis of the analytical

Fig. 5.10a) and numerical results shown in Fig. 5.14 has been carried out. It was confirmed that the range of the amplitudes of the numerically generated solitons agrees well with the theoretically predicted, from A_0 to 3.2 A_0

When the forcing is relatively narrow, it can retain for a while only one soliton, which after a few oscillations within the forcing zone, eventually escapes and freely moves ahead. This is illustrated by Fig. 5.15. In this figure one can see at $t = 0$ the KdV soliton (blue line) and the forcing (slightly taller pulse shown by red line). In the coordinate frame where the forcing is in the rest, the KdV soliton moves to the left first attaining the maximal deviation from the centre at $t \approx 60$; then it moves to the right attaining the maximal deviation from the centre at $t \approx 280$; then it moves again to the left, and so on. However, after three oscillations back and force, it leaves the forcing zone after $t = 1040$ and freely moves further as shown in the figure at $t = 2400$. These 3 oscillations and the amplitude of the detached soliton are predicted theoretically and depicted in Fig. 5.10b). It corresponds to the one of the curves on the phase plane which describes a radiation from the soliton This situation is different when

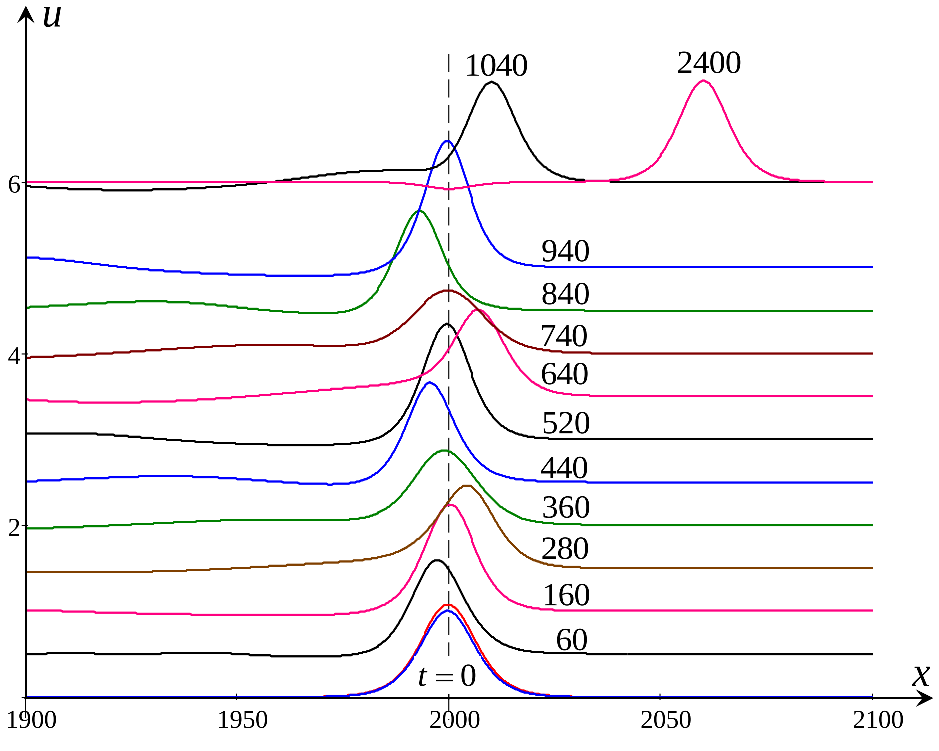

Figure 5.15: Three oscillations of initial KdV soliton (blue line at $t = 0$) and its subsequent separation from the forcing zone at $t > 1040$. The Gardner-type forcing is shown by red line at $t = 0$; dashed vertical line shows the position of forcing maximum. The numerical solution was obtained with the following parameters of Eq. 5.1 $\alpha = 1$, $\alpha_1 = -0.125$, $\beta = 6$, $B = 0.85$, and $L = 4000$.

$B > 1$ and the forcing is negative (see Fig. 5.12). Among numerous situations

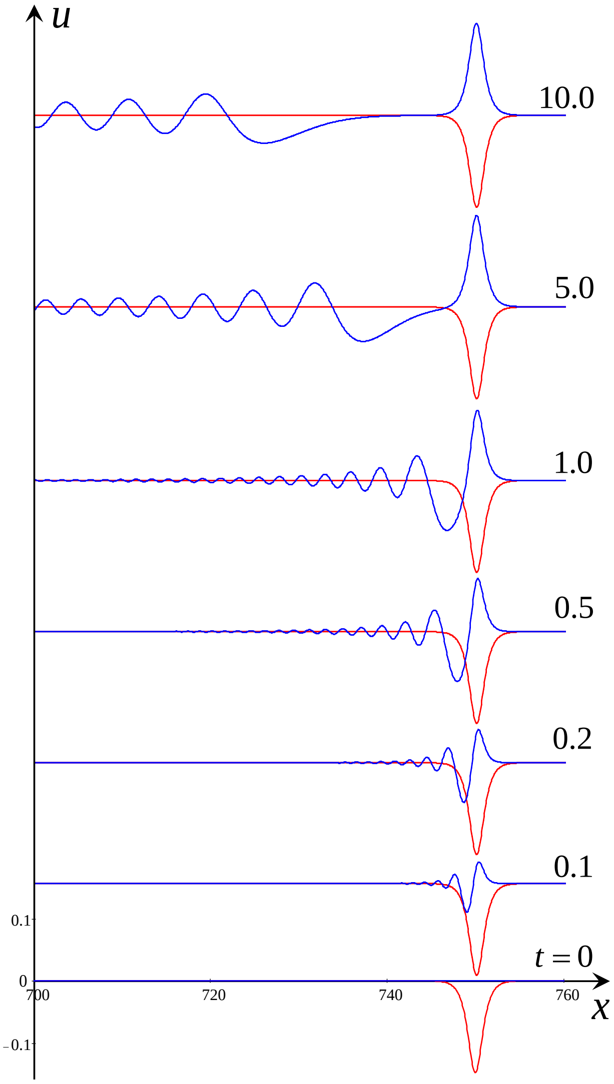

Figure 5.16: Generation of a soliton (blue lines) by the negative forcing (red lines) from a random numerical noise.

arising in this case we shall describe here the most typical scenarios occurring at $B = 12.5$ and corresponding to the phase plane shown in Fig. 5.12d). In this case there is a stable equilibrium state of the node type, which means that a soliton can emerge from small perturbations under the influence of a forcing. This was observed in numerical study with the zero initial condition as shown in Fig. 5.16 at $t = 0$ (all subsequent numerical calculations were obtained with the following parameters in Eq. (5.1): $\alpha = 6$, $\alpha_1 = 465.75$, $\beta = 1$, $B = 12.5$, and the total length of computational domain $L = 1500$). From a random numerical noise a perturbation grows within the forcing zone and becomes well visible at $t = 0.1$. Then it continues growing and developing into a soliton; this process is accompanied by emission of a quasi-linear wave train. Ultimately the wave train disappears, moving to the left and dispersing, whereas a soliton remains stable after being captured at the centre of the forcing in accordance with the theoretical prediction shown in Fig. 5.12d) The amplitude of the generated soliton agrees well with the amplitude in the stable focus point in the phase plane.

A similar situation occurs when, for the initial condition, a small-amplitude soliton is placed within the forcing well. The soliton quickly evolves into the stationary soliton captured in the centre of forcing and emits a quasi-linear dispersive wave train (see Fig. 5.17).

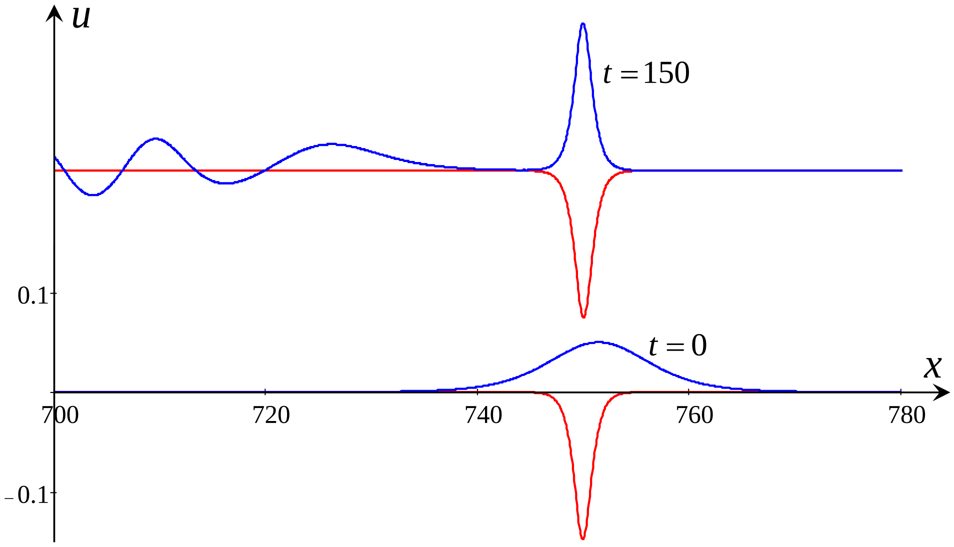

Figure 5.17: Formation of a stationary soliton (blue line at $t = 150$) by the negative forcing (red lines) from a small-amplitude KdV soliton at $t = 0$. The initial soliton was slightly shifted to the right from the centre of forcing well.

If, however, the amplitude of the initial soliton placed within the forcing zone is big, then the soliton splits under the action of forcing, so that one of its portions evolves into the stationary soliton captured in the centre of the forcing well, whereas another portion forms a soliton with different parameters freely moving with its own speed outside of the forcing zone. This process is accompanied by a quasi-linear dispersive wave train (see Fig. 5.18). Such splitting and forming of a secondary soliton is beyond the range of applicability of the asymptotic theory.
In the case when a KdV soliton was placed initially outside of the forcing zone, we observed in numerical study both the reflection from the forcing and transition trough the forcing, as the asymptotic theory predicts for the moderate and big amplitude KdV solitons. Figure 5.19 illustrates the process of soliton reflection when it approaches the forcing from the right; this corresponds to the reflecting regime shown in Fig. 5.12d) on the right of the node. Because the forcing is attractive, it generates a stationary soliton from a noise, as was described above and shown in Fig. 5.16. Therefore the external soliton shown in Fig. 5.19 actually interacts with the forcing carrying a trapped stationary soliton. It is clearly seen in this figure that while the external soliton approaches the forcing,

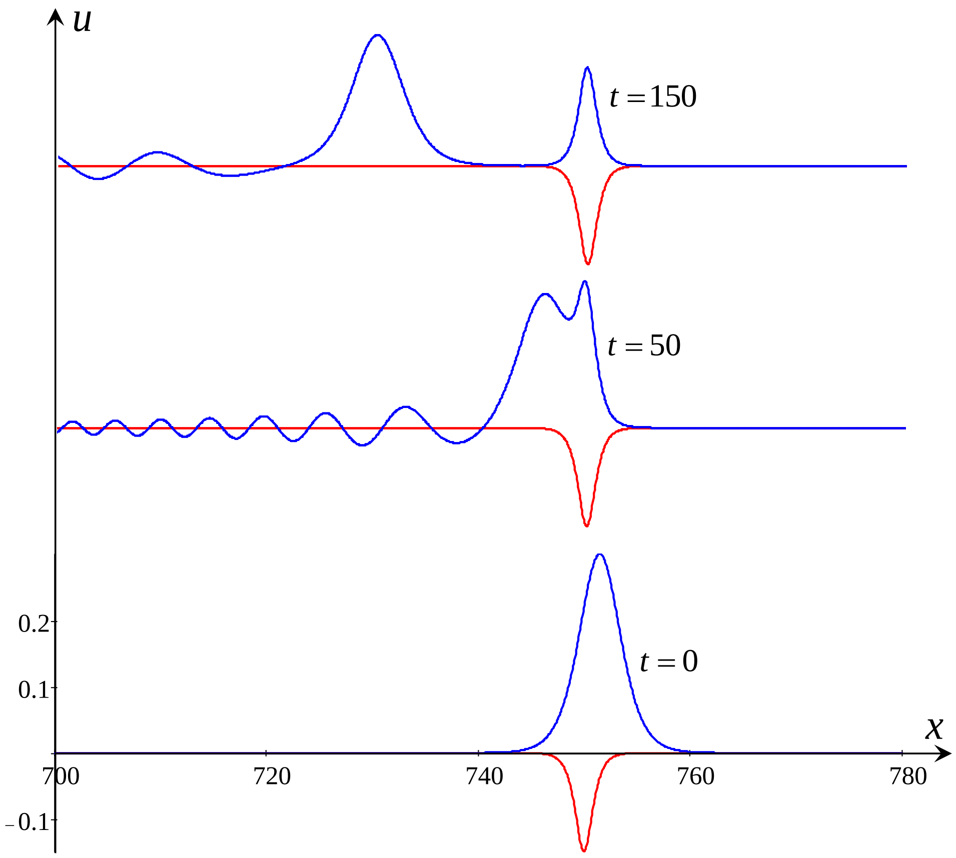

Figure 5.18: Formation of the stationary soliton (blue line at $t = 150$) by the negative forcing (red lines) from the big-amplitude KdV soliton at $t = 0$. The initial soliton was slightly shifted to the right from the forcing centre.

a small-amplitude trapped soliton forms by $t = 10$. Then the external soliton interacts with the forcing and soliton inside it and reflects back with a greater amplitude.

A similar phenomenon occurs when a soliton approaches the forcing from the left as shown in Fig. 5.20. In this figure one can see again that a stationary soliton emerges within the forcing from a noise while the external soliton approaches the forcing. Then the external soliton interacts with the forcing carrying the trapped stationary soliton and reflects back with a smaller amplitude emitting a small-amplitude wave in front of it. This corresponds to the reflecting regime shown in the phase plane of Fig. 5.12d) – see the phase trajectories on the left of the node. If the amplitude of external soliton is relatively big, then after reflection from the forcing it breaks into several solitons as shown in Fig. 5.21. The amplitudes of secondary solitons are noticeably less than the amplitude of the initial soliton; this agrees with the phase trajectories shown on the left from the node in the phase plane of Fig. 5.12d). The process of soliton breakdown onto secondary solitary waves after reflection from the forcing is not described by the asymptotic theory

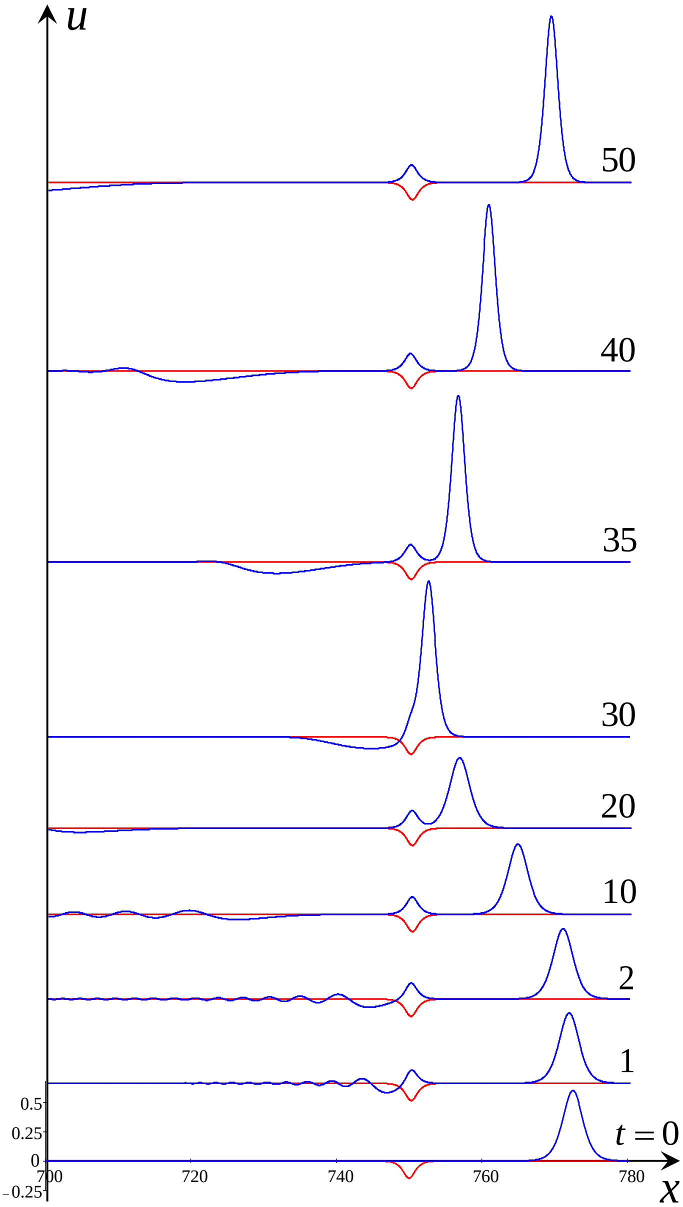

Figure 5.19: Interaction of external KdV soliton approaching from the right with the negative forcing (red lines).

in its current form. When the amplitude of external KdV soliton is too big, then the soliton simply passes through the forcing zone containing a stationary soliton and emits quasi-linear wave train. After that the soliton freely moves ahead as shown in Fig. 5.22. This agrees with the transient phase trajectories shown above the node in the phase plane of Fig. 5.12d).

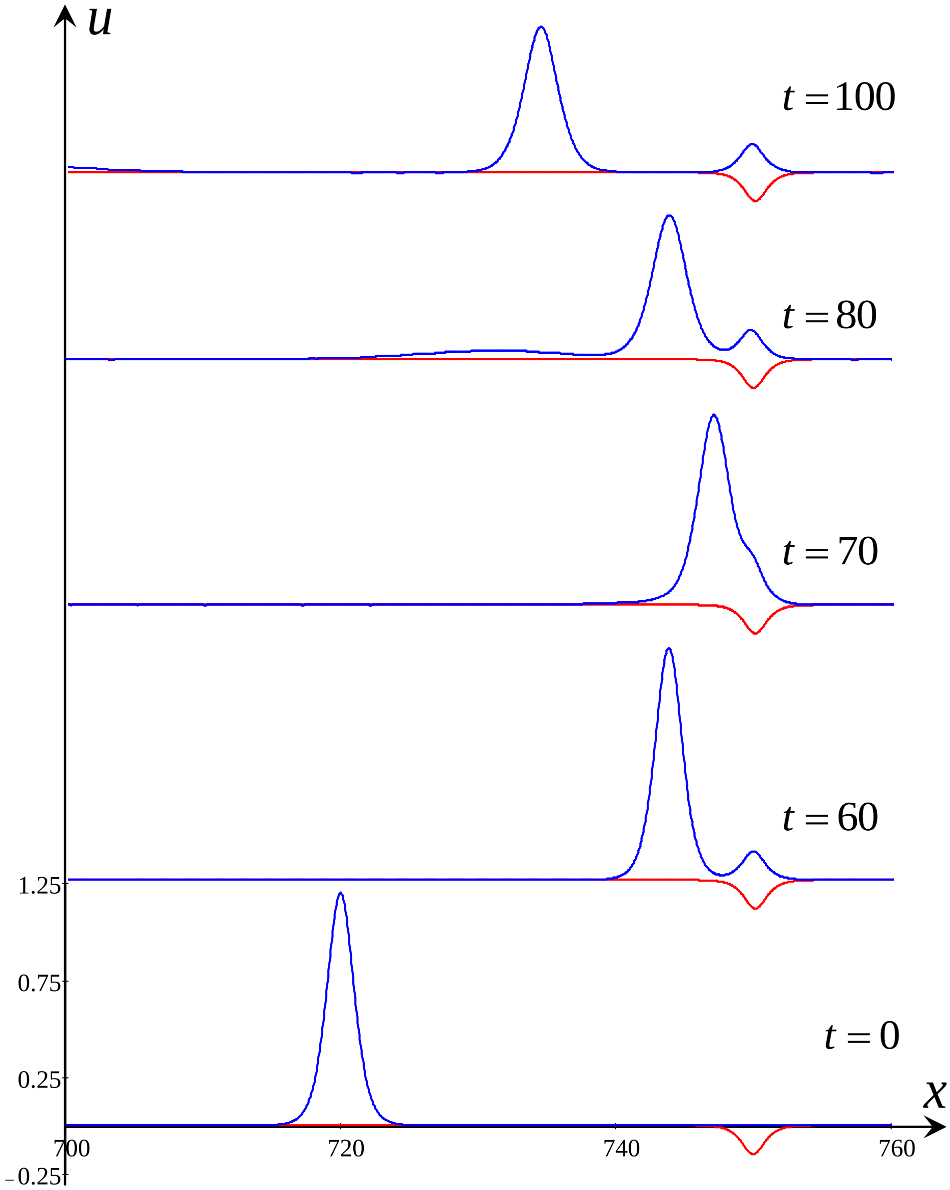

Figure 5.20: Interaction of external KdV soliton approaching from the left with the negative forcing (red lines).

5.8 Conclusion

In this Chapter we have revised the asymptotic theory developed by Grimshaw and Pelinovsky with co-authors in the series of papers [62, 63, 64, 66, 121] to describe the dynamics of solitary waves in the KdV-like equations. In those papers only limiting cases were studied, either when the forcing is infinitely narrow in comparison with the initial KdV soliton and can be approximated by the Dirac δ-function, or vice versa, when the initial KdV soliton is very narrow (approximated by the δ-function) in comparison with the forcing of KdV-soliton shape. In this Chapter we consider an arbitrary relationship between the width of initial KdV

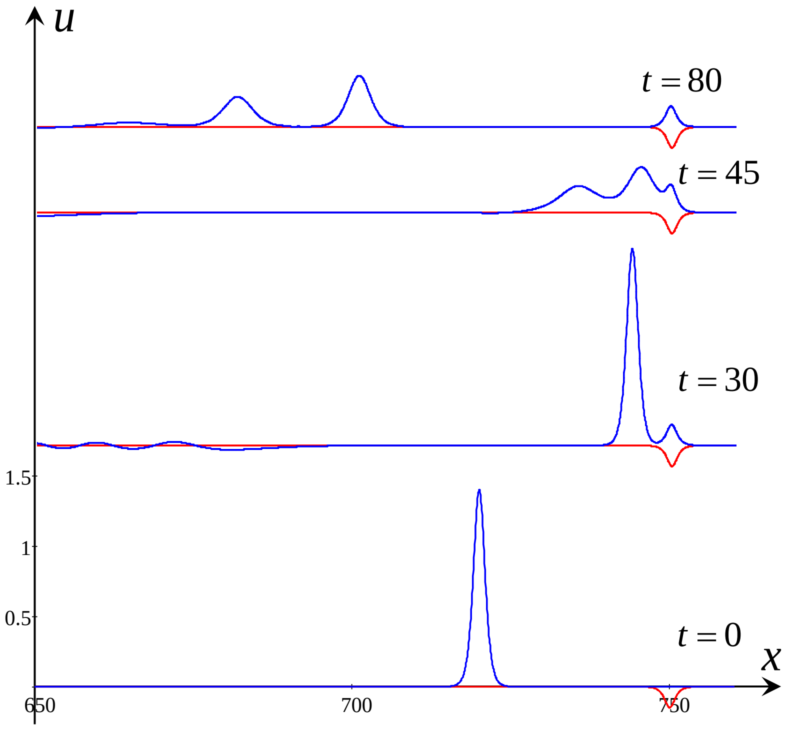

Figure 5.21: Breakdown of an incident external KdV soliton into three solitons after reflection from the negative forcing (red lines).

soliton and external forcing. We present several examples of forced KdV equation which admit exact analytical solutions both stationary and non-stationary.

In the case of small-amplitude forcing we have presented the asymptotic analysis based on equations derived in the papers cited above and have shown that in many cases solutions of approximate equations can be solved analytically, albeit the solutions look very cumbersome. In the limiting cases of very narrow or very wide forcing our results converge to those obtained in the papers by Grimshaw and Pelinovsky[66]. In the meantime, we show that there are some physically interesting regimes which were missed in their papers due to approximations of soliton and forcing by the δ-function. In particular, the equilibrium state of a stable focus in Fig. 5.3b) was mistakenly identified as a centre. Physically this implies that a soliton could oscillate with an arbitrary amplitude around the centre whereas in fact, the soliton quickly approaches a stable state moving synchronously with the forcing. Secondly, the repulsive regimes, when external solitary waves reflect from the forcing, were missed in that paper. Such regimes are clearly seen in the right lower corners of phase plane shown in Figs. 5.3a), 5.8b), and 5.10a),b), as well as illustrated in Figs. 5.19 and 5.20. One of the most interesting regimes discovered in this Chapter is the permanent generation of solitary waves with a random amplitudes on a rear slope of a wide forcing as

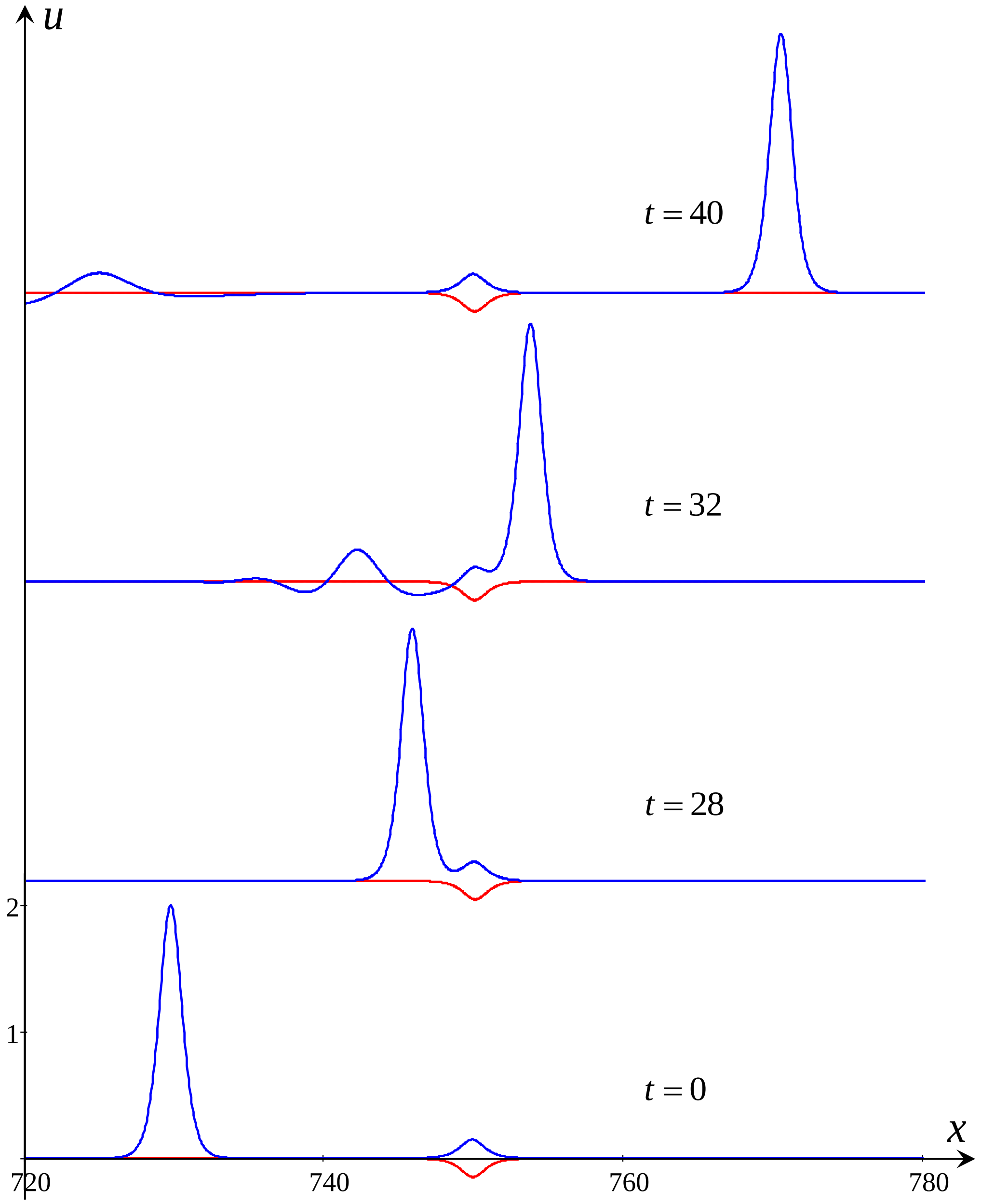

Figure 5.22: Transition of incident external KdV soliton through the negative forcing (red lines).

shown in Fig. 5.14. This effect deserves further study which will undertaken in the nearest future.

The results obtained are important in view of their applications to physical phenomena occurring when external perturbations generate pressure fields capable of exciting and supporting solitary waves. This may happen, for example, when moving atmospheric pressure generates surface waves, or a slow-moving ship generates internal waves, or when atmospheric waves are generated behind high obstacles (for example, mountain ridges or other elevations). A similar phenomena can occur in the oceans when currents flow around underwater obstacles and generate surface and internal waves. The results obtained are applicable to other areas of physics, such as plasma physics and Bose–Einstein condensate, where the highly universal forced Korteweg–de Vries equation is used.

Chapter 6

CONCLUSION AND FUTURE WORK

6.1 Research outcomes

The objective of this research was to study, investigate and develop new exact solutions for classical problems in fluid mechanics, in particular the theories of shallow water waves and solitons. Traditional methods of theoretical and mathematical physics were used, based on the complex analysis technique, asymptotic methods, classical and contemporary methods of mathematical physics, manipulations with special functions. The numerical programs were adapted from the known finite-difference algorithms [115] and implemented in Fortran, Matlab and Wolfram Mathematica.

In Chapter 1, we studied the history of the problems under consideration and reviewed the existing solutions and methods. Calculating the transformation of surface waves over varying obstacles is a long-term problem that has grown more pressing due to increasing technological and societal demands. Development of advanced models to describe the influences of depth variations of the ocean or of particular cross-sections of canals, and the effect of current speed on wave transformation has many applications, from protecting coastlines or natural treasures such as the Great Barrier Reef to the introduction of higher-level safety mechanisms to marine vessels and offshore structures.

The results obtained in the Thesis are also of interest from the viewpoint of modelling of astrophysical phenomena such as the Hawking radiation. In particular, it was rigorously shown in the Thesis that the amplitude of the scattered wave decreases with the frequency as ω^{-1}, whereas in the experiment [155] it was only roughly estimated to be exponentially decreasing.

Whenever a wave passes over a surface, the amplitude and wavenumber of the transmitted wave may be significantly increased compared to the amplitude and wavenumber of the incident wave. To calculate the impact of a transmitted wave on offshore or coastal structures, one must closely analyse and take into account the parameters of the transmitted wave. The complex nature of these effects requires deep analytical modelling in addition to the numerical results. This research looked at four vital considerations – the transformation of long linear waves in an ocean with a variable depth; long wave scattering in a canal with a rapidly varying cross-section; long linear surface waves on stationary currents in a canal of constant depth and variable width; and the revision of the forced Korteweg–de Vries equation to describe a resonant interaction of a solitary wave with external pulse-type perturbations. White spaces in previous research were noted.

In Chapter 2, it was considered and calculated the transformation of long linear waves in an ocean with a variable depth. Here, the transformation coefficients (transmission and reflection) were considered as the functions of frequency and the total depth drop for three typical models of bottom profile variation: piecewise linear, piecewise quadratic and hyperbolic tangent profiles. We compared the influence of the different bottom profiles on the wave transformation and obtained exact analytical solutions for all three reference cases.

For all of these cases exact solutions were obtained, analysed and graphically illustrated, allowing us to derive the transformation coefficients in the analytic form and compare with the available data obtained for the particular models either approximately or numerically. The results obtained were in agreement with the energy flux conservation and Lamb's formulae in the limiting case of zero frequency. We also studied wave transformation (scattering) on the underwater barriers and trenches of different shapes whose slopes can be described by the similar functions (linear, piecewise quadratic, and tanh-functions) and compared the obtained results.

In all cases we obtained qualitatively similar results which were in agreement with those earlier obtained by different authors for some particular cases by the approximate methods. In the limiting case, when the wave frequency goes to zero, we obtained the same transformation coefficients which are predicted by Lamb's theory (1932) [88] for a step-wise bottom.

However, some quantitative differences in the transformation coefficients for the different bottom profiles were found.

For wave scattering on underwater barriers or tranches it has been shown that fewer oscillations in the transformation coefficients occur for the barriers and tranches with linear slopes in comparison to the barriers and tranches with the piecewise quadratic or tanh-slopes.

More complicated real bottom profiles can be approximated with higher accuracy by the combination of linear, quadratic, and tanh-profiles similar to those used in [129], where the bottom profile was approximated by a set of step-wise functions. These results can be used, in particular, for the protection of beaches against storm surges, swells and tsunami waves.

In Chapter 3 it was considered the case of long wave scattering in a canal with a rapidly varying cross-section, where the scattering coefficients (transmission and reflection) were calculated for all possible orientations of incident wave, including background current (downstream and upstream propagation) and current type (subcritical, transcritical, and supercritical). Sometimes, the over-reflection or over-transmission can occur and the negative energy waves can appear. A spontaneous wave generation can happen in a transcritical accelerating flow, when the canal narrowing leads to the increase of the background current. This resembles a spontaneous wave generation on the horizon of an evaporating black hole due to the Hawking effect.

In examining the classic problem of water wave transformation in a canal of a variable cross-section, we studied the coefficients of transformation of long linear waves in a canal of a rectangular cross-section with an abrupt change of geometrical parameters (width and depth). The transmission and reflection coefficients were found as functions of depth ratio and width ratio.

In the study of the subcritical and supercritical flows, we succeeded in calculating the transmission and reflection coefficients in the explicit forms as functions of the depth drop and Froude number. The conditions for the over-reflection and over-transmission have been found in terms of the relationships between the Froude number and canal geometric parameters X and Y. It appears that it is not possible to do the same for transcritical flows, at least within the framework of the simplified model considered in this chapter, because of the complexities of the transition through the critical point.

In Chapter 4, we analytically studied a scattering of long linear surface waves on stationary currents in a duct of constant depth and variable width, assuming that the background velocity linearly increases or decreases with the longitudinal coordinate (gradual variation of duct width). This enabled an analytical solution, calculating the scattering coefficients as functions of incident wave frequency for all possible cases (sub-, super, and trans-critical currents). Both co-current and counter-current wave propagation in accelerating and decelerating currents were studied on a properly varying width to the canal, instead of the step-wise model considered chapter 3.

The results obtained showed that the transformation coefficients can be found in the exact analytical forms both for the co-current and counter-current wave propagation in gradually accelerating and decelerating currents, affecting not only as a model of Hawking's effect, but in application to real physical phenomena occurring in currents in non-homogenous ducts, at least at relatively small Froude numbers. When calculating the transformation coefficients of shallow water gravity waves propagating on a longitudinally varying quasi-one-dimensional current, we calculated analytically the scattering coefficients as functions of incident wave frequency for accelerating and decelerating sub-, super-, and trans-critical currents, and all possible incident wave types.

Presented analysis pertains to the dispersionless case when the wavelengths of all waves in the scattering process are far greater than water depth in the canal. However, the wavelengths can be comparable with or even less than the characteristic length of current inhomogeneity. In the long-wave limit, the scattering coefficients were expressed through the simple algebraic formulae (in agreement with the formulae derived in the previous chapter for the case of abrupt change of canal cross-section).

The analysis was based on the fact that wavelengths of scattered waves drastically decrease in the vicinity of a critical point, where $V(\xi) = 1$. Here, either the dispersion, or dissipation, or both these effects may play an important role. We showed that in certain situations, viscosity can predominate over the dispersion. Wave-current interaction is a contentious issue due to applications including the natural processes occurring in oceans and as a model of physical phenomena relating to the Hawking radiation in astrophysics [27, 29, 47, 73, 126, 131, 152, 153]. The influence of high-momentum dissipation on the Hawking radiation was considered in astrophysical application [132]. This chapter led to the finding of exactly solvable model, enabling us to construct analytical solutions and calculate the scattering coefficients in the dispersionless limit.

In Chapter 5, we considered the nonlinear models of waves transformation and revised the asymptotic theory developed by Grimshaw and Pelinovsky with coauthors in the series of papers [62, 63, 64, 66, 121]. While these authors described the dynamics of solitary waves in the KdV-like equations, their research was limited to when the forcing was infinitely narrow in comparison with the initial KdV soliton and could be approximated by the Dirac δ-function, or when the initial KdV soliton was very narrow (and approximated by the δ-function) in comparison with the forcing of KdV-soliton shape. In our research it was considered an arbitrary relationship between the width of initial KdV soliton and external forcing. There were presented also several examples of forced KdV equation which admit exact analytical solutions both stationary and non-stationary.

For a small-amplitude forcing, we presented the asymptotic analysis based on equations derived in the already mentioned papers and showed that in many cases solutions of approximate equations can be solved analytically, albeit cumbersomely. In the limiting cases of very narrow or very wide forcing our results converge with those obtained by Grimshaw and Pelinovsky [66], but show some physically interesting regimes missed in their paper due to approximation of the soliton and forcing by the δ-function.

The results obtained are important in view of their applications to physical phenomena occurring when external perturbations generate pressure fields capable of exciting and supporting solitary waves. Examples include when moving atmospheric pressure or a slow-moving ship generates waves; when atmospheric waves are generated behind high obstacles like a mountain ridge or when ocean currents flow around underwater obstacles, generating various waves. The results are also applicable to other areas of physics, such as plasma physics and Bose–Einstein condensate, where the highly universal forced Korteweg–de Vries equation is used.

6.2 Future directions

Solving the questions raised in this research has created many new questions, opening up great potential for future research that will have a tangible impact on the physical world.

Regarding Chapter 2, more research is needed to validate and explore the numerical models, but it is also vital that we apply this modelling to real-life scenarios, especially in relation to dependence of wave transmission/reflection on the parameters of the model.

The problems studied in chapters 3 and 4 need to be further generalized for waves of arbitrary length taking into account the effect of dispersion, especially for purely gravity waves where there is always one wave of negative energy for which the flow is supercritical. This negative energy mode smoothly transforms into the dispersionless mode when the flow increases. In such cases two other upstream propagating modes disappear, and the dispersion relations reduce to one. For the current study, it was too difficult to compare theoretical results of this Chapter with the numerical and experimental data and this certainly requires detailed analysis and comparison in the future.

One of the most interesting regimes discovered for the nonlinear modelling and described in Chapter 5 was the permanent generation of solitary waves with a random amplitudes on a rear slope of a wide forcing, which certainly deserves further study in the near future.

In general this Thesis opens new perspectives for further research in fundamental and applied sciences, including study of a gravitational laser (wave amplification in the vicinity of black holes), wave transformation in a nonuniform ocean covered by ice, and solitary wave generation in a deep ocean by moving sources, etc.

APPENDICES

Appendix A: Derivation of time-averaged wave-energy density for gravity waves on a background flow

Here we present the derivation of the time averaged wave energy density of traveling gravity surface wave on a background flow in shallow water when there is no dispersion. In the linear approximation on wave amplitude the depth integrated density of wave energy ("pseudo-energy" according to the terminology suggested by [106]) can be defined as the difference between the total energy density of water flow in the presence of a wave and in the absence of a wave (we remind the reader that in such approximation the wave energy density is proportional to the squared wave amplitude):

$$E = \left\langle \left[\int\limits_0^\eta \rho g z \, dz + \frac{\rho}{2} \int\limits_{-h}^\eta (U+u)^2 \, dz \right] - \frac{\rho}{2} \int\limits_{-h}^0 U^2 \, dz, \right\rangle, \tag{6.1}$$

where the angular brackets stand for the averaging over a period. The first two terms in the square brackets represent the sum of potential and total kinetic energies, whereas the negative terms in the angular brackets represent the kinetic energy density of a current per se. Removing the brackets and retaining only the quadratic terms, we obtain (the linear terms disappear after the averaging over time, whereas the cubic and higher-order terms are omitted as they are beyond the accuracy in the linear approximation):

$$E = \left\langle \frac{\rho g}{2}\eta^2 + \frac{\rho}{2} \int\limits_{-h}^0 (U+u)^2 \, dz + \frac{\rho}{2} \int\limits_{-h}^\eta 2Uu \, dz - \frac{\rho}{2} \int\limits_{-h}^0 U^2 \, dz \right\rangle$$

$$= \frac{\rho g}{2} \left\langle \eta^2 \right\rangle + \frac{\rho h}{2} \left\langle u^2 \right\rangle + \left\langle \rho U \int\limits_{-h}^0 u \, dz + \rho U \int\limits_0^\eta u \, dz \right\rangle. \tag{6.2}$$

In the last angular brackets the first integral disappears after averaging over a period of sinusoidal wave, and the last integral for perturbations of infinitesimal amplitude can be presented in accordance with the "mean value theorem for integrals" as the product $u\eta$. Then, the energy density reads:

$$E = \frac{\rho g}{2}\left\langle \eta^2 \right\rangle + \frac{\rho h}{2}\left\langle u^2 \right\rangle + \rho U \left\langle u\eta \right\rangle . \tag{6.3}$$

Eliminating u with the help of Eq. (3.8), we obtain for the downstream and upstream propagating waves

$$E = \left(\frac{\rho g}{2} + \frac{\rho}{2h}c_0^2 \pm \frac{\rho U c_0}{h}\right)\left\langle \eta^2 \right\rangle = \rho g \left(1 \pm \mathrm{Fr}\right)\left\langle \eta^2 \right\rangle , \tag{6.4}$$

where sign plus pertains to the downstream propagating wave and sign minus – to the upstream propagating wave.

Thus, we see that the wave energy density is negative when $\mathrm{Fr} > 1$, i.e., when a wave propagates against the current. In the meantime, the dispersion relation in a shallow water can be presented as $\omega = c_0|k| + \mathbf{U}\cdot\mathbf{k}$, so that for the cocurrent propagating wave with $k > 0$ we have $\omega = (c_0 + U)k = c_0k(1 + \mathrm{Fr})$, whereas for the countercurrent propagating waves with $k < 0$ we have $\omega = (c_0 - U)|k| = c_0k(\mathrm{Fr} - 1)$ (see Eq. (3.6) and explanation of Fig. 3.4). Then the group velocity $V_g = d\omega/dk = c_0(\mathrm{Fr} - 1)$ is positive if $\mathrm{Fr} > 1$ and negative if $\mathrm{Fr} < 1$. Hence, the wave energy flux for the negative energy waves in the supercritical case with $\mathrm{Fr} > 1$ is $W \equiv EV_g < 0$ and directed against the group velocity.

Notice in the conclusion that the relationship between the wave energy and frequency follows directly from the conservation of wave action density N (see Ref. [98] and references therein):

$$N = \frac{E}{\omega - \mathbf{U}\cdot\mathbf{k}} = \frac{E_0}{\omega}, \tag{6.5}$$

where E is the density of wave energy in the immovable coordinate frame (6.4) where the water flows with the constant speed $\mathbf{U}$, and E_0 and $\omega = c_0|\mathbf{k}|$ are the density of wave energy and frequency in the coordinate frame moving with the water.

Appendix B: Energy flux conservation

Let us multiply equation (4.5) by the complex-conjugate function $\overline{\varphi}$ and subtract from the result complex-conjugate equation:

$$\begin{aligned}&\overline{\varphi}\left(\frac{\partial}{\partial t}+U\frac{\partial}{\partial x}\right)\left(\frac{\partial\varphi}{\partial t}+U\frac{\partial\varphi}{\partial x}\right)-\varphi\left(\frac{\partial}{\partial t}+U\frac{\partial}{\partial x}\right)\left(\frac{\partial\overline{\varphi}}{\partial t}+U\frac{\partial\overline{\varphi}}{\partial x}\right)=\\&c_0^2U\left[\overline{\varphi}\frac{\partial}{\partial x}\left(\frac{1}{U}\frac{\partial\varphi}{\partial x}\right)-\varphi\frac{\partial}{\partial x}\left(\frac{1}{U}\frac{\partial\overline{\varphi}}{\partial x}\right)\right].\end{aligned}\tag{6.6}$$

Dividing this equation by U and rearranging the terms we present this equation in the form:

$$\begin{aligned}&\frac{\partial}{\partial t}\left[\frac{\overline{\varphi}}{U}\left(\frac{\partial\varphi}{\partial t}+U\frac{\partial\varphi}{\partial x}\right)-\frac{\varphi}{U}\left(\frac{\partial\overline{\varphi}}{\partial t}+U\frac{\partial\overline{\varphi}}{\partial x}\right)\right]+\\&\frac{\partial}{\partial x}\left[\overline{\varphi}\left(\frac{\partial\varphi}{\partial t}+U\frac{\partial\varphi}{\partial x}\right)-\varphi\left(\frac{\partial\overline{\varphi}}{\partial t}+U\frac{\partial\overline{\varphi}}{\partial x}\right)-\frac{c_0^2}{U}\left(\overline{\varphi}\frac{\partial\varphi}{\partial x}-\varphi\frac{\partial\overline{\varphi}}{\partial x}\right)\right]=0.\end{aligned}\tag{6.7}$$

If we denote

$$\mathcal{E}=\frac{\mathrm{i}}{U}\left[\bar{\varphi}\left(\frac{\partial\varphi}{\partial t}+U\frac{\partial\varphi}{\partial x}\right)-\varphi\left(\frac{\partial\bar{\varphi}}{\partial t}+U\frac{\partial\bar{\varphi}}{\partial x}\right)\right],\tag{6.8}$$

$$J=\mathcal{E}U-\mathrm{i}\,\frac{c_0^2}{U}\left(\bar{\varphi}\frac{\partial\varphi}{\partial x}-\varphi\frac{\partial\bar{\varphi}}{\partial x}\right),\tag{6.9}$$

then Eq. (6.7) can be presented in the form of the conservation law

$$\frac{\partial\mathcal{E}}{\partial t}+\frac{\partial J}{\partial x}=0,\tag{6.10}$$

For the waves harmonic in time, $\varphi=\Phi(x)e^{-i\omega t}$, both $\mathcal{E}$ and J do not depend on time, and Eq. (6.10) reduces to $J=\text{const}$. Substituting in Eq. (6.9) written in the dimensionless form solution (4.16) for $\xi<\xi_1$ and solution (4.18) for $\xi>\xi_2$, after simple manipulations we obtain

$$J=\frac{2\hat{\omega}}{V_1}\left(1-|R|^2\right),\quad \xi<\xi_1;\tag{6.11}$$

$$J=\frac{2\hat{\omega}}{V_2}\,|T|^2,\qquad\qquad \xi>\xi_2.\tag{6.12}$$

Equating J calculated in Eqs. (6.11) and (6.12), we obtain the relationship between the transformation coefficients presented in Eq. (4.34).

Using then solution (4.17) for $\xi_1 < \xi < \xi_2$, we obtain

$$\begin{aligned} J =&2\hat{\omega}\left|B_1 w_2(\xi^2) + B_2 w_3(\xi^2)\right|^2 - 2i(1-\xi^2)\left\{|B_1|^2\left[w_2'(\xi^2)\overline{w_2}(\xi^2) - \right.\right.\\ &\left.\overline{w_2'}(\xi^2)w_2(\xi^2)\right] + |B_2|^2\left[w_3'(\xi^2)\overline{w_3}(\xi^2) - \overline{w_3'}(\xi^2)w_3(\xi^2)\right] + \\ &B_1\overline{B_2}\left[w_2'(\xi^2)\overline{w_3}(\xi^2) - w_2(\xi^2)\overline{w_3'}(\xi^2)\right] - \\ &\left.\overline{B_1}B_2\left[\overline{w_2'}(\xi^2)w_3(\xi^2) - \overline{w_2}(\xi^2)w_3'(\xi^2)\right]\right\} = \text{const}. \end{aligned} \tag{6.13}$$

It was confirmed by direct calculations with the solutions (4.16)–(4.18) that J is indeed independent of ξ for given other parameters.

In a similar way, for the super-critical accelerating current one can obtain in the intermediate interval $\xi_1 < \xi < \xi_2$

$$\begin{aligned} J =&\frac{2\hat{\omega}}{\xi^2}\left|B_1\breve{w}_1(\xi^{-2}) + B_2\breve{w}_3(\xi^{-2})\right|^2 - \frac{2\mathrm{i}\,(\xi^2-1)}{\xi^4}\left\{|B_1|^2\left[\breve{w}_1'(\xi^{-2})\overline{\breve{w}_1}(\xi^{-2}) - \right.\right.\\ &\left.\overline{\breve{w}_1'}(\xi^{-2})\breve{w}_1(\xi^{-2})\right] + |B_2|^2\left[\breve{w}_3'(\xi^{-2})\overline{\breve{w}_3}(\xi^{-2}) - \overline{\breve{w}_3'}(\xi^{-2})\breve{w}_3(\xi^{-2})\right] + \\ &B_1\overline{B_2}\left[\breve{w}_1'(\xi^{-2})\overline{\breve{w}_3}(\xi^{-2}) - \breve{w}_1(\xi^{-2})\overline{\breve{w}_3'}(\xi^{-2})\right] - \\ &\left.\overline{B_1}B_2\left[\overline{\breve{w}_1'}(\xi^{-2})\breve{w}_3(\xi^{-2}) - \overline{\breve{w}_1}(\xi^{-2})\breve{w}_3'(\xi^{-2})\right]\right\} = \text{const}. \end{aligned} \tag{6.14}$$

Here the coefficients B_1 and B_2 should be taken either from Eqs. (4.59) and (4.60) for the scattering of positive energy wave or from Eqs. (4.68) and (4.69) for the scattering of negative energy wave.

The transformation coefficients R and T were derived in this Chapter in terms of the velocity potential φ. But they can be also presented in terms of elevation of a free surface η. Using Eq. (4.4) for $x < x_1$ and definition of φ just after that equation we obtain for a wave sinusoidal in space

$$(\omega - \mathbf{k}\cdot\mathbf{U_1})\eta = khu = \mathrm{i}hk^2\varphi. \tag{6.15}$$

Bearing in mind that according to the dispersion relation $\omega - \mathbf{k}\cdot\mathbf{U_1} = c_0|k|$, we find from Eq. (6.15)

$$\varphi = -\mathrm{i}\frac{c_0}{h|k|}\eta = -\mathrm{i}\frac{c_0(c_0 \pm U_1)}{h\omega}\eta, \tag{6.16}$$

where sign plus pertains to co-current propagating incident wave and sign minus – to counter-current propagating reflected wave.

Similarly for the transmitted wave for $x > x_2$ we derive

$$\varphi = -\mathrm{i}\frac{c_0(c_0 + U_2)}{h\omega}\eta. \tag{6.17}$$

Substitute expressions (6.16) and (6.17) for incident, reflected and transmitted waves into Eq. (4.34) and bear in mind that $R \equiv \varphi_r/\varphi_i$, $T \equiv \varphi_t/\varphi_i$, and ω and c_0 are constant parameters:

$$V_2 \left[(1+V_1)^2 - (1-V_1)^2 \, |R_\eta|^2\right] = V_1 \, (1+V_2)^2 \, |T_\eta|^2, \tag{6.18}$$

where

$$R_\eta \equiv \frac{\eta_r}{\eta_i} = \frac{1+V_1}{1-V_1} R, \quad \text{and} \quad T_\eta \equiv \frac{\eta_t}{\eta_i} = \frac{1+V_1}{1+V_2} T. \tag{6.19}$$

In such form Eq. (4.34) represents exactly the conservation of energy flux (see [24, 98]).

Appendix C: Derivation of matching conditions for equation (4.8)

To derive the matching conditions in the point ξ_1, let us present Eq. (4.8) in two equivalent forms:

$$\left[\left(V - \frac{1}{V}\right) \Phi\right]'' - \left[\left(1 + \frac{1}{V^2}\right) V' \Phi\right]' - 2\,\mathrm{i}\,\hat{\omega}\,\Phi' - \frac{\hat{\omega}^2}{V}\,\Phi = 0. \tag{6.20}$$

$$\left[\left(V - \frac{1}{V}\right) \Phi'\right]' - 2\,\mathrm{i}\,\hat{\omega}\,\Phi' - \frac{\hat{\omega}^2}{V}\,\Phi = 0, \tag{6.21}$$

Let us multiply now Eq. (6.21) by $\zeta = \xi - \xi_1$ and integrate it by parts with respect to ζ from $-\varepsilon$ to ε:

$$\begin{aligned} &\left\{\zeta \left[\left(V - \tfrac{1}{V}\right) \Phi' - 2\,\mathrm{i}\,\hat{\omega}\,\Phi\right] - \left(V - \tfrac{1}{V}\right) \Phi\right\}\Big|_{-\varepsilon}^{\varepsilon} + \\ &\int\limits_{-\varepsilon}^{\varepsilon} \left[\left(1 + \tfrac{1}{V^2}\right) V' + 2\,\mathrm{i}\,\hat{\omega} - \tfrac{\hat{\omega}^2}{V}\,\zeta\right] \Phi \, d\zeta = 0. \end{aligned} \tag{6.22}$$

In accordance with our assumption about the velocity, function $V(\zeta)$ is piecewise linear, and its derivative is piece-constant. Assuming that function $\Phi(\zeta)$ is limited on the entire ζ-axis, $|\Phi| \le M$, where $M < \infty$ is a constant, we see that the integral term vanishes when $\varepsilon \to 0$. The very first term, which contains ζ in front of the curly brackets $\{\ldots\}$, also vanishes when $\varepsilon \to 0$, and we have

$$\left[\left(V - \frac{1}{V}\right) \Phi\right]\Bigg|_{-\varepsilon}^{\varepsilon} = 0. \tag{6.23}$$

This implies that $\Phi(\zeta)$ is a continuous function in the point $\zeta = \zeta_1$.

If we integrate then Eq. (6.20) with respect to ζ in the same limits as above, we obtain:

$$\left[\left(V - \frac{1}{V}\right)\Phi' - 2\,\mathrm{i}\,\hat{\omega}\,\Phi\right]\Bigg|_{-\varepsilon}^{\varepsilon} - \hat{\omega}^2 \int\limits_{-\varepsilon}^{\varepsilon} \frac{\Phi(\zeta)}{V(\zeta)}\,d\zeta = 0. \tag{6.24}$$

Under the same assumptions about functions $V(\zeta)$ and $\Phi(\zeta)$, the integral term here vanishes when $\varepsilon \to 0$ and we obtain:

$$\left[\left(V - \frac{1}{V}\right)\Phi' - 2\,\mathrm{i}\,\hat{\omega}\,\Phi\right]_{-\varepsilon} = \left[\left(V - \frac{1}{V}\right)\Phi' - 2\,\mathrm{i}\,\hat{\omega}\,\Phi\right]_{\varepsilon}. \tag{6.25}$$

Due to continuity of functions $V(\zeta)$ and $\Phi(\zeta)$ in the point $\zeta = \zeta_1$, we conclude that the derivative $\Phi'(\zeta)$ is a continuous function in this point too. The same matching conditions can be derived for the point ξ_2 as well.

Appendix D: The transformation coefficients in the long-wave limit

The long-wave approximation in the dispresionless case considered here corresponds to the limit $\omega \to 0$. In such a case the wavelength of each wave is much greater than the length of the transient domain, $\lambda \gg L$, so that the current speed transition from the left domain $\xi < \xi_1$ to the right domain $\xi > \xi_2$ can be considered as sharp and stepwise. Then using the relationships (see [95])

$${}_2F_1(a, b; b; s) = (1 - s)^{-a} \quad \text{and} \quad s\,{}_2F_1(1, 1; 2; s) = -\ln(1 - s),$$

we can calculate functions (4.19) and (4.22), as well as (4.50) and (4.53), and their derivatives and obtain in the leading order in $\hat{\omega}$ the following asymptotic expressions (bearing in mind that $\zeta = \xi^2$ and $\eta = \xi^{-2}$):

$$\begin{aligned}
&w_2(\zeta) = -\ln(1 - \zeta), && w_2'(\zeta) = \frac{1}{1 - \zeta}, && w_3(\zeta) = 1, && w_3'(\zeta) = O(\hat{\omega}^2),\\
&\tilde{w}_2(\zeta) = -\ln(1 - \zeta), && \tilde{w}_2'(\zeta) = \frac{1}{1 - \zeta}, && \tilde{w}_3(\zeta) = 1, && \tilde{w}_3'(\zeta) = O(\hat{\omega}^2),\\
&\breve{w}_1(\eta) = 1, && \breve{w}_1'(\eta) = -\frac{\mathrm{i}\,\hat{\omega}}{2}\frac{1}{1 - \eta}, && \breve{w}_3(\eta) = 1, && \breve{w}_3'(\eta) = \frac{\mathrm{i}\hat{\omega}}{2\eta},\\
&\hat{w}_1(\eta) = 1, && \hat{w}_1'(\eta) = \frac{\mathrm{i}\,\hat{\omega}}{2}\frac{1}{1 - \eta}, && \hat{w}_3(\eta) = 1, && \hat{w}_3'(\eta) = -\frac{\mathrm{i}\hat{\omega}}{2\eta}.
\end{aligned}$$

Using these formulae, one can readily calculate the limiting values of transformation coefficients in the long-wave approximation when $\hat{\omega} \to 0$. Their values are presented in the corresponding subsections.

REFERENCES

[1] M. J. Ablowitz and H. Segur. *Solitons and the Inverse Scattering Transform.* Philadelphia: SIAM, 1981.

[2] J. Adamek, X. Busch, and R. Parentani. “Dissipative fields in de Sitter and black hole spacetimes: Quantum entanglement due to pair production and dissipation”. In: *Phys. Rev. D* 87 (2013), p. 124039.

[3] T. R. Akylas. “On excitation of long nonlinear water waves by moving pressure distribution”. In: *J.Fluid Mech.* 141: (1984), pp. 455–66.

[4] J. Adcroft et al. *MITgcm User Manual.* MIT Department of EAPS., 2008.

[5] A. Amo et al. “Acoustic Black Hole in a Stationary Hydrodynamic Flow of Microcavity Polaritons”. In: *Phys. Rev. Lett.* 114 (2015), p. 036402.

[6] Y. Auregan and V. Pagneux. “Slow sound in lined flow ducts”. In: *J. Acoust. Soc. Am.* 138 (2015), p. 605.

[7] Y. Auregan et al. “Slow sound in a duct, effective transonic flows, and analog black holes”. In: *Phys. Rev. D* 92 (2015), p. 081503.

[8] C. Barrabes, V. Frolov, and R. Parentani. “Stochastically fluctuating black hole geometry, Hawking radiation, and the trans-Planckian problem”. In: *Phys. Rev. D* 62 (2000), p. 044020.

[9] E. F. Bartolomeusz. “The reflection of long waves at a step”. In: *Proc. Cambridge Phil. Soc.* (1958), pp. 106–118.

[10] A. Y. Basovich and V. I. Talanov. “Transformation of short surface waves on inhomogeneous currents”. In: *Izv. Amos. Ocean. Phys.* 13 (1977), pp. 514–519.

[11] F. Belgiorno et al. “Hawking Radiation from Ultrashort Laser Pulse Filaments”. In: *Phys. Rev. Lett.* 105 (2010), p. 203901.

[12] K. A. Belibassakis, Th. P. Gerostathis, and G. A. Athanassoulis. “A coupled-mode model for water wave scattering by horizontal, non-homogeneous current in general bottom topography”. In: *Appl. Ocean Res.* 33 (2011), pp. 384–397.

[13] K.A Belibassakis et al. “A coupled-mode model for water wave scattering by vertically sheared currents in variable bathymetry regions”. In: *Wave Motion* 74 (2017), pp. 73–92.

[14] B. Brasnett and T. Warn. “The amplification and capture of atmospheric solitons by topography: a theory of the onset of regional blocking”. In: *J. Atm. Sci.* 40: (1983), pp. 28–38.

[15] L. M. Brekhovskikh and V. V Goncharov. *Introduction to the mechanics of continuous media.* Moscow: Nauka, 1982.

[16] R. Brout et al. “Hawking radiation without trans-Planckian frequencies”. In: *Phys. Rev. D* 52 (1995), p. 4559.

[17] X. Busch, I. Carusotto, and R. Parentani. “Spectrum and entanglement of phonons in quantum fluids of light”. In: *Phys. Rev. A* 89 (2014), p. 043819.

[18] X. Busch and R. Parentani. “Dynamical Casimir effect in dissipative media: When is the final state nonseparable?” In: *Phys. Rev. D* 88 (2013), p. 045023.

[19] M. Cabral and R. Rosa. “Chaos for a damped and forced KdV equation”. In: *Physica D* 192 (2004), pp. 265–278.

[20] G. F. Carrier and H. P. Greenspan. “Water waves of finite amplitude on a sloping beach”. In: *Journal of Fluid Mechanics* 4 (1958), pp. 97–109.

[21] I. Carusotto and D. Gerace. “Analog Hawking radiation from an acoustic black hole in a flowing polariton superfluid”. In: *Phys. Rev. B* 86 (2012), p. 144505.

[22] E. N. Churaev, S. V. Semin, and Y. A. Stepanyants. “Transformation of internal waves passing over a bottom step”. In: *J. Fluid Mech.* 768 (2015), R3–1–R3–11.

[23] S. Churilov, A. Ermakov, and Y. Stepanyants. “Wave scattering in spatially inhomogeneous currents”. In: *Phys. Rev. D* 96 (2017), 064016, 25 pp.

[24] S. Churilov et al. “Scattering of long water waves in a canal with suddenly changed cross-section in the presence of a current”. In: *Phys. Rev. Fluids* (2017).

[25] R. H. Clarke, R. K. Smith, and D. G. Reid. “The morning glory of the Gulf of Carpentaria: an atmospheric undular bore”. In: *Monthly Weather Review* 109 (1981), pp. 1726–1750.

[26] S. L. Cole. “Transient waves produced by flow past a bump”. In: *Wave Motion* 7: (1985), pp. 579–87.

[27] A. Coutant and R. Parentani. “Undulations from amplified low frequency surface waves”. In: *Phys. Fluids* 26 (2014), p. 044106.

[28] A. Coutant, R. Parentani, and S. Finazzi. “Black hole radiation with short distance dispersion, an analytical S-matrix approach”. In: *Phys. Rev. D* 85 (2012), p. 024021.

[29] A. Coutant and S. Weinfurtner. “The imprint of the analogue Hawking effect in subcritical flows”. In: *Phys. Rev. D* 94 (2016), p. 064026.

[30] E. A. Cox et al. “On chaotic wave patterns in periodically forced steady-state KdVB and extended KdVB equations”. In: *Proc. R. Soc. A* 461 (2005), pp. 2857–2885.

[31] R. G. Dean. “Long wave modification by linear transitions”. In: *Journal of the Waterways, Harbors, and Coastal Engineering Division* 90 (1964), pp. 1–29.

[32] R. G. Dean and R. A. Dalrymple. *Water Wave Mechanics for Engineers and Scientists*. Prentice-Hall, Englewood Cliffs, 1984.

[33] P. Devillard, F. Dunlop, and B. Souillard. “Localization of gravity waves on a channel with random bottom”. In: *Journal of Fluid Mechanics* 186 (1988), pp. 521–538.

[34] I. Didenkulova and E. Pelinovsky. “Analytical solutions for tsunami waves generated by submarine landslides in narrow bays and channels.” In: *Pure and Applied Geophysics* 170 (2013), pp. 1661–1671.

[35] I. Didenkulova and E. Pelinovsky. “On shallow water rogue wave formation in strongly inhomogeneous channels”. In: *J. Phys. A: Math. and Theor.* 49 (2016), p. 194001.

[36] M. W. Dingemans. *Water wave propagation over uneven bottoms*. World Scientific, Singapore, 1997.

[37] R. B. Dingle. *Asymptotic expansions: Their derivation and interpretation*. Academic Press, 1973.

[38] K. Djidjeli et al. “A linearized implicit pseudo-spectral method for certain non-linear water wave equations”. In: *Commun. Numer. Meth. Engng* 24 (1998), pp. 977–993.

[39] V. D. Djordjevic and L. G. Redekopp. “The fussion and disintegration of internal solitary waves moving over two-dimensional topography”. In: *J. Phys. Oceanogr.* 8 (1978), pp. 1016–1024.

[40] R. A. Duine, A. S. Nunez, and A. Roldan-Molina. “Magnonic Black Holes”. In: *Phys. Rev. Lett.* 118 (2017), p. 061301.

[41] K. Dysthe. “Lecture notes on linear wave theory”. In: *A lecture given at the Summer School “Water Waves and Ocean Currents* (21–29 June) (2004), pp. 1–21.

[42] A. Ermakov and Y. Stepanyants. “Soliton interactions with external forcing within the Korteweg–de Vries equation”. In: *Website: https://kdvforcing.-wordpress.com/.* (2018).

[43] A. M. Ermakov and Y. A. Stepanyants. “Soliton Interaction with External Forcing within the Korteweg–de Vries Equation”. In: *Chaos: An Interdisciplinary Journal of Nonlinear Science* 29 (2019), p. 013117.

[44] A. M. Ermakov and Y. A. Stepanyants. “Transformation of long linear waves in the coastal zone with a variable bathymetry.” In: *Pure and Applied Geophysics* https://doi.org/10.1007/s00024-019-02259-4 (2019).

[45] L.-P. Euvé et al. “Observation of noise correlated by the Hawking effect in a water tank”. In: *Phys. Rev. Lett.* 117 (2016), p. 121301.

[46] A. L. Fabrikant and Yu. A. Stepanyants. *Propagation of waves in shear flows.* World Scientific, Singapore, 1998.

[47] D. Faccio et al., eds. *Analogue gravity phenomenology.* Lecture Notes in Physics. v. 870. Switzerland: Springer International Publishing, 2013.

[48] F. Ferrario et al. “The effectiveness of coral reefs for coastal hazard risk reduction and adaptation”. In: *Nature Communications* 5 (2014), p. 3794.

[49] E. R. Gazizov and D. V. Maklakov. “Waveless gravity flow over an inclined step”. In: *J. Appl. Mech. Tech. Phys.* 45 (2004), pp. 379–388.

[50] J. P. Germain. “Coefficients de reflexion et de transmission en eau peu profonde”. In: *Rozprawy Hydrotechniczne* (1984), pp. 5–118.

[51] A. R. Giniyatullin et al. “Transformation of narrowband wavetrains of surface gravity waves passing over a bottom step”. In: *Math. Model. Natural Proc.* 9 (2014), pp. 32–41.

[52] I. S. Gradshteyn and I. M. Ryzhik. *Table of integrals, series, and products.* 7th ed. Academic Press, Amsterdam et al., 2007.

[53] A. E. Green and P. M. Naghdi. “A nonlinear theory of water waves for finite and infinite depths”. In: *Philos. Trans. Roy. Soc. London. Ser.* 320 (1986), pp. 37–70.

[54] A. E. Green and P. M. Naghdi. “Directed fluid sheets”. In: *Proc. Roy. Soc. London. Ser.* 347 (1976), pp. 447–473.

[55] A. E. Green and P. M. Naghdi. “Further developments in a nonlinear theory of water waves for finite and infinite depths”. In: *Philos. Trans. Roy. Soc. London. Ser.* 324 (1987), pp. 47–72.

[56] A. E. Green and P. M. Naghdi. “Water waves in a nonhomogeneous incompressible fluid”. In: *J. Appl. Mech.* 44 (1977), pp. 523–528.

[57] R. Grimshaw. “Resonant flow of a rotating fluid past an obstacle: the general case”. In: *Stud. Appl. Maths.* 83: (1990), pp. 249–69.

[58] R. Grimshaw. “Resonant forcing of barotropic coastally trapped waves”. In: *J.Phys. Oceanogr.* 17: (1987), pp. 53–65.

[59] R. Grimshaw. “Transcritical flow past an obstacle”. In: *ANZIAM J.* 52: (2010), pp. 1–25.

[60] R. Grimshaw and M. Maleewong. “Transcritical flow over two obstacles: forced Korteweg–de Vries framework”. In: *J. Fluid Mech.* 809: (2016), pp. 918–940.

[61] R. Grimshaw and H. Mitsudera. “Slowly–varying solitary wave solutions of the perturbed Korteweg–de Vries equation revisited”. In: *Stud. Appl. Math.* 90: (1993), pp. 75–86.

[62] R. Grimshaw and E. Pelinovsky. “Interaction of a solitary wave with an external force in the extended Korteweg–de Vries equation”. In: *Int. J. Bifurcation and Chaos* 12 (2002), pp. 2409–2419.

[63] R. Grimshaw, E. Pelinovsky, and A. Bezen. “Hysteresis phenomena in the interaction of a damped solitary wave with an external force”. In: *Wave Motion* 26: (1997), pp. 253–274.

[64] R. Grimshaw, E. Pelinovsky, and P. Sakov. “Interaction of a solitary wave with an external force moving with variable speed”. In: *Stud. Appl. Math.* 97: (1996), pp. 235–276.

[65] R. Grimshaw, E. Pelinovsky, and T. Talipova. “Fission of a weakly nonlinear interfacial solitary wave at a step”. In: *Geophys. Astrophys. Fluid Dyn.* 102 (2008), pp. 179–194.

[66] R. Grimshaw, E. Pelinovsky, and X. Tian. “Interaction of a solitary wave with an external force”. In: *Physica D* 77: (1994), pp. 405–433.

[67] R. Grimshaw and N. Smyth. “Resonant flow of a stratified fluid over topography”. In: *J. Fluid Mech.* 169: (1986), pp. 429–64.

[68] R. Grimshaw and X. Tian. “Periodic and chaotic behaviour in a reduction of the perturbed Korteweg–de Vries equation”. In: *Proc. R. Soc. A Math. Phys. Eng. Sci.* 445 (1994), pp. 1–21.

[69] R. Grimshaw and Y. Zengxin. “Resonant generation of finite–amplitude waves by the flow of a uniformly stratified fluid over topography”. In: *J. Fluid Mech.* 229: (1991), pp. 603–28.

[70] R. Grimshaw, D. H. Zhang, and K. W. Chow. “Generation of solitary waves by transcritical flow over a step”. In: *Journal of Fluid Mechanics* 587 (2007), pp. 235–254.

[71] D. L. Harris and A. Vila-Concejo. “Wave transformation on a coral reef rubble platform”. In: *Journal of Coastal Research* 65 (2013), pp. 506–510.

[72] S. W. Hawking. “Particle creation by black holes”. In: *Communications in Mathematical Physics* 43 (1975), pp. 199–220.

[73] T. Jacobson. “Black hole evaporation and ultrashort distances”. In: *Phys. Rev. D* 44 (1991), p. 1731.

[74] T. Jacobson. “Black hole radiation in the presence of a short distance cutoff”. In: *Phys. Rev. D* 48 (1993), p. 728.

[75] P. C. Jain, R. Shankar, and D. Bhardwaj. “Numerical Solution of the Korteweg-de Vries (KdV) Equation”. In: *Chaos* 8 (1997), pp. 943–951.

[76] G. Jannes et al. “Hawking radiation and the boomerang behavior of massive modes near a horizon”. In: *Phys. Rev. D* 83 (2011), p. 104028.

[77] W. L. Jones. “Reflexion and stability of waves in stably stratified fluids with shear flow: a numerical study”. In: *J. Fluid Mech.* 34 (1968), pp. 609–624.

[78] K. Kajiura. “On the partial reflection of water waves passing over a bottom of variable depth.” In: *Proceedings of the tsunami meetings, 10th Pacific Science Congress, IUGG Monograph* 24 (1961), pp. 206–234.

[79] A. M. Kamchatnov. “Self-similar wave breaking in dispersive Korteweg-de Vries hydrodynamics”. In: *Chaos* 29 (2019), p. 023106.

[80] A. M. Kamchatnov et al. “Undular bore theory for the Gardner equation”. In: *Physical review E* 86 (2012), p. 036605.

[81] J. T. Kirby and R. A. Dalrymple. “Propagation of obliquely incident water waves over a trench”. In: *Journal of Fluid Mechanics* 133 (1983), pp. 47–63.

[82] I. A. Korostil. *PhD thesis: Models of morning glory as interacting nonlinear waves.* School of Mathematical Sciences Monash University, 2017.

[83] I. A. Korostil and S. R. Clarke. “Fourth-order numerical methods for the coupled Korteweg–de Vries equations”. In: *ANZIAM J* 56 (2015), pp. 275–285.

[84] J. N. Kreisel. “Surface waves”. In: *Quart. Appl. Math.* 7 (1949), p. 21.

[85] Yu. M. Krylov. “Diffraction of waves in a liquid”. In: *Proceedings of the state Institute of Oceanography* (1949), pp. 13–18.

[86] A. Kurkin, S. Semin, and Y. Stepanyants. “Transformation of surface waves over a bottom step”. In: *Izv. Atmos. Ocean. Phys.* 51 (2015), pp. 214–223.

[87] A. A. Kurkin, S. V. Semin, and Yu. A. Stepanyants. “Transformation of surface waves above the bottom ledge”. In: *Izvestia RAN. FAO.* 51 (2015), pp. 242–252.

[88] H. Lamb. *Hydrodynamics.* 6th ed. Cambridge University Press, 1932.

[89] L. D. Landau and E. M. Lifshitz. *Fluid Mechanics.* Pergamon Press, Oxford, 1987.

[90] S. J. Lee, G. T. Yates, and T. Y. Wu. “Experiments and analyses of upstream–advancing solitary waves generated by moving disturbances”. In: *J. Fluid Mech.* 199: (1989), pp. 569–93.

[91] S. Liberati and L. Maccione. “Astrophysical Constraints on Planck Scale Dissipative Phenomena”. In: *Phys. Rev. Lett.* 112 (2014), p. 151301.

[92] R. Lin, Y. Zeng, and W-X. Ma. “Solving the KdV hierarchy with self-consistent sources by inverse scattering method”. In: *Physica A* 291: (2001), pp. 287–298.

[93] M. S. Longuet-Higgins. “Surface manifestations of turbulent flow”. In: *J. Fluid Mech.* 308 (1996), pp. 15–29.

[94] M. A. Losada, C. Vidal, and R. Medina. “Experimental study of the evolution of a solitary wave at an abrupt junction”. In: *J. Geophys. Res.* 94 (1989), pp. 14557–14566.

[95] Y. L. Luke. *Mathematical Functions and their Approximations.* Academic Press, New York, 1975.

[96] J. Macher and R. Parentani. “Black/white hole radiation from dispersive theories”. In: *Phys. Rev. D* 79 (2009), p. 124008.

[97] V. Maderich et al. “Interaction of a large amplitude interfacial solitary wave of depression with a bottom step”. In: *Phys. Fluids* 22 (2010), p. 076602.

[98] P. Maissa, G. Rousseaux, and Y. Stepanyants. “Negative energy waves in shear flow with a linear profile”. In: *Eur. J. Mech. – B/Fluids* 56 (2016), pp. 192–199.

[99] P. Maissa, G. Rousseaux, and Y. Stepanyants. “Wave blocking phenomenon of surface waves on a shear flow with a constant vorticity”. In: *Phys. Fluids* 28 (2016), p. 032102.

[100] B. A. Malomed. “Interaction of a moving dipole with a soliton in the KdV equation”. In: *Physica D* 32 (1988), pp. 393–408.

[101] J. S. Marshal and P. M. Naghdi. “Wave reflection and Transmission by steps and rectangular obstacles in channels of finite depth”. In: *Theoret. Comput. Fluid Dynamics.* (1990), pp. 287–301.

[102] J. Marshall et al. “A Finite-volume, incompressible Navier-Stokes model for studies of the ocean on parallel computers”. In: *J. Geophys. Res.* 102 (1997), pp. 5753–5766.

[103] J. Marshall et al. “Hydrostatic, quasi-hydrostatic, and non-hydrostatic ocean modelling”. In: *J. Geophys. Res.* 102 (1997), pp. 5733–5752.

[104] S. R. Massel. “Harmonic generation by waves propagating over a submerged step”. In: *Coastal Eng.* 7 (1983), pp. 357–380.

[105] S. R. Massel. *Hydrodynamics of the coastal zone.* Amsterdam: Elsvier, 1989.

[106] M. E. McIntyre. “On the ‘wave momentum’ myth”. In: *J. Fluid Mech.* 106 (1981), pp. 331–347.

[107] C. C Mei. *Basic gravity wave theory. Handbook of coastal and ocean engineering. V. 1: Wave phenomena and coastal structures, Chapter 1.* Ed. by J. B. Herbich, Gulf Publishing Co., 1990, pp. 1–62.

[108] C. C. Mei and J. L. Black. “Scattering of surface waves by rectangular obstacles in waters of finite depth”. In: *J. Fluid Mech.* 38 (1969), pp. 499–511.

[109] W. K. Melville and K. R. Helfrich. “Transcritical two–layer flow over topography”. In: *J. Fluid Mech.* 178: (1987), pp. 31–52.

[110] J. W. Miles. “Surface-wave scattering matrix for a shelf”. In: *J. Fluid Mech* 28 (1967), pp. 755–767.

[111] N. R. Mirchina and E. N. Pelinovski. “Nonlinear transformation of long waves at a bottom step”. In: *J. Korean Society of Coastal and Ocean Engineers* 4 (1992), pp. 161–167.

[112] H. Mitsudera and R. Grimshaw. “Generation of mesoscale variability by resonant interaction between a baroclinic current and localized topography”. In: *J. Phys. Oceanogr.* 21: (1991), pp. 737–65.

[113] J. N. Newman. “Propagation of water waves past long two-dimensional obstacles”. In: *J. Fluid Mech.* 23 (1965), pp. 23–29.

[114] I. S. Nudner. “Deformation of Waves at a Rectangular Ledge.” In: *Trudy coordin. meeting on hydraulic engineering* 84 (1973), pp. 75–80.

[115] M. Obregon and Y. Stepanyants. “On numerical solution of the Gardner–Ostrovsky equation”. In: *Math. Model. Nat. Phenom.* 7 (2012), 113—130.

[116] M. A. Obregon, E. Sanmiguel-Rojas, and R. Fernandez-Feria. “High accuracy numerical methods for the Gardner–Ostrovsky equation”. In: *Applied Mathematics and Computation* 240 (2014), pp. 140–148.

[117] F. W. J. Olver. *Introduction to Asymptotics and Special Functions.* Academic Press, London et al., 1974.

[118] L. A. Ostrovsky et al. “Beyond the KdV: Post-explosion development”. In: *Chaos* 25: (2015), p. 097620.

[119] R. Parentani. “Quantum metric fluctuations and Hawking radiation”. In: *Phys. Rev. D* 63 (2001), p. 041503.

[120] A. Patoine and T. Warn. “The interaction of long, quasi – stationary baroclinic waves with topography”. In: *J. Atm. Sci.* 39 (1982), pp. 1018–25.

[121] E. Pelinovsky. “Autoresonance processses in the interaction of of solitary waves with external fields”. In: *Hydromechanics* 2: (2000), pp. 67–73.

[122] E. Pelinovsky. “On the transformation of a single wave on a shelf with a horizontal bottom”. In: *Theoretical and experimental studies on the problem of tsunamis. Nauka M* (2016), pp. 61–63.

[123] E. Pelinovsky et al. “Solitary wave transformation on the underwater step: theory and numerical experiments”. In: *Applied Math Computations* 217 (2010), pp. 1704–1718.

[124] E. N. Pelinovsky. *Hydrodynamics of Tsunami Waves.* N. Novgorod, IAP RAS, 1996.

[125] D. H. Peregrine. “Calculations of the development of an undular bore”. In: *J. Fluid Mech.* 25 (1966), pp. 321–330.

[126] T. G. Philbin. “An exact solution for the Hawking effect in a dispersive fluid”. In: *Phys. Rev. D* 94 (2016), p. 064053.

[127] T. G. Philbin et al. “Fiber-Optical Analog of the Event Horizon”. In: 319 (2008), pp. 1367–1370.

[128] L. Pitaevskii and S. Stringari. *Bose-Einstein Condensation.* Oxford University Press, 2003.

[129] V. Rey, M. Belzons, and E. Guazzellit. “Propagation of surface gravity waves over a rectangular submerged bar”. In: *J. Fluid Mech.* 235 (1992), pp. 453–479.

[130] S. Robertson. “The theory of Hawking radiation in laboratory analogues”. In: *J. Phys. B: At. Mol. Opt. Phys.* 45 (2012), p. 163001.

[131] S. Robertson, F. Michel, and R. Parentani. “Scattering of gravity waves in subcritical flows over an obstacle”. In: *Phys. Rev. D* 93 (2016), p. 124060.

[132] S. Robertson and R. Parentani. “Hawking radiation in the presence of high-momentum dissipation”. In: *Phys. Rev. D* 92 (2015), p. 044043.

[133] S. J. Robertson. “The theory of Hawking radiation in laboratory analogues”. In: *J. Phys. B* 45 (2012), p. 163001.

[134] G. Rousseaux. “Analogue Gravity Phenomenology: Analogue Spacetimes and Horizons, from Theory to Experiment edited by D. Faccio, F. Belgiorno, S. Cacciatori, V. Gorini, S. Liberati, and U. Moschella”. In: *The basics of water waves theory for analogue gravity* (2013), pp. 81–107.

[135] G. Rousseaux et al. “Horizon effects with surface waves on moving water”. In: *New J. Phys.* 12 (2010), p. 095018.

[136] G. Rousseaux et al. “Observation of negative-frequency waves in a water tank: a classical analogue to the Hawking effect?” In: *New J. Phys.* 10 (2008), p. 053015.

[137] N. Sanford et al. “Stability of traveling wave solutions to the Whitham equation”. In: *Physics Letters A* 378 (2014), pp. 2100–2107.

[138] R. Schutzhold and W. G. Unruh. “Gravity wave analogues of black holes”. In: *Phys. Rev. D* 66 (2002), p. 044019.

[139] F. J. Seabra-Santos, D. P. Renouard, and A. M. Temperville. “Numerical and experimental study of the transformation of a solitary wave over a shelf or isolated obstacle”. In: *J. Fluid Mech.* 176 (1987), pp. 117–134.

[140] R. Smith. “The reflection of short gravity waves on a non-uniform current”. In: *Math. Proc. Camb. Phil. Soc.* 78 (1975), pp. 517–525.

[141] N. Smyth. “Modulation theory solution for resonant flow over topography”. In: *Proc. Roy. Soc. London A* 409: (1987), pp. 79–97.

[142] L. N. Sretensky. *Theory of wave motions of a fluid.* The main edition of the physical and mathematical literature of the publishing house Nauka. M., 1977.

[143] J. Steinhauer. “Observation of quantum Hawking radiation and its entanglement in an analogue black hole”. In: *Nature Physics* 12 (2016), pp. 959–965.

[144] J. Steinhauer. “Observation of self-amplifying Hawking radiation in an analogue black hole laser”. In: *Nature Physics* 10 (2014), pp. 864–869.

[145] Yu. A. Stepanyants. “On the Soliton Propagation in an Inhomogeneous Long Line”. In: *Radio Engineering and Electronics* 22 (1977), pp. 995–1002.

[146] M. Stiassnie and G. Dagan. “Partial reflexion of water waves by non-uniform adverse currents”. In: *J. Fluid Mech.* 92 (1979), pp. 119–129.

[147] J. J. Stoker. *Water waves: The mathematical theory with applications.* John Willey & Sons Inc., 1958.

[148] K. Takano. “Effet d’un changement brusque de profondeur sur une houle irrotationelle”. In: *La mer* (1967), pp. 100–116.

[149] K. Takano. “Effets d’un obstacle parallelepipedique sur la propagation de la houle (The effect of a rectangular obstacle on wave propagation)”. In: *La Houille Blanche* (1960), pp. 247–267.

[150] T. Talipova et al. “Internal solitary wave transformation over a bottom step: Loss of energy”. In: *Phys. Fluids* 25 (2013), p. 032110.

[151] K. Trulsen and C. C. Mei. “Double reflection of capillary/gravity waves by a non-uniform current: a boundary-layer theory”. In: *J. Fluid Mech.* 251v (1993), pp. 239–271.

[152] W. G. Unruh. “Experimental Black hole Evaporation?” In: *Phys. Rev. Lett.* 46 (1981), p. 1351.

[153] W. G. Unruh. “Sonic analogue of black holes and the effects of high frequencies on black hole evaporation”. In: *Phys. Rev. D* 51 (1995), p. 2827.

[154] M. Wang. “Exact solutions for a compound KdV-Burgers equation”. In: *Phys. Lett. A* 213: (1996), pp. 279–287.

[155] S. Weinfurtner et al. “Measurement of stimulated Hawking emission in an analogue system”. In: *Phys. Rev. Lett.* 106 (2011), p. 021302.

[156] G. B. Whitham. *Linear and Nonlinear Waves.* John Willey & Sons Inc., 1974.

[157] T. Y. Wu. “Generation of upstream advancing solitons by moving disturbances”. In: *J.Fluid Mech.* 184: (1987), pp. 75–99.